Hendrawan Diandaru Bayu Aji

Hybrid BEM-FEM for 2D and 3D dynamic soil-structure interaction considering arbitrary layered half-space and nonlinearities

Schriftenreihe des Lehrstuhls
Geomechanik und Geotechnik
Christian-Albrechts-Universität zu Kiel

8

Schriftenreihe des Lehrstuhls Geomechanik und Geotechnik
Christian-Albrechts-Universität zu Kiel
Heft 8

ISSN 2365-7162

Herausgeber:

Lehrstuhl für Geomechanik und Geotechnik

Christian-Albrechts-Universität zu Kiel

Prof. Dr.-Ing. habil. Frank Wuttke

Ludewig-Meyn-Straße 10

24118 Kiel

Telefon: ++49 – (0)431 – 880 2857

Telefax: ++49 – (0)431 – 880 7606

Internet: www.geotechnics.ifg.uni-kiel.de

Bezugsadresse:

Christian-Albrechts-Universität zu Kiel
Lehrstuhl für Geomechanik und Geotechnik

Hybrid BEM-FEM for 2D and 3D dynamic soil-structure interaction considering arbitrary layered half-space and nonlinearities

DISSERTATION

in fullfillment of the requirements for the degree
"Doktor-Ingenieur" (Dr.-Ing.)"
of the Faculty of Mathematics and Natural Sciences
at Kiel University

submitted by

Hendrawan Diandaru Bayu Aji

Kiel, 2023

Gutachter:

1. Prof. Dr.-Ing. habil. Frank Wuttke
   Kiel University
2. Prof. Dr. Petia Dineva
   Bulgarian Academy of Sciences

Tag der mündlichen Prüfung: 03.05.2023
Zum Druck genehmigt: 21.06.2023

Der Dekan

Eidesstattliche Erklärung

Hiermit erkläre ich, dass ich die vorliegende Arbeit "Hybrid BEM-FEM for 2D and 3D dynamic soil-structure interaction considering arbitrary layered half-space and nonlinearities" nach Inhalt und Form—abgesehen von der Beratung durch meinen Betreuer—selbständig verfasst und keine weiteren Quellen und Hilfsmittel als die im Quellenverzeichnis angegeben verwendet habe. Diese Arbeit hat weder ganz, noch im Teilen, bereits an anderer Stelle im Rahmen eines Prüfungsverfahrens oder einer Promotionskomission zur Erlangung des Doktorgrades vorgelegen. Ich erkläre, dass die vorliegende Arbeit gemäss den Grundsätzen zur Sicherung guter wissenschaftlicher Praxis der Deutschen Forschungsgemeinschaft erstellt wurde. Ich erkläre, dass mir nie ein akademischer Grad entzogen wurde.

Kiel, Mai 2023
Hendrawan Diandaru Bayu Aji

Vorwort des Herausgebers

Die vorliegende Promotionsschrift von Herrn Dr.-Ing. Hendrawan D.B. Aji ist dem Forschungs- und Arbeitsgebiet *Bodendynamik* und speziell dem *Erdbebeningenieurwesen* zuzuordnen. In dieser Dissertation wurde eine effektive hybride Methodik zur Beschreibung von elastischen Wellenfeldern in beliebig geschichteten Halbraumen und für die Beschreibung der linearen und nichtlinearen Boden-Bauwerk-Interaktion für 2D und 3D Abbildungen entwickelt. Grundlage der Entwicklung ist die vollständige Kopplung von FE- und BE-Modellen im Frequenzbereich bzw. auch als sequentieller Prozeß im Frequenz-Zeit-Bereich. Die Kopplung als FEM-hosted, direkte Kopplungsmethode, wurde als Makro-Finites-Element am Rand des FEM Bereiches definiert. Der Vorteil dieser Herangehensweise ist die effektive Simulation von Wellenfeldern auch für sehr große geologische Formationen und der Berüchsichtigung von komplexen Boden-Bauwerks-Interaktionen oder anderen nichtlinearen Prozessen in definierten FEM Gebieten. Neben der zeiteffektiven Numerik, nimmt ebenfalls die Genauigkeit der Simulation deutlich zu, da deutlich weniger Vernetzungen in dem großen Gebiet als eine reine FEM Abbildung erforderlich werden. Weiterhin kann durch die Nutzung der BE-Methoden, die Sommerfeld Abstrahlungsbedingung, leicht erfüllt werden und stellt kein Problem bzw. zusätzlichen Aufwand, wie in der normalen Nutzung von FEM dar. Die bereits in anderen Arbeiten genutzte Makro-Finites-Element Methodik wurde in der vorliegenden Arbeit auf den 3D Fall und für beliebige Schichtungsabfolgen erweitert. Ebenso liegt die Modellierung als Subroutine für die Nutzung in Abaqus für eine weitere Nutzung vor. Die genutzten Formulierungen wurden an analytischen und numerischen Beispielen validiert. Neben der hybriden Kopplung und Modellentwicklung, wurde der vollständige 3D Momententensor zur Abbildung komplexer Erdbebenherde als räumliche Dipol-Quellen implementiert. Durch die Implementierung der sequentiellen Frequenz-Zeit-Bereichs Methodik können die Makro-Finite-Elemente für die Abbildung der nichtlinearen dynamischen Boden-Bauwerk-Interaktion genutzt werden. Die Anwendung der Entwicklung wurde an mehreren Fallbeispielen, wie der Interaktion von Brückenfundierungen, Gebäuden, Containments unter Erdbeben und von seismisch induzierten Wellenfeldern in großen geologischen Speicherformationen oder Fracking, dokumentiert. Die Dissertationsschrift beinhaltet die konsequente Weiterentwicklung von bisherigen Ansätzen und als auch Neuentwicklungen zu bodendynamischen Simulationen in heterogenen Halbräumen bzw. der dynamischen Boden-Bauwerk-Interaktion.

Kiel, im Mai 2023 Frank Wuttke

Acknowledgements

I would like to begin this dissertation with *Bismillahirrahmanirrahim* (in the name of Allah, the Most Gracious, the Most Merciful). Only with His permission I am arrived in this point, cherishing the gift of knowledge.

I am forever grateful to Prof. Dr.-Ing. F. Wuttke for the opportunity to join his research group back in 2016. I would also like to express my gratitude to Prof. P. Dineva who has also advised me during this research. This work is built on the foundation of inspiration, influence, and support, and using the materials of guidance, discussion, and patience that they have given me in abundance throughout the research period.

I would like to also appreciate my present and former colleagues in the Chair of Geomechanics and Geotechnics of the Institute of Geosciences, CAU Kiel, whose vibrations have interacted with, influenced, and enriched my own oscillation of knowledge and way of thinking.

Last but not least, I would like to thank my parents, my wife Irma, and my children Bella and Ghaissan, whose unyielding love and support carry me forward against the challenges.

Hendrawan Diandaru Bayu Aji

Abstract

Experiences and studies have shown that soil-structure interaction (SSI) effect has a vital role in the dynamic behaviour of a soil-structure system. This is true in earthquake-resistant design and in cases of low-level vibrations such as those coming from induced seismicity, energy production, or in the case of vibration-sensitive buildings, e.g., microelectronics factories, research laboratories, etc. Despite this, analyses involving dynamic SSI are still challenging for practicing engineers due to their complexity and accessibility. The demands for more economical structures and to reduce CO_2 emission mean that a more precise soil-structure analysis/design tool will be more important. In this thesis, the hybrid BEM-FEM implementation is aimed at practicality by combining commercial software and an in-house code. The pre-processing task can be performed under one graphical environment. It is then enhanced with the capability to compute different types of dynamic sources and other improvements to increase its efficiency, accuracy, and modeling flexibility, which is essential when dealing with 3D problems.

Further, the underlying soil is commonly a layered profile with arbitrary geometries. The material properties vary over the depth without following a specific pattern. Most existing solutions solve the problem through simplification of the geometry and pattern. Layer-wise condensation is developed to solve these cases using hybrid BEM-FEM. The derivation of the method and its scheme for numerical implementation is presented. The method significantly reduces the computational memory requirement. Another challenge in the dynamic SSI is the consideration of secondary nonlinearities, which can be addressed using the hybrid method in the time domain. However, the time domain BEM and iterative hybrid method are computationally costly, and implementation of such a hybrid method on commercial software is tedious. The solution to address this case using a sequential frequency-time domain procedure is presented. The relatively simple approach makes it possible to consider the nonlinearities in the simulation without using the time domain BEM and without requiring additional iterations. Verification studies show that these methods are able to accurately compute the effect of the layering and nonlinearities.

Case studies demonstrating the application of the enhanced hybrid method are presented: (1) investigation of dynamic behaviour of typical integral bridges; (2) foundation-soil-foundation interaction problem subjected to ground-borne vibrations where the damage state of the geological media is considered using dilute approximation; (3) structure-soil-structure interaction problem subjected

to short- and medium-range of transient excitations; and (4) nonlinear dynamic SSI of a 2D arch bridge and a 3D multi-storey structure under point source and double-couple source excitations, respectively. These case studies are aimed to investigate the following critical factors: (1) the dynamic site effect due to impedance contrast of soil layers, (2) lateral inhomogeneity effect, (3) influence of the dynamic source properties, (4) conversion of body waves into surface waves, (5) soil-foundation or soil-structure dynamic interaction, and (6) influence of secondary nonlinearities. The results show that the complex wave field on the surface and the structure's response are highly influenced by these key factors and their interactions.

Zusammenfassung

Erfahrungen und Studien zeigten, dass der Boden-Bauwerk-Interaktionseffekt (BBI) eine entshceidende Rolle für das dynamische Verhalten eines Boden-Bauwerk-Systems spielt. Dies gilt sowohl für die erdbebensichere Design als auch für schwache Erschütterungen oder bei erschütterungs-empfindlichen Gebäuden. Denoch sind Analysen, die dynamischen BBI einbeziehen, aufgrund ihrer Komplexität und Zugänglichkeit immer noch eine Herausforderung für praktizierende Ingenieure. Die Forderungen nach wirtschaftlicheren Strukturen und die Verringerung des CO_2-Ausstoßes bedeuten, dass ein präziseres Boden-Struktur-Analyse- und Entwurfswerkzeug immer wichtiger wird. In dieser Arbeit wird die hybride BEM-FEM-Implementierung durch die Kombination von kommerzieller Software und einem hauseigenen Code auf Praktikabilität ausgerichtet. Anschließend wird die Software um die Möglichkeit erweitert, verschiedene Arten von dynamischen Quellen zu berechnen und andere Verbesserungen vorzunehmen, um die Effizienz, die Genauigkeit, und die Flexibilität der Modellierung zu erhöhen, was bei der Bearbeitung von 3D-Problemen von entscheidender Bedeutung ist.

Darüber hinaus ist der darunter liegende Boden in der Regel ein geschichtetes Profil mit willkürlicher Geometrie. Die Materialeigenschaften variieren in der Tiefe, ohne einem bestimmten Muster zu folgen. Die meisten bestehenden Lösungen lösen das Problem durch Vereinfachung der Geometrie und des Musters. Die schichtweise Kondensation wird entwickelt, um diese Fälle mit Hilfe der hybriden BEM-FEM zu lösen. Die Herleitung der Methode und ihr Schema für die numerische Umsetzung werden vorgestellt. Die Methode reduziert den Speicherbedarf für die Berechnung erheblich. Eine weitere Herausforderung bei der dynamischen SSI ist die Berücksichtigung sekundärer Nonlinearitäten, die mit der hybriden Methode im Zeitbereich gelöst werden kann. Die BEM im Zeitbereich und die iterative Hybridmethode sind jedoch sehr rechenaufwändig, und die Implementierung einer solchen hybriden Methode mit kommerzieller Software ist mühsam. Es wird eine Lösung für diesen Fall vorgestellt, bei der ein sequentielles Verfahren im Frequenz-Zeit-Bereich zum Einsatz kommt. Der relativ einfache Ansatz ermöglicht es, die Nonlinearitäten in der Simulation zu berücksichtigen, ohne die Zeitbereichs-BEM zu verwenden und ohne zusätzliche Iterationen zu benötigen. Verifikationsstudien zeigen, dass diese Methoden in der Lage sind, die Auswirkungen der Schichtung und der Nonlinearitäten genau zu berechnen.

Es werden Fallstudien vorgestellt, die die Anwendung der verbesserten hybriden BEM-FEM demonstrieren: (1) Untersuchung des dynamischen Verhaltens typischer integraler Brücken; (2) Fundament-Boden-Fundament-Interaktionsproblem unter dem Einfluss von Bodenschwingungen, wobei der Schädigungszustand des geologischen Mediums unter Verwendung einer verdünnten Näherung berücksichtigt wird; (3) Struktur-Boden-Struktur-Interaktionsproblem unter kurz- und mittelfristigen transienten Erregungen; und (4) nonlineare dynamische SSI einer 2D- Bogenbrücke und eines 3D-Mehrgeschossbauwerks unter Punktquellen- bzw. Doppelkoppelquellenerregungen. Diese Fallstudien zielen darauf ab, die folgenden Schlüsselfaktoren zu untersuchen: (1) der dynamische Standorteffekt aufgrund des Impedanzkontrasts der Bodenschichten, (2) der Effekt der lateralen Inhomogenität, (3) der Einfluss der dynamischen Quelleneigenschaften, (4) die Umwandlung von Körperwellen in Oberflächenwellen, (5) die dynamische Interaktion zwischen Fundament und Boden bzw. zwischen Bauwerk und Boden, und (6) der Einfluss sekundärer Nonlinearitäten. Die Ergebnisse zeigen, dass das komplexe Wellenfeld an der Oberfläche und die Reaktion des Bauwerks in hohem Maße von diesen Schlüsselfaktoren und ihren Wechselwirkungen beeinflusst werden.

Contents

List of Figures

List of Tables

Chapter 1

Introduction

1.1 Background and motivation

The term **soil-structure interaction** (**SSI**) describes the reciprocity between a supporting ground/soil and the structure built on it, where each one affects the response of the other. In a more detailed form, the term is also referred to as soil-foundation-structure interaction. For simplicity, the term SSI will be used throughout this monograph. SSI, both static and dynamic, has been continuously researched since its conception in the 19^{th} century. The pace has further increased in recent decades, driven by the development of computers and numerical methods, the industrial needs for more economical but robust structures, and the demands for improved earthquake-resistant design (Kausel, 2010). Under civil engineering, understanding the mechanism and the effects of dynamic SSI is an intersectional concern between geotechnical and structural engineering disciplines. The current study is particularly focused on the **dynamic SSI**. This study also addresses the analysis of **structure-soil-structure interaction** (**SSSI**), where multiple structures interact and influence each other (Wong and Trifunac, 1975).

In the **dynamic-resistant design of structures**, i.e., determining the stresses and displacements due to dynamic loads, SSI is one of the critical factors (Wolf, 1985). It has been recognized that the change in the structure's response due to the interactions between the ground and structure becomes significant when the supporting ground/soil is not firm (Kramer, S. L., 1996). Therefore, the consideration of SSI becomes more critical in such cases, while it may be neglected for structures founded on stiff soil. One of the main practical uses of dynamic SSI analyses is in **earthquake engineering**, as earthquakes remain one of the most dangerous natural hazards. For example, due to the 2004 Indian Ocean earthquake, 227,898 people were killed or were missing and presumed dead, and 1.7

million people were displaced (U.S.G.S., 2012). The 2008 Sichuan (China) earthquake caused 70,000 people dead, with another 370,000 people injured and 18,000 missings (Yön, Sayın, and Onat, 2017). In addition to the field of earthquake engineering, dynamic SSI is also an essential aspect in the engineering of structures for **vibrations mitigation**, such as those occurring from transportation, machinery operation, construction, mining, energy generation, etc., or in the case of vibration-sensitive buildings such as microelectronic productions, medical facilities, research facilities.

The dynamic SSI is composed of **kinematic and inertial interactions**. Without the presence of any structure, ground-borne vibrations, such as those induced by earthquakes, machinery operations, transportation, wind turbines, blasting, etc., result in deformation of the ground surface referred to as the **free-field motion** (Wolf, 1985; Kramer, S. L., 1996). The **kinematic interaction** describes the deviation in the response of the soil-structure system compared to the free-field response due to the geometry and the higher stiffness of the foundation relative to the surrounding soil. The foundation's position, whether it is built on or embedded in the soil, also contribute to this point. The effects of the foundation's higher stiffness on the spatial variation of the motion over the contact horizontal plane and over the embedment depth are referred to as the base slab averaging and the embedment effect, respectively (FEMA, 2020). The ground motion also activates the structure's inertial response due to the mass distribution throughout the structure, which thereby retransmits the energy back into the supporting soil. This is referred to as the **inertial interaction** (Kramer, S. L., 1996). The inertial response also leads to internal base shear forces and moments against which the structure and its foundation must be designed. The flexibility of the supporting soil (compared to fixed-base assumption) and the propagation and absorption of waves by the supporting soil also yield the actual natural frequency and damping of the structure as an integral part of the soil-structure system. Thus, these dynamic characteristic depends not only on the geometry and material properties of the structure but also on the material properties of the underlying soil. These phenomena are often referred to as the **period lengthening** and **increase of effective damping**, based on the comparison of these properties to those when the structure is analysed using zero Dirichlet (fixed-base) boundary conditions. Due to all of these effects, in the field of structural dynamics and earthquake engineering, SSI is one of the key factors determining the earthquake or the dynamic resistance of the structure.

The commonly recognized understandings of the SSI effect on structural design are as follows: (1) In the case that a structure is founded on stiff soil, the difference of the structural response including the SSI effect is **negligible** when compared to the response with fixed displacement boundary conditions; (2) but in the case that the structure is coupled with soft soil, then the SSI can be **considerable**. The latter is particularly important in the case of heavier structures. On flexible or slender structures, the period lengthening and the increased effective damping lead to reduced base shear force but can also lead to **higher displacement demand**. On stiff structures, the SSI effects can lead to **higher base shear force**.

However, experiences and studies have shown that these understandings are not always true. Due to the nature of its layering, the geological profile can amplify certain frequency content of the propagating seismic waves. The presence of a softer layer near or on the ground surface, which is common in cities built on deltas or dried basins, results in **site amplification**. This was particularly apparent in the damages found in **Mexico City** during the **1985 earthquake**, which originated in Michoacán, 320 km away. The site amplification subsequently results in destructive resonance for many multi-storey buildings (Resendiz and Roesset, 1987). When the SSI effect is taken into account, the period lengthening of these buildings was found to be about 1.0 s higher than the result from frequency analysis with fixed-base. A study of the collapse of **Hanshin Expressway** in **the Kobe earthquake** concluded that period lengthening also led to a stronger response (Mylonakis et al., 2006).

In the majority of studies concerning dynamic SSI, an assumption of a homogenous half-space is taken to simplify the problem, e.g., Dominguez, 1993; Mossessian and Dravinski, 1990. For the soil layering effect, most studies consider stratified half-space with horizontal interfaces, e.g., Manolis et al., 2017. In reality, the surrounding/supporting soil strata have an **arbitrary number of layers** and **arbitrary geometries**. The material properties often vary over the depth without following a specific pattern. To the best of the author's knowledge, the consideration of arbitrary layered half-space in a hybrid numerical method combining the boundary element method (BEM) and the finite element method (FEM) for two-dimensional (2D) and three-dimensional (3D) problems is not yet realized prior to this study.

Another critical aspect in the simulation of dynamic SSI is the **material and geometrical nonlinearities**. Experimental investigation showed that the linear elastic model for soils is valid in small strain cases ($< 10^{-5}$) (Vucetic, 1994). This

is experienced by the soil-structure systems during weak seismic events located far from the seismic source or during operational duty, e.g., traffic or machinery-induced vibrations. During strong ground shaking, where the soil experiences shear strains $> 10^{-4}$, the supporting soil and the structural members can experience material nonlinearity which can significantly alter the system's response (Pitilakis et al., 2006; Bolisetti, Whittaker, and Coleman, 2018; Tamhidi and Ghannad, 2020). Another aspect that influences the SSI during such a magnitude of ground shaking is the contact nonlinearity in which the foundation is separated from the adjacent soil (**sliding**, **uplifting**, and **gapping**) (Gazetas and Apostolou, 2004). To consider the material or contact nonlinearities, or both, the time domain formulation and solution are required. However, from the perspective of hybrid BEM-FEM, the BEM in the time domain has a relatively high computational cost, rendering it less attractive in comparison to the BEM in the frequency domain (Dominguez, 1993).

The consideration of SSI in dynamic structural design was not always deemed necessary, and it was recommended to be neglected in some earlier seismic codes such as ATC-3, 1978 or NEHRP, 1997 (Mylonakis and Gazetas, 2000). The reasons are that (1) by neglecting the SSI effect, the design result was expected to be on the safer side, and; (2) the analyses considering SSI are deemed too complex. Due to the latter reason, the consideration of SSI is often only briefly described in recent building codes to avoid complicating the guidance. In the current days of practical engineering, the consideration of SSI effects is still often weighed as too complex since it requires the mastery of complicated mathematical expressions and high computational capacity. In **Eurocode 8 - part 5** (CEN, 2004), the consideration of SSI effect is to be taken in (a) structures where P-δ has a significant effect, (b) structures with massive or deep-seated foundations, (c) slender structures, and (d) structures supported on very soft soils ($C_{S,max} < 100$ m/s). Additionally, Eurocode 8 also requires that SSI effects on piles be assessed. One example of the attempts to promote the implementation of SSI consideration in the structural design was the release of the practical guide by the Federal Emergency Management Agency (FEMA, 2020). The revised ASCE Standard 4, "Seismic Analysis of Safety-Related Nuclear Structures and Commentary," provides guidance on nonlinear SSI analyses that includes the consideration of material nonlinearity, embedment effect, failure of soil at soil-foundation interface, pore fluid-soil interaction, uplifting and sliding of the foundation, and gapping effects (Coleman, Bolisetti, and Whittaker, 2016). Even when the SSI effect results in the reduction of base shear load, the consideration of SSI can be used as the

justification for more economical designs. This is in line with the demand to reduce CO_2 emission, considering the cement industry is one of the most significant contributors (Cao et al., 2021).

The challenge in considering SSI in practical engineering activities is even higher for **3D cases** due to the higher modeling and computation efforts. There are instances where such analysis is necessary. The conditions can be summarized into the following: (1) when soil layering vary three-dimensionally, (2) when boundary conditions of the problem vary three-dimensionally, and (3) when the structure of interest has a 3D characteristic that strongly influences its response (Kramer, S. L., 1996). Additionally, the increasingly denser population, commercial, and industrial centers lead to dynamic interaction involving a complex of structures and its surrounding soil strata which also mandates a 3D analysis. The term site-city interaction (Bard et al., 2006) was coined for such large scale phenomenon.

1.2 Summary of contributions

The current work presents endeavours to address the challenges described in the above paragraphs that are still largely present in civil engineering dealing with soil-structure interaction.

- The necessity and pertinence of an efficient, accurate, and accessible numerical tool for the simulation of 2D and 3D dynamic SSI are addressed by the implementation and improvement of hybrid BEM-FEM, combining commercial software package ABAQUS and an in-house code written in MATLAB®. The in-house code is developed such that pre-processing tasks can be performed using the ABAQUS environment to facilitate explicit visualization, which makes it more accessible and reduces error.
- Consideration of different types of dynamic sources is included to simulate wave propagation.
- Layered half-space with arbitrary layering geometries and a number of layers is handled by the development of the layer-wise condensation algorithm that is incorporated seamlessly into the hybrid BE-FE method.
- Nonlinearities of the material behaviour (soil and structure) and the soil-foundation interface (sliding, uplift, and/or gapping) are addressed by combining solutions for the frequency and time domains.

- Industrial applications of the developed hybrid method are presented with topics covering studies on the dynamic behaviour of integral bridges, soil-foundation interaction considering damaged geological media, structure-soil-structure interaction considering the influence of arbitrarily layered geological media, nonlinear dynamic analyses of a 2D arch bridge spanning a region with inhomogeneous geological profile, a 3D multi-storey building founded on a sedimentary basin, and a seismic simulation involving an actual geometrical data.

1.3 Organization of the dissertation

The dissertation consists of **ten chapters**, and it is organized as follows:

- Chapter 1 introduces the background and motivation of this dissertation, the scope, and the organization.
- Chapter 2 presents state-of-the-art mechanical models for the solution of wave motion in a half-space and SSI problems, followed by the classic formulation of dynamic elasticity, the Green's function, and the fundamental coupling of BEM-FEM.
- Chapter 3 discusses the basic numerical enhancements that are implemented to increase the accuracy and efficiency of the hybrid BEM-FEM numerical implementation, including the consideration of embedded dynamic source and incident wave, handling of non-smooth nodes in BEM using dummy elements, mirror algorithm to reduce BEM computation, and handling of non-conforming BE-FE interface.
- Chapter 4 presents the derivation of the layer-wise condensation (LWC) method to handle arbitrary layered half-space in a hybrid BEM-FEM based on the macro-element concept. Verifications of the method in comparison to existing references are given.
- Chapter 5 discusses the implementation and verification of sequential time-frequency domain procedure (SFTDP) to handle material, geometrical and contact nonlinearities. The applicability of the procedure for soft and hard media is presented.
- Chapter 6 presents the application of the hybrid numerical method to study the 3D dynamic behavior of typical integral bridges.

- Chapter 7 presents the application of the hybrid numerical method for case studies of 3D foundation-soil-foundation interaction considering the damaged state of geological media.
- Chapter 8 presents the application of the hybrid numerical method and the LWC for case studies of 3D structure-soil-structure interaction of a pair of containment structures considering arbitrary layered half-space.
- Chapter 9 presents the application of the hybrid numerical method and the sequential frequency-time domain analysis for case studies of a 2D arch bridge and 3D multi-storey building considering secondary nonlinearities.
- Chapter 10 presents the conclusions and outlook.

Due to the length of this dissertation, **anchor words** or **phrases** are given in bold text throughout the manuscript to guide the readers and enable faster reading.

Chapter 2

Overview of models for SSI and basic formulations

2.1 Chapter overview

This chapter presents the current state of mechanical models for the SSI problem and the backbone mathematical formulations of this dissertation. The description of the classical formulation of the equation of motion in elastic continua is presented in the second section (2.3). The mathematical foundation of the boundary element method is presented in the third section (2.4), followed by the finite element method in Section 2.5. Afterward, the coupling method of BEM-FEM based on the macro-element concept is given in Section 2.6.

2.2 Mechanical models for the soil-structure interaction problem

The soil-structure interaction (SSI) phenomena are described in the following mechanical models, having in mind the historical retrospection of their creation:

a) **The empirical Winkler foundation** (Winkler, 1867) replacing the supporting soil with a bed of elastic or nonlinear springs and dashpots resting on a rigid base. Justification and refinement of the Winkler hypothesis in 3D elasticity for a thin layer resting on a stiff half-space are presented in Kaplunov, Prikazchikov, and Sultanova, 2018, where the area of validity of the Winkler model is discussed. Higher-order corrections to the Winkler formulation are additionally studied by the authors. Extension of the method to include nonlinear behavior of near-field supporting soil, including gapping effect,

referred to as beam on nonlinear Winkler foundation (BNWF), can be found in Gajan et al., 2010; Halabian and El Naggar, 2002.

b) **Lamb's solution** (Lamb, 1904) for the response of the elastic half-space subjected to oscillating forces. Studies on footings restings on the surface of a half-space based on this can be found in Reissner, 1936; Sung, 1953; Bycroft, 1956; Richart, Woods, and Hall, 1970.

c) **Direct numerical approach** considering the subgrade soil, the foundation, and the superstructure as a single unit modeled by FEM, BEM, or scaled BEM-FEM, see Antes and Von Estorff, 1989; Abate et al., 2010; Liao et al., 2007; Dineva et al., 2014. The complexity of the soil–structure numerical models stems from the requirement to accurately represent the infinite extension of the soil region, ensuring that Sommerfeld's radiation condition is wholly fulfilled. The following family of finite element models and corresponding computational techniques have been developed in order to minimize spurious reflections of waves at the artificial boundaries of the infinite domain and, thus, allow the radiation of the elastodynamic waves to infinity: the absorbing boundary conditions (ABC) method, see Baffet et al., 2012; the perfectly matched layers (PML), see Fontara et al., 2018; the scaled boundary finite element method (SBFEM), see Schauer and Rodriguez, 2019; the thin layer method (TLM), see Kausel, 1994.

d) **Indirect (sub-structuring) models** that solve the SSI problem by decomposing the superstructure-foundation-soil system into subdomains, coupled to each other, by taking into account the compatibility and equilibrium conditions at their interfaces, see Chuhan and Wolf, 1998. Equations for the subdomains are solved independently, and the results are iterated until convergence is achieved. Thus, this method can handle material, geometrical, or contact nonlinearities directly. Some examples of the works in this field can be found in Elleithy, Al-Gahtani, and El-Gebeily, 2001; von Estorff and Hagen, 2005; Soares Jr, von Estorff, and Mansur, 2004; Soares, 2008; Z. Jahromi, Izzuddin, and Zdravkovic, 2008; Boumaiza and Aour, 2014; Soares and Godinho, 2015. An efficient domain decomposition method to model 3D SSI is presented in Hackenberg, 2016; Freisinger, Hackenberg, and Müller, 2020 using a coupled Integral Transform Method (ITM)-FEM approach. Elastodynamic Green's functions for systems with one boundary surface, as a half-space or a full-space with either a spherical or cylindrical

cavity, are derived via ITM. The FEM zone is then coupled to the ITM substructure on the cylindrical or spherical interaction surface. The ITM, leading to analytical solutions of the Lamé differential equation, can describe the behavior of the infinite medium completely. It is valid under certain assumptions, see Hackenberg, 2016: the material of the soil has to be homogeneous with linear elastic material behavior; the introduction of surfaces is possible for simple geometries; and layers in the material can only be taken into account if they are parallel to the respective surface. The advantages of the BEM for modeling of semi-infinite geological domain compared to the ITM are as follows: material can be continuously inhomogeneous, see Manolis et al., 2017; the surface's geometry can be arbitrary; and multilayered half-space with inclined layers can be considered, see Manolis and Beskos, 1988; Dominguez, 1993.

e) **Hybrid methods**, mainly focusing on (1) FEM hosted, where the nodal forces are expressed throughout the BEM domain nodal tractions and the entire BEM influence matrices and tractions are converted to FEM-like stiffness matrix and nodal forces, see Wearing, Sheikh, and Burstow, 1991; Ganguly, Layton, and Balakrishna, 2000; von Estorff and Firuziaan, 2000; Bode, Hirschauer, and Savidis, 2002; François, Coulier, and Degrande, 2015; Galvín and Romero, 2014b; or (2) BEM hosted, where the FEM formulation is transformed into BEM matrix system of equations, see Brebbia and Georgiou, 1979; and (3) Macro-element approach, where the BEM influence matrices and tractions are converted into a macro finite element, see Vasilev et al., 2015

A specialized mathematical approach based on asymptotic hyperbolic-elliptic formulations for elastic surface waves is efficiently extended to 3D SSI problems involving analysis of surface and underground structures, see Kaplunov and Prikazchikov, 2013; Kaplunov and Prikazchikov, 2017; Erbaş et al., 2017; Erbaş et al., 2018.

In order to **represent dynamic engineering problems realistically**, the mechanical models describing 3D geological regions containing underground or surface engineering structures must include the following **key factors**: *(1)* the type and characteristics of the source radiating waves in geological media; *(2)* the inhomogeneity and heterogeneity of the wave path from the source to the observer point; *(3)* the local geological profile with non-parallel layers, surface, and subsurface relief, the existence of discontinuities, such as cracks, inclusions, faults, plus underground/surface structures, etc.; *(4)* the nonlinear behavior of the near-field

soil region (close to the foundation) in the case of moderate or severe earthquake shaking, see Gazetas and Apostolou, 2004, and Harden et al., 2005; *(5)* the 3D wave motion. The results obtained in the literature showed that the 3D SSI could be significantly more complex and difficult to predict than the 2D cases, see Vicencio and Alexander, 2021. For several reasons, it has been proven impossible to include all these factors in 3D SSI problems. The primary one is the sheer complexity of the 3D models describing real dynamic scenarios in a complex geological location.

Hybrid approaches seem to be the best choice for 3D SSI problems that involve sub-regions with different characteristics, as they combine different computational tools within the subdomains, thus making the best use of their respective advantages. In the proposed analysis, the author is interested only in coupling between the FEM and BEM. The BEM has been proven as a highly accurate numerical technique for elastodynamic problems in infinite and semi-infinite media, see Manolis and Beskos, 1988. The BEM requires two basic ingredients: a reciprocal relation and a fundamental solution of the governing equation. When a fundamental solution (or a half-space Green's function) is used within a BEM formulation, it provides an elegant, powerful tool for investigating the dynamic responses of complex materials and structures. The BEM is described in several books; see, for instance, Manolis and Beskos, 1988, Dominguez, 1993, and Manolis et al., 2017. The fundamental solution used in constructing the boundary integral equations obeys the radiation condition; thus, infinitely extended boundaries are automatically incorporated. This is in contrast to other numerical methods where the special transmitting and/or non-reflecting viscous boundaries must be used. The FEM is the most popular numerical method for civil engineering due to its simplicity, flexibility, and accessibility. An existing wide library of element types, constitutive models, contact definitions, and solvers is readily available in the FEM. The features and advantages of the FEM and BEM are presented in Table 2.1. Recommended readings on the topic of the FEM are Bathe, 1996; Logan, 2007; Fish and Belytschko, 2007; Ferreira and Fantuzzi, 2009, among others. In this study, a commercial FEM software package, ABAQUS, is used.

The following conclusions can be drawn from the above descriptions:

1) There is a paucity of **high-performance methodologies** for treating SSSI problems, taking into account all components along the wave path, namely: *(a)* embedded source radiating waves; *(b)* inhomogeneous and heterogeneous arbitrary, non-parallelly layered wave path; *(c)* local geological region

TABLE 2.1: A comparison of the FEM and BEM, after Liu, 2009.

FEM	BEM
Features	
• Derivative-based (local) approach	• Integral-based (global) approach
• Domain mesh: 2D and 3D mesh	• Boundary mesh: 1D and 2D mesh
• Sparse matrices, in many cases also symmetrical	• Nonsymmetrical, dense matrices
• Available in many commercial packages for general and specialized purposes	• Fewer commercial software packages
Advantages	
• Solution is fast	• The problem dimensionality is decreased by one, and due to this, mesh generation is fast
• Suitable for general structure analysis or large mechanical systems	• Suitable for stress concentration problems (e.g., fracture mechanics)
• Suitable for problems with material, geometrical, and contact nonlinearities	• Suitable for infinite domain problems
• Composite materials (macroscale analysis)	• Composite materials (e.g., microscale continuum models)

with its specific geometry and mechanical properties containing important infrastructure facilities.

2) **Existing large-scale commercial finite element software** (e.g., ABAQUS, ANSYS, FLAC3D) have a limitation when considering semi-infinite, far-field geological regions where the radiation conditions must be satisfied. For example, the infinite element definition in ABAQUS and the absorbing boundary in FLAC3D, which are based on the work of Lysmer and Kuhlemeyer Lysmer and Kuhlemeyer, 1969, are limited in accuracy and application since they only effectively absorb orthogonally impinging wave, see Dassault Systèmes Simulia Corp, 2014 and Itasca Consulting Group, Inc., 2022. The above disadvantage can be overcome by the development of an efficient hybrid technique based on the finite macro-element concept. The library of different macro-elements can extend the existing FEM software capabilities to model semi-infinite zones with different complex mechanical properties such as anisotropy, poroelasticity, inelasticity, arbitrary layering, etc.

3) The majority of the mentioned references assumed a homogeneous half-space as a soil model. However, the soil region is usually an **arbitrary layered or graded half-space**. The foundation was considered a rigid body in most of the previously cited references. However, for large-size foundations, flexibility may play an important role. A rigidity assumption may be admissible but needs careful verification.

4) Most of the models consider stratified half-space, and there are few works modeling layers with **arbitrary geometry** of their interface boundaries.

5) Simulations of 3D dynamic problems considering nonlinearities are often burdened by **high computational cost**.

6) Engineering design and analysis **considering SSI** are still considered a complex and challenging task for **practicing engineers**. This dissertation is an endeavor to bridge the gap between **scientific research and practical engineering** by presenting the following ideas: to merge the pre-processing task of the finite zone and semi-infinite zone into a single software package and to create a procedure in which the computation tasks can be distributed, and the results later can be transferred and reused for optimization. The result is a numerical tool that is expected to increase the ability of practicing engineers to conduct a more realistic engineering analysis.

The above conclusions further underline this study's motivations and scope as described in Chapter 1. This dissertation is focused on the hybrid BEM-FEM based on the macro-element approach as it retains the simplicity of the FEM-hosted approach. In this dissertation, the macro-element approach is extended by adding an algorithm to handle arbitrary points on the BEM model by using dummy elements and an algorithm to make the macro-element reusable and transferable. Further, an enhancement to handle the nonconforming nodal interface between the BE- and FE-zones is introduced by taking advantage of the contact definition in ABAQUS.

2.3 Equation of motion in elastic continua

In a Cartesian coordinate system $Ox_1x_2x_3$, consider an elastic body Ω with a volume V and a surface Γ (Figure 2.1). The **equation of motion** which describes the

equilibrium of the body is

$$\frac{\partial \sigma_{ij}}{\partial x_j} + f_i = \rho \frac{\partial^2 u_i}{\partial t^2}, \quad \mathbf{x}(x_1, x_2, x_3) \in \Omega, \tag{2.1}$$

where $\sigma_{ij}, i = j = 1, 2, 3$, is the stress tensor, $u_i, i = 1, 2, 3$, is the displacement, t is time, ρ is the mass density, and $f_i, i = 1, 2, 3$, is the body force acting per unit volume. In the case that the body force is applied impulsively to one point located at $\mathbf{x} = \boldsymbol{\xi}$, at time $t = \tau$, and in the direction of x_n-axis, it can be written as

$$f_i(\mathbf{x}, t) = A_n \delta(\mathbf{x} - \boldsymbol{\xi}) \delta(t - \tau) \delta_{in}, \tag{2.2}$$

where $\delta(.)$ is the Dirac delta function, δ_{ij} is the Kronecker delta function, and A_n is the vector magnitude of the impulse.

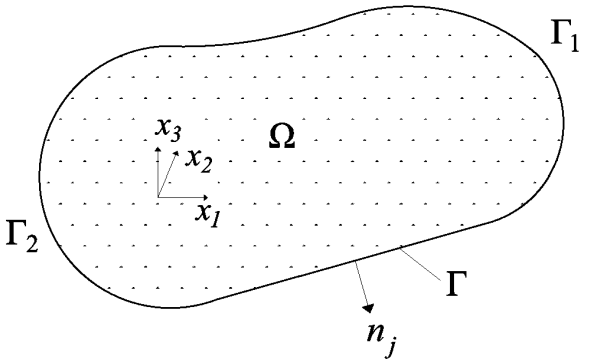

FIGURE 2.1: An arbitrary domain Ω with surface Γ, which outward normal is n_j.

The **kinematic relation** between strain and displacement assuming infinitesimal strain is described as

$$\epsilon_{ij} = \frac{1}{2}(u_{i,j} + u_{j,i}), \tag{2.3}$$

where $\epsilon_{ij}, i = 1, 2, 3, j = 1, 2, 3$, is the strain tensor and the comma between subscripts denotes spatial derivative, e.g., $u_{i,j} = \partial u_i / \partial x_j$.

The **constitutive law** between stress and strain tensors for elastic isotropic solid is given by Hooke's law as

$$\sigma_{ij} = C_{ijkl} \epsilon_{kl} \tag{2.4}$$

or in a simplified matrix form as

$$\boldsymbol{\sigma} = \mathbf{D}\, \boldsymbol{\epsilon}, \tag{2.5}$$

where C_{ijkl} is the fourth-order stiffness tensor and $\mathbf{D}$ is its simplified matrix form. The summation convention of repeated subscripts is followed. The stiffness tensor can be described in terms of the Lamé moduli, λ and μ, as

$$C_{ijkl} = \lambda\delta_{ij}\delta_{kl} + \mu(\delta_{ik}\delta_{jl} + \delta_{il}\delta_{jk}). \tag{2.6}$$

Thus, the stress-strain relation is

$$\sigma_{ij} = \lambda\delta_{ij}\epsilon_{kk} + 2\mu\epsilon_{ij}. \tag{2.7}$$

The Lamé moduli can be written in terms of Young's modulus E and Poisson's ratio ν as

$$\mu = \frac{E}{2(1+\nu)} \quad ; \quad \lambda = \frac{E\nu}{(1+\nu)(1-2\nu)}. \tag{2.8}$$

The longitundinal wave velocity C_P and shear wave velocity C_S are described as

$$C_P = \sqrt{\frac{\lambda+2\mu}{\rho}} \quad ; \quad C_S = \sqrt{\frac{\mu}{\rho}}. \tag{2.9}$$

The strain energy of the domain Ω is described as

$$\mathfrak{U} = \int_V \frac{1}{2} C_{ijkl}\epsilon_{ij}\epsilon_{kl}dV = \int_V \frac{1}{2}\sigma_{ij}\epsilon_{ij}dV, \tag{2.10}$$

whilst the total potential energy Π is given by

$$\Pi = \mathfrak{U} - \mathfrak{W}, \tag{2.11}$$

where $\mathfrak{W}$ is the total potential of the external loads.

The field equation of homogeneous, elastic, isotropic bodies is obtained by combining equations (2.1), (2.3), and (2.4), which results in the Navier's equation as follows:

$$\mu u_{i,jj} + (\lambda+\mu)u_{j,ji} + f_i = \rho\ddot{u}_i \tag{2.12}$$

or in vector form as

$$(\lambda+2\mu)\nabla\nabla\cdot\mathbf{u} - \mu\nabla\times\nabla\times\mathbf{u} + \mathbf{f} = \rho\ddot{\mathbf{u}}. \tag{2.13}$$

Here, the dot accent denotes the time derivative. The Navier's equation, which summarizes the equilibrium condition and the kinematic and constitutive relations, must be satisfied at every point in the domain Ω (Dominguez, 1993).

The stress tensor acting on the surface Γ, with the unit outward normal $n_j, j = 1, 2, 3$, of domain Ω results in traction component $t_i, i = 1, 2, 3$, in the form of

$$t_i = \sigma_{ij} n_j \quad \text{on } \Gamma. \tag{2.14}$$

The **boundary conditions** are composed of the "essential" and "natural" ones. They are also referred to as the **Dirichlet** and **Neumann** boundary conditions, respectively. Here, the essential and natural boundary conditions are applied on a part of the surface Γ. The corresponding partial surfaces are denoted as Γ_1 and Γ_2, respectively, such that $\Gamma_1 \cup \Gamma_2 = \Gamma$ and $\Gamma_1 \cap \Gamma_2 = \oslash$. The boundary conditions are

$$u_i = \bar{u}_i \quad \text{on } \Gamma_1 \text{ and} \tag{2.15a}$$
$$t_i = \bar{t}_i \quad \text{on } \Gamma_2. \tag{2.15b}$$

The **initial conditions** for displacements and their derivatives at time $t = 0$ are

$$u_i(\mathbf{x}, 0) = u_{0i}(\mathbf{x}) \tag{2.16a}$$
$$\dot{u}_i(\mathbf{x}, 0) = \dot{u}_{0i}(\mathbf{x}) \tag{2.16b}$$
$$\ddot{u}_i(\mathbf{x}, 0) = \ddot{u}_{0i}(\mathbf{x}). \tag{2.16c}$$

The displacement field due to a unidirectional unit impulse located at $\mathbf{x} = \boldsymbol{\xi}$, time $t = \tau$, and in x_n-direction is described through the elastodynamic **Green's function** or **fundamental solution**. The i-th component of the displacement field at general point $(\mathbf{x}, t)$ is denoted as $U^*_{in}(\mathbf{x}, t, \boldsymbol{\xi}, \tau)$ (Aki and Richards, 1980). Equation (2.1) can be written alternatively as

$$\frac{\partial}{\partial x_j}(C_{ijkl}\frac{\partial}{\partial x_l}U^*_{kn}) + \delta_{in}\delta(\mathbf{x} - \boldsymbol{\xi})\delta(t - \tau) = \rho\frac{\partial^2}{\partial t^2}U^*_{in} \tag{2.17}$$

2.4 The boundary element method

The boundary element method (BEM) was proposed by Rizzo, 1967, who used the direct boundary integral equation (BIE) formulations first for the 2D elastostatic problem. It has been continuously improved over the years by other researchers (Liu, 2009; Manolis et al., 2017). Some of the early developments of the BIE can be found in Rizzo, 1967; Rizzo and Shippy, 1968; Cruse, 1969; Cruse,

1973; Wilson and Cruse, 1978; among others. The term BEM was used in Banerjee and Butterfield, 1975; Brebbia, 1978; among others, as an analogy to FEM (Liu, 2009). In the BEM, the domain is discretized along its boundary, and the integral equation is approximated through numerical integration. The result is a pair of influence matrices and vectors, which are then rearranged according to the defined boundary conditions into a system of equations and subsequently solved. The standard BEM requires that the influence of every collocation point to each element be computed. This results in dense and nonsymmetric matrices, which are computationally costly. One of the significant advances in the BEM formulations is the development of the fast multipole method (FMM) (Rokhlin, 1985; Greengard, 1987; Greengard and Rokhlin, 1987), which reduces the requirement of interconnectivity between the collocation points and greatly enhanced its computation speed. The main advantage of the FMM is obtained from the combination of it with the iterative solver. As a result, the requirement to form the entire matrices of the BE subdomain is omitted. In a direct, FEM-hosted hybrid method, however, these matrices are required for the condensation and conversion procedure. In this work, the standard discretization and collocation technique is used to avoid the complexity arising from this. A brief summary of the mathematical foundation of the BEM is described in the following.

Consider the body Ω in Figure 2.1, which undergoes an elastodynamic state with the displacement field u_k and in equilibrium as described by equation (2.1). A second elastodynamic state due to a unit impulse f_k^*, which follows the description in equation (2.2), is applied to a point located at $\mathbf{x} = \boldsymbol{\xi}$ and at time $t = 0$ with the displacement field U_k^* and stress σ_{kj}^* in equilibrium as in equation (2.17). **The reciprocal theorem** between these two states, assuming zero initial conditions, dictates the following (see Dominguez, 1993):

$$\int_\Gamma (t_k * U_k^*) d\Gamma + \int_\Omega (f_k * U_k^*) d\Omega = \int_\Gamma (P_k^* * u_k) d\Gamma + \int_\Omega (f_k^* * u_k) d\Omega. \tag{2.18}$$

Here, P_k^* is the traction due to the unit impulse f_k^* with outward normal n_j, expressed by

$$P_k^* = \sigma_{kj}^* n_j \tag{2.19}$$

and the symbol $*$ denotes the Riemann convolution.

Using the properties of Dirac delta function in f_k^* and assuming zero body force in the 1st elastodynamic state, the following **boundary integral equation**

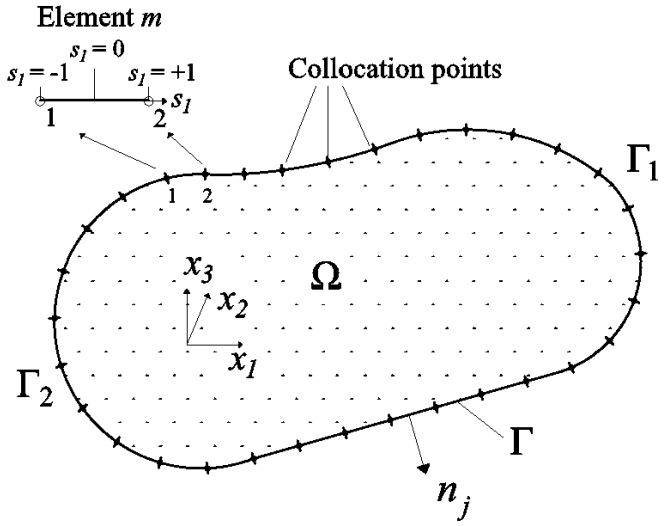

FIGURE 2.2: A cross-section of the domain Ω after discretization of its surface. Each element is a shell element. In the upper-left figure, element m, which is constructed of nodes 1 and 2, is shown in the intrinsic coordinate **s**.

(BIE) is obtained:

$$c_{lj}u_j(\boldsymbol{\xi},t) = \int_\Gamma U^*_{lj}(\mathbf{x},\boldsymbol{\xi},t) * t_j(\mathbf{x},t)d\Gamma - \int_\Gamma P^*_{lj}(\mathbf{x},\boldsymbol{\xi},t) * u_j(\mathbf{x},t)d\Gamma, \boldsymbol{\xi} \in \Gamma, \quad (2.20)$$

where $c_{lj}, l = 1,2,3, j = 1,2,3$, is the free-term depending on the geometry at the source point $\boldsymbol{\xi}$. Equation (2.20) results in singularity when the radial distance between $\mathbf{x}$ and $\boldsymbol{\xi}$ is zero. The free-term c_{lj} can then be calculated analitically by using augmented boundary near the point of interest or by using the rigid-body motion method (Dominguez, 1993).

Taking the above case of two independent elastodynamic states for time harmonic load with the same angular frequency ω, the frequency domain equivalent of BIE (2.20) is obtained as

$$c_{lj}\hat{u}_j(\boldsymbol{\xi},\omega) = \int_\Gamma \hat{U}^*_{lj}(\mathbf{x},\boldsymbol{\xi},\omega)\ \hat{t}_j(\mathbf{x},\omega)d\Gamma - \int_\Gamma \hat{P}^*_{lj}(\mathbf{x},\boldsymbol{\xi},\omega)\ \hat{u}_j(\mathbf{x},\omega)d\Gamma, \boldsymbol{\xi} \in \Gamma, \quad (2.21)$$

where the convolutions of two functions in the time domain are tranformed into piecewise products of the Fourier transform of those functions. The time-harmonic displacement $\hat{u}_j$ and traction $\hat{t}_j$ are the product of the Fourier transform given by

$$\hat{u}_j(\omega) = \mathcal{F}\{u_j(t)\}(\omega); \quad (2.22)$$

$$\hat{t}_j(\omega) = \mathcal{F}\{t_j(t)\}(\omega), \quad (2.23)$$

where the notation $\mathcal{F}\{.\}$ denotes the Fourier operation.

Let the boundary be divided into M number of elements as in Figure 2.2. The points along the boundary which form the elements are used as the source as well as the observation (receiver) points. Thus, they are referred to as the collocation points. The BIE (2.21) can now be expressed as the sum of the integrals over the element in the following discretized form:

$$c_{lj}\hat{u}_j(\boldsymbol{\xi},\omega) = \sum_{m=1}^{M}\int_{\Gamma_m} \hat{U}^*_{lj}(\mathbf{x},\boldsymbol{\xi},\omega)\ \hat{t}_j(\mathbf{x},\omega)\ d\Gamma_m - \sum_{m=1}^{M}\int_{\Gamma_m} \hat{P}^*_{lj}(\mathbf{x},\boldsymbol{\xi},\omega)\ \hat{u}_j(\mathbf{x},\omega)\ d\Gamma,\ \mathbf{x}\in\Gamma_m,\ \boldsymbol{\xi}\in\Gamma, \quad (2.24)$$

where Γ_m is the surface of element m.

The spatial coordinate of any point along or inside element m is related to the nodal coordinates of the element using **the shape (interpolation) functions** $\mathbf{N} = [N_1, N_2, ..., N_L]$, where L is the number of nodes on the element of interest. The shape functions $\mathbf{N}$ are in terms of the intrinsic coordinate $\mathbf{s}$, i.e., $\mathbf{s}(s_1)$ for a line element, $\mathbf{s}(s_1, s_2)$ for a shell element, and $\mathbf{s}(s_1, s_2, s_3)$ for a 3D solid element. Using **isoparametric formulation**, the displacement and traction fields at any point along or inside the element are related to the nodal displacement and the nodal traction, respectively, using the same interpolation functions. Inserting the shape functions into BIE (2.24), the following **discretized BIE** in vector form is obtained (Dominguez, 1993)

$$\mathbf{c}^i\ \hat{\mathbf{u}}^i = \sum_{m=1}^{M}\int_{\Gamma_m} \mathbf{U}^*\ \mathbf{N}\ \hat{\mathbf{t}}^m\ d\Gamma_m - \sum_{m=1}^{M}\int_{\Gamma_m} \mathbf{P}^*\ \mathbf{N}\ \hat{\mathbf{u}}^m\ d\Gamma_m. \quad (2.25)$$

$\hat{\mathbf{u}}^m$ and $\hat{\mathbf{t}}^m$ are the vectors of displacement and traction, respectively, of element m. $\mathbf{c}^i$ is a $N_{DoF} \times N_{DoF}$ matrix of the free-terms of the point i, where N_{DoF} is the number of degrees of freedom. $\hat{\mathbf{u}}^i$ is the displacement vector of point i, which size also depends on the problem's dimension. Equation (2.25) can be written as

$$\mathbf{c}^i\ \hat{\mathbf{u}}^i + \sum_{l=1}^{LE}\hat{\mathbf{H}}^{il}\hat{\mathbf{u}}^l = \sum_{m=1}^{M}\mathbf{G}^{im}\ \hat{\mathbf{t}}^m, \quad (2.26)$$

where

$$\hat{\mathbf{H}}^{il} = \sum_{o}\int_{\Gamma_o} \mathbf{P}^*\mathbf{N}_q\ d\Gamma_o \quad ; \quad \mathbf{G}^{im} = \int_{\Gamma_m} \mathbf{U}^*\mathbf{N}\ d\Gamma_m. \quad (2.27)$$

LE is the number of nodes in the domain Ω. The first integral in (2.27) states that

the matrix $\hat{\mathbf{H}}^{il}$ for source-receiver couple *i*-*l* is obtained by summing the integrals for node l over all adjacent elements. This is because node l can be a part of more than one element, and the nodal displacement vector $\hat{\mathbf{u}}^l$ is the same for every element where the node belongs. Subscript q is the local node designation for the node l, whereas the notation l is the global node designation. In contrast, the nodal traction vector of node l, $\hat{\mathbf{t}}^l$, of element m can be different from that of any adjacent element. Therefore the integral of the displacement fundamental solution in matrix $\mathbf{G}^{im}$ cannot be assembled similarly. However, in the case that the traction $\hat{\mathbf{t}}^m$ is part of the unknowns, the treatment of matrix $\mathbf{G}^{im}$ is the same as that of the matrix $\hat{\mathbf{H}}^{il}$. The size of $\hat{\mathbf{t}}^m$ is $N_{DoF} \times L$.

Collecting BIE (2.26) for all collocation points results in a system of equation that is expressed as

$$\mathbf{H}\,\hat{\mathbf{u}} = \mathbf{G}\,\hat{\mathbf{t}}, \tag{2.28}$$

where $\hat{\mathbf{u}}$ and $\hat{\mathbf{t}}$ are the displacement and traction vectors at nodes along the boundary Γ of the domain Ω, which sizes under normally prescribed boundary conditions are $N_{DoF} \times LE$ and $N_{DoF} \times L \times M$, respectively. The influence matrices $\mathbf{H}$ and $\mathbf{G}$ are as follows:

$$\mathbf{H} = \sum_{l=1}^{LE} \mathbf{H}^{il} \quad \text{for } i = 1, ..., LE; \tag{2.29}$$

$$\mathbf{G} = \sum_{m=1}^{M} \mathbf{G}^{im} \quad \text{for } i = 1, ..., LE, \tag{2.30}$$

where

$$\mathbf{H}^{il} = \begin{cases} \hat{\mathbf{H}}^{il} & \text{for } i \neq l, \\ \mathbf{c}^i + \hat{\mathbf{H}}^{il} & \text{for } i = l. \end{cases} \tag{2.31}$$

When a solution for the above equation (2.28) is sought, it must be rearranged according to the prescribed boundary conditions and the unknown variables. However, for the hybrid BEM-FEM, this is not necessary as the only prescribed boundary conditions are the zero traction along the free surface, i.e., the discretized boundary that is not part of the interface with the finite element zone nor with other BE subdomains. The product of $(\mathbf{G}\,\mathbf{t})$ is a null matrix for the free surface, and that would leave a system of equation (such as that in (2.28)) with unknown variables in both sides: displacement field is unknown everywhere, and traction field is unknown along the BE-FE interface. This equation is then condensed into a compact form in terms of the unknowns along the BE-FE interface and then

transformed into a FEM-like stiffness matrix. The procedure will be discussed later in Section 2.6.

Two types of singularities in the integrals of the fundamental solutions' kernels exist when the radial distance r between the source and receiver points is zero. The displacement fundamental solution-based kernels exhibit a weak singularity of the type $O(\ln r)$ for 2D or $O(1/r)$ for 3D, and the appropriate quadrature rule solves these integrals. The traction fundamental solution-based kernels exhibit a strong singularity of the type $O(1/r)$ for 2D or $O(1/r^2)$ for 3D. These singularities can be solved using the analytical solution or the rigid-body motion method (Dominguez, 1993).

For **transient elastodynamics**, the BIE, assuming zero body forces and quiescent past, is given by Antes and Von Estorff, 1989,

$$c_{lj}u_j(\boldsymbol{\xi},t) = \int_0^{t^*}\int_\Gamma U^*_{lj}(\mathbf{x},\boldsymbol{\xi},t-\tau)\; t_j(\mathbf{x},\tau)\; d\Gamma\; d\tau - \int_0^{t^*}\int_\Gamma P^*_{lj}(\mathbf{x},\boldsymbol{\xi},t-\tau)\; u_j(\mathbf{x},\tau)\; d\Gamma\; d\tau,\; \mathbf{x}\in\Gamma,\; \boldsymbol{\xi}\in\Gamma, \quad (2.32)$$

where a limit is applied to the integration over time such that $t^* = t+\varepsilon, \varepsilon \rightarrow 0$, to avoid ending the integration at the peak of Dirac δ function (Dominguez, 1993). After spatial and temporal discretizations and application of spatial interpolation functions, equation (2.32) can be written as

$$\mathbf{H}_{(qq)}\;\mathbf{u}_{(q)} = \mathbf{G}_{(qq)}\;\mathbf{t}_{(q)} + \sum_{o=1}^{q-1}\left[\mathbf{G}_{(qo)}\;\mathbf{t}_{(o)} - \mathbf{H}_{(qo)}\;\mathbf{u}_{(o)}\right], \quad (2.33)$$

where $\mathbf{H}_{(qo)}$ and $\mathbf{G}_{(qo)}$ are the influence matrices, expressed as

$$\mathbf{H}_{(qo)} = \sum_{l=1}^{LE}\mathbf{H}^{il}_{(qo)} \quad \text{for } i = 1,...,LE; \quad (2.34a)$$

$$\mathbf{G}_{(qo)} = \sum_{m=1}^{M}\mathbf{G}^{im}_{(qo)} \quad \text{for } i = 1,...,LE. \quad (2.34b)$$

Here, the two subsciprts under round brackets denote the time difference between time steps t_o to t_q whilst the two superscripts denote the source-receiver

couple. The influence matrix components $\mathbf{H}^{il}_{(qo)}$ and $\mathbf{G}^{im}_{(qo)}$ are given by

$$\mathbf{H}^{il}_{(qo)} = \begin{cases} \hat{\mathbf{H}}^{il}_{(qo)} & \text{for } i \neq l; \\ \mathbf{c}^i + \hat{\mathbf{H}}^{il}_{(qo)} & \text{for } i = l; \end{cases} \tag{2.35a}$$

$$\hat{\mathbf{H}}^{il}_{(qo)} = \int_{t_o}^{t_q} \sum_n \int_{\Gamma_n} \mathbf{P}^*(t)\, \mathbf{N}\, d\Gamma_n\, d\tau; \tag{2.35b}$$

$$\mathbf{G}^{im}_{(qo)} = \int_{t_o}^{t_q} \int_{\Gamma_m} \mathbf{U}^*(t)\, \mathbf{N}\, d\Gamma_m\, d\tau; \tag{2.35c}$$

where the integrals over time domain in $\hat{\mathbf{H}}^{il}_{(qo)}$ and $\mathbf{G}^{im}_{(qo)}$ are solved by using time interpolation functions. The latter is also solved by using integration by parts, see Dominguez, 1993. In (2.35), matrices $\mathbf{U}^*(t)$ and $\mathbf{P}^*(t)$ are the fundamental solutions in the time domain and subscript n denotes the element where the node l is a part of.

As the described in Section 2.2, the 2nd ingredient of the BEM is **the Green's functions** or **the fundamental solutions**. The elastodynamic solution for the displacement in k-direction due to a unit load in l-direction was first given by Stokes in 1849. For time-harmonic problem with angular frequency ω, the solution is as follows (Dominguez, 1993):

$$\hat{U}^*_{lk}(\mathbf{x}, \boldsymbol{\xi}, \omega) = \frac{1}{\alpha \pi \rho C_S^2} \left[\psi \delta_{lk} - \chi r_{,l} r_{,k} \right], \tag{2.36}$$

where

$$\psi = \frac{e^{-k_{is}r}}{r} + \left(\frac{1}{k_{is}^2 r^2} + \frac{1}{k_{is} r} \right) \frac{e^{-k_{is}r}}{r} - \frac{C_S^2}{C_P^2} \left(\frac{1}{k_{ip}^2 r^2} + \frac{1}{k_{ip} r} \right) \frac{e^{-k_{ip}r}}{r}; \tag{2.37a}$$

$$\chi = \left(\frac{3}{k_{is}^2 r^2} + \frac{3}{k_{is} r} + 1 \right) \frac{e^{-k_{is}r}}{r} - \frac{C_S^2}{C_P^2} \left(\frac{3}{k_{ip}^2 r^2} + \frac{3}{k_{ip} r} + 1 \right) \frac{e^{-k_{ip}r}}{r} \tag{2.37b}$$

for 3D problem and

$$\psi = K_0(k_{is} r) + \frac{1}{k_{is} r} \left[K_1(k_{is} r) - \frac{C_S}{C_P} K_1(k_{ip} r) \right]; \tag{2.38a}$$

$$\chi = K_2(k_{is} r) - \frac{C_S^2}{C_P^2} K_2(k_{ip} r) \tag{2.38b}$$

for 2D one. Additionally,

$$\alpha = \begin{cases} 4 & \text{for 3D problem;} \\ 2 & \text{for 2D problem;} \end{cases} \tag{2.39a}$$

$$k_{ip} = i\left(\frac{\omega}{C_P}\right); \quad k_{is} = i\left(\frac{\omega}{C_S}\right). \tag{2.39b}$$

Here, $i = \sqrt{-1}$, $(\mathbf{x}, \boldsymbol{\xi})$ is the source-receiver couple, r is the source-receiver radial distance, and $K_n(.)$ is the Bessel function of the 2$^{\text{nd}}$ kind, order of n. $r_{,j}$ is the direction cosine, i.e., $r_{,j} = r_j/r$. For very low frequency, equation (2.36) reduces to the elastostatic fundamental solution, which was given by Lord Kelvin (Beer, Smith, and Duenser, 2008). The displacement fundamental solution in the time domain is as follows (Dominguez, 1993):

$$U^*_{lk}(\mathbf{x}, \boldsymbol{\xi}, t, \tau) = \frac{1}{4\pi\rho}\left\{ \frac{t}{r^2}\left(\frac{3r_{,l}r_{,k}}{r} - \frac{\delta_{lk}}{r}\right)\left[\mathcal{H}\left(t - \frac{r}{C_P}\right) - \mathcal{H}\left(t - \frac{r}{C_S}\right)\right] + \right.$$
$$\left. \frac{r_{,l}r_{,k}}{r}\left[\frac{1}{C_P^2}\delta\left(t - \frac{r}{C_P}\right) - \frac{1}{C_S^2}\delta\left(t - \frac{r}{C_S}\right)\right] + \frac{\delta_{lk}}{rC_S^2}\delta\left(t - \frac{r}{C_S}\right)\right\} \tag{2.40}$$

for 3D problem and

$$U^*_{lk}(\mathbf{x}, \boldsymbol{\xi}, t, \tau) = \frac{1}{2\pi\rho}\left\{ \frac{1}{C_P}\frac{\mathcal{H}(C_P t - r)}{r^2}\left[\left(2R_1 + \frac{r^2}{R_1}\right)r_{,l}r_{,k} - R_1\delta_{lk}\right] - \right.$$
$$\left. \frac{1}{C_S}\frac{\mathcal{H}(C_S t - r)}{r^2}\left[\left(2R_2 + \frac{r^2}{R_2}\right)r_{,l}r_{,k} - \left(R_2 + \frac{r^2}{R_2}\right)\delta_{lk}\right]\right\} \tag{2.41}$$

for 2D problem. The time scalar couple (t, τ) is the time distance/delay between the applied impulse at the source and the measurement at the receiver. In the above equation, it is represented by $(t - r/C_P)$ or $(t - r/C_S)$. Here, $R_1 = (C_P^2 t^2 - r^2)^{1/2}$, $R_2 = (C_S^2 t^2 - r^2)^{1/2}$, and $\mathcal{H}(.)$ is the Heaviside step function. The k component of traction on a surface with a unit outward normal of n_j due to a unit load in l-direction is expressed as $P^*_{lk} = C_{lqrs}U^*_{rk,s}n_q$. The explicit expression for the time-harmonic solution is (Dominguez, 1993)

$$\hat{P}^*_{lk} = \frac{1}{\alpha\pi}\left[\left(\frac{d\psi}{dr} - \frac{1}{r}\chi\right)\left(\delta_{lk}\frac{\partial r}{\partial n} + r_{,k}n_l\right) - \frac{2}{r}\chi\left(n_k r_l - 2r_{,l}r_{,k}\frac{\partial r}{\partial n}\right) - \right.$$
$$\left. 2\frac{dx}{dr}r_{,l}r_{,k}\frac{\partial r}{\partial n} + \left(\frac{C_P^2}{C_S^2} - 2\right)\left(\frac{d\psi}{dr} - \frac{dx}{dr} - \frac{\alpha}{2r}\chi\right)r_{,l}n_k\right], \tag{2.42}$$

where the components for 3D and 2D problems are of those in (2.38a)-(2.39a). Other form of fundamental solutions for non-homogeneous media can be found in Manolis et al., 2017; Fontara, 2015. Alternatively, one can also take advantage of the **half-space Green's function**, see, e.g., Bode, Hirschauer, and Savidis, 2002; Galvín and Romero, 2014a.

2.5 The finite element method

The development of the finite element method can be traced back to the 1940s in the works of Hrennikoff, 1941, McHenry, 1943, and Courant, 1943. McHenry used a lattice of line elements for stress-strain analysis in solids, while Courant proposed the use of the variational form for this and introduced piecewise interpolation functions for triangular subregions that are used to approximate the whole region. Turner et al., 1956, proposed treatment of two-dimensional elements where stiffness matrices for truss elements, beam elements, and 2D triangular and rectangular plane stress elements are derived using what is now known as a direct stiffness matrix. A solution for the rectangular-plate bending problem was proposed by Melosh, 1961. 3D problems were later considered in the works of Gallagher, Padlog, and Bijlaard, 1962 and Melosh, 1963, among others. The latter also considered material nonlinearity. Dynamic problem was considered later in Archer, 1965 (Logan, 2007; Fish and Belytschko, 2007). These few early developments provide a glimpse of the research that kickstarted the booming era of FEM, which is also attributed to the development of computers and computer-aided design (CAD). Further detailed descriptions can be found in Bathe, 1996; Fish and Belytschko, 2007; Logan, 2007; Ferreira and Fantuzzi, 2009; among others. The FEM formulations can be derived using direct stiffness methods, variational methods (including minimum potential energy principle), or weighted residual method (including Galerkin's collocation, subdomain, and least squares methods), see Bathe, 1996; Logan, 2007; Fish and Belytschko, 2007. In this section, a brief description of the derivation of the FEM formulation using **the principle of minimum potential energy** is presented.

Let us consider the elastic body Ω in Figure 2.1. The body is subjected to prescribed boundary conditions of displacement and traction on Γ_1 and Γ_2, respectively, and body forces per unit volume f_i as before. The body after volume discretization is presented in Figure 2.3. The displacement at any chosen point i, $\acute{\mathbf{u}}^i$, inside the element m can be interpolated from the nodal displacements using

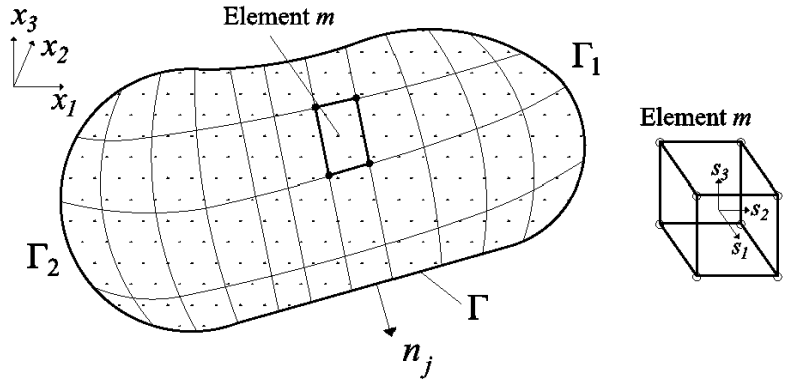

FIGURE 2.3: A cross-section of domain Ω after discretization of its volume into finite solid elements. Solid element m is shown in the intrinsic coordinate $\mathbf{s}$.

the isoparametric shape functions with the following expression:

$$\acute{\mathbf{u}}^i = \sum_{l=1}^{L} \mathbf{N}_l(\mathbf{s}^i)\mathbf{u}^{m(l)}, \quad l = 1, 2, ..., L, \tag{2.43}$$

where $\mathbf{u}^{m(l)}$ is the displacement matrix of node l of element m and $\mathbf{s}^i$ is the intrinsic coordinate of the point i, such that the vector position of the point i, $\mathbf{x}^i$, is related to the nodal coordinates of the element, $\mathbf{x}^{m(l)}$, as

$$\mathbf{x}^i = \sum_{l=1}^{L} \mathbf{N}_l(\mathbf{s}^i)\mathbf{x}^{m(l)}, \quad l = 1, 2, ..., L. \tag{2.44}$$

Here, L is the number of nodes on element m. The strain of element m can be derived from (2.43) and is expressed in matrix form as

$$\boldsymbol{\epsilon}^m = \mathbf{B}\mathbf{u}^m. \tag{2.45}$$

and the stress-strain relation is subsequently described as

$$\boldsymbol{\sigma}^m = \mathbf{D}\mathbf{B}\mathbf{u}^m, \tag{2.46}$$

where

$$\mathbf{B} = \left[\nabla \mathbf{N}^T \mathbf{x}^m\right]^{-1} \nabla \mathbf{N}^T. \tag{2.47}$$

Note that the components of the right hand side of (2.47) need to be rearranged in $\mathbf{B}$ such that $\mathbf{B}$ has the same column as the column matrix $\mathbf{u}^m$. $\nabla \mathbf{N}$ is the partial derivative of the shape functions with respect to the intrinsic coordinate $\mathbf{s}$. The superscript T denotes transpose operation.

The strain energy in the domain Ω is given by (2.10), which can be written in matrix form as

$$\mathfrak{U} = \int_V \frac{1}{2} \boldsymbol{\epsilon}^T \mathbf{D} \boldsymbol{\epsilon} \, dV. \tag{2.48}$$

The potential of the external loads due to the body forces and tractions is given by

$$\mathfrak{W} = \int_V \acute{\mathbf{u}}^T \acute{\mathbf{f}} \, dV + \int_{\Gamma_2} \acute{\mathbf{u}}_{\Gamma_2}^T \acute{\mathbf{t}} \, d\Gamma, \tag{2.49}$$

where $\acute{\mathbf{u}}$ is the general displacement function as in (2.43), $\acute{\mathbf{f}}$ is the applied body forces (forces per unit volume), $\acute{\mathbf{u}}_{\Gamma_2}$ is the displacement field over surface Γ_2 (where the surface tractions act), and $\acute{\mathbf{t}}$ is the surface traction (forces per unit area).

Inserting equations (2.45) and (2.43) into (2.48) and (2.49), respectively, **the total potential energy** Π is obtained as follows (Bathe, 1996; Logan, 2007):

$$\Pi = \frac{1}{2} \int_V \mathbf{u}^T \mathbf{B}^T \mathbf{D} \mathbf{B} \mathbf{u} \, dV - \int_V \mathbf{u}^T \mathbf{N}^T \acute{\mathbf{f}} \, dV - \int_{\Gamma_2} \mathbf{u}_{\Gamma_2}^T \mathbf{N}_{\Gamma_2}^T \acute{\mathbf{t}} \, d\Gamma. \tag{2.50}$$

Here, $\mathbf{u}$ is the nodal displacement matrix of the domain Ω, i.e., $\mathbf{u}$ is a result of superposition of $\mathbf{u}^m$, and $\mathbf{N}_{\Gamma_2}$ is the matrix of shape functions that are applicable for the surface Γ_2. After discretization of the domain into finite elements, the volume and surface integrals of equation (2.50) can be substituted by the sums of the element integrals as

$$\begin{aligned} \Pi = & \frac{1}{2} \sum_{m=1}^{M} \int_{V^m} [\mathbf{u}^m]^T \mathbf{B}^T \mathbf{D} \mathbf{B} \mathbf{u}^m \, dV^m - \\ & \sum_{m=1}^{M} \int_{V^m} [\mathbf{u}^m]^T \mathbf{N}^T \acute{\mathbf{f}}^m \, dV^m - \sum_{m=1}^{M} \int_{\Gamma_2^m} [\mathbf{u}^m]^T \mathbf{N}_{\Gamma_2}^T \acute{\mathbf{t}}^m \, d\Gamma_m. \end{aligned} \tag{2.51}$$

Collecting $\mathbf{u}^m$ in $\mathbf{u}$ and applying **the principle of minimum potential energy** by taking the partial derivative of Π with respect to the nodal displacements as zero, the following is obtained

$$\begin{aligned} \frac{\partial \Pi}{\partial \mathbf{u}} = & \left[\sum_{m=1}^{M} \int_{V^m} \mathbf{B}^T \mathbf{D} \mathbf{B} \, dV^m \right] \mathbf{u} - \\ & \sum_{m=1}^{M} \int_{V^m} \mathbf{N}^T \acute{\mathbf{f}}^m \, dV^m - \sum_{m=1}^{M} \int_{\Gamma_2^m} \mathbf{N}_{\Gamma_2}^T \acute{\mathbf{t}}^m \, d\Gamma_m = 0. \end{aligned} \tag{2.52}$$

Equation (2.52) describes the state of equilibrium of the domain Ω.

In the dynamic problem, where time-dependent loads are applied rapidly,

the inertia forces of the system are activated. In addition, the system's energy dissipates over time, which can be described as velocity-dependent damping forces. **The inertia force** and **the damping force** terms can be inserted into the body force part of (2.52). Using d'Alembert's principle, the body force in element m is redescribed as follows (Bathe, 1996; Logan, 2007):

$$\int_{V^m} \mathbf{N}^T \acute{\mathbf{f}}^m \, dV^m \Rightarrow \int_{V^m} \mathbf{N}^T [\acute{\mathbf{f}}^m - \rho^m \mathbf{N} \ddot{\mathbf{u}}^m - \zeta^m \mathbf{N} \dot{\mathbf{u}}^m] \, dV^m. \tag{2.53}$$

The acceleration and velocity inside the element $\acute{\mathbf{u}}^m$ and $\acute{\mathbf{u}}^m$, respectively, are approximated from the nodal accelerations $\ddot{\mathbf{u}}^m$ and the nodal velocities $\dot{\mathbf{u}}^m$ in the same manner as the displacement and traction, i.e., by means of the shape functions. ζ is the damping parameter. Inserting (2.53) into (2.52) and collecting the nodal accelerations and velocities in $\ddot{\mathbf{u}}$ and $\dot{\mathbf{u}}$, the following equation is obtained

$$\mathbf{M}\ddot{\mathbf{u}} + \mathbf{C}\dot{\mathbf{u}} + \mathbf{K}\mathbf{u} = \mathbf{f}, \tag{2.54}$$

where $\mathbf{u}$ is the time-dependent nodal displacement, i.e., $\mathbf{u} = \mathbf{u}(t)$, and $\dot{\mathbf{u}}$ and $\ddot{\mathbf{u}}$ are its time derivatives. The stiffness matrix $\mathbf{K}$, the mass matrix $\mathbf{M}$, the damping matrix $\mathbf{C}$, and the nodal external force vector $\mathbf{f}$ are described as

$$\mathbf{K} = \sum_{m=1}^{M} \mathbf{K}^m = \sum_{m=1}^{M} \int_{V^m} \mathbf{B}^T \mathbf{D} \mathbf{B} \, dV^m; \tag{2.55a}$$

$$\mathbf{C} = \sum_{m=1}^{M} \mathbf{C}^m = \sum_{m=1}^{M} \int_{V^m} \zeta^m \mathbf{N}^T \mathbf{N} \, dV^m; \tag{2.55b}$$

$$\mathbf{M} = \sum_{m=1}^{M} \mathbf{M}^m = \sum_{m=1}^{M} \int_{V^m} \rho^m \mathbf{N}^T \mathbf{N} \, dV^m; \tag{2.55c}$$

$$\mathbf{f} = \sum_{m=1}^{M} \int_{V^m} \mathbf{N}^T \acute{\mathbf{f}}^m dV^m + \sum_{m=1}^{M} \int_{\Gamma_2^m} \mathbf{N}_{\Gamma_2}^T \acute{\mathbf{t}}^m \, d\Gamma_m. \tag{2.55d}$$

In (2.55d), the nodal force loads that are defined directly on specific nodes can also be inserted. The numerical integration of (2.55a)-(2.55d) can be performed using Gauss quadrature. The solution for **time-harmonic problem** is obtained by expressing the displacements and the forces as

$$u_j(t) = \hat{u}_j e^{i\omega t} \text{ and} \tag{2.56a}$$

$$f_j(t) = \hat{f}_j e^{i\omega t}, \text{where } j = 1, 2, 3, \text{ and } i = \sqrt{-1}. \tag{2.56b}$$

Here, $\hat{u}_j$ and $\hat{f}_j$ are the complex amplitudes of the displacements and the

loads, respectively. After replacing the accelerations and the velocities as derivatives of the time-harmonic displacements, (2.54) can be written as (Wolf, 1985; Chopra, 1995)

$$\hat{\mathbf{u}} = \left[(\mathbf{K} + i\mathbf{K}_s) + i\omega\mathbf{C} - \omega^2\mathbf{M}\right]^{-1}\hat{\mathbf{f}}, \tag{2.57}$$

where $\mathbf{K}_s$ is the structural damping matrix.

The solution in **transient analysis** can be obtained by solving the numerical integration with respect to the time variable using approximation such as the Newmark-beta method or central difference method (Chopra, 1995). In ABAQUS, two dynamics analysis types are available: **explicit** and **implicit**. The explicit solver is based on the forward Euler method and the central difference operator, while the implicit solver is based on the backward Euler method and modified Newmark's method. In the implicit dynamic analysis, the state of equilibrium at time t_{j+1} is obtained from the values at time t_j and at time t_{j+1} itself, where $t_{j+1} = t_j + \Delta t$ and Δt is the time interval. The equilibrium equation (2.54) at time t_j is expressed as (Chopra, 1995)

$$\mathbf{M}\ddot{\mathbf{u}}_{(j)} + \mathbf{C}\dot{\mathbf{u}}_{(j)} + \mathbf{K}\mathbf{u}_{(j)} = \mathbf{f}_{(j)}. \tag{2.58}$$

The difference between equilibrium states at time t_{j+1} and t_j gives the incremental equation

$$\mathbf{M}\Delta\ddot{\mathbf{u}}_{(j)} + \mathbf{C}\Delta\dot{\mathbf{u}}_{(j)} + \mathbf{K}\Delta\mathbf{u}_{(j)} = \Delta\mathbf{f}_{(j)}, \tag{2.59}$$

where the subscript (j) denotes the considered time step. Given certain initial displacements and initial velocities

$$\mathbf{u}_{(0)} = \bar{\mathbf{u}}, \tag{2.60a}$$

$$\dot{\mathbf{u}}_{(0)} = \bar{\dot{\mathbf{u}}}, \tag{2.60b}$$

the acceleration can be computed as

$$\ddot{\mathbf{u}}_{(j)} = [\mathbf{M}]^{-1}[\mathbf{f}_{(j)} - \mathbf{C}\dot{\mathbf{u}}_{(j)} - \mathbf{K}\mathbf{u}_{(j)}],\ j = 0. \tag{2.61}$$

As the displacements and its time derivatives at this time step are known, the incremental values for the next time step can be computed as

$$\Delta\mathbf{u}_{(j)} = [\hat{\mathbf{K}}]^{-1}\Delta\mathbf{P}_{(j)},\ j = 0, 1, 2, ..., \tag{2.62}$$

where

$$\hat{\mathbf{K}} = \mathbf{K}_{tan_{(j)}} + \frac{\gamma}{\beta\Delta t}\mathbf{C} + \frac{1}{\beta(\Delta t)^2}\mathbf{M}, \tag{2.63a}$$

$$\Delta\mathbf{P}_{(j)} = \Delta\mathbf{f}_{(j)} + \left[\frac{1}{\beta\Delta t}\mathbf{M} + \frac{\gamma}{\beta}\mathbf{C}\right]\dot{\mathbf{u}}_{(j)} + \left[\frac{1}{2\beta}\mathbf{M} + \Delta t\Big(\frac{\gamma}{2\beta}\Big)\mathbf{C}\right]\ddot{\mathbf{u}}_{(j)}. \tag{2.63b}$$

Here, $\mathbf{K}_{tan}$ is the global tangent stiffness matrix, i.e., for linearly elastic material behaviour, $\mathbf{K}_{tan} = \mathbf{K}$; γ provides a linearly varying weighting between the influence of the initial and the final accelerations on the velocity; and β provides the weighting between the influence of the initial and the final acceleration on the displacement. In ABAQUS, the coefficients γ and β are enhanced using an additional coefficient that reduces high-frequency artificial numerical noise, as proposed by Hilber, Hughes, and Taylor, 1977 (Dassault Systèmes Simulia Corp, 2014).

Knowing the increment of displacement, the increments of velocity and acceleration can be obtained using Newmark's approximations as follows:

$$\Delta\dot{\mathbf{u}}_{(j)} = \frac{\gamma}{\beta\Delta t}\Delta\mathbf{u}_{(j)} - \frac{\gamma}{\beta}\dot{\mathbf{u}}_{(j)} + \Delta t\Big(1 - \frac{\gamma}{2\beta}\Big)\ddot{\mathbf{u}}_{(j)}; \tag{2.64a}$$

$$\Delta\ddot{\mathbf{u}}_{(j)} = \frac{1}{\beta(\Delta t)^2}\Delta\mathbf{u}_{(j)} - \frac{1}{\beta\Delta t}\dot{\mathbf{u}}_{(j)} - \frac{1}{2\beta}\ddot{\mathbf{u}}_{(j)}. \tag{2.64b}$$

The displacement and its time derivatives for the next time step are then calculated as

$$\mathbf{u}_{(j+1)} = \mathbf{u}_{(j)} + \Delta\mathbf{u}_{(j)};\ \dot{\mathbf{u}}_{(j+1)} = \dot{\mathbf{u}}_{(j)} + \Delta\dot{\mathbf{u}}_{(j)};\ \ddot{\mathbf{u}}_{(j+1)} = \ddot{\mathbf{u}}_{(j)} + \Delta\ddot{\mathbf{u}}_{(j)}. \tag{2.65}$$

When **a nonlinear material** is considered, e.g., elastoplastic material behaviour, equation (2.46) can be written in the incremental form as

$$\Delta\boldsymbol{\sigma}^m = \mathbf{D}_{ep}\mathbf{B}\ \Delta\mathbf{u}^m, \tag{2.66}$$

where $\mathbf{D}_{ep}$ is the elastoplastic stress-strain constitutive matrix. For transient nonlinear dynamic analyses, the equilibrium for each time step is achieved through iteration, e.g., the Newton-Raphson iteration scheme or its modified form, based on the state of the internal and external forces. The increment of displacement $\Delta\mathbf{u}$ for time step (j), obtained through iterative process, is expressed as

$$\Delta\mathbf{u}_{(j)}^{[k]} = \Delta\mathbf{u}_{(j)}^{[k-1]} + \delta\mathbf{u}_{(j)}^{[k]},\ k = 1, 2, ..., \tag{2.67}$$

where superscript $[k]$ is the iteration step. In this case, equation (2.62) is enhanced into

$$\delta \mathbf{u}_{(j)}^{[k]} = [\hat{\mathbf{K}}^{[k]}(\mathbf{D}_{ep}^{[k-1]})]^{-1}\mathbf{R}_{(j)}^{[k]},\ j = 0, 1, 2, ..,\ k = 1, 2, ..., \tag{2.68}$$

which describes the contribution of displacement increment of a single iteration step $[k]$. The notation $\mathbf{R}$ is the residual between internal and external forces, expressed as

$$\mathbf{R}_{(j)}^{[k]} = \Delta \mathbf{P}_{(j)} - \breve{\mathbf{f}}(\Delta \boldsymbol{\sigma}^{[k]}) - \left[\frac{\gamma}{\beta \Delta t}\mathbf{C} + \frac{1}{\beta(\Delta t)^2}\mathbf{M}\right]\Delta \mathbf{u}_{(j)}^{[k]}, \tag{2.69}$$

where $\breve{\mathbf{f}}$ denotes the internal resisting force vector, given by

$$\breve{\mathbf{f}} = \int_V \mathbf{B}^T \boldsymbol{\sigma}\, dV = \sum_{m=1}^{M} \int_{V^m} \mathbf{B}^T \boldsymbol{\sigma}^m dV^m, \tag{2.70}$$

and the last part of (2.69) is the contribution of the dynamic part to the equilibrium. The internal force is updated in iteration step $[k]$ using equation (2.66) after obtaining the updated displacement $\Delta \mathbf{u}_{(j)}^{[k]}$, followed by the calculation of strain using the relation

$$\Delta \boldsymbol{\epsilon}_{(j)}^{[k]} = \mathbf{B}\ \Delta \mathbf{u}_{(j)}^{[k]}. \tag{2.71}$$

In equation (2.68), matrix $\hat{\mathbf{K}}^{[k]}(\mathbf{D}_{ep}^{[k-1]})$ considers the global tangent stifness matrix $\mathbf{K}_{tan}$ which includes the updated constitutive stress-strain matrix based on the state of stresses of the previous iteration step. The convergence can be defined through a tolerance value, described, e.g., as (Chopra, 1995; von Estorff and Firuziaan, 2000)

$$\left|\frac{\Delta \mathbf{u}^{[k]}}{\Delta \mathbf{u}}\right| < \text{tol., or} \tag{2.72a}$$

$$|\mathbf{R}^{[k]}| < \text{tol.} \tag{2.72b}$$

The implementation of the FEM for linear and nonlinear dynamics in ABAQUS is further detailed in the theory manual (Dassault Systèmes Simulia Corp, 2014).

2.6 The hybrid BEM-FEM based on the macro-element concept

The coupling of BE-FE was first proposed in Zienkiewicz, Kelly, and Bettess, 1977 and later extended for dynamic problems in Spyrakos and Beskos, 1986. From

the perspective of the coupling procedure, the hybrid BEM-FEM can be generally classified into (1) **direct method** and (2) **iterative method**. The method classification is summarized in Figure 2.4.

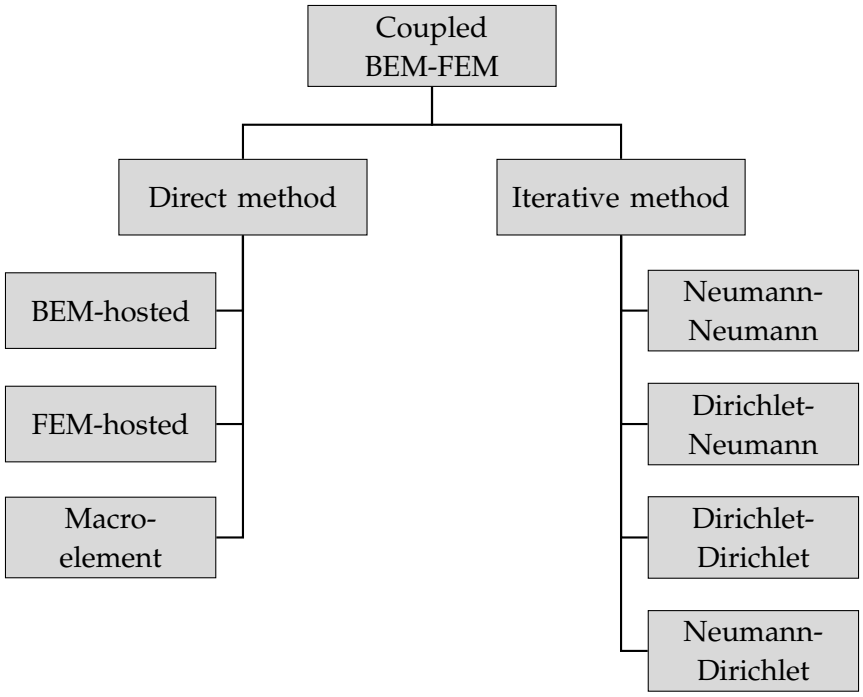

FIGURE 2.4: Classification of the coupled/hybrid BEM-FEM.

The iterative method

In the iterative method, the domain is decomposed into two subdomains. A trial boundary condition is given to both subdomains along their shared interface, where each equilibrium is solved independently. The results are then compared, and a new boundary condition is formulated iteratively until convergence for a single time step is achieved. The iterative method can be further divided according to the type of boundary condition used for the subdomains (Figure 2.4). Schematic flowcharts of the iterative method employing (1) the same boundary conditions and (2) mixed boundary conditions as input along the subdomain interface are shown in Figures 2.5 and 2.6, respectively. The advantage of the iterative method in comparison to the direct method is that (1) the need to combine both (BE and FE) systems of equations (SEs) is avoided and (2) since both subdomains are solved with their respective solvers, optimized and specialized solvers can be employed to the full extent. The combination of the SEs is one of the drawbacks of the direct method since the FEM and BEM matrices have different characteristics. In this field, Elleithy, Al-Gahtani, and El-Gebeily, 2001, extended

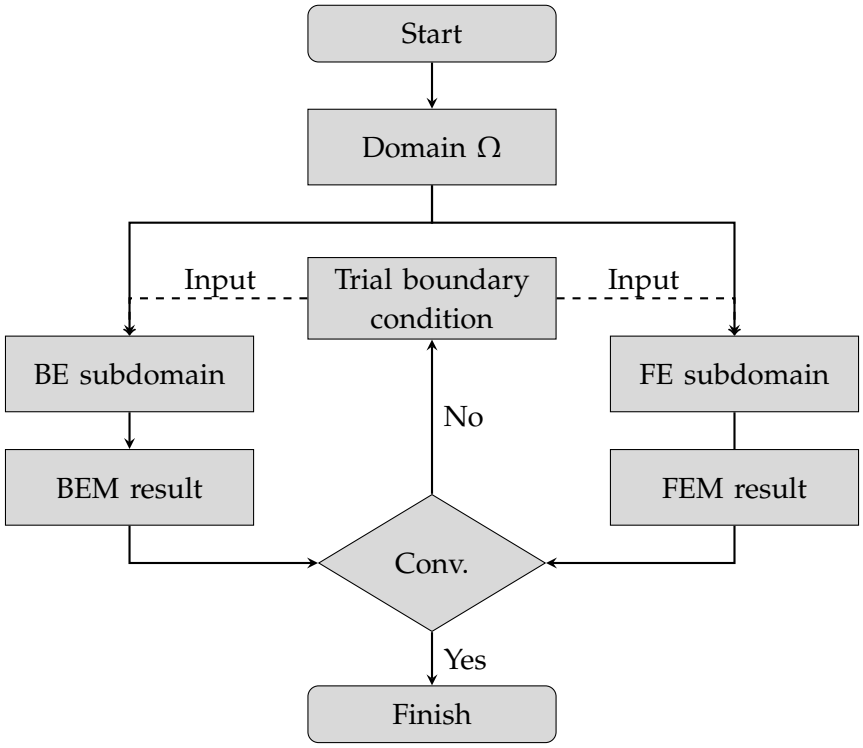

FIGURE 2.5: A schematic flowchart of the iterative method using the same boundary conditions as input along the subdomain interface, i.e., Dirichlet-Dirichlet or Neumann-Neumann.

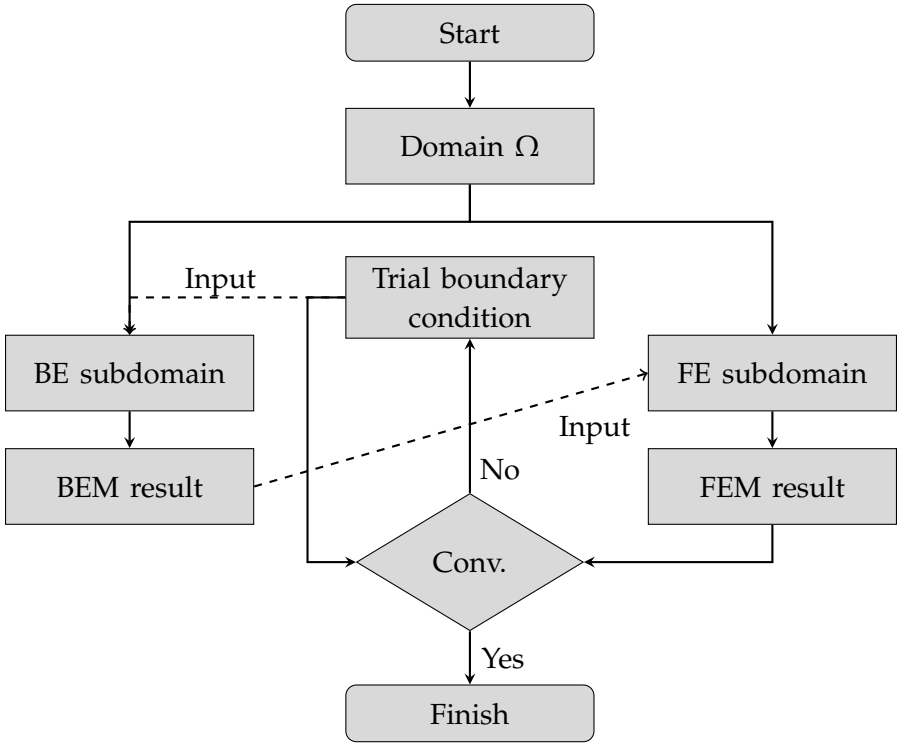

FIGURE 2.6: A schematic flowchart of the iterative method using a mixed type of boundary condition as input along the subdomain interface, i.e., Dirichlet-Neumann or Neumann-Dirichlet.

the work by Lin et al., 1996, and Feng and Owen, 1996, by improving the convergence rate for elastostatics. This was later extended for elastoplastic case in Elleithy, Tanaka, and Guzik, 2004, and for nonlinear dynamic analyses in Soares Jr, von Estorff, and Mansur, 2004; von Estorff and Hagen, 2005; Soares, 2008. An adaptive algorithm that avoided the domain partitioning to be predefined was later studied in Elleithy, 2008; Elleithy and Grzhibovskis, 2009; Soares and Godinho, 2015. Despite the promising potential, the usage of this method is limited in problem scale and the degree of nonlinearity due to the main drawback: **the necessary inter-domain iterations**. This drawback is especially problematic in cases with large interface areas or cases involving nonlinearities since the nonlinear iterations (generally included within the FE zone) are then nested inside the inter-domain iterations.

The direct method

The direct hybrid BE-FE method can be further classified into (1) FEM-hosted (e.g., in Wearing, Sheikh, and Burstow, 1991; Ganguly, Layton, and Balakrishna, 2000; von Estorff and Firuziaan, 2000; Bode, Hirschauer, and Savidis, 2002; François, Coulier, and Degrande, 2015; Galvín and Romero, 2014b), (2) BEM-hosted (e.g., in Brebbia and Georgiou, 1979), and (3) Macro-element approach, see the previous Section 2.2. The latter is similar to the FEM-hosted approach in that the BEM influence matrices and nodal traction vector are converted into FEM-like stiffness and structural damping matrices and nodal forces vector. In the classical FEM-hosted approach, these matrices and vector are superpositioned into the system of equation of the FE subdomain through its shared common nodes along the subdomain's interface. This method requires both subdomains to have **conforming discretizations** along the interface. In the numerical implementation, this transforms into a further requirement of having shared node numbering between the two. Although this problem is not considered a significant drawback for 2D problems, where domain discretization and node numbering sequence can be easily arranged, it becomes a significant hindrance for realistic 3D modeling. In the macro-element approach, the converted BE properties are made into a **substructure** that is then attached to the FE subdomain. In this dissertation, the assembly of the BE vector and matrices (via the substructure) is performed through the **common surfaces** instead of the shared common nodes. The drawback of the method is that the resulting global matrices and vector are larger in comparison to the ones of the FEM-hosted. However, it results in a very convenient **modeling flexibility** since the need to have conforming discretizations and

node numberings are entirely omitted. The other advantage is the ability to **transfer and reuse** the substructure for other FE models, provided that their interfaces have the same dimension and shape. This approach is thus an optimum one for engineering design or optimization, where the model has to be changed often or where computation jobs are performed by separate entities, e.g., by structural and geotechnical engineers.

In this section, a general description and the basic formulation of the coupling between BE and FE using the direct method is provided. Further details regarding the newly proposed assembly method are discussed in Section 3.5.

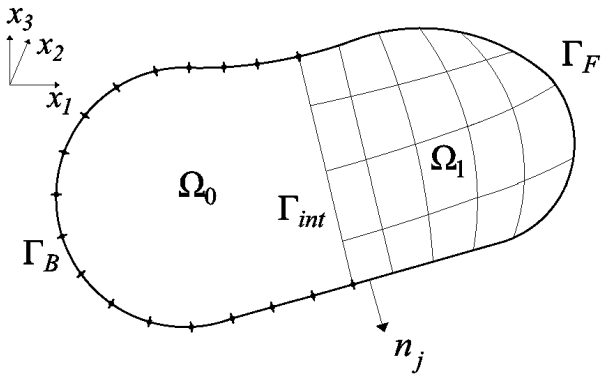

FIGURE 2.7: A cross-section of domain Ω after discretization into boundary elements in Ω_0 and finite elements in Ω_1. The interface between the subdomains is denoted as Γ_{int}.

In coordinate system $Ox_1x_2x_3$, consider the domain Ω as shown in Figure 2.7. The domain identical to the one discussed in the previous sections is now partitioned into BE and FE zones, denoted as Ω_0 and Ω_1, respectively. The interface boundary between both regions is with notation Γ_{int}. The boundaries of Ω_0 and Ω_1 that are not part of the interface are denoted as Γ_B and Γ_F, respectively, such that $\Gamma_{\Omega_0} = \Gamma_B \cup \Gamma_{int}$ and $\Gamma_{\Omega_1} = \Gamma_F \cup \Gamma_{int}$. The normal vectors to boundary Γ_{int} for each aforementioned domain are in opposite directions.

The material properties of the zone Ω_0 are density ρ_0; Lamé moduli λ_0, μ_0; longitudinal wave velocity $C_{P_0} = \sqrt{(\lambda_0 + 2\mu_0)/\rho_0}$; and shear wave velocity $C_{S_0} = \sqrt{\mu_0/\rho_0}$, while the material properties of both layers in the finite zone Ω_1 are as follows: λ_1, μ_1, C_{P_1}, C_{S_1}.

The equations of motion for Ω_1 and Ω_0 assuming zero body forces, are as follows:

$$\sigma_{ij,j}^{(\Omega_1)}(\mathbf{x},t) = \rho^{(\Omega_1)} \frac{\partial^2 u_i^{(\Omega_1)}(\mathbf{x},t)}{\partial t^2}, \quad \mathbf{x} \in \Omega_1; \tag{2.73}$$

$$\sigma_{ij,j}^{(\Omega_0)}(\mathbf{x},t) = \rho^{(\Omega_0)} \frac{\partial^2 u_i^{(\Omega_0)}(\mathbf{x},t)}{\partial t^2}, \quad \mathbf{x} \in \Omega_0. \tag{2.74}$$

Here, the superscripts inside round brackets denote the subdomain.

Along the interface surface boundary Γ_{int}, **compatibility and equilibrium conditions of displacements and tractions**, respectively, are satisfied, i.e. $u_i^{(\Omega_0)} = u_i^{(\Omega_1)}$ and $t_i^{(\Omega_0)} = -t_i^{(\Omega_1)}$. The boundary Γ_B is a traction-free surface, i.e., $t_i^{(\Omega_0)} = \sigma_{ij}^{(\Omega_0)} n_j^{(\Omega_0)} = 0$ along Γ_B. Along Γ_F, mixed boundary conditions of displacement and traction are assigned.

Following the procedure described in Section 2.4, equation (2.73) transforms into equation (2.75) in the frequency domain as follows (Dominguez, 1993):

$$\mathbf{H}^{(\Omega_0)} \hat{\mathbf{u}}^{(\Omega_0)} = \mathbf{G}^{(\Omega_0)} \hat{\mathbf{t}}^{(\Omega_0)}, \tag{2.75}$$

where $\mathbf{H}^{(\Omega_0)}$ and $\mathbf{G}^{(\Omega_0)}$ are the influence matrices; $\hat{\mathbf{u}}^{(\Omega_0)}, \hat{\mathbf{t}}^{(\Omega_0)}$ are the displacement and traction vectors at nodes on Γ_{Ω_0}. The matrix equation (2.75) can be decoupled into the following form:

$$\begin{bmatrix} \mathbf{H}_{11}^{(\Omega_0)} & \mathbf{H}_{12}^{(\Omega_0)} \\ \mathbf{H}_{21}^{(\Omega_0)} & \mathbf{H}_{22}^{(\Omega_0)} \end{bmatrix} \begin{bmatrix} \hat{\mathbf{u}}_1^{(\Omega_0)} \\ \hat{\mathbf{u}}_2^{(\Omega_0)} \end{bmatrix} = \begin{bmatrix} \mathbf{G}_{11}^{(\Omega_0)} & \mathbf{G}_{12}^{(\Omega_0)} \\ \mathbf{G}_{21}^{(\Omega_0)} & \mathbf{G}_{22}^{(\Omega_0)} \end{bmatrix} \begin{bmatrix} \hat{\mathbf{t}}_1^{(\Omega_0)} \\ \hat{\mathbf{t}}_2^{(\Omega_0)} \end{bmatrix} \tag{2.76}$$

where the index "1" in the matrices $\mathbf{H}^{(\Omega_0)}$, $\mathbf{G}^{(\Omega_0)}$ and vectors $\hat{\mathbf{t}}^{(\Omega_0)}$, $\hat{\mathbf{u}}^{(\Omega_0)}$ refers to the interface boundary Γ_{int}, while index "2" refers to the boundary Γ_B. In resume, notation (Ω_0) means that semi-infinite homogeneous elastic isotropic region Ω_0 is under consideration in equation (2.76); $\hat{\mathbf{u}}_1^{(\Omega_0)}$, $\hat{\mathbf{t}}_1^{(\Omega_0)}$ are the vectors of nodal displacements and tractions along the interface boundary Γ_{int}; and $\hat{\mathbf{u}}_2^{(\Omega_0)}$, $\hat{\mathbf{t}}_2^{(\Omega_0)}$ are the vectors of nodal displacements and tractions along the traction-free surface Γ_B.

Applying the **condensation procedure** in Vasilev et al., 2015, the following relation between traction $\hat{\mathbf{t}}_1^{(\Omega_0)}$ and displacement $\hat{\mathbf{u}}_1^{(\Omega_0)}$ vectors along the contact boundary Γ_{int} is derived:

$$\hat{\mathbf{t}}_1^{(\Omega_0)} = \mathbf{E}\, \hat{\mathbf{u}}_1^{(\Omega_0)}, \tag{2.77a}$$

where

$$\mathbf{E} = \left[\mathbf{G}_{11}^{(\Omega_0)} - \mathbf{H}_{12}^{(\Omega_0)}\mathbf{A}_{\mathbf{t}}\right]^{-1}\left[\mathbf{H}_{11}^{(\Omega_0)} - \mathbf{H}_{12}^{(\Omega_0)}\mathbf{A}_{\mathbf{u}}\right]; \tag{2.77b}$$

$$\mathbf{A}_{\mathbf{t}} = \left[\mathbf{H}_{22}^{(\Omega_0)}\right]^{-1}\mathbf{G}_{21}^{(\Omega_0)}; \quad \mathbf{A}_{\mathbf{u}} = \left[\mathbf{H}_{22}^{(\Omega_0)}\right]^{-1}\mathbf{H}_{21}^{(\Omega_0)}. \tag{2.77c}$$

The conversion of the BEM matrix into FEM-compatible form is performed using the mapping of the nodal traction $\hat{\mathbf{t}}$ into the nodal force $\hat{\mathbf{f}}^{(\Omega_0)}$. In equation (2.55d), the integral for traction (the 2nd part of the right-hand side) can be modified by inserting the shape functions $\mathbf{N}$ to interpolate the surface traction inside an element $\acute{\mathbf{t}}^m$ from its nodal values $\mathbf{t}^m$. The result can be written as

$$\hat{\mathbf{f}}^{(\Omega_0)} = [\mathbf{M}^*]\,\hat{\mathbf{t}}_1^{(\Omega_0)}, \tag{2.78}$$

where

$$\mathbf{M}^* = \sum_{m=1}^{M}\Lambda^m; \quad \Lambda^m = \int_{\Gamma_m}\mathbf{N}^T\mathbf{N}\,d\Gamma_m. \tag{2.79}$$

Here, the notation M is the number of boundary elements along Γ_{int}; Γ_m is the boundary of the element; and Λ^m is the elemental mapping matrix.

After the substitution of equation (2.78) into equation (2.77a), the following generalized expression for the nodal force vector $\hat{\mathbf{f}}^{(\Omega_0)}(\mathbf{x} \in \Gamma_{int}, \omega)$ is obtained:

$$\hat{\mathbf{f}}^{(\Omega_0)} = \mathbf{K}^{(\Omega_0)}\hat{\mathbf{u}}_1^{(\Omega_0)}, \tag{2.80}$$

where

$$\mathbf{K}^{(\Omega_0)} = [\mathbf{M}^*]\,\mathbf{E}. \tag{2.81}$$

Note that equation (2.80) is complex-valued with complex-valued stiffness matrix, displacement, and free-term vectors, i.e., we have the following:

$$\mathbf{K}^{(\Omega_0)} = \Re(\mathbf{K})^{(\Omega_0)} + i\Im(\mathbf{K})^{(\Omega_0)}; \quad \hat{\mathbf{u}}^{(\Omega_0)} = \Re(\hat{\mathbf{u}})^{(\Omega_0)} + i\Im(\hat{\mathbf{u}})^{(\Omega_0)}. \tag{2.82}$$

The wave field in the finite zone Ω_1 is described using equation (2.57) as follows:

$$\left[-\omega^2\mathbf{M}^{(\Omega_1)} + i\omega\mathbf{C}^{(\Omega_1)} + \left(\mathbf{K}^{(\Omega_1)} + i\mathbf{K}_s^{(\Omega_1)}\right)\right]\hat{\mathbf{u}}^{(\Omega_1)} = \hat{\mathbf{f}}^{(\Omega_1)}, \tag{2.83}$$

where $i = \sqrt{-1}$; $\mathbf{M}^{(\Omega_1)}$, $\mathbf{C}^{(\Omega_1)}$, and $\mathbf{K}^{(\Omega_1)}$ are the matrices of mass, viscous damping, and stiffness, respectively; $\mathbf{K}_s^{(\Omega_1)}$ is the structural damping matrix; $\hat{\mathbf{u}}^{(\Omega_1)}$ and $\hat{\mathbf{f}}^{(\Omega_1)}$ are vectors of nodal displacement and nodal force of the FE zone, respectively. The matrix $\mathbf{C}^{(\Omega_1)}$ contains the damping defined through Rayleigh and/or proportional damping, whilst the matrix $\mathbf{K}^{(\Omega_1)}$ contains the damping defined through structural damping.

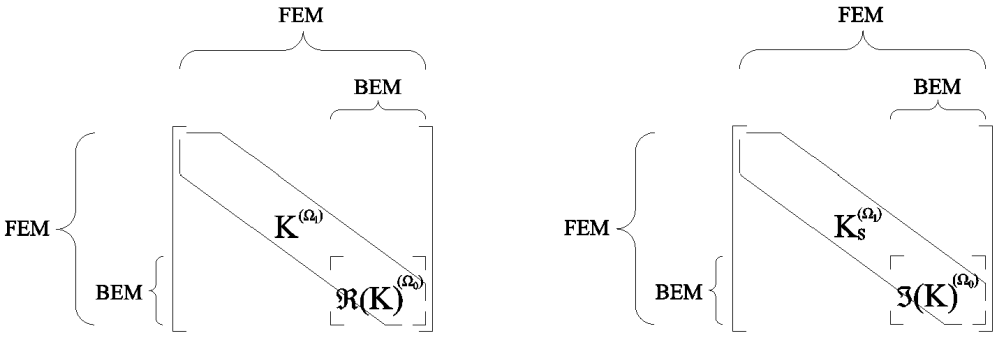

(A) (B)

FIGURE 2.8: Illustration of the assembly of (**A**) the global stiffness matrix **K**, and (**B**) the global structural damping matrix $\mathbf{K}_s$ through shared nodes along the subdomain interface.

The method used to couple the BEM properties into the FE environment of ABAQUS is based on the **substructure generation procedure** in which a substructure of the BEM model for semi-infinite domain Ω_0 is created and attached to the FEM model of the domain Ω_1 via prescribed tied common nodes where compatibility and equilibrium conditions are satisfied. ABAQUS model of the whole system includes sub-models concerning near-field Ω_1 and far-field Ω_0 zones in the following form:

$$\left[-\omega^2\mathbf{M} + i\omega\mathbf{C} + (\mathbf{K} + i\mathbf{K}_s)\right]\hat{\mathbf{u}} = \hat{\mathbf{f}}, \tag{2.84}$$

where **M**, **C**, and **K** are the corresponding mass, viscous damping, and stiffness matrices of the whole global system, respectively; $\mathbf{K}_s$ is the structural damping matrix of the whole hybrid model and $\hat{\mathbf{f}}$ is the vector presenting the external load. Comparing and fitting equations (2.80), (2.83) and (2.84) and taking advantage of the substructure procedure available in ABAQUS, we can derive the following relations for the **hybrid assembly**:

- The global stiffness matrix can be assembled from the stiffness matrix of FEM region $\mathbf{K}^{(\Omega_1)}$ and the real part of the stiffness matrix of BEM region $\Re(\mathbf{K}^{(\Omega_0)})$.

- The global structural damping matrix is assembled from the damping matrix of FEM model $\mathbf{K}_s^{(\Omega_1)}$ and the imaginary part of the stiffness matrix of the BEM zone $\Im(\mathbf{K}^{(\Omega_0)})$.
- The global load vector $\hat{\mathbf{f}} = \hat{\mathbf{f}}^{(\Omega_1)}$.
- The global viscous damping matrix is expressed by $\mathbf{C} = \mathbf{C}^{(\Omega_1)}$, where viscous damping matrix $\mathbf{C}^{(\Omega_1)}$ contains the damping defined through the Rayleigh and/or proportional damping definition of the FEM model.
- The global mass matrix is $\mathbf{M} = \mathbf{M}^{(\Omega_1)}$.
- The unknowns are the nodal displacements along (1) the FEM mesh and (2) the BEM mesh along the FE-BE interface.

The assembly of the global stiffness matrix and structural damping matrix is illustrated in Figure 2.8. The hybrid numerical scheme presented here is a 3D generalization of the hybrid scheme in Vasilev et al., 2015.

The general scheme of the modeling and computation is illustrated in Figure 2.9. The processes performed in MATLAB® and ABAQUS are not necessarily manual back-and-forth tasks since the processing phases in steps 3 through 6 can be executed under one set of code written in MATLAB®; it can send command to the operating system to execute ABAQUS.

During the **dicretization of the BEM region**, the surface boundary is discretized into either linear (3-node triangle and 4-node quadrilateral) or quadratic (6-node triangles and 8-node quadrilateral) isoparametric boundary elements, where continuous polynomial approximations are used for the boundary geometry, the displacement, and the traction vectors.

The well-known problem in hybrid techniques based on BEM and FEM is that FEM leads to sparse symmetric positive definite matrices, while BEM based on collocation technique leads to full, non-symmetric ones. Following the assembly of the stiffness matrix of BEM into the FEM system of equation, as described in the previous section, the stiffness and structural damping matrices of the whole model are both **unsymmetric**. ABAQUS provides unsymmetric matrix storage and solution scheme, which can be activated either by (1) using the syntax "*STEP, UNSYMM=YES" in the ABAQUS/Standard input file or by (2) choosing the unsymmetric equation solver in the step editor when using ABAQUS/CAE graphical user interface. This option is available for use in a direct-solution steady-state dynamic analysis.

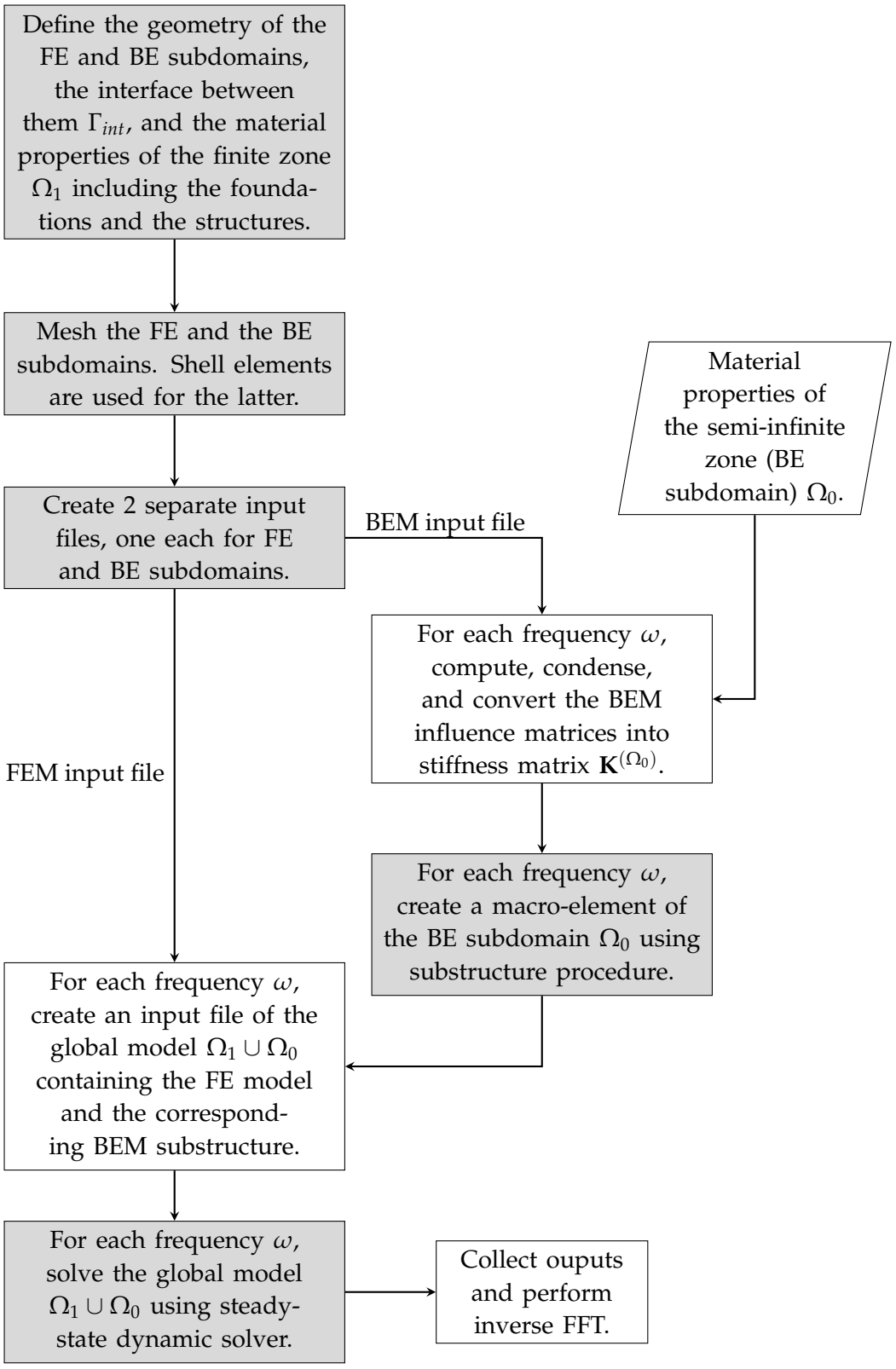

FIGURE 2.9: A schematic flowchart of the hybrid FEM-BEM based on the macro-element concept in the frequency domain. The grey color marks processes performed in the ABAQUS environment, while the white marks those performed in MATLAB.

2.7 Chapter summary

This chapter provides readers with basic concepts of the numerical methods and the coupling method used trough out this work. Further details of the FEM or the BEM can be perused in the textbooks referenced in each corresponding section. The following Chapter 3 describes the basic numerical enhancements developed and implemented based on these formulations.

Chapter 3

Basic numerical enhancements

3.1 Chapter overview

This chapter presents several basic numerical enhancements formulated and implemented for the hybrid BEM-FEM. Most enhancements are performed on the BEM formulation, which is a large part of the computation. The overview is followed by the description of the method to handle embedded transient dynamic point source, incident wave, and double-couple source in Section 3.2. It is followed by the description of the method to handle arbitrary non-smooth nodes in a half-space BE model using the enhanced analytical solution and dummy (enclosing) elements in Section 3.3. To reduce the computational load, the implementation of the mirroring algorithm based on the reciprocity of Green's function is presented in Section 3.4. It is followed by the description of the contact definition to handle the non-conforming BE-FE interface, which omits the need to have matching meshes and shared common nodes between both subdomains (Section 3.5). These enhancements mainly work in the background but result in a very convenient modeling flexibility and increase the solution efficiency, two features of great import in practical engineering. The chapter ends with verification studies of the hybrid method in Section 3.6. A part of this chapter is published in H.D.B. Aji, F. Wuttke, P. Dineva (2021). "3D hybrid model of foundation-soil-foundation dynamic interaction". In: *Z. für Angew. Math. Mech.* (*ZAMM*) 101, e202000351. DOI: 10.1002/zamm.202000351.

3.2 Inclusion of an embedded transient dynamic point source, an incident wave, or a double-couple source

Let us now extend the problem described in Section 2.6 into a closer idealization of real-world dynamic SSI problem as shown in Figure 3.1. Consider a 3D finite

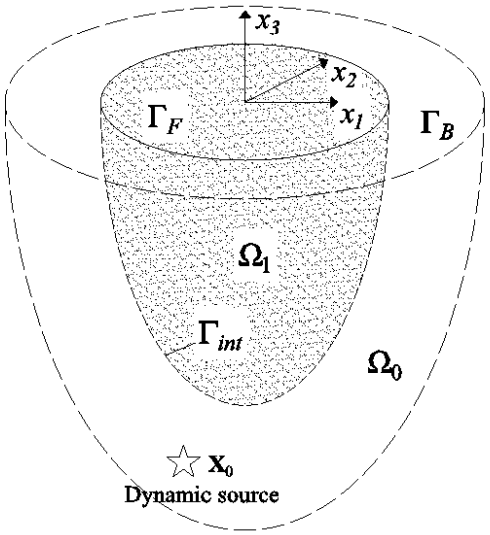

FIGURE 3.1: Problem geometry presenting the general configuration of the finite region Ω_1 embedded in a half-space Ω_0 with a dynamic source at $\mathbf{X}_0$.

geological region Ω_1 which is embedded in a semi-infinite elastic isotropic media Ω_0 with **transient dynamic load** comprising either (a) an incident plane wave or (b) waves generated by an embedded source (caused by seismic or other types of dynamic events) at point $\mathbf{X}_0(X_{01}, X_{02}, X_{03})$. This is possible since the BEM is suitable and accurate to handle the infinite or semi-infinite domain. The interface boundary between both regions Ω_1 and Ω_0 is with notation Γ_{int}, whilst the surface Γ_F and Γ_B are the free-surface of ranges Ω_1 and Ω_0, respectively. The boundary of the finite region Ω_1 is $\Gamma_{\Omega_1} = \Gamma_{int} \cup \Gamma_F$, whereas the boundary of the external semi-infinite zone Ω_0 is $\Gamma_{\Omega_0} = \Gamma_{int} \cup \Gamma_B$. The normal vectors to boundary Γ_{int} for each subdomain are in opposite directions.

Material properties of the geological semi-infinite zone Ω_0 are density ρ_0; Lamé constants λ_0, μ_0; the longitudinal wave velocity C_{P_0}; and the shear wave velocity C_{S_0}, while the material properties of the finite range Ω_1 are as follows: λ_1, μ_1, C_{P_1}, C_{S_1}.

To include the transient dynamic body force in Ω_0, the equation of motion in (2.74) is modified into the following:

$$\sigma_{ij,j}^{(\Omega_0)}(\mathbf{x},t) + f_i^{(\Omega_0)}(\mathbf{X}_0,t) = \rho^{(\Omega_0)} \frac{\partial^2 u_i^{(\Omega_0)}(\mathbf{x},t)}{\partial t^2}, \quad \mathbf{x} \in \Omega_0, i = 1,2,3, j = 1,2,3. \quad (3.1)$$

The equation of motion for subdomain Ω_1 remains the same as in (2.73). When an embedded dynamic point source located at $\mathbf{X}_0(X_{01}, X_{02}, X_{03})$ is considered, the dynamic force having the amplitude $f_i^{(\Omega_0)}(f_1^{(\Omega_0)}, f_2^{(\Omega_0)}, f_3^{(\Omega_0)})$ and the time history function $f(t)$ is presented as

$$f_i^{(\Omega_0)}(\mathbf{X}_0, t) = f_i^{(\Omega_0)} f(t)\delta(\mathbf{x} - \mathbf{X}_0). \tag{3.2}$$

Consider a dynamic state with a quiescent past, i.e., the initial conditions for displacements and their first derivatives with respect to time are zero. The solution to the problem of the transient wave is obtained by the use of the following well-known numerical procedure, see Chaillat, Bonnet, and Semblat, 2009: (a) the fast Fourier transform (FFT) is applied to the governing equations (3.1) and (2.73); (b) the corresponding boundary-value problem is solved in the frequency domain; and (c) the inverse fast Fourier transform (IFFT) is applied to the solutions in the frequency domain and finally solutions in the time domain are obtained.

After the application of FFT to equations (2.73) and (3.1), the frequency-dependent equations of motion have the following form:

$$\sigma_{ij,j}^{(\Omega_1)}(\mathbf{x}, \omega) + \rho^{(\Omega_1)}\omega^2 \hat{u}_i^{(\Omega_1)}(\mathbf{x}, \omega) = 0, \quad \mathbf{x} \in \Omega_1; \tag{3.3}$$

$$\sigma_{ij,j}^{(\Omega_0)}(\mathbf{x}, \omega) + \rho^{(\Omega_0)}\omega^2 \hat{u}_i^{(\Omega_0)}(\mathbf{x}, \omega) = -f_i^{(\Omega_0)} \hat{f}(\omega)\delta(\mathbf{x} - \mathbf{X}_0), \quad \mathbf{x} \in \Omega_0, \tag{3.4}$$

where ω is the circular frequency in rad/sec. The term $f_i(\mathbf{X}_0, t) = f_i^{(\Omega_0)} f(t)\delta(\mathbf{x} - \mathbf{X}_0)$ becomes $f_i^{(\Omega_0)} \hat{f}(\omega)\delta(\mathbf{x} - \mathbf{X}_0)$ in the frequency domain. The term $\hat{f}(\omega)$ is obtained by performing the FFT on $f(t)$, expressed as

$$\hat{f}(\omega) = \mathcal{F}\{f(t)\}(\omega). \tag{3.5}$$

Boundary conditions for semi-infinite region Ω_0 are as follows:

- Along the free-surface Γ_B, the tractions $\hat{t}_i^{(\Omega_0)} = \sigma_{ij}^{(\Omega_0)} n_j^{(\Omega_0)}$ are zero, $n_j^{(\Omega_0)}$ are the components of the outward normal to the surface Γ_B.
- Along the interface surface boundary Γ_{int}, compatibility and equilibrium conditions of displacements and tractions, respectively, are satisfied, i.e., $\hat{u}_i^{(\Omega_0)} = \hat{u}_i^{(\Omega_1)}$ and $\hat{t}_i^{(\Omega_0)} = -\hat{t}_i^{(\Omega_1)}$.
- Sommerfeld's radiation condition is satisfied at infinity.

Boundary conditions for finite region Ω_1 are detailed in the following:

- Along the free-surface Γ_F, the tractions are zero, i.e. $\hat{t}_i^{(\Omega_1)} = \sigma_{ij}^{(\Omega_1)} n_j^{(\Omega_1)} = 0$, $n_j^{(\Omega_1)}$ are the components of the outward normal to the surface Γ_F.
- Along the interface surface boundary Γ_{int}, compatibility and equilibrium conditions of displacements and tractions are satisfied.

The solution of the defined mechanical problem in the frequency domain satisfies the governing equations (2.73) and (3.1) and the boundary conditions discussed above.

After application of the reciprocal theorem to equation (3.4), the following **BIE** is obtained:

$$c_{lj}\hat{u}_j^{(\Omega_0)}(\boldsymbol{\xi},\omega) = \int_{\Gamma_{\Omega_0}} \hat{U}_{lj}^{*(\Omega_0)}(\mathbf{x},\boldsymbol{\xi},\omega)\hat{t}_j^{(\Omega_0)}(\mathbf{x},\omega)d\Gamma_{\Omega_0} - \int_{\Gamma_{\Omega_0}} \hat{P}_{lj}^{*(\Omega_0)}(\mathbf{x},\boldsymbol{\xi},\omega)\hat{u}_j^{(\Omega_0)}(\mathbf{x},\omega)d\Gamma_{\Omega_0} + f_j^{(\Omega_0)}\hat{f}(\omega)\hat{U}_{lj}^{*(\Omega_0)}(\mathbf{x},\mathbf{X}_0,\omega), \mathbf{x}\in\Gamma_{\Omega_0}, \boldsymbol{\xi}\in\Gamma_{\Omega_0}, \quad (3.6)$$

where $\mathbf{x}$, $\boldsymbol{\xi}$ is the source-receiver couple. The last part of (3.6) is obtained after the application of the reciprocal theorem and using the property of the integral of Dirac delta function, see Manolis et al., 2017.

In the case that the dynamic load is presented by an **incident plane wave**, the total wave field in Ω_0 can be described as the superposition product of the free-field motion, $\hat{u}_i^{ff}, \hat{t}_i^{ff}, i = 1,2,3$, and the scattered wave field, $\hat{u}_i^{sc}, \hat{t}_i^{sc}$ (due to wave scattering by Γ_{int}), as follows, see Vasilev et al., 2015:

$$\hat{u}_i^{(\Omega_0)}(\mathbf{x},\omega) = \hat{u}_i^{ff(\Omega_0)}(\mathbf{x},\omega) + \hat{u}_i^{sc(\Omega_0)}(\mathbf{x},\omega), \quad (3.7a)$$

$$\hat{t}_i^{(\Omega_0)}(\mathbf{x},\omega) = \hat{t}_i^{ff(\Omega_0)}(\mathbf{x},\omega) + \hat{t}_i^{sc(\Omega_0)}(\mathbf{x},\omega), i = 1,2,3. \quad (3.7b)$$

The corresponding BIE is written as follows:

$$c_{lj}(\hat{u}_j^{(\Omega_0)}(\boldsymbol{\xi},\omega) - \hat{u}_j^{ff(\Omega_0)}(\boldsymbol{\xi},\omega)) = \int_{\Gamma_{\Omega_0}} \hat{U}_{lj}^{*(\Omega_0)}(\mathbf{x},\boldsymbol{\xi},\omega)(\hat{t}_j^{(\Omega_0)}(\mathbf{x},\omega) - \hat{t}_j^{ff(\Omega_0)}(\mathbf{x},\omega))d\Gamma_{\Omega_0} - \int_{\Gamma_{\Omega_0}} \hat{P}_{lj}^{*(\Omega_0)}(\mathbf{x},\boldsymbol{\xi},\omega)(\hat{u}_j^{(\Omega_0)}(\mathbf{x},\omega) - \hat{u}_j^{ff(\Omega_0)}(\mathbf{x},\omega))d\Gamma_{\Omega_0}, \mathbf{x}\in\Gamma_{\Omega_0}, \boldsymbol{\xi}\in\Gamma_{\Omega_0}. \quad (3.8)$$

The BIE (3.8) above is written with respect to the scattered wave field. The **free-field motion** at point $\mathbf{x}(x_1, x_2)$ due to an incident P-wave with an amplitude A_P^{inc} and an incident wave angle θ^{inc} in the case of a time-harmonic excitation can be computed as follows (Wolf, 1985; Dineva et al., 2014):

$$\begin{pmatrix} u_1^{ff}(\mathbf{x},\omega) \\ u_2^{ff}(\mathbf{x},\omega) \end{pmatrix} = A_P^{inc} \begin{Bmatrix} k/k_p \\ -i\iota/k_p \end{Bmatrix} e^{-\iota x_2 - ikx_1} + A_P^{inc} R_{PP} \begin{Bmatrix} k/k_p \\ i\iota/k_p \end{Bmatrix} e^{\iota x_2 - ikx_1} + A_P^{inc} R_{PS} \begin{Bmatrix} i\iota'/k_p \\ -k/k_p \end{Bmatrix} e^{\iota' x_2 - ikx_1}, \quad (3.9)$$

where the wavenumbers are

$$k_p = \frac{\omega}{C_P};\ k_s = \frac{\omega}{C_S}; \quad (3.10a)$$

and

$$k = k_p \cos\theta^{inc}; \iota = ik_p \sin\theta^{inc};\ \iota' = \sqrt{k^2 - k_s^2};\ i = \sqrt{-1} \quad (3.11a)$$

$$\Delta(k) = (2k^2 - k_s^2)^2 - 4k^2 \iota\, \iota'; \quad (3.11b)$$

$$R_{PP} = -[(2k^2 - k_s^2)^2 + 4k^2 \iota\, \iota']/\Delta(k);\ R_{PS} = -4ik\iota(2k^2 - k_s^2)/\Delta(k). \quad (3.11c)$$

The angle θ^{inc} is measured anticlockwise from the axis Ox_1 to the direction of the wave propagation. The free-field motion at point $\mathbf{x}(x_1, x_2)$ due to an incident SV-wave with an amplitude of A_{SV}^{inc} is given by

$$\begin{pmatrix} u_1^{ff}(\mathbf{x},\omega) \\ u_2^{ff}(\mathbf{x},\omega) \end{pmatrix} = A_P^{inc} \begin{Bmatrix} -i\iota'/k_s \\ -k/k_s \end{Bmatrix} e^{-\iota' x_2 - ikx_1} + A_{SV}^{inc} R_{SS} \begin{Bmatrix} i\iota'/k_s \\ -k/k_s \end{Bmatrix} e^{\iota' x_2 - ikx_1} + A_{SV} R_{SP} \begin{Bmatrix} k/k_s \\ i\iota/k_s \end{Bmatrix} e^{\iota x_2 - ikx_1}, \quad (3.12)$$

where

$$k = k_s \cos\theta^{inc}; \iota = \sqrt{k^2 - k_p^2};\ \iota' = ik_s \sin\theta^{inc};\ i = \sqrt{-1} \quad (3.13a)$$

$$\Delta(k) = (2k^2 - k_s^2)^2 - 4k^2 \iota\, \iota'; \quad (3.13b)$$

$$R_{SS} = -[(2k^2 - k_s^2)^2 + 4k^2 \iota\, \iota']/\Delta(k);\ R_{SP} = 4ik\iota'(2k^2 - k_s^2)/\Delta(k). \quad (3.13c)$$

In the case of a 3D problem, equations (3.9) and (3.12) can be implemented by assuming x_2 as the vertical coordinate x_3 and x_1 as any horizontal coordinate of point $\mathbf{x}$.

The inclusion of **a double-couple dynamic source** can be derived as follows. The equivalent of equation (3.6) in the time domain is written as

$$c_{lj}u_j^{(\Omega_0)}(\boldsymbol{\xi},t) = \int_{\Gamma_{\Omega_0}} U_{lj}^{*(\Omega_0)}(\mathbf{x},\boldsymbol{\xi},t) * t_j^{(\Omega_0)}(\mathbf{x},t)d\Gamma_{\Omega_0} - \int_{\Gamma_{\Omega_0}} P_{lj}^{*(\Omega_0)}(\mathbf{x},\boldsymbol{\xi},t) * u_j^{(\Omega_0)}(\mathbf{x},t)d\Gamma_{\Omega_0} + f_j^{(\Omega_0)} f(t) * U_{lj}^{*(\Omega_0)}(\mathbf{x},\mathbf{X}_0,t), \boldsymbol{\xi} \in \Gamma_{\Omega_0}, \mathbf{x} \in \Gamma_{\Omega_0}, \mathbf{X}_0 \in \Omega_0. \quad (3.14)$$

Following the procedure by Aki and Richards, 1980, the body force is now applied at an infinitesimal distance of Δl_k from point $\mathbf{X}_0$, and the gradient of the Green's function (equation (2.40)) is taken over direction k. The last term of the above equation is now written as

$$f_j^{(\Omega_0)} f(t)\Delta l_k * \frac{\partial U_{lj}^{*(\Omega_0)}(\mathbf{x},\mathbf{X}_0,t)}{\partial x_k} = M_{jk}^{(\Omega_0)} f(t) * U_{lj,k}^{*(\Omega_0)}(\mathbf{x},\mathbf{X}_0,t), \quad (3.15)$$

where $M_{jk}^{(\Omega_0)} = f_j^{(\Omega_0)}\Delta l_k$ is the moment tensor. Equation (3.14) now reads

$$c_{lj}u_j^{(\Omega_0)}(\boldsymbol{\xi},t) = \int_{\Gamma_{\Omega_0}} U_{lj}^{*(\Omega_0)}(\mathbf{x},\boldsymbol{\xi},t) * t_j^{(\Omega_0)}(\mathbf{x},t)d\Gamma_{\Omega_0} - \int_{\Gamma_{\Omega_0}} P_{lj}^{*(\Omega_0)}(\mathbf{x},\boldsymbol{\xi},t) * u_j^{(\Omega_0)}(\mathbf{x},t)d\Gamma_{\Omega_0} + M_{jk}^{(\Omega_0)} f(t) * U_{lj,k}^{*(\Omega_0)}(\mathbf{x},\mathbf{X}_0,t), \boldsymbol{\xi} \in \Gamma_{\Omega_0}, \mathbf{x} \in \Gamma_{\Omega_0}, \mathbf{X}_0 \in \Omega_0. \quad (3.16)$$

The product of moment tensor and the derivative of the Green's function is written explicitly for 3D problem as (Aki and Richards, 1980)

$$\begin{aligned} M_{jk}f(t) * U_{lj,k}^{*} = {} & \left(\frac{15r_{,l}r_{,j}r_{,k} - 3r_{,l}\delta_{jk} - 3r_{,j}\delta_{lk} - 3r_{,k}\delta_{lj}}{4\pi\rho}\right)\frac{t}{r^4} \\ & M_{jk}\left(f\left(t-\frac{r}{C_P}\right) - f\left(t-\frac{r}{C_S}\right)\right) \\ & + \left(\frac{6r_{,l}r_{,j}r_{,k} - r_{,l}\delta_{jk} - r_{,j}\delta_{lk} - r_{,k}\delta_{lj}}{4\pi\rho\, C_P^2}\right)\frac{1}{r^2}M_{jk}f\left(t-\frac{r}{C_P}\right) \\ & - \left(\frac{6r_{,l}r_{,j}r_{,k} - r_{,l}\delta_{jk} - r_{,j}\delta_{lk} - 2r_{,k}\delta_{lj}}{4\pi\rho\, C_S^2}\right)\frac{1}{r^2}M_{jk}f\left(t-\frac{r}{C_S}\right) \\ & + \frac{r_{,l}r_{,j}r_{,k}}{4\pi\rho\, C_P^3}\frac{1}{r}M_{jk}\dot{f}\left(t-\frac{r}{C_P}\right) - \left(\frac{r_{,l}r_{,j} - \delta_{lj}}{4\pi\rho\, C_S^3}\right)r_{,k}\frac{1}{r}M_{jk}\dot{f}\left(t-\frac{r}{C_S}\right). \quad (3.17) \end{aligned}$$

Note that in comparison to equation (2.40), the above relation is obtained by replacing the Heaviside step function with the time function described in equation (3.2). In addition, the spatial derivatives are taken with respect to the source point $\boldsymbol{\xi}$ as opposed to the field point $\mathbf{x}$.

The equivalent displacement function for 2D problems assuming a line source parallel to the plane's normal can be derived from equation (2.41) as follows:

$$\begin{aligned}
M_{jk}f(t) * U^{*}_{lj,k} = \frac{1}{2\pi\rho C_P}\Bigg\{\frac{1}{r}\Bigg[\left(\frac{4}{R_1}+\frac{8R_1}{r^2}-\frac{r^2}{R_1^3}\right)r_{,l}r_{,j}r_{,k} \\
-\left(\frac{2R_1}{r^2}+\frac{1}{R_1}\right)\left(r_{,l}\delta_{jk}+r_{,j}\delta_{lk}+r_{,k}\delta_{lj}\right)\Bigg]M_{jk}f\left(C_Pt-r\right) \\
+\frac{1}{r^2}\Bigg[\left(2R_1+\frac{r^2}{R_1}\right)r_{,l}r_{,j}r_{,k}-R_1r_{,k}\delta_{lj}\Bigg]M_{jk}\dot{f}\left(C_Pt-r\right)\Bigg\} \\
-\frac{1}{2\pi\rho C_S}\Bigg\{\frac{1}{r}\Bigg[\left(\frac{4}{R_2}+\frac{8R_2}{r^2}-\frac{r^2}{R_2^3}\right)r_{,l}r_{,j}r_{,k} \\
-\left(\frac{2R_2}{r^2}+\frac{1}{R_2}\right)\left(r_{,l}\delta_{jk}+r_{,j}\delta_{lk}+r_{,k}\delta_{lj}\right)+\frac{r^2}{R_2^3}r_{,k}\delta_{lj}\Bigg]M_{jk}f\left(C_St-r\right) \\
+\frac{1}{r^2}\Bigg[\left(2R_2+\frac{r^2}{R_2}\right)r_{,l}r_{,j}r_{,k}-\left(R_2+\frac{r^2}{R_2}\right)r_{,k}\delta_{lj}\Bigg]M_{jk}\dot{f}\left(C_St-r\right)\Bigg\}. \quad (3.18)
\end{aligned}$$

The moment tensor M_{jk} is obtained according to the moment amplitude M_0 and the fault geometry: strike angle ϕ_{DC}, dip angle δ_{DC}, and rake angle γ_{DC}. It is written as (Aki and Richards, 1980)

$$\begin{aligned}
M_{jk} = M_0\Bigg(&\cos\delta_{DC}\cos\gamma_{DC}\begin{bmatrix}0 & 0 & -\cos\phi_{DC}\\ 0 & 0 & -\sin\phi_{DC}\\ -\cos\phi_{DC} & -\sin\phi_{DC} & 0\end{bmatrix} \\
&+\sin\delta_{DC}\cos\gamma_{DC}\begin{bmatrix}-\sin 2\phi_{DC} & \cos 2\phi_{DC} & 0\\ \cos 2\phi_{DC} & \sin 2\phi_{DC} & 0\\ 0 & 0 & 0\end{bmatrix} \\
&-\cos 2\delta_{DC}\sin\gamma_{DC}\begin{bmatrix}0 & 0 & \sin\phi_{DC}\\ 0 & 0 & -\cos\phi_{DC}\\ \sin\phi_{DC} & -\cos\phi_{DC} & 0\end{bmatrix} \\
&+\sin 2\delta_{DC}\sin\gamma_{DC}\begin{bmatrix}-\sin^2\phi_{DC} & \frac{1}{2}\sin 2\phi_{DC} & 0\\ \frac{1}{2}\sin 2\phi_{DC} & -\cos^2\phi_{DC} & 0\\ 0 & 0 & 1\end{bmatrix}\Bigg). \quad (3.19)
\end{aligned}$$

In this implementation, the north direction, which is the reference line for the strike angle measurement, is set along the x_1 direction.

In the 2D case, it is implied that the double-couple line source is along the east-west direction. Therefore, application in 2D cases is limited to slip movement or rupture with no east-west component, e.g., {$\phi_{DC} = 270^\circ$, δ_{DC} between 0-90°, $\gamma_{DC} = 90^\circ$} or {ϕ_{DC}=0, δ_{DC}=0, γ_{DC}=0}. In equation (3.19), the components of the 2nd rows and columns are omitted for 2D.

We can write the equivalent of equation (2.28) or (2.75) for equations (3.6), (3.8), and (3.16) by applying discretization and collocation procedures to them. The results can be summarized into the following **boundary element equation**:

$$\mathbf{H}^{(\Omega_0)}\hat{\mathbf{u}}^{(\Omega_0)} - \mathbf{G}^{(\Omega_0)}\hat{\mathbf{t}}^{(\Omega_0)} = \Phi^{(\Omega_0)}, \tag{3.20}$$

where the term $\Phi^{(\Omega_0)}$ depends on the type of the dynamic problem being considered.

$$\Phi^{(\Omega_0)} = \begin{cases} 0, \quad \text{for a dynamic source from within } \Omega_1; \\ f_j^{(\Omega_0)}\hat{f}(\omega)U_{lj}^{*(\Omega_0)}(\mathbf{x}, \mathbf{X}_0, \omega), \quad \text{for an embedded point source;} \\ \mathbf{H}^{(\Omega_0)}\hat{\mathbf{u}}^{ff(\Omega_0)} - \mathbf{G}^{(\Omega_0)}\hat{\mathbf{t}}^{ff(\Omega_0)}, \quad \text{for an incident plane wave; and} \\ \mathcal{F}\left\{\sum_1^{N_{DC}} M_{jk}^{(\Omega_0)} f(t) * U_{lj,k}^{*(\Omega_0)}(\mathbf{x}, \mathbf{X}_0, t)\right\}(\omega), \text{for double-couple sources.} \end{cases} \tag{3.21}$$

N_{DC} is the number of double-couple sources.

Following the above relation, the matrix equation (2.76) is now written as

$$\begin{bmatrix} \mathbf{H}_{11}^{(\Omega_0)} & \mathbf{H}_{12}^{(\Omega_0)} \\ \mathbf{H}_{21}^{(\Omega_0)} & \mathbf{H}_{22}^{(\Omega_0)} \end{bmatrix} \begin{bmatrix} \hat{\mathbf{u}}_1^{(\Omega_0)} \\ \hat{\mathbf{u}}_2^{(\Omega_0)} \end{bmatrix} - \begin{bmatrix} \mathbf{G}_{11}^{(\Omega_0)} & \mathbf{G}_{12}^{(\Omega_0)} \\ \mathbf{G}_{21}^{(\Omega_0)} & \mathbf{G}_{22}^{(\Omega_0)} \end{bmatrix} \begin{bmatrix} \hat{\mathbf{t}}_1^{(\Omega_0)} \\ \hat{\mathbf{t}}_2^{(\Omega_0)} \end{bmatrix} = \begin{bmatrix} \Phi_1^{(\Omega_0)} \\ \Phi_2^{(\Omega_0)} \end{bmatrix}, \tag{3.22}$$

where the index "1" refers to the interface boundary Γ_{int} and index "2" refers to the boundary Γ_B, as before. Equation (2.77a) can now be enhanced as (Vasilev et al., 2015)

$$\hat{\mathbf{t}}_1^{(\Omega_0)} = \mathbf{E}\,\hat{\mathbf{u}}_1^{(\Omega_0)} - \mathbf{p}, \tag{3.23}$$

where

$$\mathbf{p} = \left[\mathbf{G}_{11}^{(\Omega_0)} - \mathbf{H}_{12}^{(\Omega_0)}\mathbf{A}_\mathbf{t}\right]^{-1}\left[\Phi_1^{(\Omega_0)} - \mathbf{H}_{12}^{(\Omega_0)}\Theta\right]; \quad \Theta = \left[\mathbf{H}_{22}^{(\Omega_0)}\right]^{-1}\Phi_2^{(\Omega_0)}; \tag{3.24}$$

and the relation in (2.77b) remains. Equation (2.80) is now written as

$$\hat{\mathbf{f}}^{(\Omega_0)} = \mathbf{K}^{(\Omega_0)} \hat{\mathbf{u}}_1^{(\Omega_0)} - \mathbf{r}^{(\Omega_0)}, \tag{3.25}$$

where

$$\mathbf{K}^{(\Omega_0)} = [\mathbf{M}^*]\,\mathbf{E}; \quad \mathbf{r}^{(\Omega_0)} = [\mathbf{M}^*]\,\mathbf{p}. \tag{3.26}$$

The assembly of the SEs of the subdomains are the same as described in Section 2.6 with one addition: the assembly of the dynamic load vector $\mathbf{r}^{(\Omega_0)}$ into the global load vector $\hat{\mathbf{f}}$. The load vector can be obtained from the assembly of the vector of external loads assigned on the FEM model $\hat{\mathbf{f}}^{(\Omega_1)}$ and the vector of dynamic force term of the BEM model $\mathbf{r}^{(\Omega_0)}$. The workflow in Figure 2.9 is now enhanced as in Figure 3.2.

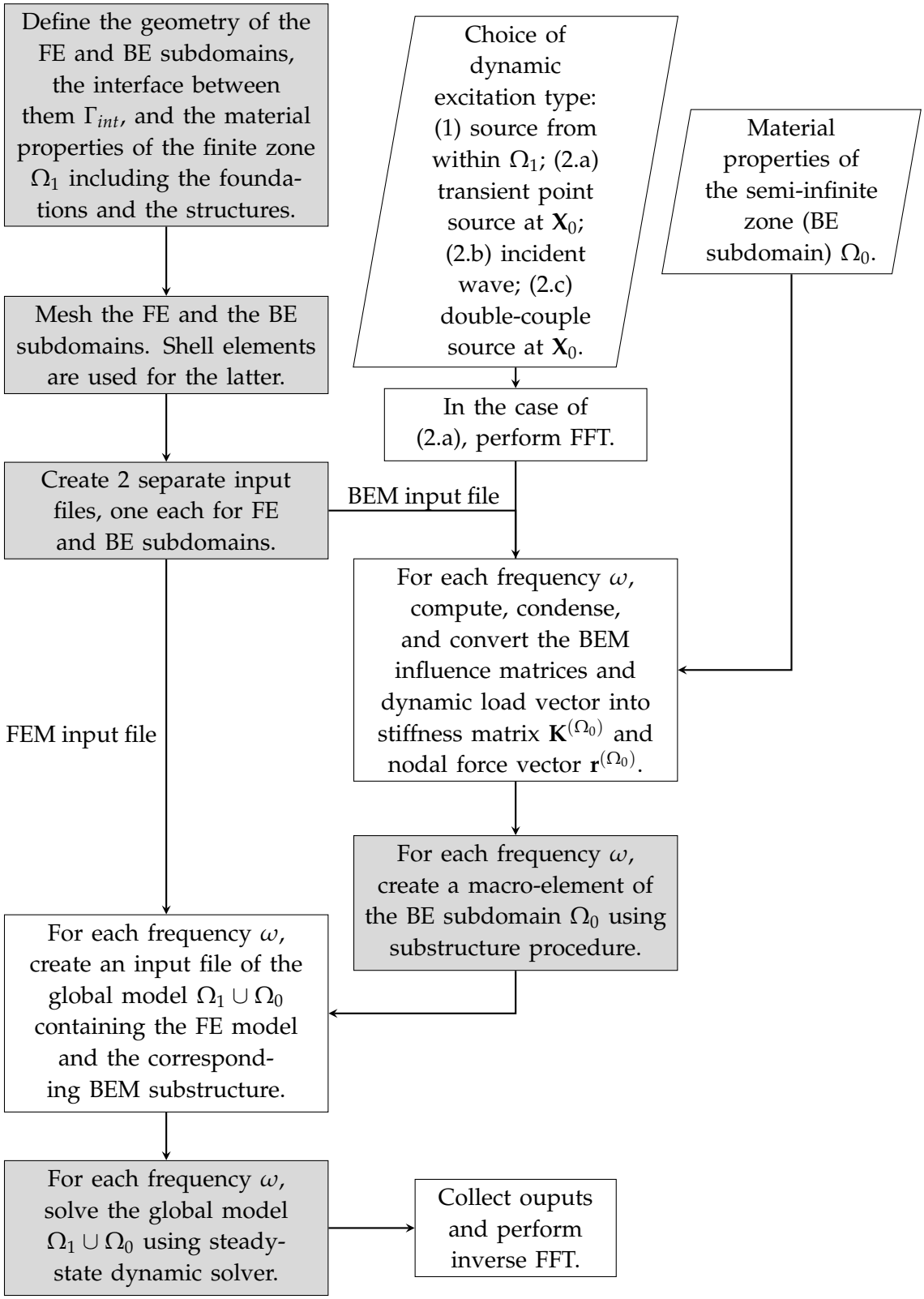

FIGURE 3.2: A schematic flowchart of the hybrid FEM-BEM based on the macro-element concept considering various types of dynamic sources. The grey color marks processes performed in the ABAQUS environment, while the white marks those performed in MATLAB.

3.3 Computation of the jump-term for arbitrary non-smooth nodes in the BE model

As described in Section 2.4, two types of integrals are obtained after discretization of boundary integral equations, depending on whether or not the radial distance r between the source and receiver points is zero: (a) at $r \neq 0$ the integrals are regular, and there are no singularities, the solution is numerical; (b) at $r = 0$ there are **two types of singularities**: (*) the displacement-based kernels exhibit a weak singularity of the type $O(\ln r)$ for 2D or $O(1/r)$ for 3D, and these integrals are solved by appropriate quadrature rule; (**) the traction-based kernels exhibit a singularity of the type $O(1/r)$ for 2D or $O(1/r^2)$ for 3D and these integrals can be solved analytically or using the rigid-body motion method, see Dominguez, 1993; Beer, Smith, and Duenser, 2008. This section briefly describes the explicit analytical solution and its enhancement that is well-suited for 2D problems, followed by the application of the rigid-body motion method for both 2D and 3D cases.

Let us examine the reciprocal form of the two elastodynamic states of a 2D subdomain Ω_0 in equation (2.18). Using the properties of the Dirac delta function in f_k^* and assuming zero body forces, we obtained the following form in the frequency domain

$$\hat{u}_j(\boldsymbol{\xi}, \omega) = \int_\Gamma \hat{U}_{lj}^*(\mathbf{x}, \boldsymbol{\xi}, \omega)\hat{t}_j(\mathbf{x}, \omega)d\Gamma - \int_\Gamma \hat{P}_{lj}^*(\mathbf{x}, \boldsymbol{\xi}, \omega)\hat{u}_j(\mathbf{x}, \omega)d\Gamma, \xi \in \Gamma_{\Omega_0}. \quad (3.27)$$

An **augmented boundary** Γ_{aug} near the point of interest $\boldsymbol{\xi}$ is created at a distance of r_{aug} from the point of interest $\boldsymbol{\xi}$, see Figure 3.3. Consider an infinitesimal surface along Γ_{aug} described as

$$d\Gamma_{aug} = r_{aug}\, d\theta. \quad (3.28)$$

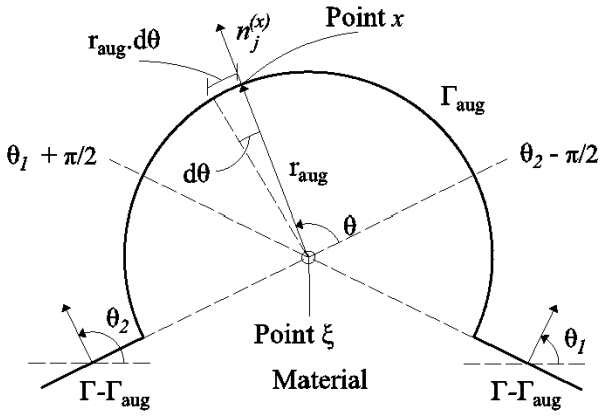

FIGURE 3.3: Illustration of the augmented boundary Γ_{aug} around point $\boldsymbol{\xi}$.

Implementing the augmented boundary, the right-hand side of (3.27) can be written as

$$\begin{aligned}\int_\Gamma \hat{U}^*_{lj}(\mathbf{x},\boldsymbol{\xi},\omega)\ \hat{t}_j(\mathbf{x},\omega)d\Gamma - \int_\Gamma \hat{P}^*_{lj}(\mathbf{x},\boldsymbol{\xi},\omega)\ \hat{u}_j(\mathbf{x},\omega)d\Gamma = \\ \lim_{r_{aug}\to 0}\int_{\Gamma-\Gamma_{aug}} \hat{U}^*_{lj}(\mathbf{x},\boldsymbol{\xi},\omega)\ \hat{t}_j(\mathbf{x},\omega)d\Gamma - \\ \lim_{r_{aug}\to 0}\int_{\Gamma-\Gamma_{aug}} \hat{P}^*_{lj}(\mathbf{x},\boldsymbol{\xi},\omega)\ \hat{u}_j(\mathbf{x},\omega)d\Gamma + \\ \lim_{r_{aug}\to 0}\int_{\Gamma_{aug}} \hat{U}^*_{lj}(\mathbf{x},\boldsymbol{\xi},\omega)\ \hat{t}_j(\mathbf{x},\omega)d\Gamma_{aug} - \\ \lim_{r_{aug}\to 0}\int_{\Gamma_{aug}} \hat{P}^*_{lj}(\mathbf{x},\boldsymbol{\xi},\omega)\ \hat{u}_j(\mathbf{x},\omega)d\Gamma_{aug}, \quad (3.29)\end{aligned}$$

The third part of the right-hand side of (3.29) vanishes as $r_{aug} \to 0$. The fourth part can be solved analytically since the $O(1/r)$ term in the traction fundamental solution and the r term from the integral solution over the semicircle boundary cancel each other out. This yields in the jump-term $c_{lj}, l = 1,2, j = 1,2$, in BIE (2.20) that can be written as

$$c_{lj}\hat{u}_j(\mathbf{x},\omega) = \lim_{r_{aug}\to 0}\int_{\Gamma_{aug}} \hat{P}^*_{lj}(\mathbf{x},\boldsymbol{\xi},\omega)\ \hat{u}_j(\mathbf{x},\omega)\ d\Gamma_{aug}. \quad (3.30)$$

The jump-term c_{lj} is the same as in the case of elastostatic because the elastodynamic fundamental solution tends to be the static one as $r \to 0$ (Dominguez, 1993).

The elastostatic **fundamental solution** that computes **tractions** at point **x** due

to a unit point load at point $\boldsymbol{\xi}$ is given by Lord Kelvin as (Dominguez, 1993; Beer, Smith, and Duenser, 2008)

$$P^*_{lj(static)}(\mathbf{x},\boldsymbol{\xi}) = \frac{C_2}{r}\left[C_3\delta_{lj} + 2r_{,l}r_{,j}\frac{\mathbf{r}\,\mathbf{n}}{\|r\|} - C_3(1-\delta_{lj})(n_j r_{,l} - n_l r_{,j})\right], \tag{3.31}$$

where

$$C_2 = \frac{1}{4\pi(1-\nu)};\ C_3 = 1-2\nu. \tag{3.32}$$

The vector $\mathbf{r} = r_j, j = 1,2$, is the distance vector between the $\boldsymbol{\xi}$ and $\mathbf{x}$ while $\mathbf{n} = n_j, j = 1,2$, is the unit normal of the surface at point $\mathbf{x}$. Inserting (3.31) into the integral in (3.30), one obtains the explicit expression of c_{lj} after integrating from $\theta_2 - \pi/2$ to $\theta_1 + \pi/2$ as (Dominguez, 1993)

$$[c_{lj}] = \mathbf{I} - \frac{1}{8\pi(1-\nu)}\begin{bmatrix} C_4 + \sin 2\theta_1 - \sin 2\theta_2 & \cos 2\theta_2 - \cos 2\theta_1 \\ \cos 2\theta_2 - \cos 2\theta_1 & C_4 - \sin 2\theta_1 + \sin 2\theta_2 \end{bmatrix}, \tag{3.33}$$

where

$$C_4 = 4(1-\nu)(\pi + \theta_2 - \theta_1), \tag{3.34}$$

θ_1 is the angle between the unit normal of the element that precedes the node $\boldsymbol{\xi}$ and Ox_1 axis, θ_2 is the angle between the unit normal of the element that follows $\boldsymbol{\xi}$ and the Ox_1 axis, and $\mathbf{I}$ is a 2×2 unit matrix. The jump-term (3.33) is accurate for point $\boldsymbol{\xi}$ when **the two adjacent elements are of equal length**.

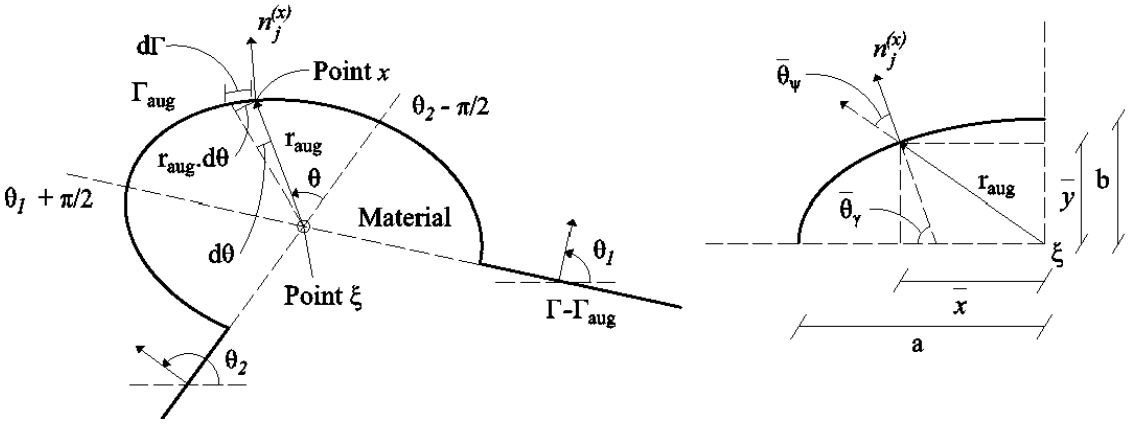

FIGURE 3.4: Illustration of the augmented boundary Γ_{aug} in the case that the adjacent elements have different lenghts. The right figure illustrates an idealized condition where the angle θ, i.e., the angle that is measured anticlockwise from $\theta_2 - \pi/2$ to $\theta_1 + \pi/2$, is $\pi/2$.

In the case that **the elements are of different length**, the accuracy can be maintained by modifying the non-diagonal terms of (3.33) as follows. Due to the

different lengths, the augmented boundary of the integral in (3.30) is now in an eccentric shape that is closer to an ellipse, see Figure 3.4 (left figure). Assuming an ideal angle between the adjacent elements of $\pi/2$ as in Figure 3.4 (right figure), the position of the target point $\mathbf{x}$ along Γ_{aug} in local coordinate $(\bar{x}, \bar{y})$ follows an ellipsoid form as

$$\frac{\bar{x}^2}{a^2} + \frac{\bar{y}^2}{b^2} = 1 \tag{3.35}$$

with the partial derivative over $\bar{x}$ of

$$\frac{2\bar{x}}{a^2} + \frac{2\bar{y}}{b^2}\frac{\partial \bar{y}}{\partial \bar{x}} = 0. \tag{3.36}$$

Here, $\bar{x}$ is inline with the tangent line of the proceeding element while $\bar{y}$ is perpendicular to $\bar{x}$ line. Thus, the tangent line to the ellipse in terms of the local coordinate is

$$\frac{\partial \bar{y}}{\partial \bar{x}} = -\frac{\bar{x}b^2}{\bar{y}a^2}. \tag{3.37}$$

Since

$$\tan\theta = \frac{\bar{y}}{\bar{x}}, \tag{3.38}$$

the normal vector to boundary Γ_{aug} at point $\mathbf{x}$ can be obtained as the negative reciprocal of the tangent line as

$$n_j = \tan\bar{\theta}_\gamma = \frac{\bar{y}a^2}{\bar{x}b^2} = \frac{a^2}{b^2}\tan\theta. \tag{3.39}$$

With the above relation, all components surrounding $\bar{\theta}_\gamma$ can be calculated as

$$\bar{x}_\gamma = r_{aug}\cos\theta\, C_5^2;\; r_\gamma = r_{aug}\left[\cos^2\theta\, C_5^4 + \sin^2\theta\right]^{\frac{1}{2}};\; C_5 = \frac{b}{a}. \tag{3.40}$$

C_5 is the ratio between the length of the following element to the length of the preceding element, i.e., the eccentricity of the augmented boundary. The radius and the normal direction sine and cosine are

$$r_{,\bar{x}} = \cos\theta;\; r_{,\bar{y}} = \sin\theta; \tag{3.41}$$

$$n_{,\bar{x}} = \frac{\cos\theta\, C_5^2}{\left[\cos^2\theta\, C_5^4 + \sin^2\theta\right]^{\frac{1}{2}}};\; n_{,\bar{y}} = \frac{\sin\theta}{\left[\cos^2\theta\, C_5^4 + \sin^2\theta\right]^{\frac{1}{2}}}. \tag{3.42}$$

We can define the $d\Gamma_{aug}$ as

$$d\Gamma_{aug} = \frac{r_{aug}\, d\theta}{\cos\bar{\theta}_{\psi}}; \tag{3.43}$$

$$\cos\bar{\theta}_{\psi} = \frac{\mathbf{n}\,\mathbf{r}}{\|\mathbf{n}\|\,\|\mathbf{r}\|} = n_{,j}\, r_{,j} = \frac{\cos^2\theta\, C_5^2 + \sin^2\theta}{\left[\cos^2\theta\, C_5^4 + \sin^2\theta\right]^{\frac{1}{2}}}. \tag{3.44}$$

We examine explicitly the integral of the non-diagonal part of (3.31), i.e., the third part of the right-hand side, using the preceding relations as

$$\int_{\theta_2-\pi/2}^{\theta_1+\pi/2} \frac{C_2C_3}{r_{aug}}\left[n_{,\bar{x}}r_{,\bar{y}} - n_{,\bar{y}}r_{,\bar{x}}\right] d\Gamma_{aug} = \int_{\theta_2-\pi/2}^{\theta_1+\pi/2} C_2C_3\left[\frac{\sin\theta\cos\theta(C_5^2-1)}{\cos^2\theta\, C_5^2 + \sin^2\theta}\right] d\theta, \tag{3.45}$$

which results in

$$\begin{aligned} c_{lj} &= -\frac{C_2C_3}{2}(1-\delta_{ij})\ln(\|(C_5^2-1)\cos^2\theta + 1\|)\Big|_{\theta_2-\pi/2}^{\theta_1+\pi/2} \\ &= -\frac{C_2C_3}{2}(1-\delta_{ij})\Big[\ln(\|(C_5^2-1)\sin^2\theta_1 + 1\|) - \\ &\qquad \ln(\|(C_5^2-1)\sin^2\theta_2 + 1\|)\Big]. \end{aligned} \tag{3.46}$$

The above relation (3.46) is applicable for general 2D problems with **arbitrary geometry** since it is free from the local coordinate term and takes into account the influence of the length difference between the two adjacent elements. When used in conjunction with (3.33), the results are also accurate for θ other than $\pi/2$.

The equivalent form of (3.33) for 3D problems can be derived similarly. This solution is only valid in models where all elements have the same size. The three-dimensional equivalent form of (3.46) is difficult to construct since an arbitrary point in 3D problems can be connected to more than two elements and may have different sizes. A general solution is also given in Mantic, 1993. However, implementing such a solution requires the elements to be numbered in a particular sequence. This is a rather complex task in a 3D model building with realistic arbitrary geometry.

Since this study is aimed at practicality and general applicability, the use of **the rigid-body motion method** is chosen for 3D problems, see Dominguez, 1993; Beer, Smith, and Duenser, 2008. The solution can be derived using the

assumption that the body is moving freely in space and the overall boundary of the domain is traction-free. The mathematical expression can be derived from equation (2.26) by applying zero tractions and collecting the terms related to point "i" in the left-hand side as

$$\mathbf{c}^i\,\hat{\mathbf{u}}^i + \hat{\mathbf{H}}^{ii}\hat{\mathbf{u}}^i = -\sum_{l=1}^{LE}\hat{\mathbf{H}}^{il}\hat{\mathbf{u}}^l. \tag{3.47}$$

Following the procedure described in Dominguez, 1993 (Chapter 2), the diagonal terms of the traction-based kernels $\hat{\mathbf{H}}^{ii}$ can be computed as

$$\hat{\mathbf{H}}^{ii} = -\sum_{l=1}^{LE}\hat{\mathbf{H}}_s^{il} + (\hat{\mathbf{H}}^{ii} - \hat{\mathbf{H}}_s^{ii}), \quad \text{for } i \neq l. \tag{3.48}$$

Here, $\hat{\mathbf{H}}_s$ is the static part of the traction-based kernels while $(\hat{\mathbf{H}} - \hat{\mathbf{H}}_s)$ is the dynamic part of the kernels. Using the method, the jump-term can be computed by summing all traction-based kernel static coefficients of all collocation points except for the point "i". The above relation is valid for half-space model. For a model of an infinite medium, the relation is as follows:

$$\hat{\mathbf{H}}^{ii} = \left(\mathbf{I} - \sum_{l=1}^{LE}\hat{\mathbf{H}}_s^{il}\right) + (\hat{\mathbf{H}}^{ii} - \hat{\mathbf{H}}_s^{ii}), \quad \text{for } i \neq l, \tag{3.49}$$

where $\mathbf{I}$ is a unit matrix of a suitable dimension.

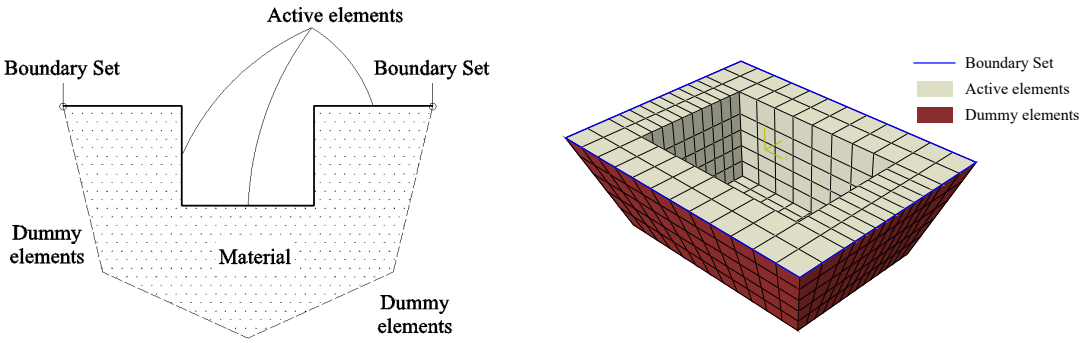

(A) (B)

FIGURE 3.5: Illustrations of dummy elements in a half-space model that allow the use of rigid-body motion method: (**A**) a sketch of a half-space problem with a valley and (**B**) an isometric view of the BEM mesh in ABAQUS.

The rigid-body motion method requires that a domain boundary is finite. Thus, it cannot be applied to arbitrary non-smooth nodes of an open polygon (in

2D case) or an open surface (in 3D case) geometry. To overcome this, the discretized half-space is enhanced with **dummy elements** and/or helper node to create an enclosed geometry, see Figure 3.5. The cost of the additional dummy elements are rather insignificant; they are only required for the computation of the static part of the traction fundamental solution and thus, they are only required to be calculated once.

The boundary elements that represent the relief of the half-space are refered to as "**active elements**" since they are considered for the complete computation in all frequencies. For the outer edges of the active boundary elements, the rigid-body motion calculation results in coefficients that depend on the shape, i.e., the angle θ. To correctly model the half-space, these values are overridden with value of $0.5\mathbf{I}$, where $\mathbf{I}$ is a unit matrix of 2×2 for 2D or 3×3 for 3D. For this, the edges where the active and the dummy elements meet are collected in a set named "**Boundary**". In ABAQUS, a **set** is a collection of regions or entities, e.g., nodes, elements, or surfaces, which can be used in the assignment of material definition, boundary condition, contact definition, etc. In this case, the node set "Boundary" is passed on to the in-house MATLAB® code. Based on this information, the code overrides the jump-term on any nodes that belongs to the set.

The application of the rigid-body motion method in the current coupled BEM-FEM can be summarized in the following steps:

1. Model the half-space with the relief and add enclosing geometry, i.e., edges or surfaces.
2. Create a geometry set that includes the dummy elements and another set that includes the outer edges of the half-space (Boundary Set).
3. The in-house MATLAB® code recognizes the dummy elements and considers the rest active elements. After computation of the BEM model, the in-house code recognizes the Boundary Set and overrides the jump-term c_{lj} of the nodes that belong to it.

Thus, the problem is shifted from the mathematical domain into simply modeling and numerical programming. Using this approach, any arbitrary non-smooth point with arbitrary adjacent element sizes in both 2D and 3D can be computed accurately.

3.4 Use of symmetry to reduce the BEM computation

One of the main drawbacks of BEM is the requirement to compute all influence coefficients between all collocation points. One can take advantage of the properties of Green's function or fundamental solutions to reduce the computational load. In a homogeneous boundary of a homogeneous domain, consider a unit impulse applied in the j-direction at $\mathbf{x} = \boldsymbol{\xi}^{(m)}$ and another unit impulse in the l-direction at point $\mathbf{x} = \boldsymbol{\xi}^{(n)}$. The following **spatial reciprocity** holds true (Aki and Richards, 1980):

$$\hat{U}^*_{lj}(\boldsymbol{\xi}^{(n)}, \boldsymbol{\xi}^{(m)}, \omega) = \hat{U}^*_{jl}(\boldsymbol{\xi}^{(m)}, \boldsymbol{\xi}^{(n)}, \omega), l = 1, 2, j = 1, 2. \tag{3.50}$$

The spatial reciprocity can be expanded as follows. If we consider that $\boldsymbol{\xi}^{(n)}$ is the mirror symmetry of $\boldsymbol{\xi}^{(m)}$ along Ox_l axis, $l = 1, 2$, then the following relations can be obtained:

- If $\boldsymbol{\xi}^{(n)}$ is a mirror symmetry of $\boldsymbol{\xi}^{(m)}$ along the Ox_2 axis such that $\boldsymbol{\xi}^{(n)}(-\xi_1, \xi_2)$, where ξ_1 and ξ_2 are the spatial components of $\boldsymbol{\xi}^{(m)}$, then

$$\hat{U}^*_{lj}(\boldsymbol{\xi}^{(n)}(-\xi_1, \xi_2), \boldsymbol{\xi}^{(m)}(\xi_1, \xi_2), \omega) = \mathfrak{M}_{lj} \circ \hat{U}^*_{lj}(\boldsymbol{\xi}^{(m)}(\xi_1, \xi_2), \boldsymbol{\xi}^{(n)}(-\xi_1, \xi_2), \omega). \tag{3.51}$$

- If $\boldsymbol{\xi}^{(n)}$ is a mirror symmetry of $\boldsymbol{\xi}^{(m)}$ along the Ox_1 axis such that $\boldsymbol{\xi}^{(n)}(\xi_1, -\xi_2)$, where ξ_1 and ξ_2 are the spatial components of $\boldsymbol{\xi}^{(m)}$, then

$$\hat{U}^*_{lj}(\boldsymbol{\xi}^{(n)}(\xi_1, -\xi_2), \boldsymbol{\xi}^{(m)}(\xi_1, \xi_2), \omega) = \mathfrak{M}_{lj} \circ \hat{U}^*_{lj}(\boldsymbol{\xi}^{(m)}(\xi_1, \xi_2), \boldsymbol{\xi}^{(n)}(\xi_1, -\xi_2), \omega). \tag{3.52}$$

Here, the symbol $\circ$ denotes the Hadamard (entrywise) operation. The operator $\mathfrak{M}_{lj}$ is defined as

$$\mathfrak{M}_{lj} = \begin{bmatrix} 1 & -1 \\ -1 & 1 \end{bmatrix}. \tag{3.53}$$

The reciprocity relations can be expanded for the case of **a mirror symmetry source-couple**. Consider the source-couple $(\boldsymbol{\xi}^{(m)}, \boldsymbol{\xi}^{(n)})$ as before and its mirror

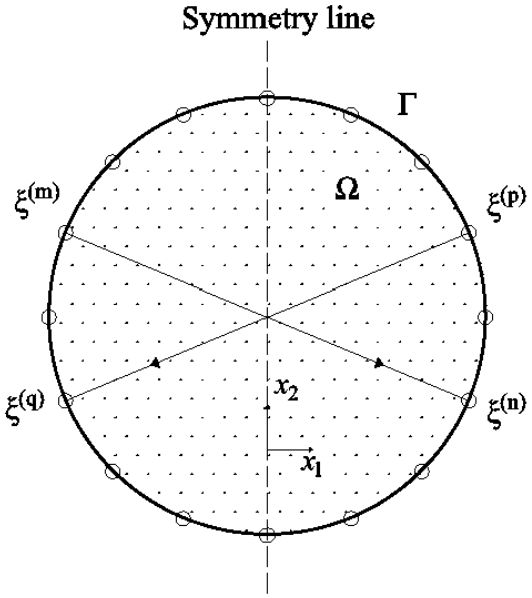

FIGURE 3.6: Source-receiver couple $(\boldsymbol{\xi}^{(m)}, \boldsymbol{\xi}^{(n)})$ and its mirror symmetry couple $(\boldsymbol{\xi}^{(p)}, \boldsymbol{\xi}^{(q)})$.

symmetry $(\boldsymbol{\xi}^{(p)}, \boldsymbol{\xi}^{(q)})$ due to a line along Ox_2 as shown in Figure 3.6. The following reciprocity expression can be derived:

$$\hat{U}^*_{lj}(\boldsymbol{\xi}^{(q)}(-\xi_1^{(n)}, \xi_2^{(n)}), \xi^{(p)}(-\xi_1^{(m)}, \xi_2^{(m)}), \omega) = \mathfrak{M}_{lj} \circ \hat{U}^*_{lj}(\boldsymbol{\xi}^{(n)}(\xi_1^{(n)}, \xi_2^{(n)}), \boldsymbol{\xi}^{(m)}(\xi_1^{(m)}, \xi_2^{(m)}), \omega). \quad (3.54)$$

The equivalent for a symmetry line along Ox_1 is as follows:

$$\hat{U}^*_{lj}(\boldsymbol{\xi}^{(q)}(\xi_1^{(n)}, -\xi_2^{(n)}), \xi^{(p)}(\xi_1^{(m)}, -\xi_2^{(m)}), \omega) = \mathfrak{M}_{lj} \circ \hat{U}^*_{lj}(\boldsymbol{\xi}^{(n)}(\xi_1^{(n)}, \xi_2^{(n)}), \boldsymbol{\xi}^{(m)}(\xi_1^{(m)}, \xi_2^{(m)}), \omega). \quad (3.55)$$

Since the traction fundamental solution is a product of the displacement one, the relations can be passed on as

$$\hat{P}^*_{lj}(\boldsymbol{\xi}^{(q)}(-\xi_1^{(n)}, \xi_2^{(n)}), \xi^{(p)}(-\xi_1^{(m)}, \xi_2^{(m)}), \omega) = \mathfrak{M}_{lj} \circ \hat{P}^*_{lj}(\boldsymbol{\xi}^{(n)}(\xi_1^{(n)}, \xi_2^{(n)}), \boldsymbol{\xi}^{(m)}(\xi_1^{(m)}, \xi_2^{(m)}), \omega); \quad (3.56)$$

$$\hat{P}^*_{lj}(\boldsymbol{\xi}^{(q)}(\xi_1^{(n)}, -\xi_2^{(n)}), \xi^{(p)}(\xi_1^{(m)}, -\xi_2^{(m)}), \omega) = \mathfrak{M}_{lj} \circ \hat{P}^*_{lj}(\boldsymbol{\xi}^{(n)}(\xi_1^{(n)}, \xi_2^{(n)}), \boldsymbol{\xi}^{(m)}(\xi_1^{(m)}, \xi_2^{(m)}), \omega). \quad (3.57)$$

Equations (3.54 - 3.57) are valid for 3D problems by modifying the operator $\mathfrak{M}_{lj}$ as follows:

$$\mathfrak{M}_{lj} = \begin{cases} \begin{bmatrix} 1 & -1 & -1 \\ -1 & 1 & 1 \\ -1 & 1 & 1 \end{bmatrix} & \text{for mirror symmetry along } Ox_2 - Ox_3 \text{ plane,} \\ \\ \begin{bmatrix} 1 & -1 & 1 \\ -1 & 1 & -1 \\ 1 & -1 & 1 \end{bmatrix} & \text{for mirror symmetry along } Ox_1 - Ox_3 \text{ plane.} \end{cases} \tag{3.58}$$

For the current hybrid BEM-FEM application, **the influence matrices** between point p and q in (2.29) can be computed from the influence matrices between point m and n, i.e., without having to perform any numerical integration, as

$$\mathbf{H}^{pq} = \mathfrak{M} \circ \mathbf{H}^{mn} \quad \text{for } (m, n, p, q = 1, 2, ..., LE), (l, j = 1, 2, 3); \tag{3.59}$$

$$\mathbf{G}^{pq} = \mathfrak{M} \circ \mathbf{G}^{mn} \quad \text{for } (m, p = 1, 2, ..., LE), (n, q \in \Gamma_{int}), (l, j = 1, 2, 3); \tag{3.60}$$

provided that points p and q are the mirror symmetry counterparts of points m and n, respectively. This operation is valid for the global **H** matrix but only valid for a part of the **G** matrix in which the receiver elements belong to the BE-FE interface, i.e., the elements where the traction values are unknown. This operation can be performed more effectively when applied on the global **H** matrix and part of **G** matrix, i.e., after the assembly of the element matrices is completed.

For the calculation of the force term due to dynamic sources such as those in Section 3.2, the symmetry operation for the traction-based kernels must be performed on a per-element basis since the traction values on two adjacent elements may be different. The expression for reciprocity between element a and its mirror symmetry element b is

$$\begin{aligned} \mathbf{G}^{pq} = \mathfrak{M} \circ \mathbf{G}^{mn} \quad & \text{for } (m, p = 1, 2, ..., LE), \\ & (n \in \text{element } a), (q \in \text{element } b), (l, j = 1, 2, 3). \end{aligned} \tag{3.61}$$

To utilize this approach, the following 6 steps are inserted:

1. The BEM model is divided into three quadrants (Figure 3.7) for 3D case (2

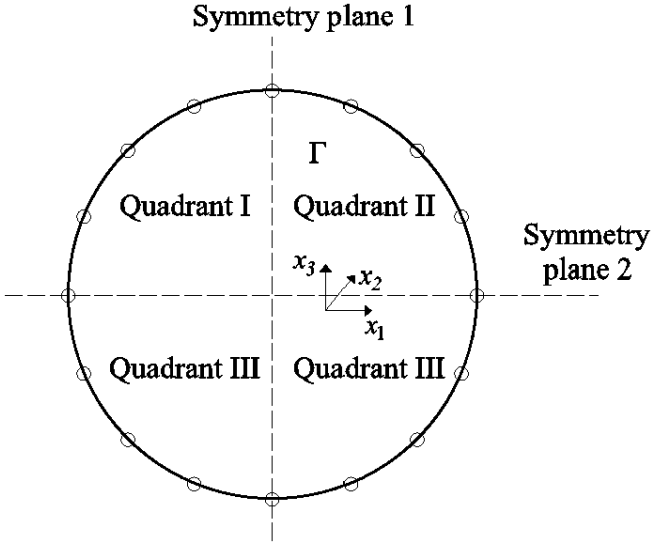

FIGURE 3.7: A cross-section view of a discretized Ω_1 where a double-symmetrical BEM model is divided into 3 quadrants.

quadrants in 2D case). Each quadrant is given a named set to be passed on to the in-house code.

2. The in-house code recognizes the quadrants and proceeds to search for the symmetry pair of every node and element in the BEM model.

3. Numerical integrations are then performed on the elements in the first quadrant. Due to the nature of the BEM formulation, computation of the 1st quadrant includes the sources from the whole BEM model, i.e., the sources from all quadrants, which results in rectangular matrices since the number of sources is much higher than the receivers.

4. The influence matrices are then mirrored to the second quadrant.

5. Subsequently, the matrices of the 1st and the 2nd quadrants are mirrored to the 3rd quadrant.

6. The resulting matrices of the 2nd and the 3rd quadrants are then superpositioned to the matrices of the 1st quadrant to obtain the complete influence matrices.

Although this approach is **not generally applicable**, there are many instances where it can be used. The algorithm can be modified easily to include a symmetry line or plane which is not along the main axis, i.e., at $x_1 \neq 0$ or $x_2 \neq 0$. The mirroring method **significantly reduces** the BEM computation load in 3D problems since only 25% of the total elements have to be computed. Total elapsed

computation time is reduced by circa 60% since an additional computation time is still required for the mirroring operation.

3.5 Solution to the non-conforming BE-FE interface

In Section 2.6 and Section 3.2, the assembly procedure of the BEM stiffness matrices and nodal force vector into the FEM SEs is described, where it is performed through shared common nodes. As discussed in the same sections, this type of procedure requires that **the meshes of the BEM and FEM models conform to each other along the BE-FE interface**. Further, the node numbering and sequences of both meshes must be the same to send the information correctly. In real 3D modeling jobs, this translates into a rather problematic task for **the following drawbacks**:

- The modeling tasks of the finite and semi-infinite regions may be performed by different persons, i.e., geotechnical and structural engineers.
- The structural model or the finite region may need to be modified often to optimize the design or to revise/update the assumptions. This will mean that the semi-infinite model then has to be modified accordingly.
- The pre-processing software may not facilitate a thorough or deep intervention from the user to its node numbering algorithm since this is optimized to produce banded FEM matrices.
- The model geometry may simply be too complex that conforming meshes of solid elements in the finite region and shell elements along the semi-infinite zone cannot be materialized.

To overcome this challenge, one can take advantage of the contact interaction definitions in ABAQUS, in which three options are provided: general contact, contact pairs, and contact element. The first two options are generally recommended, while the latter is for special cases only (Dassault Systèmes Simulia Corp, 2014). **"Tied" contact** is available under **contact pairs** option to join two surfaces together with no relative motion. This type of contact allows for dissimilar meshes to be joined.

In the "tied" contact definition, one must define one of the surfaces as a **master surface** and the other as a **slave surface**. ABAQUS enforces a kinematic constraint such that the slave surface does not penetrate the master surface. Therefore, the best practice is to assign the surface with the finer mesh as the slave

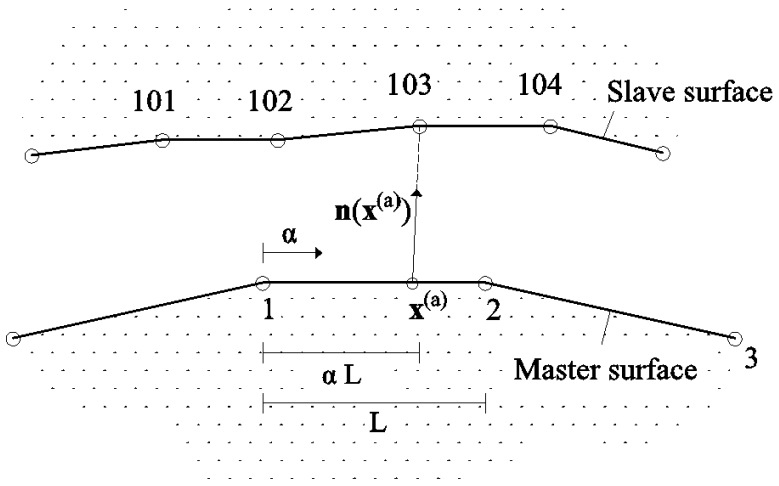

FIGURE 3.8: Interaction between a node on the slave surface and its pairing nodes on the master surface in a contact pair in ABAQUS.

surface. At the beginning of the analysis, ABAQUS pairs each node on the slave surface to the nearest neighbouring nodes of the master surface. An illustration is given in Figure 3.8 where node 103 is the considered node on the slave surface, and nodes 1 and 2 are the pairing nodes on the master surface. ABAQUS then creates an "**anchor**" point along the master surface, $\mathbf{x}^{(a)}$, which can be expressed as

$$\mathbf{x}^{(a)} = (1-\alpha)\mathbf{x}^{(1)} + \alpha\mathbf{x}^{(2)}, \tag{3.62}$$

where $\mathbf{x}^{(j)}$ is the coordinate vector of node j and α is calculated such that the line $\mathbf{x}^{(a)} - \mathbf{x}^{(103)}$ coincides with $\mathbf{n}(\mathbf{x}^{(a)})$. The unit normal $\mathbf{n}(\mathbf{x}^{(a)})$ is based one a smooth transition of the unit normal vectors of the nodes of the master surface, e.g., $\mathbf{n}(\mathbf{x}^{(a)})$ is based on $\mathbf{n}(\mathbf{x}^{(1)})$ and $\mathbf{n}(\mathbf{x}^{(2)})$; $\mathbf{n}(\mathbf{x}^{(2)})$ is obtained by averaging the normal of segments $\mathbf{x}^{(1)} - \mathbf{x}^{(2)}$ and $\mathbf{x}^{(2)} - \mathbf{x}^{(3)}$. The above spatial interpolation relation (3.62) can be generalized as

$$\mathbf{x}^{(a)} = \sum_{l=1}^{LM^{(a)}} \mathbf{N}_l \mathbf{x}^{(l)}, \quad l = 1, 2, ..., LM^{(a)}, \tag{3.63}$$

which is similar to equation (2.43) before. The notation $LM^{(a)}$ denotes the number of pairing nodes on the master surface related to point a, which depends on the dimension of the problem. This relation is then used for displacement such that

$$\hat{\mathbf{u}}^{(a)} = \sum_{l=1}^{LM^{(a)}} \mathbf{N}_l \hat{\mathbf{u}}^{(l)}, \quad l = 1, 2, ..., LM^{(a)}. \tag{3.64}$$

In this implementation of hybrid BEM-FEM, the macro finite element (or substructure) of the BE subdomain is joined using tied contact to the surfaces of the FE zone along the BE-FE interface. The substructure is defined as the master surface, while the latter is defined as the slave surface. There are two solid reasons for this: (1) the mesh on the FE zone tends to be finer compared to the one of the BE zone; and (2) since the finer mesh is assigned as the slave surface, the computation of the contact converges more quickly, and the setup results in a faster computation. The equation relating the displacement of a slave node a on the finite region Ω_1 along the interface to the displacements of the neighbouring nodes in the substructure (Ω_0) can be expressed as follows:

$$\hat{\mathbf{u}}^{(a)(\Omega_1)} = \sum_{l=1}^{LM^{(a)}} \mathbf{N}_l \hat{\mathbf{u}}^{(l)(\Omega_0)}, \quad a \in \Omega_1; l \in \Omega_0; l = 1, 2, ..., LM^{(a)}, \tag{3.65}$$

where the superscripts (Ω_0) and (Ω_1) denote the domain. Note that the above equation is also valid for time domain formulation. The coefficients of the stiffness and the damping matrices of point a and those of the pairing nodes $l = 1, 2, ..., LM^{(a)}$ **act in parallel**. Using the above relation, the total number of unknowns is slightly reduced. The effective nodal force acting on point a can be obtained as

$$\hat{\mathbf{f}}^{(a)(\Omega_1)} = \mathbf{K}^{(a)(\Omega_1)} \sum_{l=1}^{LM^{(a)}} \mathbf{N}_l \hat{\mathbf{u}}^{(l)(\Omega_0)}. \tag{3.66}$$

In the case that an embedded transient dynamic source or incident wave is considered, the dynamic nodal force vector $\mathbf{r}^{(\Omega_0)}$ is distributed along the interface into effective nodal forces such that for point a, it is expressed as

$$\hat{\mathbf{f}}^{(a)(\Omega_1)} + \sum_{l=1}^{LM^{(a)}} \mathbf{r}_{eff}^{(\Omega_0)} = \sum_{l=1}^{LM^{(a)}} \mathbf{r}^{(\Omega_0)}. \tag{3.67}$$

This implementation omits the need to conventionally assemble the BE vector and matrices to the FE SEs through the shared nodes. Instead, the substructure is defined using a completely different nodal subset. The consequence is that the global matrices and vector are larger than the ones of the traditional FEM-hosted approach. Illustration of the assembly of the global stiffness matrix $\mathbf{K}$, global structural damping matrix $\mathbf{K}_s$, and the global force vector $\hat{\mathbf{f}}$ is given in Figure 3.9. However, this approach brings **the following advantages**: (1) discretization of the FE and BE models, as well as the modeling of the BE-FE interface, are more

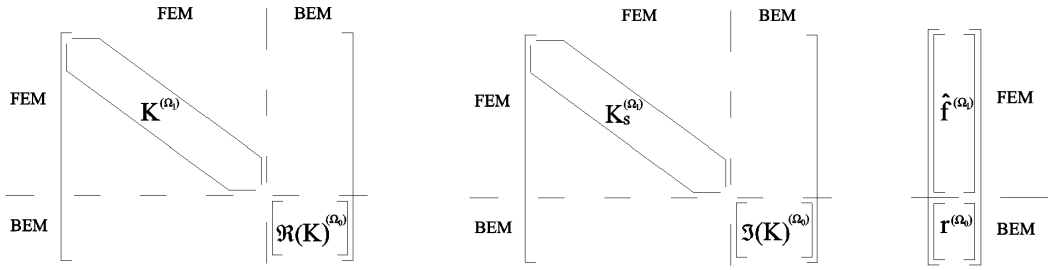

(A) (B) (C)

FIGURE 3.9: Illustration of the assembly of (**A**) the global stiffness matrix **K**, (**B**) the global structural damping matrix $\mathbf{K}_s$, and (**C**) the global force vector $\hat{\mathbf{f}}$ using tied contact pair.

accessible and more flexible, especially for 3D realistic models since meshes of both subdomains do not need to conform; (2) since the substructure is using **a different nodal subset**, it is **transferable** and **reusable** for other FE models; (3) due to the transferability of the substructure, **modeling and computation tasks can be distributed** into separate entities; (4) the possibility to reuse the substructure means that computation time can be significantly reduced, which is helpful for parametric studies, designs, or optimization tasks.

3.6 Verification of the enhanced hybrid computational scheme

What follows is the solution of benchmark examples to present the accuracy and convergence study of the described hybrid numerical scheme and establish its accuracy level. As far as the discretization approach is applied in both BEM and FEM models, the relative size of the discretization elements and possible mismatches (i.e. small elements abutting large ones) can cause spurious wave reflections not otherwise present. The accuracy criterion used in the discretization procedure states that $\lambda_S/l_{BE} \geq 10$, where l_{BE} is the length of the corresponding element and λ_S is the shear wavelength. In the case that quadratic elements are in use, it is shown in the following examples that $\lambda_S/l_{BE} \geq 5$ is sufficient.

Test example 1: wave propagation in a homogeneous half-space due to incident waves

The first benchmark example considers the geometry presented in Figure 3.1 assuming that the local finite geological region Ω_1 is a square cuboid, see Figure

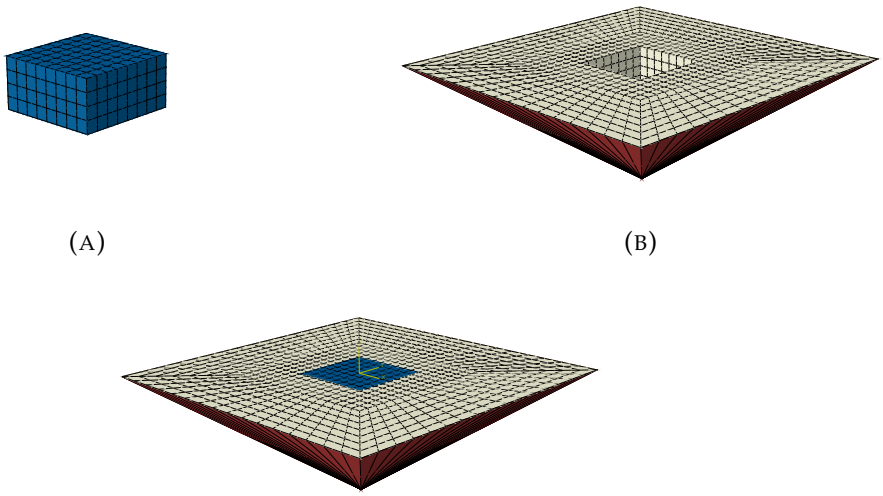

(A) (B)

(C)

FIGURE 3.10: The geometry of test example 1: (**A**) the FEM region, (**B**) the BEM region, and (**C**) the whole BEM-FEM model.

3.10, with the same material properties as those of the semi-infinite region Ω_0. This means that the 1st numerical scheme verification concerns the wave propagation in a homogeneous half-space due to incident normal time-harmonic P- or SV-wave. The FEM region, the BEM zone, and the global BEM-FEM model are shown in Figures 3.10a, 3.10b, and 3.10c, respectively. The dimension of the surface of the BEM model is 8×8 m^2. The FEM region is a square cuboid which has a width of 2 m and a depth of 1 m. Thus, the BEM-FEM interface is a parallelepiped of the exact sizes. In Figure 3.10, the dummy elements are red colored. The same material properties are applied to both zones. The material properties are as follows: Lamé constants $\lambda = \mu = 4.5$ MPa and Poisson's ratio of 0.25. The incident P- or SV-wave considered here is a wave propagating in the vertical direction, i.e., in the direction of the coordinate axis x_3 in Figure 3.1. The shearing direction in the case of SV-wave is in the direction of the coordinate axis x_1, see Figure 3.1. The following frequencies are considered: 0.05 Hz, 20 Hz, and 43.3 Hz for the P-wave; and 0.05 Hz, 20 Hz, and 40 Hz for the SV-wave.

Two mesh sizes, Mesh A and Mesh B, are compared here to show the convergence. The mesh sizes of the boundary and finite elements in both meshes are 1/4 m and 1/6 m, respectively, which correspond to 1/5 and 1/7.5 of the shortest shear wavelength ($\lambda_S = 1.25$ m for 40 Hz). Ratios β_P and β_S relate the longest wavelength to the length of the discretized free-surface of the half-space (Γ_B in

Figure 3.1), written for the shear wave as

$$\beta_S = \lambda_S / l_{\Gamma_B}. \tag{3.68}$$

The length l_{Γ_B} of the model in Figure 3.10 is 3 m which corresponds to $\beta_P = 577.35$ for P-wave case at 0.05 Hz and $\beta_S = 333.33$ for SV-wave case at 0.05 Hz. The numbers of elements used for this example, in the case of $\lambda_S / l_{BE} = 5$ and $\beta_S = 333.33$, are 256 quadratic hexahedral finite elements and 1024 quadratic quadrilateral boundary elements for Mesh A and; 864 quadratic hexahedral finite elements and 2112 quadratic quadrilateral boundary elements for Mesh B.

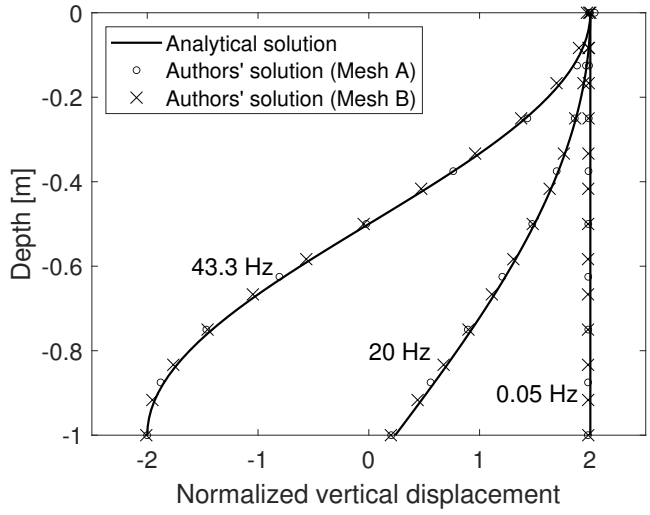

(A)

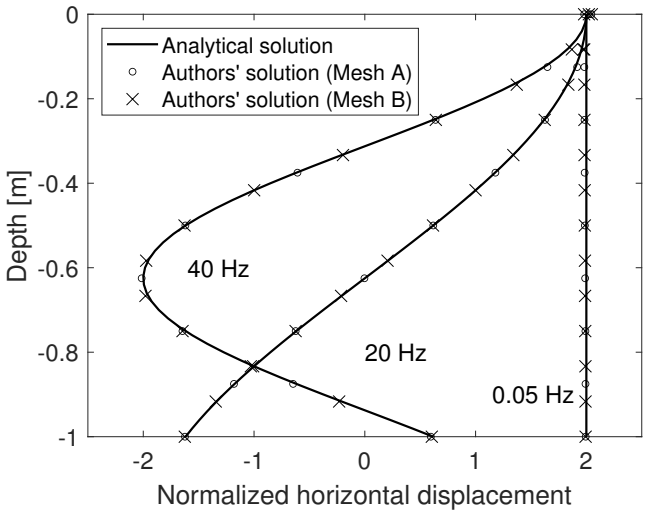

(B)

FIGURE 3.11: Displacements in the FEM zone along line $x_1 = 0$, $x_2 = 0$ of test example 1: (**A**) normalized vertical displacement due to vertical incident P-wave and (**B**) normalized horizontal displacement due to vertical incident SV-wave.

The normalized by incident wave amplitude displacements along the line $x_1 = 0$, $x_2 = 0$ inside the FEM zone for the case of $\beta_P = 577.35$, $\beta_S = 333.33$ are shown in Figures 3.11a and 3.11b. Outstanding agreements between the analytical solution for free-field wave motion in homogeneous elastic isotropic half-space presented in Achenbach, 1975, and solutions obtained by the hybrid BEM-FEM for test example 1 are apparent. In the case of incident P-wave, the relative errors to the analytical solution in the cases of $\beta_P = 1732.05$ and $\beta_P = 577.35$ for a frequency of 0.05 Hz using Mesh A are 2.11% and 2.00%, respectively. The error of the results obtained from Mesh B with $\beta_P = 577.35$ relative to the analytical solution is 1.36%, meaning that the relative difference between the two results of Mesh A and Mesh B is 0.65%. In the case of incident SV-wave, the relative errors for the lowest considered frequency of 0.05 Hz and $\beta_S = 577.35$ are 0.50% and 0.41% for Mesh A and B, respectively. A numerical experiment done using Mesh A in the case of incident plane SV-wave with β_S of 1000.0, 333.33, and 250.0 show relative errors of 3.07%, 0.50%, and 0.49%.

Test example 2: response of a rigid massless foundation rested on a homogeneous half-space under vertical harmonic loading

The 2nd test example concerns the dynamic response of a rigid massless foundation resting on a homogeneous elastic isotropic half-space due to vertical harmonic loading applied to the foundation. In this test example, the foundation is included in the FEM region, and the half-space is modeled in the BEM zone. The dimension of the square foundation is 1 m. The material properties of the half-space are taken from Chuhan, Chongmin, and Pekau, 1991, as follows: Lamé constants $\lambda = 180$ GPa, $\mu = 90$ GPa, and Poisson's ratio of 1/3. To handle the rigid foundation, the rigid-body constraint available in ABAQUS, which ties the degree of freedoms of a solid into a reference point, is used. Thus, no elastic material definition is required for the foundation. The vertical compliance of the foundation due to vertical harmonic loading is defined as (Gazetas, 1991; Chuhan, Chongmin, and Pekau, 1991)

$$V_{vv} = \frac{\hat{u}_3 \mu b}{2P}, \tag{3.69}$$

where $\hat{u}_3$ is the vertical displacement at the bottom center of the foundation, b is the width of the foundation, and P is the amplitude of the applied time-harmonic load. To reveal the sensitivity of the result to the size of the discretized free-surface of the half-space, a numerical experiment is performed using β_S of ∞, 1125, and 562.5, assuming the lowest frequency of 2 Hz. The case of $\beta_S = \infty$

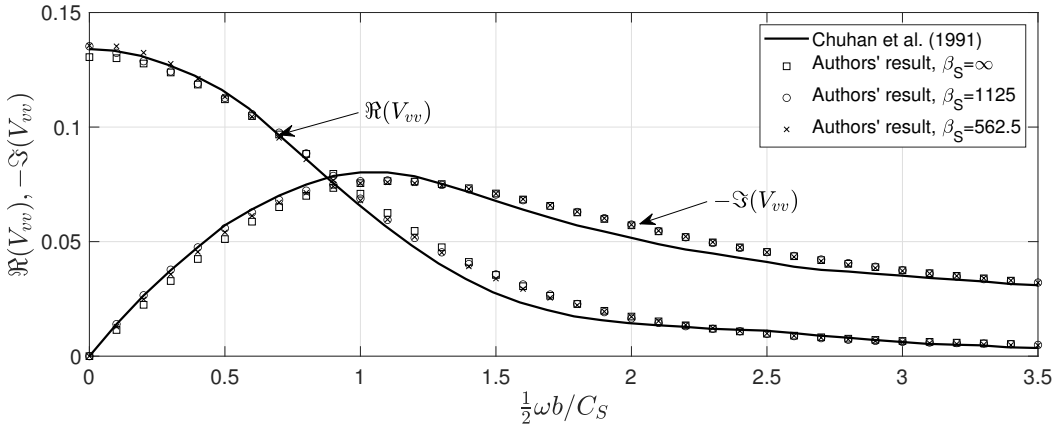

FIGURE 3.12: Comparison of the author's solution for vertical compliances of rectangular rigid massless foundation resting on homogeneous half-space with results in Chuhan, Chongmin, and Pekau, 1991.

means that no free surface is discretized; only the boundary of the half-space under the foundation is considered. The foundation is modeled using 32 quadratic hexahedral finite elements, 16 of which are in contact with the half-space. The half-space is modeled using 480, 680, and 1320 quadratic boundary elements for the respective three β_S.

Figure 3.12 shows a comparison between the authors' results obtained by the hybrid computational approach based on the BEM and FEM with the solutions obtained by 3D pure BEM in Chuhan, Chongmin, and Pekau, 1991. The relative difference between the results of the models with $\beta_S = \infty$ and $\beta_S = 1125$ is 4.73% while the relative difference of the latter with the results of the model with $\beta_S = 562.5$ is 3.29%.

Test example 3: wave propagation due to a double-couple source in a homogeneous infinite space and half-space

In the third test example, the validity of the inclusion of a double-couple type dynamic source is tested. Two cases are considered: (1) a finite soil box Ω_1 located in a homogeneous infinite space Ω_0; (2) a finite soil box Ω_1 located in a homogeneous half-space Ω_0 with the traction-free surface along the plane x_3=0. The material properties are as follows: C_P=6000 m/s, C_S=3464.11 m/s, ρ=2500 kg/m^3. No material damping is considered. In both cases, the soil box is a solid cube of 50 m in size modeled in the FE subdomain. In the case of infinite space, the BE region is a shell cube surrounding the soil box. The center of the model is at **x**(0, 0, 0). In the case of half-space, the BE subdomain includes surfaces around

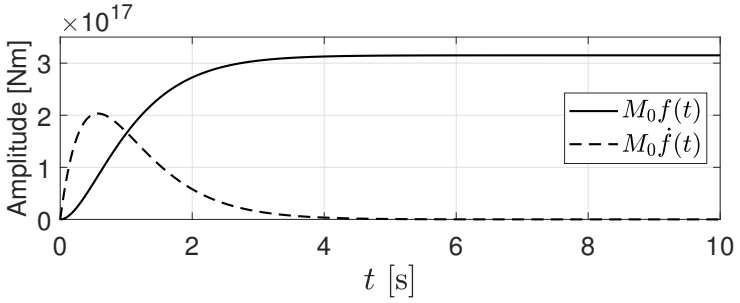

FIGURE 3.13: The seismic moment M_0 versus time for test example 3.

the soil box, except for its top surface and traction-free surfaces l_{Γ_B} in the vicinity of the soil box. The soil box is placed symmetrically such that the center of its top surface is at **x**(0, 0, 0). Three types of BE models with different sizes of l_{Γ_B} are considered to examine the convergence of the solution: (*i*) 50 m, (*ii*) 75 m, and (*iii*) 100 m.

For both cases, the double-couple source is located either (*a*) at $\mathbf{X}_0$(-1 km, 0, -7 km) or (*b*) at $\mathbf{X}_0$(5 km, 5 km, -5 km). The fault geometry is described in the former case by zero strike, dip, and rake angles. This results in a moment tensor M_{ij} with only M_{xz} and M_{zx} as non-zero components, see equation (3.19). In the case of source (*b*), the strike, dip, and rake angles are $\phi_{DC} = 30°$, $\delta_{DC} = 65°$, $\gamma_{DC} = 40°$. In all cases, the seismic moment M_0 is 3.15E+17 Nm and the time function is set according to Beresnev and Atkinson, 1997, as

$$f(t) = \left[1 - (1 + \frac{t}{\eta})e^{-\frac{t}{\eta}}\right] \tag{3.70}$$

with parameter controlling the rate of displacement increase η of 0.57, see Figure 3.13. The double-couple dynamic load's time series has a duration of 16 s with a time interval of 0.0156 s. After Fourier operation, the interval of the discrete frequencies is 0.0625 Hz, and the highest considered frequency is 3.875 Hz. The largest element size is 1/20 of the shortest shear wavelength.

The results of hybrid simulation for the infinite space problem are compared to the closed-form solution in equation (3.17), which is valid for a field point in an unbounded domain. The equivalent solution for a point located on the surface of a half-space domain can be approximated using the following formula. Writing equation (3.16) for a point $\mathbf{x} = \boldsymbol{\xi}$, located on a traction-free surface, results in

$$c_{lj}u_j(\boldsymbol{\xi}, t) + \int_\Gamma P^*_{lj}(\boldsymbol{\xi}, \boldsymbol{\xi}, t) * u_j(\boldsymbol{\xi}, t)d\Gamma = M_{jk}f(t) * U^*_{lj,k}(\boldsymbol{\xi}, \mathbf{X}_0, t), \boldsymbol{\xi} \in \Gamma, \mathbf{X}_0 \in \Omega. \tag{3.71}$$

For a time-harmonic elastodynamic problem, the integral in the second term of the left-hand side of equation 3.71 is obtained by computing the dynamic part of the traction-based kernel, see equation (3.47). Assuming low frequency vibration, this term vanishes, and the analytical solution for displacement of point $\boldsymbol{\xi}$ on the surface of a half-space due to a double-couple source located at $\mathbf{X}_0$ can be approximated as

$$u_j(\boldsymbol{\xi}, t) = \left[c_{lj}\right]^{-1} M_{jk} f(t) * U^*_{lj,k}(\boldsymbol{\xi}, \mathbf{X}_0, t). \tag{3.72}$$

For a point on a smooth surface, c_{lj} is $0.5\mathbf{I}$, where $\mathbf{I}$ is a unit matrix of an appropriate size.

Comparative plots of the displacements between the hybrid simulation with the closed form solution for a point $\mathbf{x}(0,\ 0,\ 0)$ located in an infinite space due to a dynamic load from the source location and fault geometry of type (*a*) and type (*b*) are given in Figures 3.14 and 3.15, respectively, which show excellent agreements. The comparisons of the results for a point located on the surface of a half-space due to a wave propagating from the source location and fault geometry of type (*a*) are given in Figure 3.16, which also show a good agreement. The relative differences between the results obtained for the half-space model with the geometry of type (*i*) and (*ii*) are 5.96% and 2.48% for horizontal and vertical displacements, respectively. The relative differences between the results for type (*ii*) and (*iii*) are 3.92% and 1.53%. To extend the numerical experiment, another set of simulations using the following material properties is performed: C_P=3000 m/s, C_S=1732.05 m/s, ρ=2200 kg/m^3. The relative average differences between the results for all sets of simulations and the analytical solution are summarized in Figure 3.17a. Modifying the ratio β_S into

$$\beta^*_S = (\lambda_S)^{0.15} / l_{\Gamma_B} \tag{3.73}$$

results in a more consistent error prediction, see Figure 3.17b.

In sum, the verification study is based on comparing the author's solutions obtained by the proposed hybrid FEM-BEM with results obtained by other authors and with the analytical result for free-field wave motion in homogeneous elastic isotropic half-space or infinite space under dynamic loads. It can be summarized that $\beta_S \leq 500$ or $\beta^*_S \leq 0.075$ in combination with $\lambda_S / l_{BE} \geq 5$ seems to be sufficient to obtain good accuracy. The comparison shows that the proposed hybrid computational technique works accurately and can be used for SSI simulations.

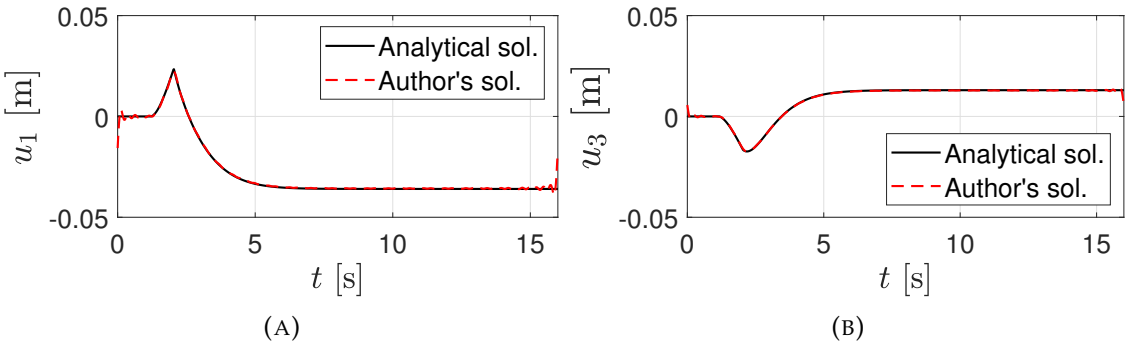

FIGURE 3.14: Comparison of author's solution for displacement components u_j for point $\mathbf{x}(0,0,0)$ in an infinite space due to source location and fault geometry of type (*a*) with the analytical solution: (**A**) u_1 and (**B**) u_3.

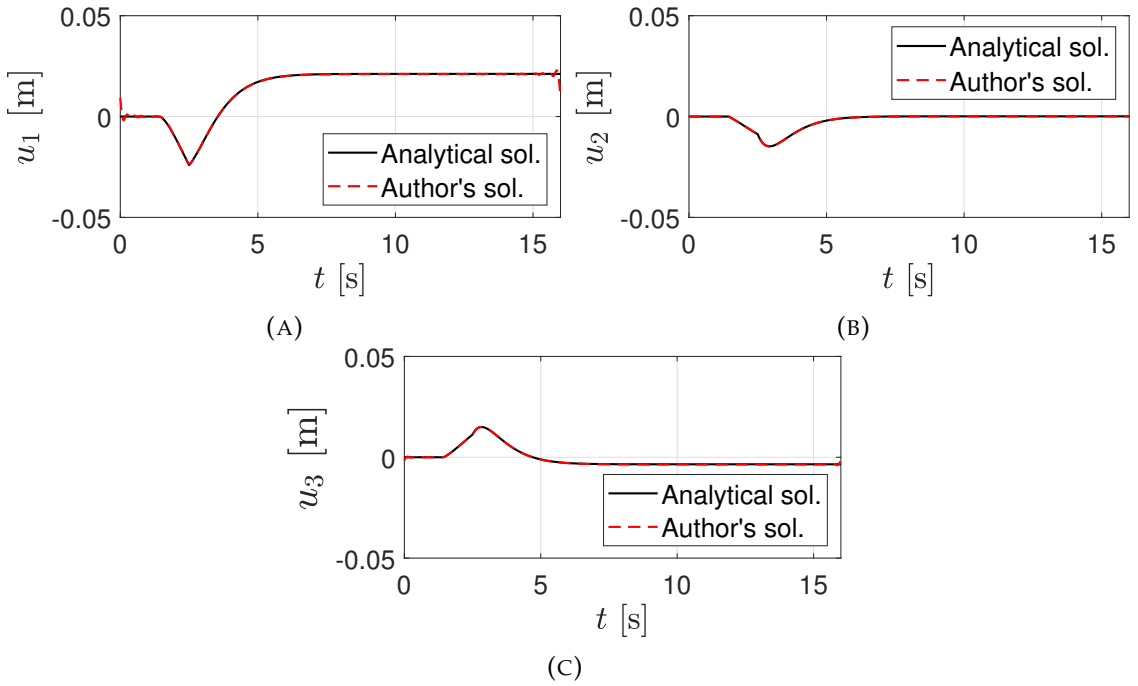

FIGURE 3.15: Comparison of author's solution for displacement components u_j for point $\mathbf{x}(0,0,0)$ in an infinite space due to source location and fault geometry of type (*b*) with the analytical solution: (**A**) u_1, (**B**) u_2, (**C**) u_3.

3.7 Chapter summary

In this chapter, several numerical improvements and implementations are detailed. The inclusion of different types of dynamic sources makes the hybrid numerical method a versatile engineering tool. To the best of the author's knowledge, the application of the double-couple source formulation on the hybrid BEM-FEM has not been realized before. The use of enclosing (dummy) elements for the jump-terms computation and the use of symmetry have been implemented

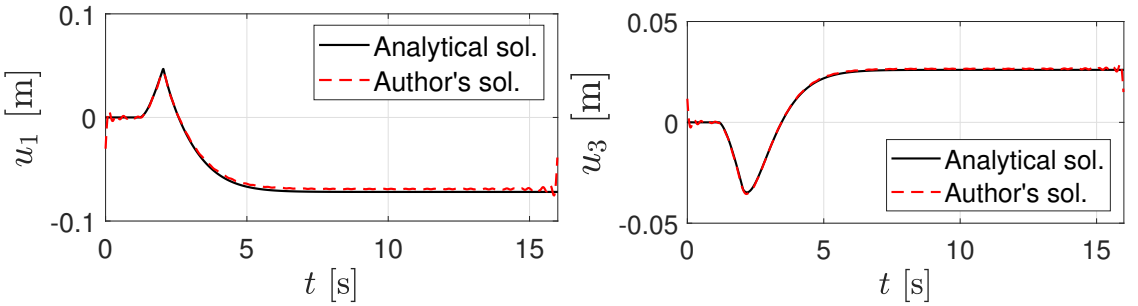

(A) (B)

FIGURE 3.16: Comparison of author's solution for displacement components u_j for point $\mathbf{x}(0,0,0)$ on the surface of a half-space due to source location and fault geometry of type (a) with the analytical solution: (**A**) u_1 and (**B**) u_3. Traction-free surface of the BE model l_{Γ_B} is 75 m.

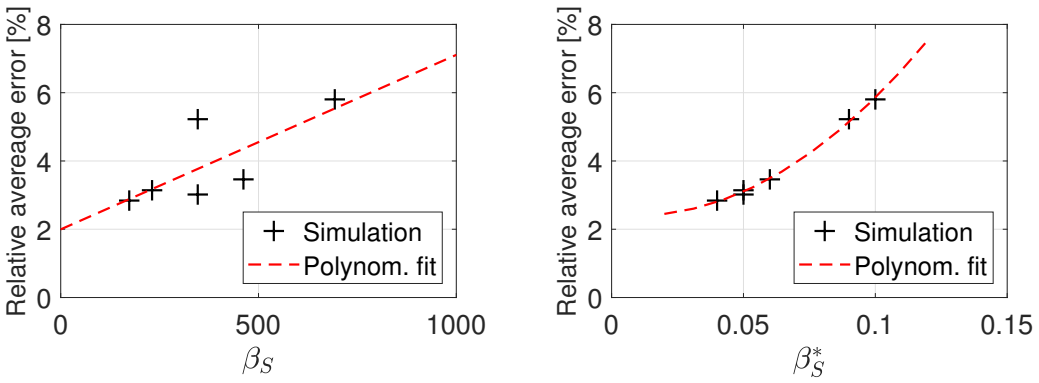

(A) (B)

FIGURE 3.17: β_S (**A**) and β_S^* (**B**) versus relative average differences (with respect to the analytical solution) for test example 3.

by other researchers. However, it is not yet implemented in the context of hybrid BEM-FEM where the whole domain is modeled using one pre-processor. The simple method to handle non-conforming BE-FE interface unlocks several practical advantages and computational efficiency. The hybrid method's accuracy and its solution's convergence are proven through several examples of dynamic problems. This chapter and the basic formulations in Chapter 2 become the foundations for the methods described in the following two chapters, which enable the computation of arbitrary layering and the inclusion of nonlinearities.

Synthetic examples presented in Chapter 6 and Chapter 7 show practical engineering applications of the hybrid method described up to this chapter to solve dynamic SSI problems.

Chapter 4

Layer-wise condensation (LWC) method for the computation of arbitrary layered half-space

4.1 Chapter overview

This chapter delivers details regarding the layer-wise condensation (LWC) method. The chapter begins with the mathematical description of the boundary value problem (Sections 4.2 and 4.3), followed by the derivation of the LWC algorithm for a three-layered semi-infinite media Ω_0 with arbitrary layering interface in Section 4.4. The generalized scheme of the method for a semi-infinite media with an arbitrary number of layers and geometry is given in Section 4.5. Integration of the method into the hybrid BEM-FEM scheme is presented in Section 4.6 followed by verification study in Section 4.7. The content of this chapter is published in H.D.B. Aji, F. Wuttke, P. Dineva (2022). "3D structure-soil-structure interaction in an arbitrary layered half-space". In: *Soil Dynamics and Earthquake Engineering* 159, 107352. DOI: 10.1016/j.soildyn.2022.107352.

4.2 Problem statement and definition of the boundary value problem (BVP)

The LWC method combines **the multi-domain boundary element method** (**MDBEM**) with the **condensation/substructuring procedure** commonly used in the FEM or hybrid BEM-FEM. The MDBEM is a well-known approach to model multilayered media and large-scale problems, see Dominguez, 1993; Manolis et al., 2017. The basic idea of the multi-domain approach is to write the integral

equations for each subdomain individually and then couple the subdomains under interface boundary conditions. In the MDBEM, the computational domain is divided into a number of subdomains with corresponding BIE formulation; the BEM algebraic equations are established for each subdomain; and the global system of equations is formed by assembling results of all subdomains in terms of the equilibrium and consistency conditions over common interface nodes. The problematic points in the models of layered half-space are as follows: *(a)* at a large number of layers, a system with a high number of degrees of freedom is obtained, leading to much higher computational effort; *(b)* the assembling difficulties of the system of equations directly affects the computational efficiency; *(c)* the coefficient matrix of the global system of equations based on the MDBEM is sparse, and therefore the well-developed solvers for sparse systems can be employed to solve it; *(d)* results show that the number of subdomains and the refinement level of the mesh is the two dominant factors affecting the solution accuracy; *(e)* to the best of the author's knowledge, the MDBEM matrices are not compatible with the condensation procedure of the BE subdomain in the direct, FEM-hosted hybrid BE-FE method or the original macro-element concept. The current work avoids all these problematic points by applying the computational condensation technique.

In a coordinate system $Ox_1x_2x_3$, consider a finite geological region Ω_1 which is located in the first layer of a semi-infinite elastic isotropic layered media Ω_0 with an embedded transient dynamic source at point $\mathbf{X}_0(X_{01}, X_{02}, X_{03})$, see Figure 4.1.

The near-field soil region Ω_1 is assumed to be **linear elastic isotropic** characterized by the **small-strain soil stiffness**. The linear elastic model for soils is reasonably valid in the case the strain is small, e.g., in the interval 10^{-6}–10^{-4}, and this occurs at weak seismic events at considerable distances from the seismic source. Vucetic (Vucetic, 1994) showed that a linear soil model is restricted to small shear strain amplitudes, up to 10^{-5}, which suggests that the linear elastic approximation can provide reasonable estimates of the soil response only for small to moderate ground motions. Linear elastic models should result in accurate response predictions for low-intensity shaking. However, they are inadequate for extreme shaking which may results in highly nonlinear soil, structure, or foundation response.

The main focus of this chapter is to enhance the hybrid BEM-FEM approach based on the macro-element concept with the layer-wise condensation method, thus, allowing modeling of the 3D wave motion in a half-space with inclined

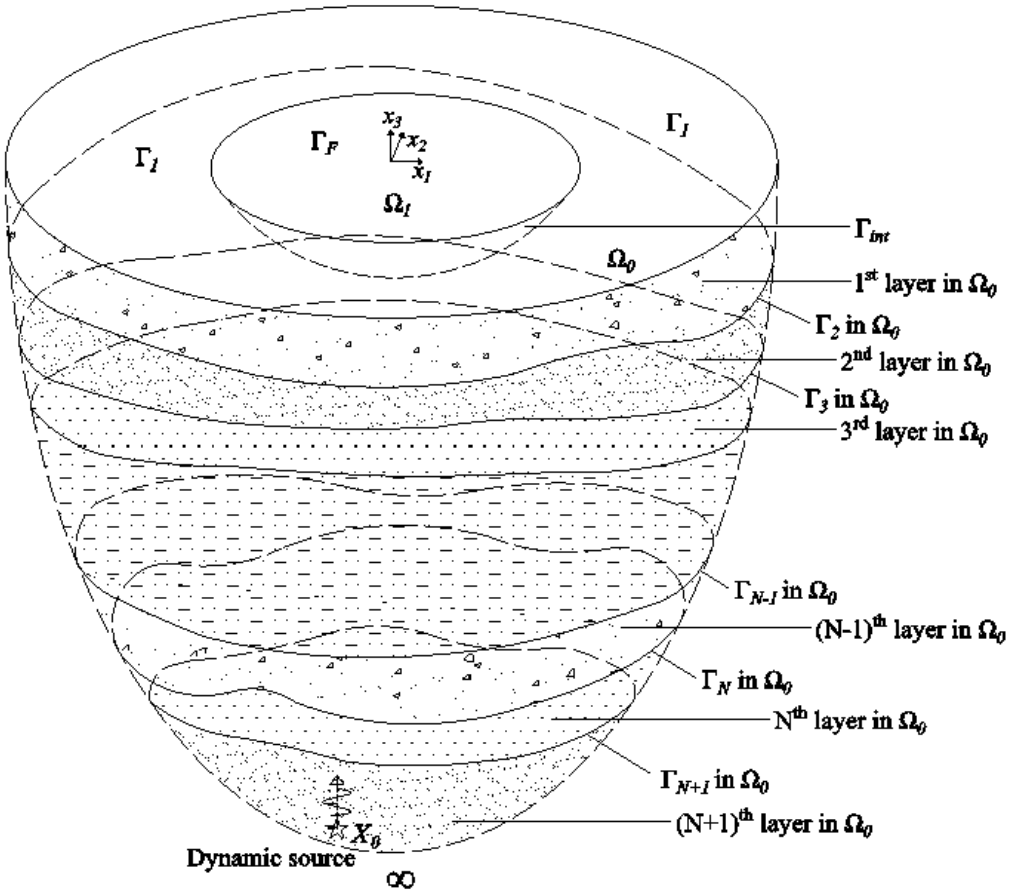

FIGURE 4.1: Problem geometry presenting the general configuration of a finite region Ω_1 embedded in the first layer Ω_{01} of an arbitrary layered half-space Ω_0 with a dynamic source at point $\mathbf{X}_0$.

elastic isotropic layers of arbitrary number and geometry. The complexity of the proposed model analysis taking into account the nonlinear soil behaviour in the near-field region close to the foundation, is detailed in Section 5.

The interface boundary between both regions Ω_1 and Ω_0 is designated with notation Γ_{int} as before. Note that Γ_{int} for each region has the opposite normal vectors. The external boundary of the finite region Ω_1 is $\Gamma_{\Omega_1} = \Gamma_{int} \cup \Gamma_F$.

The external semi-infinite zone Ω_0 is layered with $N+1$ homogeneous elastic isotropic layers Ω_{0k}, $k = 1, 2, ..., N+1$, with infinitely extended boundaries. These layers are with arbitrary geometry of their boundaries Γ_i, $i = 1, 2, ..., N+1$, where the boundary Γ_{N+1} is the boundary between the N^{th} layer and the semi-infinite in depth $(N+1)^{th}$ layer containing the dynamic source $\mathbf{X}_0$. The free-surface boundary Γ_1 is the top boundary of the first layer where the finite region Ω_1 is located. Note that the notation Γ_1 refers to the free surface of the first layer, but outside of the surface Γ_F, which is the free surface of the region Ω_1. The

boundary of the semi-infinite region Ω_0 is defined as the boundary of all $N+1$ layers, i.e. $\Gamma_{\Omega_0} = \Sigma_{k=1}^{N+1}\Gamma_{\Omega_{0k}}$. The boundary of the first Ω_{01} layer is denoted as $\Gamma_{\Omega_{01}} = \Gamma_1 \cup \Gamma_{int} \cup \Gamma_2$, the boundary of the N^{th} layer is $\Gamma_{\Omega_{0N}} = \Gamma_N \cup \Gamma_{N+1}$ and the boundary of the $N+1$ layer $\Gamma_{\Omega_{0N+1}} = \Gamma_{N+1}$. Note that the layers $[1, N]$ are infinite along Ox_1 and Ox_2 axes and are finite only in Ox_3 direction.

The material properties of the geological semi-infinite zone Ω_0 are density ρ_{0i}, Lamé constants λ_{0k}, μ_{0k}, longitudinal wave velocity $C_{P_{0k}}$ and shear wave velocity $C_{S_{0k}}$, where $k = 1, 2, ..., N+1$. The material properties of the finite range Ω_1 are λ_1, μ_1, C_{P_1}, and C_{S_1}.

The initial boundary-value problem for the wave propagation in the geological region under consideration consists of governing equations in 3D elastodynamics, initial conditions, and boundary conditions discussed below. **The equations of motion for the domains** are given by

$$\sigma_{ij,j}^{(\Omega_1)}(\mathbf{x},t) = \rho^{(\Omega_1)}\frac{\partial^2 u_i^{(\Omega_1)}(\mathbf{x},t)}{\partial t^2},\ \mathbf{x}(x_1,x_2,x_3) \in \Omega_1; \tag{4.1}$$

$$\sigma_{ij,j}^{(\Omega_{0k})}(\mathbf{x},t) = \rho^{(\Omega_{0k})}\frac{\partial^2 u_i^{(\Omega_{0k})}(\mathbf{x},t)}{\partial t^2},$$
$$\mathbf{x}(x_1,x_2,x_3) \in \Omega_{0k},\ k = 1,2,...,N; \tag{4.2}$$

$$\sigma_{ij,j}^{(\Omega_{0k})}(\mathbf{x},t) + f_i^{(\Omega_0)}(\mathbf{X}_0,t) = \rho^{(\Omega_{0k})}\frac{\partial^2 u_i^{(\Omega_{0k})}(\mathbf{x},t)}{\partial t^2},$$
$$\mathbf{x}(x_1,x_2,x_3) \in \Omega_{0k},\ k = N+1. \tag{4.3}$$

Here, $\partial^2 u_i^{(\Omega_1)}/\partial t^2$, $\sigma_{ij}^{(\Omega_1)}$ $(i = 1,2,3; j = 1,2,3)$ are accelerations and stresses belonging to the finite region Ω_1; Ω_{0k} is the k^{th} layer of semi-infinite layered region Ω_0; $\mathbf{x}(x_1,x_2,x_3)$ is the vector position; $\mathbf{X}_0(X_{01},X_{02},X_{03}) \in \Omega_{0N+1}$ is the coordinate vector of the dynamic source location point; $\partial^2 u_i^{(\Omega_{0k})}/\partial t^2$, $k = 1,2,...,N+1, i = 1,2,3$, are the acceleration components in the k^{th} layer; and $\sigma_{ij}^{(\Omega_{0k})}$ are the stress tensor components in the k^{th} layer. The dynamic force is presented as $f_i^{(\Omega_0)}(\mathbf{X}_0,t) = f_i^{(\Omega_0)}f(t)\delta(\mathbf{x}-\mathbf{X}_0)$, where $f_i^{(\Omega_0)}(f_1^{(\Omega_0)}, f_2^{(\Omega_0)}, f_3^{(\Omega_0)})$ is the amplitude and $f(t)$ is the time history function. The vector f_i has a unit of force per unit volume, see Manolis and Beskos, 1988 and Dominguez, 1993.

The initial conditions for displacements and their first derivatives with respect to time are zero. After application of the direct FFT with respect to the time variable in equations (4.1)-(4.3), the frequency ω dependent equations of motion

have the following form:

$$\sigma_{ij,j}^{(\Omega_1)}(\mathbf{x},\omega) + \rho^{(\Omega_1)}\omega^2 \hat{u}_i^{(\Omega_1)}(\mathbf{x},\omega) = 0,\ \mathbf{x}(x_1,x_2,x_3) \in \Omega_1; \tag{4.4}$$

$$\sigma_{ij,j}^{(\Omega_{0k})}(\mathbf{x},\omega) + \rho^{(\Omega_{0k})}\omega^2 \hat{u}_i^{(\Omega_{0k})}(\mathbf{x},\omega) = 0,$$
$$\mathbf{x}(x_1,x_2,x_3) \in \Omega_{0k},\ k = 1,2,...,N; \tag{4.5}$$

$$\sigma_{ij,j}^{(\Omega_{0k})}(\mathbf{x},\omega) + \rho^{(\Omega_{0k})}\omega^2 \hat{u}_i^{(\Omega_{0k})}(\mathbf{x},\omega) = -f_i^{(\Omega_{0k})}\hat{f}(\omega)\delta(\mathbf{x}-\mathbf{X}_0),$$
$$\mathbf{x}(x_1,x_2,x_3) \in \Omega_{0k},\ k = N+1, \tag{4.6}$$

where the term $f_i^{(\Omega_0)}(\mathbf{X}_0,t) = f_i^{(\Omega_0)} f(t)\delta(\mathbf{x}-\mathbf{X}_0)$ becomes $f_i^{(\Omega_0)}\hat{f}(\omega)\delta(\mathbf{x}-\mathbf{X}_0)$ in the frequency domain.

Boundary conditions for the layered semi-infinite region Ω_0 are as follows:

- Along the free-surface $\Gamma_1 \in \Omega_{01}$, the tractions $\hat{t}_i^{(\Omega_{01})} = \sigma_{ij}^{(\Omega_{01})} n_j^{(\Omega_{01})}$ are zero, where $n_j^{(\Omega_{01})},\ j = 1,2,3$, are the components of the outward normal to the surface Γ_1.
- Along the interface boundary Γ_{int} between the region Ω_1 and the soil layer Ω_{01}, the compatibility and equilibrium conditions of the displacements and tractions, respectively, are satisfied, i.e., $\hat{u}_i^{(\Omega_{01})} = \hat{u}_i^{(\Omega_1)}$ and $\hat{t}_i^{(\Omega_{01})} = -\hat{t}_i^{(\Omega_1)}$.
- Along the interface boundary between layers $\Gamma_i,\ i = 2,3,...,N+1$, the compatibility and equilibrium conditions of the displacements and tractions, respectively, are satisfied.
- The Sommerfeld's radiation condition is satisfied at infinity.

The boundary conditions for the finite region Ω_1 are the same as described in Section 3.2 and are not repeated here for brevity. The solution of the mechanical problem in the frequency domain defined here satisfies the governing equations (4.4)-(4.6) and the boundary conditions discussed above.

4.3 Macro-finite element formulation via BEM modeling of wave propagation in a semi-infinite layered region

Following the procedures described in Section 2.4 and Section 3.2 (Dominguez, 1993; Manolis et al., 2017), the wave field in the far-field semi-infinite layered zone Ω_0 is described by a system of N boundary integral equations (BIEs) (4.7) along

the boundary $\Gamma_{\Omega_{0k}}$, $k = 1, 2, ..., N$ and boundary integral equation (4.8) along the boundary $\Gamma_{\Omega_{0N+1}}$. Note that $\Gamma_{\Omega_{01}} = \Gamma_1 \cup \Gamma_{int} \cup \Gamma_2$, $\Gamma_{\Omega_{02}} = \Gamma_2 \cup \Gamma_3$,..., $\Gamma_{\Omega_{0N}} = \Gamma_N \cup \Gamma_{N+1}$, and $\Gamma_{\Omega_{0N+1}} = \Gamma_{N+1}$.

$$c_{lj}\hat{u}_j^{(\Omega_{0k})}(\mathbf{x},\omega) = \int_{\Gamma_{\Omega_{0k}}} \hat{U}_{lj}^{*(\Omega_{0k})}(\mathbf{x},\boldsymbol{\xi},\omega)\ \hat{t}_j^{(\Omega_{0k})}(\boldsymbol{\xi},\omega)d\Gamma - \int_{\Gamma_{\Omega_{0k}}} \hat{P}_{lj}^{*(\Omega_{0k})}(\mathbf{x},\boldsymbol{\xi},\omega)\ \hat{u}_j^{(\Omega_{0k})}(\boldsymbol{\xi},\omega)d\Gamma, \text{for } \mathbf{x} \in \Gamma_{\Omega_{0k}},\ k = 1, 2, ..., N; \quad (4.7)$$

$$c_{lj}\hat{u}_j^{(\Omega_{0N+1})}(\mathbf{x},\omega) = \int_{\Gamma_{N+1}} \hat{U}_{lj}^{*(\Omega_{0N+1})}(\mathbf{x},\boldsymbol{\xi},\omega)\ \hat{t}_j^{(\Omega_{0N+1})}(\boldsymbol{\xi},\omega)d\Gamma - \int_{\Gamma_{N+1}} \hat{P}_{lj}^{*(\Omega_{0N+1})}(\mathbf{x},\boldsymbol{\xi},\omega)\ \hat{u}_j^{(\Omega_{0N+1})}(\boldsymbol{\xi},\omega)d\Gamma + f_j^{(\Omega_{0N+1})}\hat{f}(\omega)\hat{U}_{lj}^{*(\Omega_{0N+1})}(\mathbf{x},\mathbf{X}_0,\omega),\ \text{for } \mathbf{x} \in \Gamma_{N+1},\ l,j = 1,2,3. \quad (4.8)$$

Note that upper indices of the fundamental solution and of its corresponding traction in BIEs (4.7) and (4.8) indicate the number of the corresponding soil layer Ω_{0k}.

BIEs (4.7) and (4.8) are transformed into the matrix equation (4.9) after application of the well-known discretization and collocation procedures, see Dominguez, 1993:

$$\mathbf{H}^{(\Omega_{0k})}\hat{\mathbf{u}}^{(\Omega_{0k})} - \mathbf{G}^{(\Omega_{0k})}\hat{\mathbf{t}}^{(\Omega_{0k})} = \Phi^{(\Omega_{0k})}, \quad (4.9)$$

where

$$\Phi^{(\Omega_{0k})} = \begin{cases} 0 & \text{for } k = 1, 2, ..., N, \\ f_j^{(\Omega_{0k})}\hat{f}(\omega)U_{lj}^{*(\Omega_0 k)}(\mathbf{x},\mathbf{X}_0,\omega) & \text{for } \mathbf{x} \in \Omega_{0N+1},\ k = N+1. \end{cases} \quad (4.10)$$

The matrices $\mathbf{H}^{(\Omega_0)}$ and $\mathbf{G}^{(\Omega_0)}$ are the influence matrices with the size of $3Lx3L$, where L is the number of nodes along all existing boundaries in Ω_0; $\hat{\mathbf{u}}^{(\Omega_0)}, \hat{\mathbf{t}}^{(\Omega_0)}$ are the displacement and traction vectors at nodes along these boundaries. Equation (4.9) is the same as equation (3.20).

The system of boundary integral equations (4.7) and (4.8) and their matrix form (4.9) is in respect to the **unknown total wave displacements and tractions along the existing boundaries**. What follows is to define correctly the macro-finite element describing wave field along the interface boundary Γ_{int} between the finite local region Ω_1 and the semi-infinite layered half-space outside it. This

will be done by the following three steps: (a) description of the layer-wise condensation approach which is illustrated in Section 4.4 by considering a simple example of three-layered half-space subjected to transient dynamic load concentrated at point $\mathbf{X}_0$; (b) a generalization of the layer-wise condensation approach for the case of N layers rested on the seismic bed, described as the $(N+1)$ layer, which is presented in Section 4.5; (c) derivation of the correlation between the nodal traction along the interface boundary Γ_{int} coming from the BEM model of the semi-infinite zone and the nodal forces along Γ_{int} necessary for the FEM model of the finite local region Ω_1 which is described in Section 4.6.

4.4 Layer-wise condensation approach applied for a three-layered half-space subjected to transient dynamic load concentrated at point $\mathbf{X}_0$

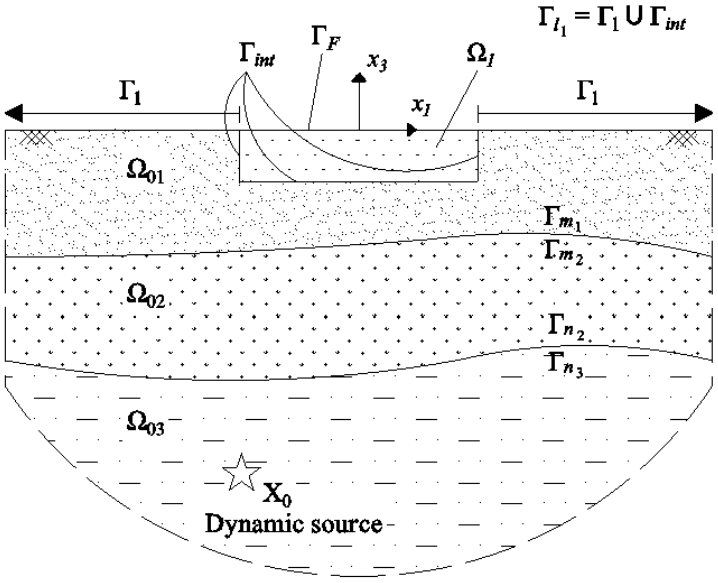

FIGURE 4.2: A layered half-space $\Omega_0 = \Sigma_{k=1}^{3}\Omega_{0k}$ containing a finite region Ω_1 and an embedded dynamic source in semi-infinite layer Ω_{03} at point $\mathbf{X}_0$.

The arbitrary layered semi-infinite media will be modeled further by applying the layer-wise condensation approach. In order to illustrate it in a relatively simple way, we will consider a semi-infinite domain $\Omega_0 = \Sigma_{k=1}^{3}\Omega_{0k}$ with **three layers**, see Figure 4.2. The first layer Ω_{01} has top boundary $\Gamma_{l_1} = \Gamma_1 \cup \Gamma_{int}$ and bottom boundary Γ_{m_1}; the second layer Ω_{02} has top boundary Γ_{m_2} and bottom boundary Γ_{n_2}; and the third layer Ω_{03}, which is semi-infinite in depth, has only

the top boundary Γ_{n_3}. In other words, the boundaries $\Gamma_1 \cup \Gamma_{int}$; Γ_2; Γ_3 in Figure 4.1 are now denoted as Γ_{l_1}; Γ_{m_1} and Γ_{m_2}; Γ_{n_2} and Γ_{n_3}, respectively, in Figure 4.2. The matrix equation (4.9) reads now as equation (4.11) having in mind the inserted above notations:

$$\begin{bmatrix} \mathbf{H}_{l_1l_1} & \mathbf{H}_{l_1m_1} & 0 \\ \mathbf{H}_{m_1l_1} & \mathbf{H}_{m_1m_1} & 0 \\ 0 & \mathbf{H}_{m_2m_2} & \mathbf{H}_{m_2n_2} \\ 0 & \mathbf{H}_{n_2m_2} & \mathbf{H}_{n_2n_2} \\ 0 & 0 & \mathbf{H}_{n_3n_3} \end{bmatrix} \begin{bmatrix} \hat{\mathbf{u}}_l \\ \hat{\mathbf{u}}_m \\ \hat{\mathbf{u}}_n \end{bmatrix} - \begin{bmatrix} \mathbf{G}_{l_1l_1} & \mathbf{G}_{l_1m_1} & 0 \\ \mathbf{G}_{m_1l_1} & \mathbf{G}_{m_1m_1} & 0 \\ 0 & -\mathbf{G}_{m_2m_2} & \mathbf{G}_{m_2n_2} \\ 0 & -\mathbf{G}_{n_2m_2} & \mathbf{G}_{n_2n_2} \\ 0 & 0 & -\mathbf{G}_{n_3n_3} \end{bmatrix} \begin{bmatrix} \hat{\mathbf{t}}_l \\ \hat{\mathbf{t}}_m \\ \hat{\mathbf{t}}_n \end{bmatrix} = \begin{bmatrix} 0 \\ 0 \\ 0 \\ 0 \\ \mathbf{F}_{n_3} \end{bmatrix}, \quad (4.11)$$

where $\mathbf{F}_{n_3} = f_j^{(\Omega_{03})} \hat{f}(\omega) U^{*(\Omega_{03})}(\mathbf{x}, \mathbf{X}_0, \omega)$.

The influence matrices $\mathbf{H}_{ij}$ and $\mathbf{G}_{ij}$ written in the notations used in equation (4.11) can be read in the following manner: first two lower indices show the boundary where the source nodes are, while the next two lower indices show the boundary of the field points. For example, $\mathbf{H}_{l_1m_1}$ and $\mathbf{G}_{l_1m_1}$ are the influence matrices when the source points are along the boundary $\Gamma_{l_1} = \Gamma_1 \cup \Gamma_{int}$ and the field points are along the boundary Γ_{m_1}. Vectors $\hat{\mathbf{u}}_l$, $\hat{\mathbf{t}}_l$; $\hat{\mathbf{u}}_m$, $\hat{\mathbf{t}}_m$; $\hat{\mathbf{u}}_n$, $\hat{\mathbf{t}}_n$ stand for displacements and tractions on the boundaries $\Gamma_l = \Gamma_{l_1}$, $\Gamma_m = \Gamma_{m_1} \cup \Gamma_{m_2}$ and $\Gamma_n = \Gamma_{n_1} \cup \Gamma_{n_2}$, respectively. The compatibility and equilibrium of displacement and traction, respectively, along the layer interfaces, hold $\hat{\mathbf{u}}_m = \hat{\mathbf{u}}_{m_1} = \hat{\mathbf{u}}_{m_2}$ and $\hat{\mathbf{t}}_m = \hat{\mathbf{t}}_{m_1} = -\hat{\mathbf{t}}_{m_2}$. In equation (4.11), the traction vectors are written for the sign of the upper layer, and this results in the negative sign for $\mathbf{G}_{m_2m_2}$, $\mathbf{G}_{n_2m_2}$ and $\mathbf{G}_{n_3n_3}$. Note that the vector $\hat{\mathbf{t}}_l$ contains unknown tractions along the interface boundary Γ_{int}, and it has zero traction values along the traction-free boundary Γ_1. For this reason, the components of the matrices $\mathbf{G}_{l_1l_1}$ and $\mathbf{G}_{m_1l_1}$ which correspond to Γ_1 can be neglected and thus, the $\mathbf{G}_{l_1l_1}$ matrix can be made into a square, i.e., an invertible matrix, with only the components corresponding to non-zeroth traction components along the interface boundary Γ_{int}.

The 5^{th} row of equation (4.11) can be written as

$$\hat{\mathbf{u}}_n = [\mathbf{H}_{n_3n_3}]^{-1} \left[-\mathbf{G}_{n_3n_3} \hat{\mathbf{t}}_n + \mathbf{F}_{n_3} \right]. \quad (4.12a)$$

After insertion of relation (4.12a) into the 4$^{\text{th}}$ row of equation (4.11), we obtain

$$\mathbf{H}_{n_2m_2}\hat{\mathbf{u}}_m + \mathbf{H}_{n_2n_2}\left[\mathbf{H}_{n_3n_3}\right]^{-1}\left[-\mathbf{G}_{n_3n_3}\hat{\mathbf{t}}_n + \mathbf{F}_{n_3}\right] + \mathbf{G}_{n_2m_2}\hat{\mathbf{t}}_m - \mathbf{G}_{n_2n_2}\hat{\mathbf{t}}_n = 0. \quad (4.12b)$$

Written for $\hat{\mathbf{t}}_n$, the above equation reads as equation (4.12c)

$$\hat{\mathbf{t}}_n = \left[\mathbf{A}_{G_2}\right]^{-1}\left[\mathbf{H}_{n_2m_2}\hat{\mathbf{u}}_m + \mathbf{G}_{n_2m_2}\hat{\mathbf{t}}_m + \mathbf{H}_{n_2n_2}\left[\mathbf{H}_{n_3n_3}\right]^{-1}\mathbf{F}_{n_3}\right]. \quad (4.12c)$$

Here, $\mathbf{A}_{G_2}$ is defined as

$$\mathbf{A}_{G_2} = \mathbf{H}_{n_2n_2}\left[\mathbf{H}_{n_3n_3}\right]^{-1}\mathbf{G}_{n_3n_3} + \mathbf{G}_{n_2n_2}. \quad (4.12d)$$

After inserting equation (4.12a) into the 3$^{\text{rd}}$ row of equation (4.11) we obtain

$$\mathbf{H}_{m_2m_2}\hat{\mathbf{u}}_m + \mathbf{H}_{m_2n_2}\left[\mathbf{H}_{n_3n_3}\right]^{-1}\left[-\mathbf{G}_{n_3n_3}\hat{\mathbf{t}}_n + \mathbf{F}_{n_3}\right] + \mathbf{G}_{m_2m_2}\hat{\mathbf{t}}_m - \mathbf{G}_{m_2n_2}\hat{\mathbf{t}}_n = 0. \quad (4.12e)$$

Now collecting the terms related to $\hat{\mathbf{t}}_n$ to the left-hand side yields

$$\left[\mathbf{H}_{m_2n_2}\left[\mathbf{H}_{n_3n_3}\right]^{-1}\mathbf{G}_{n_3n_3} + \mathbf{G}_{m_2n_2}\right]\hat{\mathbf{t}}_n = \mathbf{H}_{m_2m_2}\hat{\mathbf{u}}_m + \mathbf{G}_{m_2m_2}\hat{\mathbf{t}}_m + \mathbf{H}_{m_2n_2}\left[\mathbf{H}_{n_3n_3}\right]^{-1}\mathbf{F}_{n_3}. \quad (4.12f)$$

Let us define the following relation

$$\mathbf{A}_{G_1} = \mathbf{H}_{m_2n_2}\left[\mathbf{H}_{n_3n_3}\right]^{-1}\mathbf{G}_{n_3n_3} + \mathbf{G}_{m_2n_2}. \quad (4.12g)$$

After insertion of equation (4.12c) into equation (4.12f), the following equation is derived

$$\left[\mathbf{H}_{m_2m2} - \mathbf{A}_{G_1}\left[\mathbf{A}_{G_2}\right]^{-1}\mathbf{H}_{n_2m_2}\right]\hat{\mathbf{u}}_m + \left[\mathbf{G}_{m_2m_2} - \mathbf{A}_{G_1}\left[\mathbf{A}_{G_2}\right]^{-1}\mathbf{G}_{n_2m_2}\right]\hat{\mathbf{t}}_m = \mathbf{F}_{m_2}, \quad (4.12h)$$

where

$$\mathbf{F}_{m_2} = \left[\mathbf{A}_{G_1}\left[\mathbf{A}_{G_2}\right]^{-1}\mathbf{H}_{n_2n_2} - \mathbf{H}_{m_2n_2}\right]\left[\mathbf{H}_{n_3n_3}\right]^{-1}\mathbf{F}_{n_3}. \quad (4.12i)$$

Equation (4.12h) replaces the 3$^{\text{rd}}$, 4$^{\text{th}}$, and 5$^{\text{th}}$ rows of matrix equation (4.11) and condenses layer 3 into layer 2 and as a final result, the unknowns $\hat{\mathbf{u}}_n$ and $\hat{\mathbf{t}}_n$ are omitted. The procedure can be perpetuated to further condense the influence matrices of layer 2 into layer 1 by writing equation (4.12h) for $\hat{\mathbf{u}}_m$ in the following

compact form

$$\hat{\mathbf{u}}_m = [\mathbf{B_H}]^{-1} \left[-\mathbf{B_G} \hat{\mathbf{t}}_m + \mathbf{F}_{m_2} \right], \tag{4.12j}$$

where

$$\mathbf{B_H} = \mathbf{H}_{m_2 m_2} - \mathbf{A}_{G_1} [\mathbf{A}_{G_2}]^{-1} \mathbf{H}_{n_2 m_2}; \tag{4.12k}$$

$$\mathbf{B_G} = \mathbf{G}_{m_2 m_2} - \mathbf{A}_{G_1} [\mathbf{A}_{G_2}]^{-1} \mathbf{G}_{n_2 m_2}. \tag{4.12l}$$

In the next step, equation (4.12j) is inserted into the 2nd row of equation (4.11) as follows:

$$\mathbf{H}_{m_1 l_1} \hat{\mathbf{u}}_l + \mathbf{H}_{m_1 m_1} [\mathbf{B_H}]^{-1} \left[-\mathbf{B_G} \hat{\mathbf{t}}_m + \mathbf{F}_{m_2} \right] - \mathbf{G}_{m_1 l_1} \hat{\mathbf{t}}_l - \mathbf{G}_{m_1 m_1} \hat{\mathbf{t}}_m = 0. \tag{4.12m}$$

From this equation, the following expression for $\hat{\mathbf{t}}_m$ is obtained:

$$\hat{\mathbf{t}}_m = [\mathbf{C}_{G_2}]^{-1} \left[\mathbf{H}_{m_1 l_1} \hat{\mathbf{u}}_l - \mathbf{G}_{m_1 l_1} \hat{\mathbf{t}}_l + \mathbf{H}_{m_1 m_1} [\mathbf{B_H}]^{-1} \mathbf{F}_{m_2} \right]. \tag{4.12n}$$

Here, $\mathbf{C}_{G_2}$ is defined as

$$\mathbf{C}_{G_2} = \mathbf{H}_{m_1 m_1} [\mathbf{B_H}]^{-1} \mathbf{B_G} + \mathbf{G}_{m_1 m_1}. \tag{4.12o}$$

Note that equation (4.12n) and equation (4.12o) are similar to equation (4.12c) and equation (4.12d), respectively, except for the different sign in front of the **G** matrix on the right-hand side of the former pair. Inserting equation (4.12j) into the 1st row of equation (4.11), one obtains

$$\mathbf{H}_{l_1 l_1} \hat{\mathbf{u}}_l + \mathbf{H}_{l_1 m_1} [\mathbf{B_H}]^{-1} \left[-\mathbf{B_G} \hat{\mathbf{t}}_m + \mathbf{F}_{m_2} \right] - \mathbf{G}_{l_1 l_1} \hat{\mathbf{t}}_l - \mathbf{G}_{l_1 m_1} \hat{\mathbf{t}}_m = 0. \tag{4.12p}$$

Collecting the terms related to $\hat{\mathbf{t}}_m$ into the left-hand side yields

$$\left[\mathbf{H}_{l_1 m_1} [\mathbf{B_H}]^{-1} \mathbf{B_G} + \mathbf{G}_{l_1 m_1} \right] \hat{\mathbf{t}}_m = \mathbf{H}_{l_1 l_1} \hat{\mathbf{u}}_l - \mathbf{G}_{l_1 l_1} \hat{\mathbf{t}}_l + \mathbf{H}_{l_1 m_1} [\mathbf{B_H}]^{-1} \mathbf{F}_{m_2}. \tag{4.12q}$$

Let us define the relation

$$\mathbf{C}_{G_1} = \mathbf{H}_{l_1 m_1} [\mathbf{B_H}]^{-1} \mathbf{B_G} + \mathbf{G}_{l_1 m_1} \tag{4.12r}$$

and insert equation (4.12n) into equation (4.12q). As a result, it is obtained the following matrix equation:

$$\left[\mathbf{H}_{l_1 l_1} - \mathbf{C}_{G_1}\left[\mathbf{C}_{G_2}\right]^{-1}\mathbf{H}_{m_1 l_1}\right]\hat{\mathbf{u}}_l - \left[\mathbf{G}_{l_1 l_1} - \mathbf{C}_{G_1}\left[\mathbf{C}_{G_2}\right]^{-1}\mathbf{G}_{m_1 l_1}\right]\hat{\mathbf{t}}_l = \left[\mathbf{C}_{G_1}\left[\mathbf{C}_{G_2}\right]^{-1}\mathbf{H}_{m_1 m_1} - \mathbf{H}_{l_1 m_1}\right]\left[\mathbf{B}_{\mathbf{H}}\right]^{-1}\mathbf{F}_{m_2}. \quad (4.12s)$$

The above equation can be rewritten in a more compact form as

$$\mathbf{H}^*\hat{\mathbf{u}}_l - \mathbf{G}^*\hat{\mathbf{t}}_l = \Phi_l, \quad (4.12t)$$

where

$$\mathbf{H}^* = \left[\mathbf{H}_{l_1 l_1} - \mathbf{C}_{G_1}\left[\mathbf{C}_{G_2}\right]^{-1}\mathbf{H}_{m_1 l_1}\right], \quad (4.12u)$$

$$\mathbf{G}^* = \left[\mathbf{G}_{l_1 l_1} - \mathbf{C}_{G_1}\left[\mathbf{C}_{G_2}\right]^{-1}\mathbf{G}_{m_1 l_1}\right], \text{ and} \quad (4.12v)$$

$$\Phi_l = \left[\mathbf{C}_{G_1}\left[\mathbf{C}_{G_2}\right]^{-1}\mathbf{H}_{m_1 m_1} - \mathbf{H}_{l_1 m_1}\right]\left[\mathbf{B}_{\mathbf{H}}\right]^{-1}\mathbf{F}_{m_2}. \quad (4.12w)$$

As a final result, we can conclude that equation (4.11) is condensed into a single row of matrix equation (4.12t) with the following terms: (a) The matrices $\mathbf{H}^*$ and $\mathbf{G}^*$ are the modified influence matrices of the surface boundary which include the influence of all the rest layers; (b) The dynamic load coming from the embedded source at point $\mathbf{X}_0$ in layer Ω_{03} is presented by the load vector Φ_l. Equation (4.12t) is similar to equation (4.12h) except for the sign in front of the modified $\mathbf{G}$ matrix. Note that signs of the modified $\mathbf{G}$ matrix in both equations are intentionally chosen to follow the signs of the unmodified $\mathbf{G}$ matrices in equation (4.11). In equation (4.12t), only unknowns of displacement $\hat{\mathbf{u}}_l$ and traction $\hat{\mathbf{t}}_l$ along the boundary Γ_l are left, which makes this equation suitable for the subsequent hybrid condensation.

4.5 Layer-wise condensation approach applied for a $(N+1)$-layered half-space subjected to transient dynamic load concentrated at point $\mathbf{X}_0$

The repetitive form of the layer-wise condensation procedure presented in the previous section renders the method suitable for numerical implementation. Consider a problem with geometry in Figure 4.1 with $N+1$ number of layers where each is designated as layer k, $k = 1, 2, ..., N+1$. In the bottommost layer, the

boundary, which is an interface to the layer above it, is marked as Γ_{n_k}, $k = N+1$. In the topmost layer and other subsequent layers except for the bottommost layer, the upper boundary is marked as Γ_{m_k}, $k = 1, 2, ..., N$, while the lower boundary is marked as Γ_{n_k}, $k = 1, 2, ..., N$. The condensation procedure can be organized in the following manner:

1) Start with the lowest layer, i.e. $k = N+1$. Compute the influence matrices, $\mathbf{H}_{n_k n_k}$ and $\mathbf{G}_{n_k n_k}$, and the force vector of the applied dynamic load $\mathbf{F}_{n_k}$.

2) Continue with the next layer above until the topmost layer, i.e., $k = N, N-1, ..., 1$. For each of these layers, execute the following computational steps:

   a) Adjust the components of influence matrices and the load vector from the previous layer, $\mathbf{H}_{n_{(k+1)} n_{(k+1)}}$, $\mathbf{G}_{n_{(k+1)} n_{(k+1)}}$ and $\mathbf{F}_{n_{(k+1)}}$, to the degree of freedom designations of the current layer. This step is necessary when the node numberings on $\Gamma_{n_{(k+1)}}$ and Γ_{n_k} are different.

   b) Compute the influence matrices for the current layer. No sign change on the assembly of the $\mathbf{G}$ matrix is required. In the case of the topmost layer, discard the contribution of the free-surface elements to the $\mathbf{G}$ matrix.

   c) Compute $\mathbf{A}_{G_1}$ and $\mathbf{A}_{G_2}$by the following relations:

$$\mathbf{A}_{G_1} = \mathbf{H}_{m_k n_k} \left[\mathbf{H}_{n_{(k+1)} n_{(k+1)}}\right]^{-1} \mathbf{G}_{n_{(k+1)} n_{(k+1)}} + \mathbf{G}_{m_k n_k}; \tag{4.13}$$

$$\mathbf{A}_{G_2} = \mathbf{H}_{n_k n_k} \left[\mathbf{H}_{n_{(k+1)} n_{(k+1)}}\right]^{-1} \mathbf{G}_{n_{(k+1)} n_{(k+1)}} + \mathbf{G}_{n_k n_k}. \tag{4.14}$$

   d) Compute the new influence matrices, $\mathbf{H}_{n_k n_k}$ and $\mathbf{G}_{n_k n_k}$, and the new load vector, $\mathbf{F}_{n_k}$, by the following relations:

$$\mathbf{H}_{n_k n_k} = \left[\mathbf{H}_{m_k m_k} - \mathbf{A}_{G_1} \left[\mathbf{A}_{G_2}\right]^{-1} \mathbf{H}_{n_k m_k}\right]; \tag{4.15}$$

$$\mathbf{G}_{n_k n_k} = \left[\mathbf{G}_{m_k m_k} - \mathbf{A}_{G_1} \left[\mathbf{A}_{G_2}\right]^{-1} \mathbf{G}_{n_k m_k}\right]; \tag{4.16}$$

$$\mathbf{F}_{n_k} = \left[\mathbf{A}_{G_1} \left[\mathbf{A}_{G_2}\right]^{-1} \mathbf{H}_{n_k n_k} - \mathbf{H}_{m_k n_k}\right] \left[\mathbf{H}_{n_{(k+1)} n_{(k+1)}}\right]^{-1} \mathbf{F}_{n_{(k+1)}}. \tag{4.17}$$

   e) Proceed with the next layer above the current one.

3) Following the described condensation procedure, the influence matrices, $\mathbf{H}^*$ and $\mathbf{G}^*$, and the load vector, Φ_l, are obtained for the top most layer, $k = 1$, i.e., $\Phi_l = \mathbf{F}_{n_1}$. These matrices describe wave scattering, reflection, and transmission through the whole arbitrary layered soil region Ω_0.

4.6 Integration of the layer-wise condensation approach with the hybrid BEM-FEM

The next stage of work concerns the derivation of a correlation between the nodal tractions along the interface boundary Γ_{int} coming from the BEM model of the semi-infinite layered zone Ω_0 and the nodal forces along Γ_{int} necessary for the FEM model of the region Ω_1.

To proceed with the BEM sub-domain condensation, equation $\mathbf{H}^*\hat{\mathbf{u}}_l - \mathbf{G}^*\hat{\mathbf{t}}_l = \Phi_l$ is decoupled into matrices corresponding to the interface boundary Γ_{int} denoted by the index "1" and free-surface Γ_1 denoted by index "2" as described in equation (3.22) of Section 3.2. After this decoupling, the following matrix equation is obtained:

$$\begin{bmatrix} \mathbf{H}_{11}^{*(\Omega_0)} & \mathbf{H}_{12}^{*(\Omega_0)} \\ \mathbf{H}_{21}^{*(\Omega_0)} & \mathbf{H}_{22}^{*(\Omega_0)} \end{bmatrix} \begin{bmatrix} \hat{\mathbf{u}}_{l1}^{(\Omega_0)} \\ \hat{\mathbf{u}}_{l2}^{(\Omega_0)} \end{bmatrix} - \begin{bmatrix} \mathbf{G}_{11}^{*(\Omega_0)} & \mathbf{G}_{12}^{*(\Omega_0)} \\ \mathbf{G}_{21}^{*(\Omega_0)} & \mathbf{G}_{22}^{*(\Omega_0)} \end{bmatrix} \begin{bmatrix} \hat{\mathbf{t}}_{l1}^{(\Omega_0)} \\ \hat{\mathbf{t}}_{l2}^{(\Omega_0)} \end{bmatrix} = \begin{bmatrix} \Phi_{l1}^{(\Omega_0)} \\ \Phi_{l2}^{(\Omega_0)} \end{bmatrix}, \quad (4.18)$$

where $\hat{\mathbf{u}}_l^{(\Omega_0)}$ and $\hat{\mathbf{t}}_l^{(\Omega_0)}$ are the nodal displacement and traction vectors along the boundary $\Gamma_l = \Gamma_1 \cup \Gamma_{int}$ and $\Phi_l^{(\Omega_0)}$ is the applied dynamic load along the same boundary due to existence of an embedded source in the most bottom layer.

Following the procedure discussed in Section 3.2 (Vasilev et al., 2015), the following relation can be derived from equation (4.18):

$$\hat{\mathbf{t}}_{l1}^{(\Omega_0)} = \mathbf{E}\,\hat{\mathbf{u}}_{l1}^{(\Omega_0)} - \mathbf{p}, \quad (4.19)$$

where

$$\mathbf{E} = \left[\mathbf{G}_{11}^{*(\Omega_0)} - \mathbf{H}_{12}^{*(\Omega_0)}\mathbf{A}_{\mathbf{t}}\right]^{-1}\left[\mathbf{H}_{11}^{*(\Omega_0)} - \mathbf{H}_{12}^{*(\Omega_0)}\mathbf{A}_{\mathbf{u}}\right]; \quad (4.20a)$$

$$\mathbf{p} = \left[\mathbf{G}_{11}^{*(\Omega_0)} - \mathbf{H}_{12}^{*(\Omega_0)}\mathbf{A}_{\mathbf{t}}\right]^{-1}\left[\Phi_{l1}^{(\Omega_0)} - \mathbf{H}_{12}^{*(\Omega_0)}\Theta\right]; \quad (4.20b)$$

$$\mathbf{A}_{\mathbf{t}} = \left[\mathbf{H}_{22}^{*(\Omega_0)}\right]^{-1}\mathbf{G}_{21}^{*(\Omega_0)}; \quad (4.20c)$$

$$\mathbf{A}_{\mathbf{u}} = \left[\mathbf{H}_{22}^{*(\Omega_0)}\right]^{-1}\mathbf{H}_{21}^{*(\Omega_0)}; \quad (4.20d)$$

$$\Theta = \left[\mathbf{H}_{22}^{*(\Omega_0)}\right]^{-1}\Phi_{l2}^{(\Omega_0)}; \quad (4.20e)$$

which are equivalent to equations (3.23) and (3.24). Thus, the remaining procedures described in Section 3.2 are valid from this point:

1) the conversion of the influence matrix $\mathbf{E}$ and the dynamic load vector $\mathbf{p}$

into stiffness and structural damping matrices $\mathbf{K}^{(\Omega_0)}$ and nodal force vector $\mathbf{r}^{(\Omega_0)}$, respectively, follows the relations in (3.25) and (3.26);

2) the assembly of the stiffness and structural damping matrices of the BEM region, $\Re(\mathbf{K}^{(\Omega_0)})$ and $\Im(\mathbf{K}^{(\Omega_0)})$, with the stiffness and structural damping matrices of the FEM region, $\mathbf{K}^{(\Omega_1)}$ and $\mathbf{K}_s^{(\Omega_1)}$ into the global stiffness and structural damping, $\mathbf{K}$ and $\mathbf{K}_s$, matrices follows the description in Section 2.6 using tied contact pair described in Section 3.5, see Figure 3.9;

3) the assembly of the nodal force vector of the BEM region $\mathbf{r}^{(\Omega_0)}$ with the nodal load vector of the FE zone $\hat{\mathbf{f}}^{(\Omega_1)}$ into the global nodal load vector $\hat{\mathbf{f}}$ follows the description in Section 3.2 using tied contact pair described in Section 3.5, see Figure 3.9.

4) the generation of substructures, solution of the global SEs using direct solution steady-state dynamic procedure, collection of outputs, and conversion of the results into time-domain solutions follow the description in Section 2.6, see also Figure 3.2.

The insertion of the LWC method into the hybrid numerical scheme (Figure 3.2) is summarized in the workflow in Figure 4.3. Since equation (4.9) is essentially the same as equation (3.20), the LWC method can also be applied for double-couple source cases. In the case of incident wave, it is only valid for cases where all layers' geometries reach the traction-free surface.

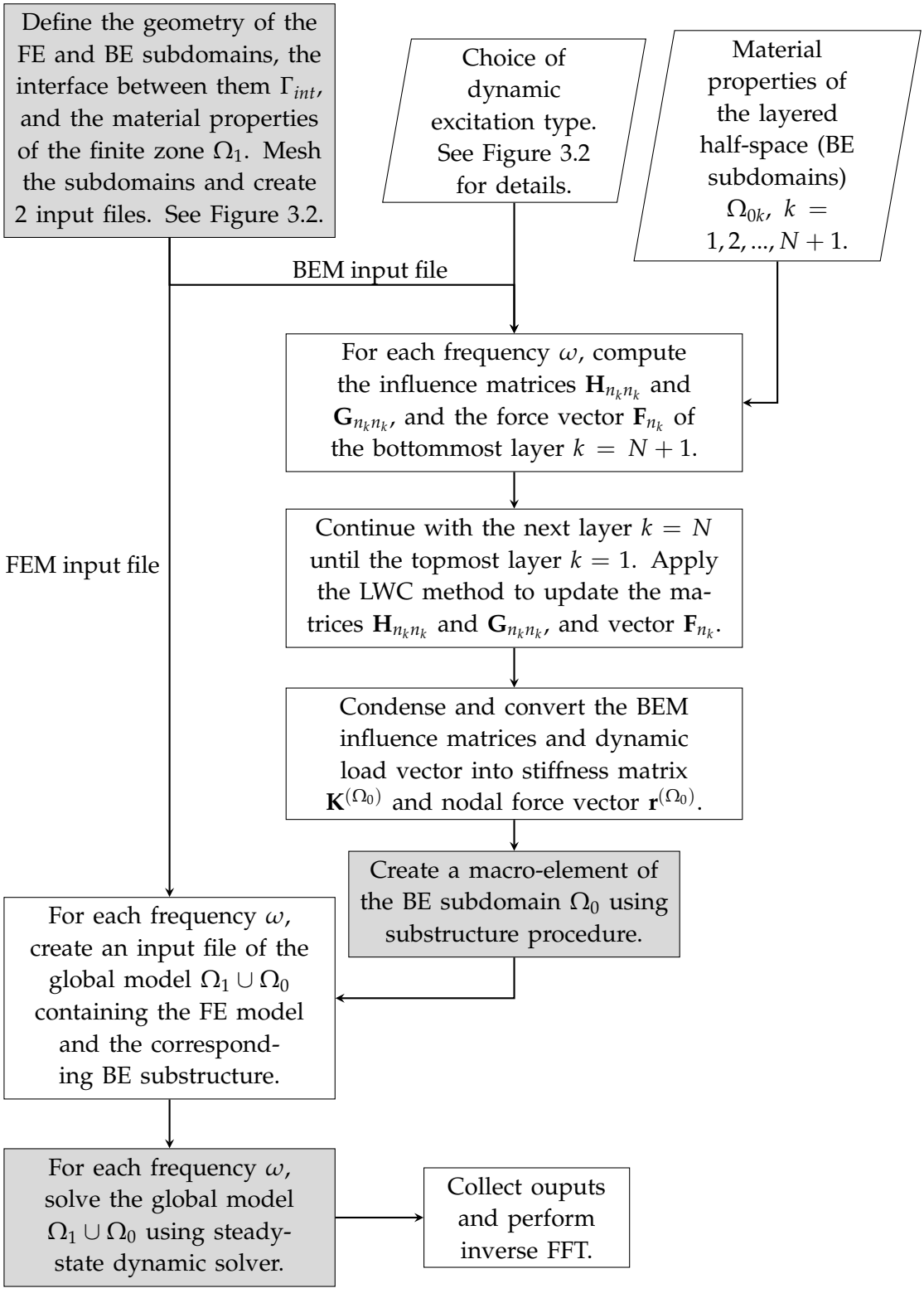

FIGURE 4.3: A schematic flowchart of the hybrid FEM-BEM based on the macro-element concept with the LWC method. The grey color marks processes performed in the ABAQUS environment, while the white marks those performed in MATLAB.

4.7 Verification study

The accuracy and convergence of the hybrid model described above and the numerical scheme accompanying it are studied by the use of appropriate chosen benchmark examples. The accuracy criterion established in Section 3.6 that $\lambda_S / l_{BE} \geq 5$ is used, where l_{BE} is the length of the corresponding element and λ_S is the shear wavelength.

Test example 1: dynamic response of a rigid massless foundation rested on a layered half-space under vertical harmonic loading

The objective of test example 1 is the dynamic response of a rigid massless foundation resting on a half-space with two layers with equal material properties. The assumption for layers with equal material properties reduces the problem into the case of a rigid massless foundation on a homogeneous half-space. The rigid foundation is under vertical harmonic load acting on its center. The FE subdomain consists only of the foundation, while the BE subdomain is presented by a free-surface layer Ω_{01} and a semi-infinite region Ω_{02}. Two types of geometry of the interface Γ_2 between the two layers of the BE subdomain are considered to show the interface geometry's influence on the solution's accuracy. In the 1st type of geometry, the layer Ω_{01} has a fixed depth $h_{\Omega_{01}} = 1$ m and is modeled with infinite, horizontal, and parallel top and bottom boundaries, see Figure 4.4a. Figure 4.4b shows the complete FEM-BEM model with this type of geometry. In the 2nd type of geometry, the bottom boundary of the layer Ω_{01} is modeled with an irregular shape extruded along x_1 axis (Figure 4.4c). The layer-wise condensation method is utilized in this test example to process the layered BEM domain without including the force term since the excitation originated from within the finite region.

The material properties of the homogeneous half-space are taken from the study by Chuhan, Chongmin, and Pekau, 1991, as follows: Lamé constants $\lambda_0 =$ 180 GPa, $\mu_0 = 90$ GPa and Poisson's ratio of 1/3. The dimension of the square foundation is 1 m $\times$ 1 m, while the BEM model's discretized free surface is 6 m by 6 m. The discretized free surface's influence on the particular problem's result is explored in Section 3.6. To expose the solution's sensitivity to the size of the interface between both layers, it is modeled with the three dimensions: 6 m $\times$ 6 m, 7 m $\times$ 7 m, and 8 m $\times$ 8 m. A ratio between the offset distance of the interface from the free-surface boundary relative to the depth of the interface $h_{\Omega_{01}}$ is defined as

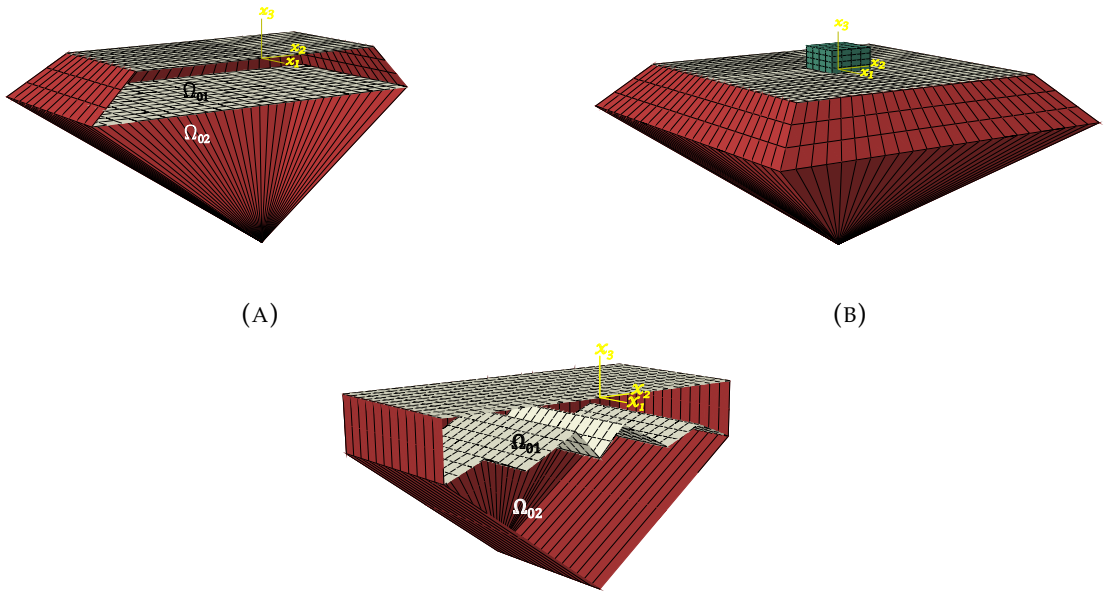

(A) (B)

(C)

FIGURE 4.4: Test example 1: (**A**) a cut view of the BEM region and (**B**) a perspective view of the complete FEM-BEM model with the geometry of type 1; (**C**) a cut view of the BEM region with the geometry of type 2.

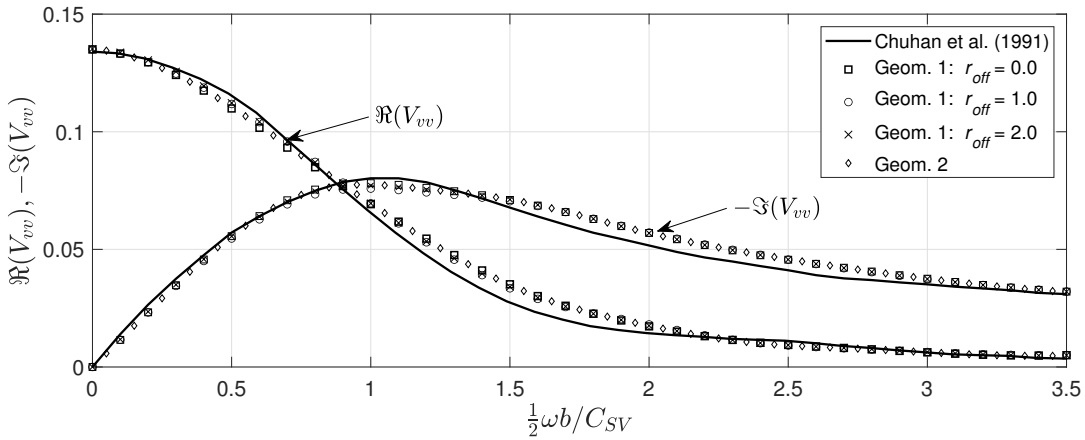

FIGURE 4.5: Vertical compliances of a rectangular rigid massless foundation resting on a half-space with two layers having equal material properties versus normalized frequency. Comparison of the author's results with those in Chuhan, Chongmin, and Pekau, 1991 for a homogeneous half-space.

follows: $r_{off} = (b_{\Gamma_2} - b_{\Gamma_1})/h_{\Omega_{01}}$, where b_{Γ_1} and b_{Γ_2} are the half-width of the discretized free-surface boundary (either along x_1 or x_2 direction) and the interface boundary, respectively. The aforementioned three dimensions correspond to the following three cases of the parameter r_{off}: 0.0, 1.0, and 2.0. Figures 4.4a and 4.4b present the geometry of the 2$^{\text{nd}}$ case, i.e., $r_{off} = 1.0$. The rigid foundation is

modeled using the rigid body constraint available in ABAQUS. The foundation's mesh consists of 64 quadratic hexahedral finite elements, 16 of which are in contact with the half-space. The same element size of 0.25 m is used for the FEM and BEM regions which correspond to $\lambda_S/l_{BE} = 4$ at the highest frequency of 5 kHz. For the 2nd case of the parameter r_{off}, the layer Ω_{01} is modeled using 1440 boundary elements, of which 288 elements are dummies, while the semi-infinite layer Ω_{02} is discretized by 672 boundary elements including 96 dummy elements. In Figure 4.4, the foundation is green, and the dummy elements are red-colored. The vertical compliance of the foundation due to vertical harmonic loading is defined as in (3.68). Figure 4.5 shows a comparison between the authors' results obtained by the hybrid computational approach based on the BEM and FEM for both geometries with the solutions obtained by 3D pure BEM in Chuhan, Chongmin, and Pekau, 1991. As can be seen, the solutions are very close, and it illustrates that the LWC method works with satisfactory accuracy.

Test example 2: wave propagation in a finite soil region located in a two-layered half-space due to dynamic point source

The 2nd test example concerns a wave propagation problem in a finite soil region Ω_1 located in the first layer Ω_{01} of a two-layered half-space Ω_0 due to a dynamic excitation located at point $\mathbf{X}_0$, see Figure 4.6. The finite region Ω_1 is a square cuboid with a width of 400 m and a depth of 50 m. The dimension of the outer edges of the mesh of the BEM region Ω_0 is 1 km $\times$ 1 km. It expands horizontally 300 m outward of the finite region. The BEM unbounded zone, which is outside of the finite soil region Ω_1 (the FEM zone), consists of 2 layers (Ω_{0k}, $k = 1, 2$) with free-surface infinite boundary Γ_1 and horizontal, infinite interface Γ_2. Two geometry types are considered to study their effect on the solution's accuracy. In the 1st type of geometry, the interface Γ_2 is horizontal along the plane $x_3 = -200$ m (Figure 4.6a), while in the 2nd type of geometry, it is modeled as irregular relief extruded along x_2 direction (Figure 4.6b). The finite and semi-infinite regions are connected by inter-regional interface Γ_{int}, while the free surface of the finite region is denoted by Γ_F. A point source is placed at $\mathbf{X}_0$(-100 m, 0, -230 m). Equal material properties are assigned for Ω_1 and Ω_{0k} ($k = 1, 2$) with the following details: Lamé moduli $\lambda = 144$ MPa, $\mu = 72$ MPa and Poisson's ratio of $1/3$. The assumption for equal material properties of the finite soil region Ω_1 and both layers of the half-space Ω_0 reduces the problem to the case of wave propagation in a homogeneous half-space due to dynamic point source located at point $\mathbf{X}_0$. The time history function used for the dynamic input is a Ricker wavelet with a duration of

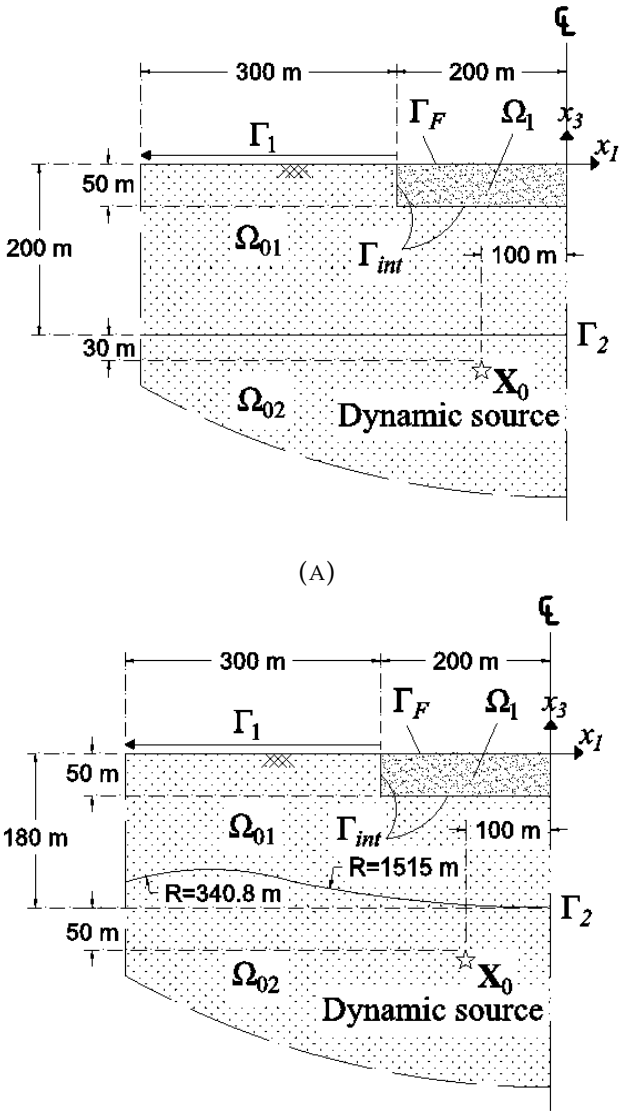

FIGURE 4.6: Test example 2: (**A**) the geometry of type 1 and (**B**) the geometry of type 2. Note that all features of both geometries are symmetrical along the plane $x_1 = 0$, depicted as the centerline, except for the dynamic source $\mathbf{X}_0$.

10 s, a time delay of 1 s, a frequency range of [0, 3] Hz, a main frequency of 1 Hz, and a time resolution of 0.01 s. The time function is transformed into the Fourier domain and then normalized with respect to the maximum absolute value of the amplitude spectrum. The frequency resolution of the transformed time-function considered for the analysis is 0.1953 Hz, and the amplitude is $f_i^{(\Omega_0)}(10^6$ N, 0, 0). The BEM and FEM regions with the geometry of type 1 are modeled with two mesh sizes to show the solution's convergence: (Mesh A) $\lambda_s/l_{BE} = 5$; (Mesh B) $\lambda_s/l_{BE} = 8$. The former mesh size is used for the model with the geometry of type 2.

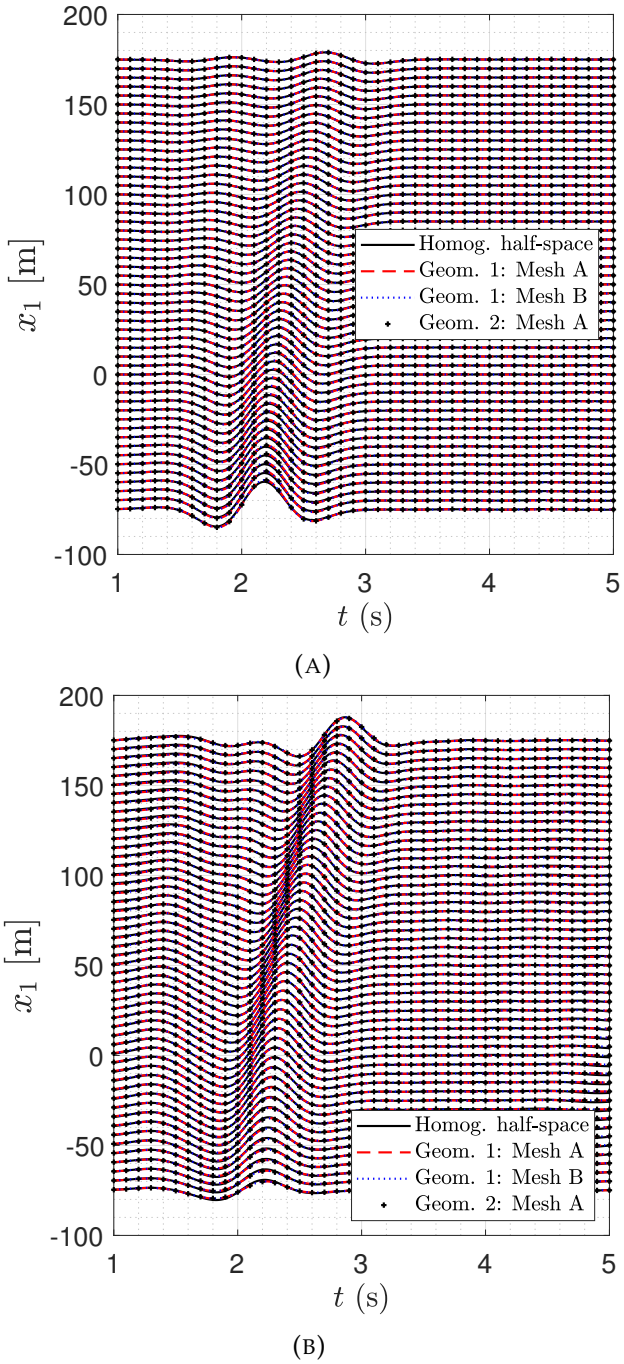

FIGURE 4.7: Comparison of displacement components (**A**) u_1 and (**B**) u_3 for test example 2 with the results obtained for the reference model at points along line $x_2 = x_3 = 0$.

Synthetic seismograms obtained for both meshes and geometries of the test example 2 and compared with the result obtained for the reference model, which is the homogeneous half-space with a mesh size of $\lambda_s/l_{BE} = 8$, are shown in Figure 4.7. The relative differences between the displacement component u_1 obtained for the reference model without any layering and test example 2 with the geometry of type 1, Mesh A, are 3.49%, 3.11%, 4.31%, and 3.65% for observer

points x(0, 0, 0), x(50 m, 0, 0), x(100 m, 0, 0), and x(150 m, 0, 0), respectively. For displacement component u_3, the relative differences are 4.37%, 3.53%, 5.20%, and 6.10%. Comparing the results obtained by using Mesh A and Mesh B for the geometry of type 1 show that the relative differences for the aforementioned observer points are as follows: (u_1) 0.81%, 1.37%, 2.53%, and 2.64%; (u_3) 2.28%, 2.23%, 3.32%, and 3.35%. The relative differences between the results obtained for the geometries of type 1 and of type 2, with Mesh A for the above observer points, are as follows: (u_1) 0.78%, 0.05%, 0.02%, 0.01%; (u_3) 0.31%, 0.09%, 0.09%, 0.05%.

In order to study **the influence of the size of the discretized BEM region on the solution's accuracy**, the BEM boundaries sizes for the geometry of type 1 are modified by assuming dimensions of 500 m $\times$ 500 m and 800 m $\times$ 800 m. A ratio relating the size of the discretized free-surface and the depth of the dynamic source at point $\mathbf{X}_0$ is defined as follows: $r_{B\mathbf{X}_0} = (L_{BE_{x_1}} - |\mathbf{X}_0(x_1)|)/\mathbf{X}_0(x_3)$, where $L_{BE_{x_1}}$ is the half-width of the discretized free-surface of the BEM region in the direction of x_1 and $\mathbf{X}_0(x_i)$ is the coordinate of point $\mathbf{X}_0$ in the x_i direction. The three dimensions of the free surface of the BEM region correspond to $r_{B\mathbf{X}_0}$ of 0.65, 1.30, and 1.74. The relative differences between the displacement component u_i obtained from the model with $r_{B\mathbf{X}_0}$ of 0.65 and 1.30 for the four observer points are as follows: (u_1) 8.22%, 11.75%, 15.52%, and 18.51%; (u_3) 7.47%, 7.68%, 20.61%, and 25.55%. The relative differences between the cases $r_{B\mathbf{X}_0} = 1.30$ and $r_{B\mathbf{X}_0} = 1.74$ are the followings: (u_1) 2.37%, 4.32%, 5.43%, and 6.74%; (u_3) 5.70%, 2.34%, 5.29%, and 6.22%. Based on these results, $r_{B\mathbf{X}_0} \geq 1.70$ is used in all subsequent simulations.

The above results highlight the excellent accuracy of the proposed hybrid computational FEM-BEM technique based on the macro-element concept and the layer-wise condensation procedure.

An illustration of **the computational cost reduction** as a result of the LWC method for test example 2 is described as follows. The BEM region of test example 2 with the geometry of type 1 consists of 3810 and 1750 nodes for layer Ω_{01} and layer Ω_{02}, respectively. An assembled global influence matrix of the BEM zone for the frequency domain analysis would require $((N_{DoF} \times L)^2 \times N_{byte} \times 2)$ bytes of computational memory, where L is the number of nodes, N_{DoF} is the number of degrees of freedom per node, N_{byte} is the memory size to store one numeric value in MATLAB®. The last multiplier is due to the complex number, which requires two numeric values per entry. For all floating-point numbers in MATLAB® in this study, an 8-byte double-precision format is used. During the computation,

three influence matrices are required to store the following integrals: *(1)* the dynamic part of the traction fundamental solution's kernel; *(2)* the static part of the traction fundamental solution's kernel (containing only real numbers); and *(3)* the displacement fundamental solution's kernel. Thus, the computation of test example 2 requires (4.451+2.226+4.451=11.129) gigabytes (GB). Using the layer-wise condensation method, the maximum memory requirement for the influence matrices occurs during the computation of layer Ω_{01} with storage of 5.226 GB for all three matrices. Thus, about 53% less memory is required. The reduction is higher when more layers are computed.

In the case of test example 2, the corresponding BVP is solved for 20 discrete frequencies in the interval [0,3] Hz. The elapsed computation time for all frequencies is approximately 102 minutes consisting of 88 minutes for BEM computation and condensation, 7 minutes for the macro finite-element (substructure) generation, and 7 minutes for the steady-state dynamic solution of the global BEM-FEM model. Due to the re-usability of the substructures, any recalculation that does not include any change in the BEM region would only cost the last part of the above computation time. A workstation with a 32-core CPU (base speed of 3.69 gigahertz), 256 GB of random-access memory, and PCIe-NVMe storage drives is used in combination with version 2020 of MATLAB® and ABAQUS.

4.8 Chapter summary

The derivation of the layer-wise condensation method and its general scheme is presented. The method can be seamlessly incorporated into the hybrid BEM-FEM scheme and works in conjunction with the numerical improvements described in Chapter 3. Verification studies considering responses of foundation under dynamic loading and wave propagation problems show that the method works well. Significant computational memory can be reduced as an effect. Further improvement to the hybrid method that enables the consideration of nonlinearities in the model is described in the following chapter.

Practical examples which show the application of the method described here are presented in Chapter 8 and Chapter 9.

Chapter 5

Nonlinear dynamic SSI analysis using the sequential frequency-time domain (SFTD) procedure

5.1 Chapter overview

This chapter discusses the sequential frequency-time domain analyses to solve dynamic problems involving nonlinearities. The introduction is given in Section 5.2, where critical points of the problem and exsiting solutions are described. It is followed by the description of the procedure, the compatibility conditions, and the error measurement in Section 5.3. Section 5.4 discusses the verification study considering a 3D multi-storey structure and taking into account soft and hard supporting soils.

5.2 Introduction and review of the exsiting solutions

During earthquake excitation, the material nonlinearity that is exhibited by the soil due to the wave motion is referred to as the soil **primary nonlinearity** while the nonlinearity of the soil due to the interaction with structures is considered as the **secondary nonlinearity** (Coleman, Bolisetti, and Whittaker, 2016). In a condition where a structure is relatively stiff compared to its supporting soil, the rotation and translation of the foundation might occur and add to the structural displacement. Thus, the structure's natural period is increased (Bielak, 1978; FEMA, 2020). In addition, the physical (with respect to the constitutive model) or geometrically (large deformations) nonlinear soil behaviour in the near-field region close to the foundation has a **strong effect on the seismic response of the soil-structure system**. As illustrations, a report by Yashinsky, 1998, concluded that the

damages on highways due to the 1989 Loma Prieta, California, earthquake were caused by the combination of soft soil and flexible piles. Similar findings were reported by Mylonakis et al., 2006, for the damages on the Hanshin Expressway due to the 1995 Kobe earthquake.

Numerical studies of this phenomenon are conducted by many authors, among them are Pitilakis et al., 2006, Tamhidi and Ghannad, 2020, and Bolisetti, Whittaker, and Coleman, 2018, where a comparative study for the application of linear, equivalent linear and nonlinear approximation of the soil behavior in the soil-structure models is presented. A study of a bilinear hysteretic structure by Bielak, 1978, on viscoelastic half-space showed that the resonant amplitude of a soil-structure system is increased compared to that of a rigid base. Harden et al., 2005, used beam on nonlinear Winkler foundation (**BNWF**) approach to study the nonlinear behavior of shallow foundations under cyclic loading. The performance of this approach was later compared to the contact interface model (CIM) in modeling the nonlinear soil-foundation interaction problems in a study by Gajan et al., 2010. Tamhidi and Ghannad, 2020, implemented the equivalent linear model according to ASCE 7-10 and the BNWF method in OpenSees (Mckenna, 2011) to simulate the influence of nonlinear soil behaviour on the ductility demand of the superstructure. **Hybrid FEM-SBFEM** was also successfully utilized to model nonlinear dynamic SSI, e.g., see Halabian and El Naggar, 2002; Bransch, 2010, where the SBFEM is used to model the far-field region and to satisfy the Sommerfeld's radiation condition at infinity. However, the SBFEM solution for layered media is computationally expensive (Ferro, 2013).

Hybrid BEM-FEM has been used to analyse the nonlinear dynamic SSI problem as well. Following the hybrid BEM-FEM in the time domain by Karabalis and Beskos, 1984, von Estorff and Firuziaan, 2000, obtained the solution for nonlinear SSI by using the direct method where the BEM influence matrices are incorporated into the nonlinear iteration algorithm of the FEM, and the equilibrium condition of displacement is enforced. The iterative method (domain decomposition) was successfully implemented as well, as reported in Rizos and Wang, 2002; Soares Jr, von Estorff, and Mansur, 2004; von Estorff and Hagen, 2005. A MATLAB® toolbox codenamed *SSIFiBo* was released by Galvín and Romero, 2014b, based on the coupling method by Soares, Mansur, and Von Estorff, 2007. Contact nonlinearity between the soil and foundation can be modeled with it.

Implementing the direct or iterative coupling method in the time domain on the ABAQUS software package is a complex task. In the direct method, the BEM stiffness matrices have to be exported into ABAQUS for every time step, whilst

in the iterative method, a higher hierarchy software must be written to control ABAQUS, MATLAB®, as well as the flow of trial boundary conditions and results data between the two solvers and to control the convergence. Furthermore, the iterative method requires an iteration scheme to be performed, see Section 2.6. Thus, it is likely unsuitable for a large domain with a considerable BE-FE interface or multiple nonlinearities.

In most of the aforementioned hybrid BEM-FEM studies, **the time domain BEM formulations** were used. In this formulation, the solution for time step q requires the influence matrices of time steps 1 until $\{q-1\}$ to be multiplied and accumulated with the corresponding past solutions, see equation (2.32). This means that, as the analysis marches forward in time, more data storage is required. In addition to this drawback, the BEM formulation in the time domain is computationally expensive compared to the frequency domain. It also exhibits artificial numerical damping, and it is prone to numerical instability as reported by Dominguez, 1993; Panagiotopulos and Manolis, 2011. Improvement by replacing the displacement-traction pair with the velocity-traction pair was suggested by Panagiotopulos and Manolis, 2011. An alternative time domain formulation using the convolution quadrature method (CQM) was proposed in Schanz and Antes, 1997a; Schanz and Antes, 1997b.

One of the ideas to avoid the time domain BEM was the development of the **hybrid frequency-time domain** (**HFTD**) approach, which stemmed from the work by Kawamoto, 1983, who used the pseudo-force term to represent the residual force between the linear elastic system, solved in the frequency domain, and the nonlinear system. The general equilibrium is written as

$$\mathbf{M\ddot{u}} + \mathbf{C\dot{u}} + \mathbf{Ku} = \mathbf{f} + \mathbf{f}^{NL}, \tag{5.1}$$

where $\mathbf{f}^{NL}$ is the pseudo-force term, which is evaluated after the solution for the unknown $\mathbf{u}(t)$ is obtained from the inverse FFT of the solution in the frequency domain $\mathbf{u}(\omega)$. The pseudo-force is then returned to the equilibrium condition in the frequency domain for the next iteration until the residual force is within a defined tolerance. Advanced implementations of the hybrid frequency-time domain method for hybrid BEM-FEM can be found in Obrembski, Clouteau, and Greffet, 2005; François, 2008. In addition, Ferro, 2013, developed and implemented the hybrid Laplace-time domain approach. However, in most of these studies, nonlinearities are only considered to **a limited extent**. The term "nonlinear" often does not cover all aspects of secondary nonlinearity. These aspects, according to the revised ASCE Standard 4 "Seismic Analysis of Safety-Related

Nuclear Structures and Commentary," are (1) material nonlinearity, (2) embedment effect, (3) failure of soil at soil-foundation interface, (4) pore fluid-soil interaction, (5) uplift and sliding of the foundation, and (6) gapping effects (Coleman, Bolisetti, and Whittaker, 2016).

In summary, the current state of nonlinear dynamic SSI analyses within the hybrid BEM-FEM framework has the following **critical points**:

- The time domain BEM formulation is used, which requires ample memory storage in realistic cases with a large domain or in cases of transient dynamic excitation with a long time duration, e.g., earthquake time history.
- Secondary nonlinearities are only partially considered.
- The geostatic stress state of the soil and the loads on the structural members are often neglected.
- Implementation of the time domain hybrid method or the HFTD method in commercial software packages such as ABAQUS is cumbersome and impractical from the user's point of view. In much commercial software, it may not be possible to modify the matrices at every time interval or time step.

An alternative method to overcome these points is presented in this chapter. To solve the problems, the author takes advantage of the fact that, in this hybrid model, the BE-FE interface can be placed at a distance from the source of nonlinearities, i.e., the structure of interest and/or soil near the foundation. Because of that, the discrepancy of the stresses or tractions along the BE-FE interface between linear and nonlinear solution can be considerably minimized. The proposed method extends the hybrid method described in Section 2.6 and Section 3.2, which is developed for the whole domain in the frequency domain, into a sequential analysis in the time domain. The outputs of the former are used as inputs for the finite region model in the latter.

5.3 Sequential frequency-time domain procedure

Consider a problem similar to the one before where domain Ω_1 is located in a semi-infinite region Ω_0. A foundation in the finite region Ω_1 supports a structure, see Figure 5.1a, where the structure is depicted as a single-degree-of-freedom model. The free surface of the foundation is denoted as Γ_f while the soil-foundation contact surfaces are collected in Γ_g. The free-surfaces of Ω_0 and Ω_1 are denoted

as Γ_B and Γ_F, respectively. Thus, the external boundary of Ω_0 and Ω_1 are $\Gamma_{\Omega_0} = \Gamma_{int} \cup \Gamma_B$ and $\Gamma_{\Omega_1} = \Gamma_{int} \cup \Gamma_F \cup \Gamma_g$, respectively.

The material properties are: (Ω_0) $\rho_0, \lambda_0, \mu_0, C_{P_0}, C_{S_0}$; $(\Omega_1)\rho_1, \lambda_1, \mu_1, C_{P_1}, C_{S_1}$; and (the structure and foundation) $\rho_f, \lambda_f, \mu_f, C_{P_f}, C_{S_f}$. Following the procedure described in Section 3.2, the system of equation of the whole system in ABAQUS is given in equation (2.84), and the solution of the unknown in the frequency

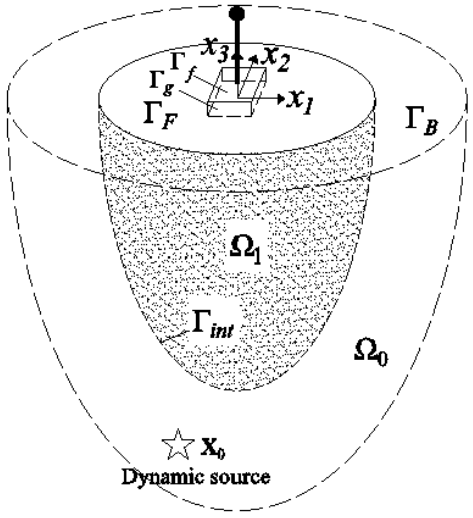

(A)

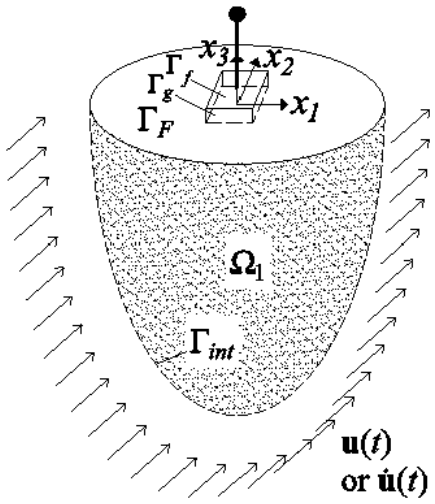

(B)

FIGURE 5.1: (**A**) The problem geometry presenting the finite region Ω_1, with a structure and a foundation located at it, embedded in a half-space Ω_0 with dynamic source at $\mathbf{X}_0$. (**B**) The finite region Ω_1 is decoupled from the global domain and initial conditions $\breve{\mathbf{u}}(t = 0)$ and boundary conditions $\breve{\mathbf{u}}(t)$ are applied to its interface Γ_{int}.

domain $\hat{\mathbf{u}}^{(\Omega_1)}(\mathbf{x},\omega), \mathbf{x} \in \Omega_1$, is obtained using the direct steady-state dynamic solver of ABAQUS, see Figures 3.2 and 4.3. $\hat{\mathbf{u}}^{(\Omega_1)}(\mathbf{x},\omega)$ contains the solution for all nodes in Ω_1 including the nodes along Γ_{int} of the FE region. It considers the following essential aspects:

- the effect of wave motion following the applied transient dynamic source at $\mathbf{X}_0$,
- the (linear elastic) material properties of the near- and far-field region, and
- the kinematic and inertial interactions between the soil and the structure.

Extracting the solution along Γ_{int} of Ω_1 from the whole solution $\hat{\mathbf{u}}^{(\Omega_1)}$, such that $\hat{\mathbf{u}}^{(\Omega_1)}(\mathbf{x},\omega), \mathbf{x} \in \Gamma_{int}$, the solution in the time domain for these nodes along the interface $\breve{\mathbf{u}}^{(\Omega_1)}(\mathbf{x},t), \mathbf{x} \in \Gamma_{int}$, can be obtained after applying the inverse FFT, i.e.,

$$\breve{\mathbf{u}}^{(\Omega_1)}(\mathbf{x},t) = \mathcal{F}^{-1}\{\hat{\mathbf{u}}^{(\Omega_1)}(\mathbf{x},\omega)\}(t), \quad \text{for } \mathbf{x} \in \Gamma_{int}, \tag{5.2}$$

where $\mathcal{F}^{-1}\{.\}$ denotes inverse Fourier operation.

Let us now consider the same finite region Ω_1 but without the semi-infinite region, see Figure 5.1b. The dynamic equilibrium of the finite region Ω_1, written in the time domain, is described in equation (2.54), repeated here as

$$\mathbf{M}^{(\Omega_1)}\ddot{\mathbf{u}}^{(\Omega_1)} + \mathbf{C}^{(\Omega_1)}\dot{\mathbf{u}}^{(\Omega_1)} + \mathbf{K}^{(\Omega_1)}\mathbf{u}^{(\Omega_1)} = \mathbf{f}^{(\Omega_1)}. \tag{5.3}$$

The compatibility and equilibrium condition of displacement that is established in Section 2.6 for the interface Γ_{int} between BE and FE region can be re-applied to bridge the frequency and time domain formulations, expressed as

$$u_j^{(\Omega_1)}(\mathbf{x},t) = \breve{u}_j^{(\Omega_1)}(\mathbf{x},t) = \mathcal{F}^{-1}\{\hat{u}_j^{(\Omega_1)}(\mathbf{x},\omega)\}(t), \quad \text{for } \mathbf{x} \in \Gamma_{int}, \tag{5.4}$$

where the left-hand side of the equation refers to the displacement in the time domain, and the rest refers to the product of the preceding frequency domain output. Thus, equation (5.3) can be rewritten in the form of

$$\begin{bmatrix} \mathbf{M}_{11}^{(\Omega_1)} & \mathbf{M}_{12}^{(\Omega_1)} \\ \mathbf{M}_{21}^{(\Omega_1)} & \mathbf{M}_{22}^{(\Omega_1)} \end{bmatrix} \begin{bmatrix} \ddot{\mathbf{u}}_1^{(\Omega_1)} \\ \breve{\ddot{\mathbf{u}}}_2^{(\Omega_1)} \end{bmatrix} + \begin{bmatrix} \mathbf{C}_{11}^{(\Omega_1)} & \mathbf{C}_{12}^{(\Omega_1)} \\ \mathbf{C}_{21}^{(\Omega_1)} & \mathbf{C}_{22}^{(\Omega_1)} \end{bmatrix} \begin{bmatrix} \dot{\mathbf{u}}_1^{(\Omega_1)} \\ \breve{\dot{\mathbf{u}}}_2^{(\Omega_1)} \end{bmatrix} + \begin{bmatrix} \mathbf{K}_{11}^{(\Omega_1)} & \mathbf{K}_{12}^{(\Omega_1)} \\ \mathbf{K}_{21}^{(\Omega_1)} & \mathbf{K}_{22}^{(\Omega_1)} \end{bmatrix} \begin{bmatrix} \mathbf{u}_1^{(\Omega_1)} \\ \breve{\mathbf{u}}_2^{(\Omega_1)} \end{bmatrix} = \begin{bmatrix} \mathbf{f}_1^{(\Omega_1)} \\ 0, \end{bmatrix} \tag{5.5}$$

where the matrices and vectors corresponding to nodes belonging to the interface Γ_{int} are denoted by subscript "2" and those corresponding to the rest of the nodes in Ω_1 are denoted by subscript "1". Equation (5.5) states that the solution of the finite region in the time domain $\mathbf{u}_1^{(\Omega_1)}(\mathbf{x},t)$ can be obtained by applying the frequency domain outputs $\breve{\mathbf{u}}^{(\Omega_1)}(\mathbf{x},t)$, $\breve{\dot{\mathbf{u}}}^{(\Omega_1)}(\mathbf{x},t)$, or $\breve{\ddot{\mathbf{u}}}^{(\Omega_1)}(\mathbf{x},t)$ as initial and boundary conditions along Γ_{int}. The initial and boundary conditions are expressed for displacement as

$$\mathbf{u}^{(\Omega_1)}(\mathbf{x},0) = \breve{\mathbf{u}}^{(\Omega_1)}(\mathbf{x},0), \quad \text{for } \mathbf{x} \in \Gamma_{int}; \text{ and} \tag{5.6}$$

$$\mathbf{u}^{(\Omega_1)}(\mathbf{x},t) = \breve{\mathbf{u}}^{(\Omega_1)}(\mathbf{x},t), \quad \text{for } \mathbf{x} \in \Gamma_{int}; \tag{5.7}$$

respectively.

In practice, however, the application of the displacement time history, i.e., $\breve{\mathbf{u}}^{(\Omega_1)}$, in a direct integration dynamic analysis in ABAQUS is **prone to numerical error** due to **its lack of differentiability**. This is because ABAQUS will compute the corresponding time derivatives of this input; since the displacement time history is linear within any two points in time, the velocity history will be piecewise constants, and the acceleration values at the time points may be infinite, as illustrated in Section 33.1.2 of its user's manual (Smith, 2014). This can be remedied by utilizing the built-in smoothing function provided by the software. However, a seemingly better choice to preserve the solution's accuracy is by using **the velocity time history**, e.g., $\breve{\dot{\mathbf{u}}}^{(\Omega_1)}$, instead of displacement. As initial displacements, initial velocities, and velocity time histories are known, the transient analysis computation can be performed as described in Section 2.5. In this work, the implicit dynamic solver is used.

The remaining **compatibility and equilibrium condition of traction** can then be used as a means of verification of the solution, expressed as

$$t_j^{(\Omega_1)}(\mathbf{x},t) = \breve{t}_j^{(\Omega_1)}(\mathbf{x},t) = \mathcal{F}^{-1}\{\hat{t}_j^{(\Omega_1)}(\mathbf{x},\omega)\}(t), \quad \text{for } \mathbf{x} \in \Gamma_{int}, \tag{5.8}$$

where the left-hand side of the equation refers to the results from (5.5) and the rest refers to the outputs of the preceding frequency domain analysis. However, since traction is not an extractable output in ABAQUS, we can instead request the stress output of representative integration points near the interface. Quantification of the discrepancies through **mean square error** (MSE) and **mean average**

error (MAE) can be defined as

$$MSE = \frac{1}{NE}\sum_{n=1}^{NE}\frac{1}{TE}\sum_{k=1}^{TE}\left(\sigma_{j(k)}^{n(\Omega_1)} - \breve{\sigma}_{j(k)}^{n(\Omega_1)}\right)^2, \quad \text{for } n \in \Gamma_{int}, \tag{5.9}$$

$$MAE = \frac{1}{NE}\sum_{n=1}^{NE}\frac{1}{TE}\sum_{k=1}^{TE}\left|\sigma_{j(k)}^{n(\Omega_1)} - \breve{\sigma}_{j(k)}^{n(\Omega_1)}\right|, \quad \text{for } n \in \Gamma_{int}, \tag{5.10}$$

respectively. Here, n denotes the considered integration point; NE is the number of them; (k) denotes the time point; and TE is the number of them within the considered time window.

The implementation of the velocity time histories as boundary conditions for the time domain model in ABAQUS can be performed by using the following keywords in the ABAQUS input file. The time histories are first written as amplitudes in text files. The inclusion of the amplitudes in the model is then performed using the keyword "*Amplitudes, name=*amplitude_name*, input= *text_file_name*.txt". Afterward, the amplitudes are attached to the corresponding nodes using the keyword "*Boundary, OP=New, type=velocity, amplitude= *amplitude_name*" followed in the next line by the node number or node set, the first degree of freedom, the last degree of freedom, and the magnitude (i.e., 1). Including "OP=New" in the above keyword is necessary for the reason given below.

To consider soil material and soil-foundation contact nonlinearities in the dynamic model, **initial geostatic stress** must be established in the finite model. To perform this correctly, a geostatic step is defined in the time domain analysis prior to the dynamic step. From this point of view, the use of velocity time history, instead of displacement one, is advantageous since the geostatic step typically results in a displacement in the range of $< 10^{-5}$ m, depending on the complexity of the geometry and the material properties. By using velocity as a boundary condition, the contradiction between the displacement values can be avoided. **Temporary encastré boundary conditions** along the interface Γ_{int} are required during the geostatic step to ensure the solution's convergence. **A static loading step** is also inserted in which the dead load and other static loads are applied to the structural members. Once the two static loading steps are completed, these boundary conditions are then released in the subsequent dynamic step using the keyword "*Boundary, OP=New" which is also used to assign the velocity boundary conditions.

The SFTD procedure is summarized in a workflow diagram shown in Figure 5.2. It is valid for dynamic SSI cases considering nonlinearities provided that

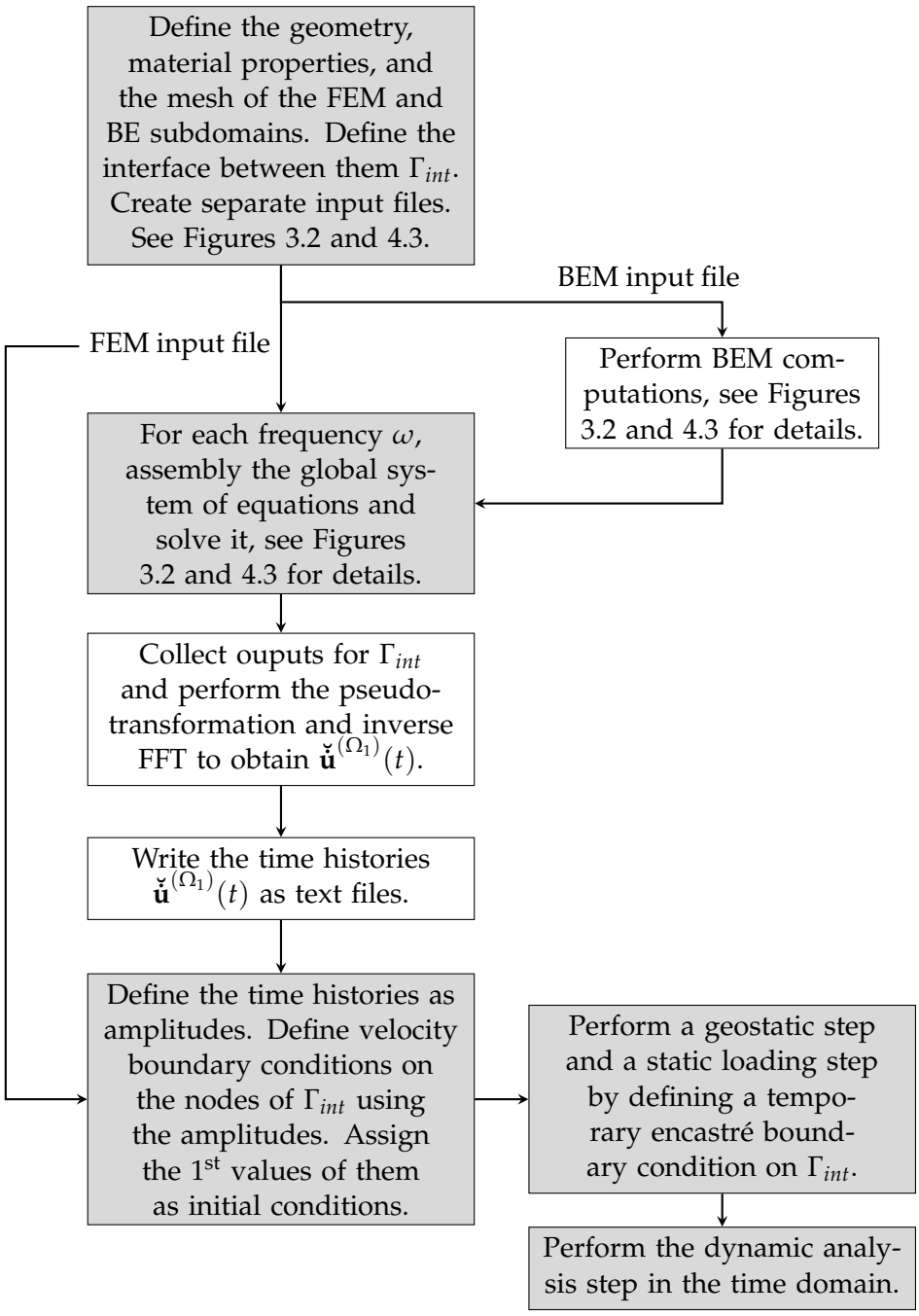

FIGURE 5.2: A schematic flowchart of the hybrid FEM-BEM for nonlinear dynamic analysis using the sequential frequency-time domain procedure. The grey color marks processes performed in the ABAQUS environment, while the white marks those performed in MATLAB.

Γ_{int} is sufficiently distanced from the sources of nonlinearities, as will be demonstrated in the following section.

5.4 Verification study considering soft and hard soil cases

The verification study considers **dynamic simulation of a multi-storey building** located on a half-space in response to ground-borne vibration, see Figure 5.3. 4 square foundations with width and thickness of 1 m and 0.3 m, respectively, support the structure. The center-to-center distance between the columns is 3 m, and the floor height is 3 m. The whole domain is excited by a transient dynamic vibration radiating from an embedded point source located at $\mathbf{X}_0$(-1 km, 0, -1 km). The finite region is decoupled into Ω_1 and Ω_1^* where the asterisk superscript marks the inclusion of nonlinear material behaviour, which in this case is the Mohr-Coulomb plasticity.

Two types of material properties are studied, referred to as *case 1* and *case 2*, to check the validity of the approach: *(1)* a relatively soft soil with $C_P = 400$ m/s, $C_S = 200$ m/s and *(2)* a hard supporting media with $C_P = 1600$ m/s, $C_S = 800$ m/s. The material properties are laid out in Table 5.1. To compensate for the harder material in *case 2*, two additional floors are used, see Figure 5.3b. **The Mohr-Coulomb plasticity** is defined as follows: friction angle of 25°, dilation angle of 0.1°, and cohesion of 2.50 kPa. In addition to the soil nonlinearity, **contact nonlinearity** is also considered by defining frictional and separable contact between the soil and the foundation. Thus, sliding, uplifting, and gapping between the soil and the foundations are taken into account.

A 10% **structural damping** is applied to all materials. This damping definition is active in the frequency domain (steady-state dynamic) analysis. In the time domain, the damping definition is replaced by **Rayleigh damping** using $\alpha_R = 2.356$ and $\beta_R = 0.00079577$, where the former is the factor for mass proportional damping and the latter is the one for stiffness proportional damping. The two values are chosen to provide approximately the same energy dissipation in the frequency range of [5, 20] Hz as the 10% structural damping.

Ricker wavelets are used as a time function of the transient excitation. In *case*

TABLE 5.1: The material properties considered for the verification study of the SFTD.

Region	λ (MN/m^2)	μ (MN/m^2)	ν	ρ (kg/m^3)
Ω_0 & Ω_1 (*case 1*)	132.00	66.00	1/3	1 650
Ω_0 & Ω_1 (*case 2*)	2 688.00	1 344.00	1/3	2 100
Foundations and structure	6 666.67	10 000.00	0.20	2 500

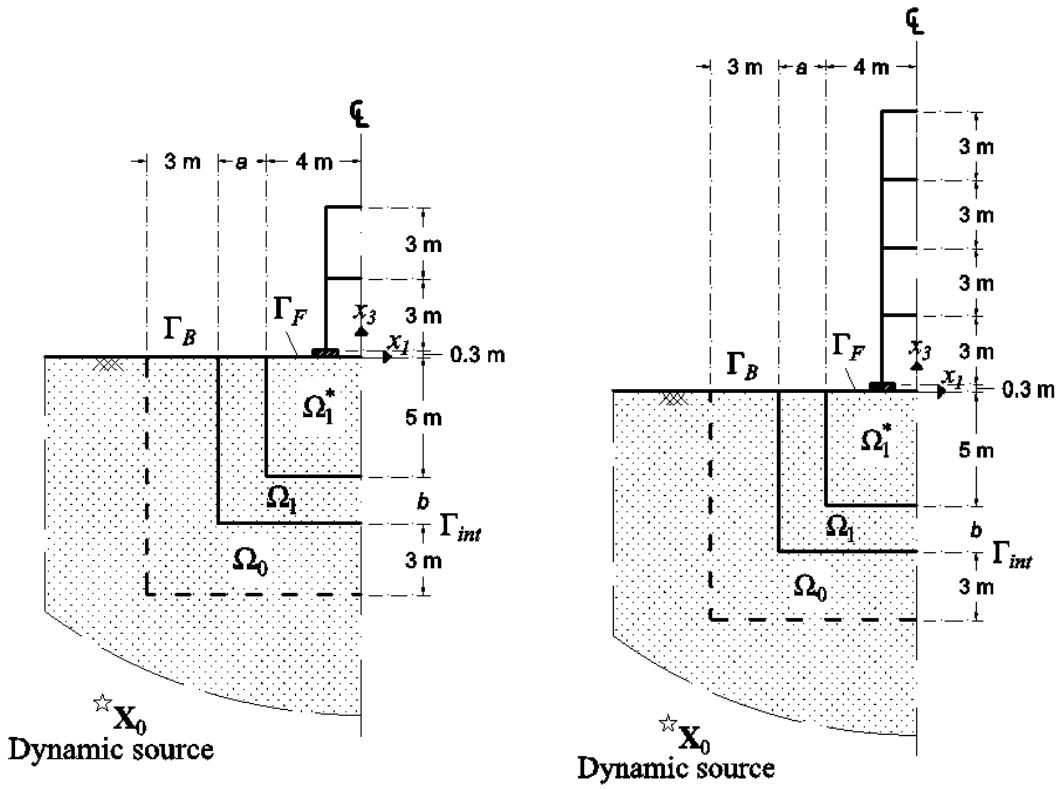

FIGURE 5.3: Sketches of the model used for the verification study presenting a multi-storey building resting on a semi-infinite half-space: (**A**) *case 1* and (**B**) *case 2*. All features in the sketch are symmetrical along the centerline except for the dynamic source at $\mathbf{X}_0$.

1, the main frequency is 5 Hz, the time delay is 0.5 s, the time interval is 0.0117 s, and the frequency resolution is 0.1953 Hz, while in *case 2*, the values are 4 Hz, 0.4 s, 0.01 s, and 0.167 Hz, respectively, see Figure 5.4. Due to the low wave velocity in case 1, a **transfer function** is applied to the wavelet so that the arriving waves will be within the time window of the simulation, which is approximately 5.9 s long. The transfer function is computed for a depth of 1 km, i.e., the depth of $\mathbf{X}_0$, and it results in an advancement of approximately 3.5 s of the main wave and a shift in the frequency range of the wavelet (Figure 5.4b). The amplitude vectors of the excitation are $f_i^{(\Omega_0)}(10^{13}$ N, 0, 0) and $f_i^{(\Omega_0)}(10^{12}$ N, 0, 0) for *case 1* and *case 2*, respectively.

Three types of geometry are considered to examine the influence of the buffer zone size on the stress compatibility condition along Γ_{int} and the structure's response. The size of the buffer zone is governed by the notations *a* and *b* in Figure 5.3, which values are laid out in Table 5.2. The numerical models of *case 1* with the geometry of type 2 and type 3 are presented in Figure 5.5 and 5.6,

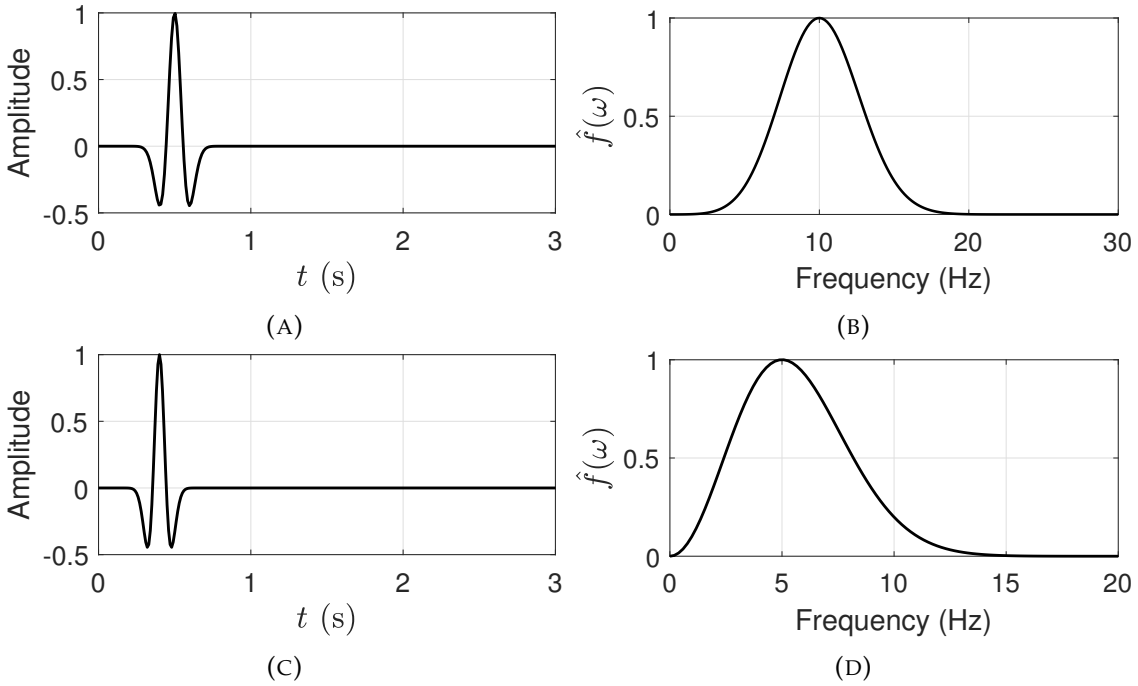

FIGURE 5.4: Ricker wavelet time histories and their (normalized) amplitude spectra used for *case 1* in (**A**) and (**B**) and *case 2* in (**C**) and (**D**). The amplitude spectrum presented in (**B**) is obtained after application of a transfer function, which is computed for the depth of $\mathbf{X}_0$.

TABLE 5.2: Values of dimensions a and b in Figure 5.3.

	Type of geometry		
Dimension	1	2	3
a (m)	2.00	5.00	14.00
b (m)	2.00	2.00	13.00

respectively. The element sizes of the BE and FE meshes of the soil model are $\lambda_S/6.67$ and $\lambda_S/10$, respectively, for *case 1* and a frequency of 20 Hz. In the time domain part of the sequential analysis, the BE meshes, i.e., the substructures, are omitted.

In this study, 8-nodes brick (hexahedral) elements with 8 integration points, i.e., C3D8 element in ABAQUS, are used for the buffer zone. Three elements are chosen as the object of observation to quantify **the compliance of the stress values** along Γ_{int}. In each of these elements, four integration points closer to Γ_{int} are considered for observation of stress and the calculation of MSE and MAE.

A geostatic step and **a static loading step** are inserted. In the geostatic step, a predefined stress field is applied to the soil model to define the geostatic stress.

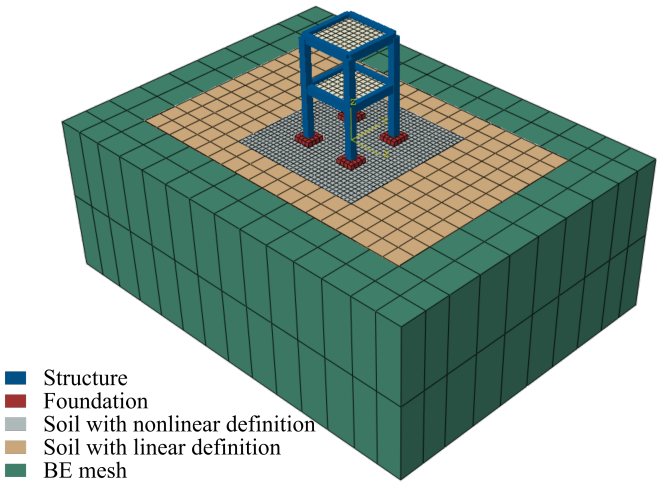

FIGURE 5.5: Numerical model of *case 1* showing the geometry of *type 2*. The BE mesh is omitted in the time domain part of the sequential analysis.

An overburden distributed load of 10 kPa is applied to avoid zero confining pressure on the solid elements of the soil model on the surface. The stresses due to this overburden pressure is also included in the predefined field to create a balance of internal-external forces. In the static loading step, gravity load is applied to the structural members, i.e., the foundations, the columns, the beams, and the slabs. In *case 1*, an additional distributed load of 5 kPa (500 kg/m^2) is assigned on the concrete slabs to represent the live load. In *case 2*, the distributed load is increased to 25 kPa. Additionally, masses of 1000 kg are assigned to beam-column joints in the model of *case 2*.

The implicit dynamic solver, see Section 2.5, is used for the time domain part of the sequential analysis. The maximum time increment is set to be the same as the time interval of the velocity time histories so sufficient details of the response can be captured.

To establish a reference model, a sequential analysis is performed **without any material and contact nonlinearities**. In this case, the soil-foundation interface is defined using tied contact, i.e., relative displacement and separation are not allowed. Comparisons of the stress components between the frequency domain result and the sequential analysis result of the model with the geometry of *type 1* at two integration points without nonlinearities are presented in Figure 5.7. The *MSE*s and *MAE*s for the time window of [0.2, 2.6] s are given in Table 5.3. Note that for the calculation of *MSE* and *MAE*, the time points of the outputs of the frequency domain are synchronized to one of the sequential analyses, and the

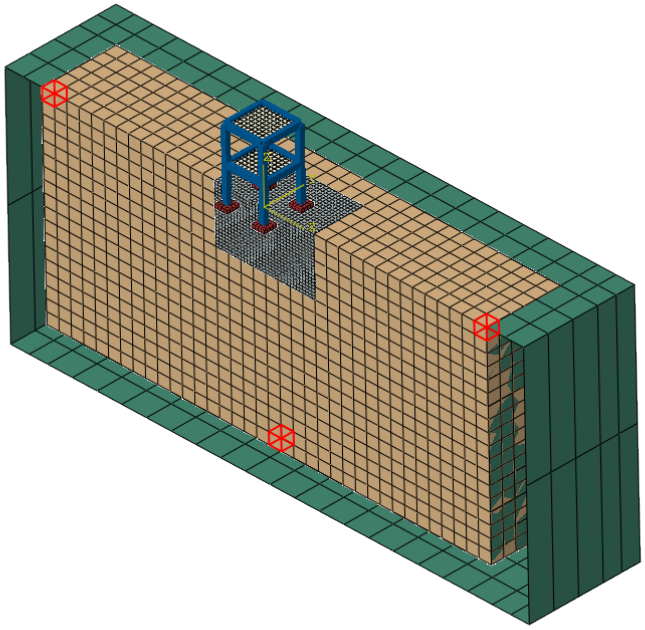

FIGURE 5.6: The elements under observation, marked with bounding red lines, are shown in the cut view of the model of *case 1* with the geometry of *type 3*.

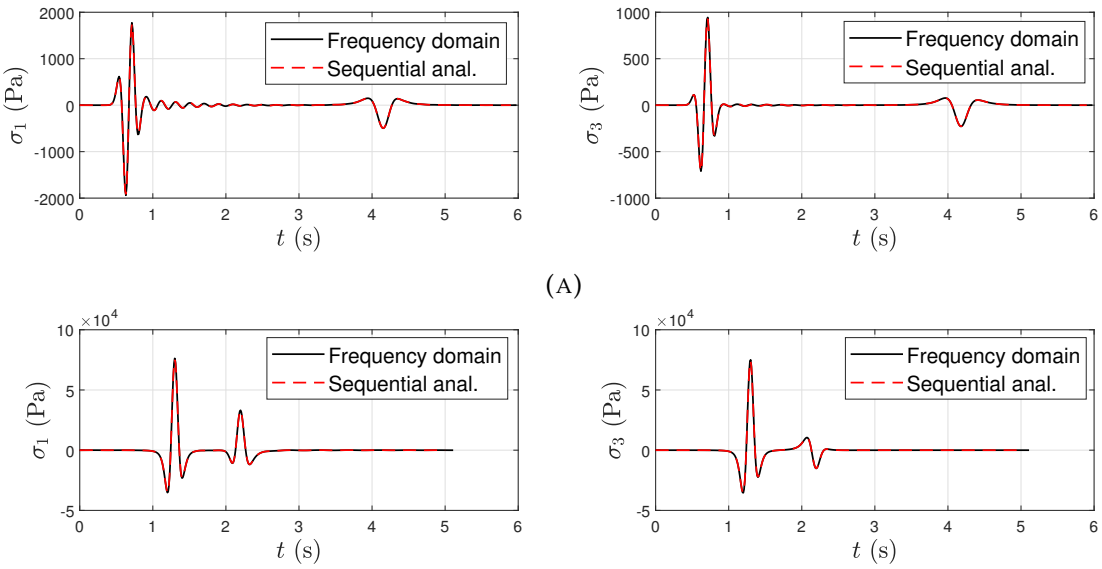

(A)

(B)

FIGURE 5.7: Comparisons of stress components σ_j between the results for the hybrid model with the geometry of *type 1* in the frequency domain and for the sequential analysis without nonlinearities. The material properties are those of *case 1* in (**A**) and *case 2* in (**B**).

amplitudes are interpolated correspondingly.

Figure 5.8 compares the stress components between the frequency domain

TABLE 5.3: *MSE*s and *MAE*s for the model with the geometry of *type 1* and material properties of *case 1* and *case 2* when the nonlinearities are not included.

	MSE (%)		*MAE* (%)	
Case	σ_1	σ_3	σ_1	σ_3
Case 1	2.40E-3	1.80E-3	0.264	0.208
Case 2	7.19E-4	5.32E-4	0.105	0.101

TABLE 5.4: *MSE*s and *MAE*s of the stress components of the sequential analysis relative to the frequency domain analysis. Material properties of *case 1* and the nonlinearities are considered.

	Type of geometry					
	Type 1		Type 2		Type 3	
Error	σ_1	σ_3	σ_1	σ_3	σ_1	σ_3
MSE (%)	0.707	0.228	0.119	0.145	0.012	0.090
MAE (%)	6.858	4.399	3.132	3.120	0.559	0.498

TABLE 5.5: *MSE*s and *MAE*s of the stress components of the sequential analysis relative to the frequency domain analysis. Material properties of *case 2* and the nonlinearities are considered.

	Type of geometry					
	Type 1		*Type 2*		*Type 3*	
Error	σ_1	σ_3	σ_1	σ_3	σ_1	σ_3
MSE (%)	0.518	0.052	0.013	0.069	5.35E-4	0.001
MAE (%)	4.224	1.763	0.918	1.527	0.113	0.151

result and the sequential analysis result of the model with material properties of *case 1*, with three types of geometry, and with all nonlinearities included. The same comparison for case 2 is given in Figure 5.9. The *MSE*s and *MAE*s for the time window of [0.2, 5.0] s of *case 1* and *case 2* are given in Table 5.4 and Table 5.5, respectively. In Figure 5.8a alone, the *MAE*s of σ_1 and σ_3 are approximately 10.6% and 5.3%, respectively. The values are 12.6% and 3.6% for Figure 5.9a. These figures show the results for a Gauss-point of the element located on the right side in Figure 5.5, i.e., behind the structure when considering the ray path. The errors are significantly lower in the other observed elements, thus, the lower total *MAE*.

To reveal the influence of the stress discrepancies along Γ_{int} to the structure's response, the relative displacements of an observation point on the roof are compared considering the three types of geometry. The comparisons of the relative displacements for *case 1* are presented in Figure 5.10 while those for *case 2* are

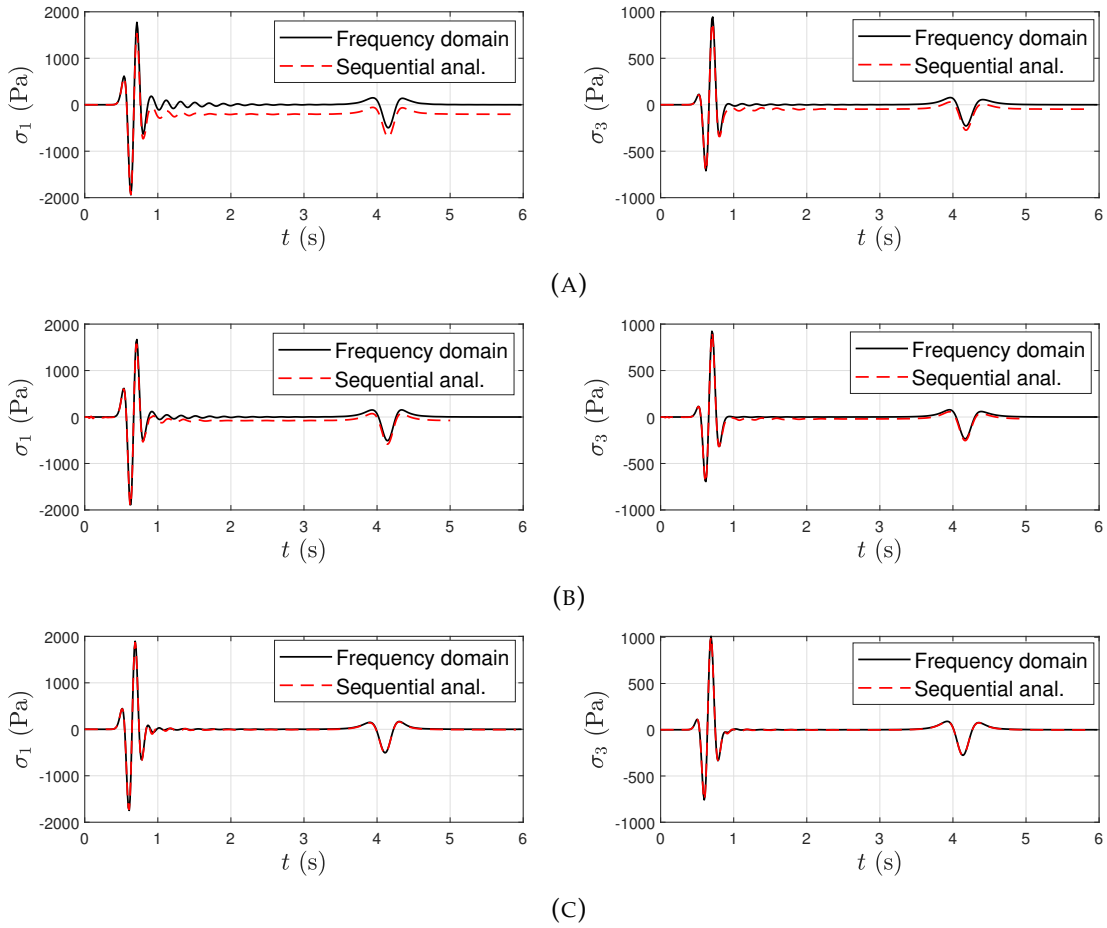

FIGURE 5.8: Comparisons of stress components σ_j between the results for the hybrid model in the frequency domain and for the sequential analysis with the nonlinearities. Three types of geometry and material properties of *case 1* are considered. (**A**) Geometry of *type 1*, (**B**) geometry of *type 2*, and (**C**) geometry of *type 3*.

shown in Figure 5.11. The *MSE*s and *MAE*s are presented in Table 5.6 and Table 5.7 for *cases 1* and *2*, respectively. The displacements for the model with the geometry of *type 3* are used as references since Figures 5.8-5.9 and Tables 5.4-5.5 show that these results comply very well to the stress compatibility and equilibrium condition. These results show that the negative influence of the stress discrepancies along Γ_{int} on the structure's response is relatively small, especially in the case of soft soil. The buffer zone size has more effect on the accuracy of the structure's response when soil with high stiffness is considered. It can be observed that a medium-sized buffer zone (geometry of *type 2*) is sufficient to obtain satisfactory results.

The effect of the material and contact nonlinearities on the structure's response in the particular soil-structure system of *case 1* is illustrated in Figure 5.12. It can be observed that the nonlinearities reduce the amplitude and the natural

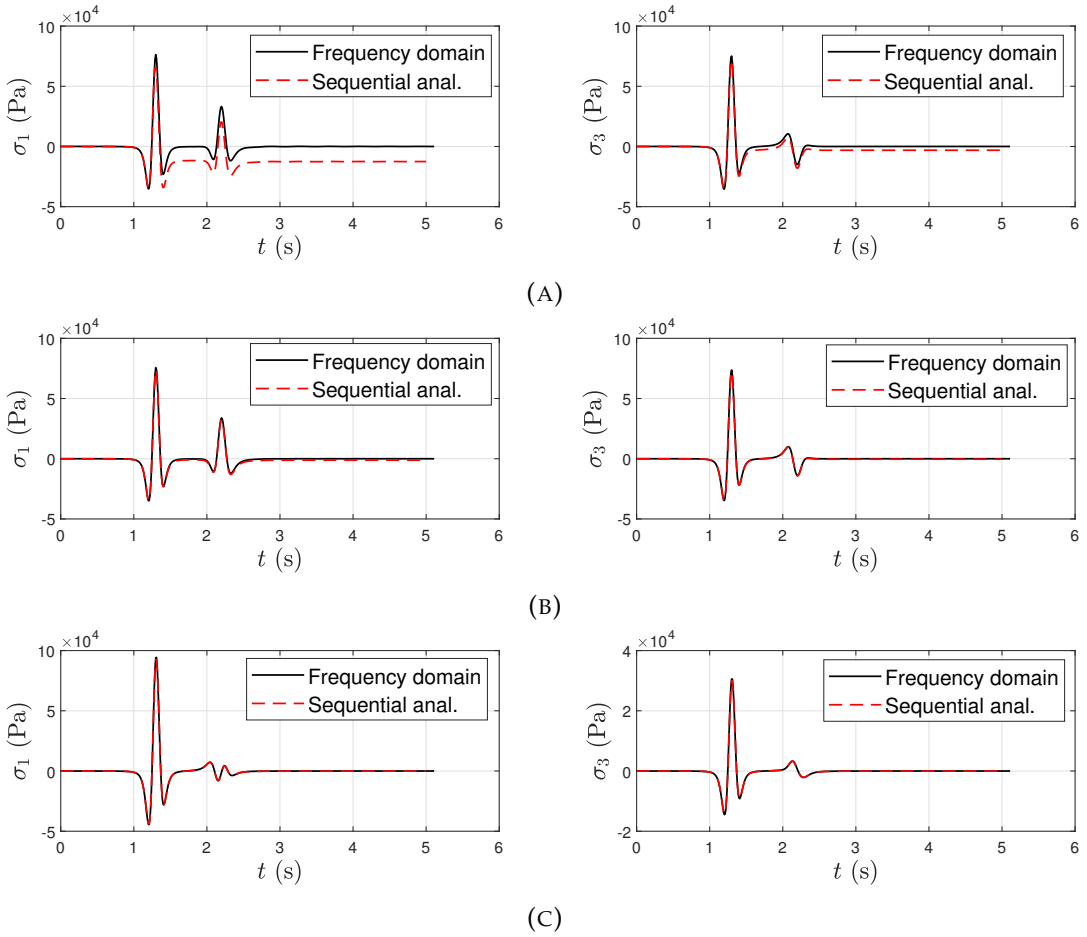

FIGURE 5.9: Comparisons of stress components σ_j between the results for the hybrid model in the frequency domain and for the sequential analysis with the nonlinearities. Three types of geometry and material properties of *case 2* are considered. (**A**) Geometry of *type 1*, (**B**) geometry of *type 2*, and (**C**) geometry of *type 3*.

frequency of the system. Due to sliding, a permanent horizontal displacement is observed in Figure 5.12a.

The elapsed computation time for *case 1* with three types of geometry is presented in Table 5.8. One hundred twenty discrete frequencies are computed for the frequency domain solution. The workstation and the software used for the computation are described in Section 4.7. It is shown in the table that even for the geometry of *type 3*, material properties of *case 1*, and a frequency range such as in Figure 5.4b, a reasonable computation time can still be achieved.

The results show that the nonlinear dynamic SSI can be simulated by extending the developed frequency domain procedure and modifying the boundary conditions of the finite model. Thus, other developed enhancements, such as

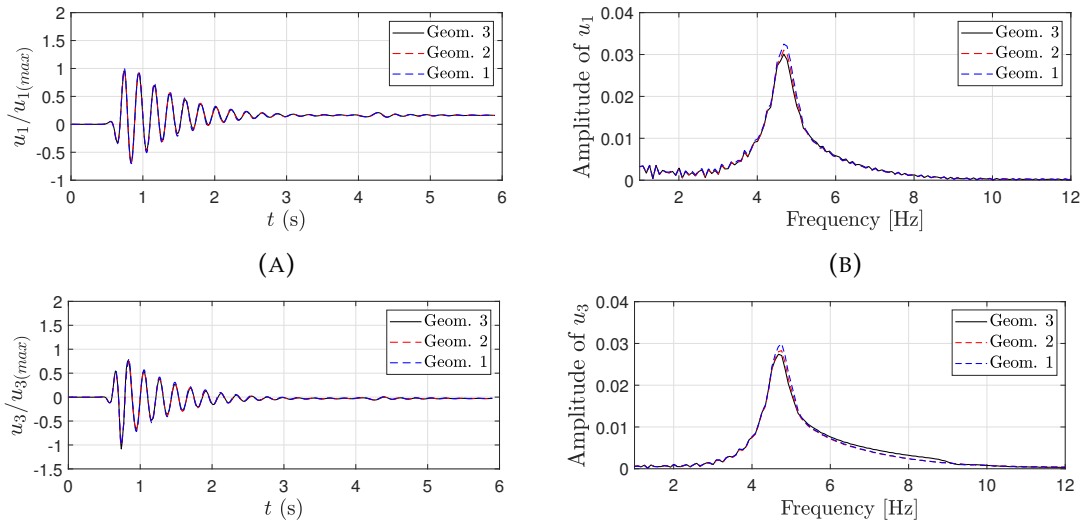

(A) (B) (C) (D)

FIGURE 5.10: Comparisons of normalized displacement components u_j of an observation point in the roof relative to its base between the results for the model with the geometry of *type 3* and the other types of geometry: (**A**) and (**C**) displacement time histories and (**B**) and (**D**) Fourier amplitudes. Material properties of *case 1* and the nonlinearities are considered.

TABLE 5.6: *MSE*s and *MAE*s of the displacements of an observation point in the roof relative to its base for the model with geometry of *type 1* and *type 2* vs the model with the geometry of *type 3*. Material properties of *case 1* and the nonlinearities are considered.

	Type of geometry			
	Type 1 vs type 3		Type 2 vs type 3	
Error	σ_1	σ_3	σ_1	σ_3
MSE (%)	0.029	0.044	0.077	0.022
MAE (%)	1.041	1.272	0.567	0.709

TABLE 5.7: *MSE*s and *MAE*s of the displacements of an observation point in the roof relative to its base for the model with the geometry of *type 1* and *type 2* vs the model with the geometry of *type 3*. Material properties of *case 2* and the nonlinearities are considered.

	Type of geometry			
	Type 1 vs type 3		Type 2 vs type 3	
Error	σ_1	σ_3	σ_1	σ_3
MSE (%)	0.428	0.155	0.047	0.036
MAE (%)	4.939	2.508	1.532	1.177

the LWC method, remain applicable. The accuracy and compliance of the compatibility conditions can be achieved by providing sufficient distance between the

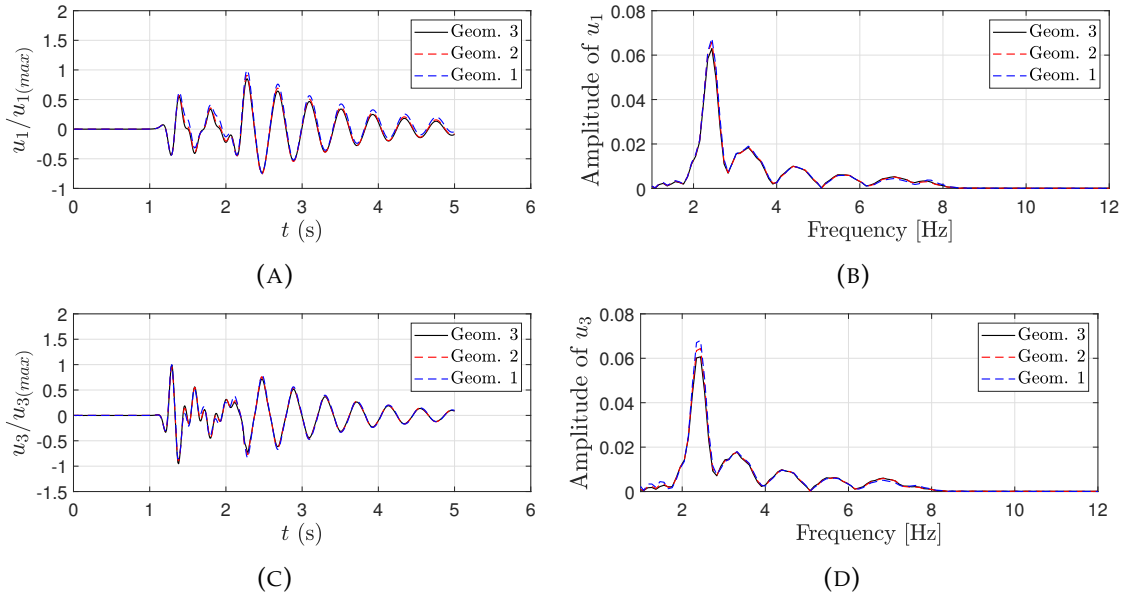

FIGURE 5.11: Comparisons of normalized displacement components u_j of an observation point in the roof relative to its base between the results for the model with the geometry of *type 3* and the other types of geometry: (**A**) and (**C**) displacement time histories and (**B**) and (**D**) Fourier amplitudes. Material properties of *case 2* and the nonlinearities are considered.

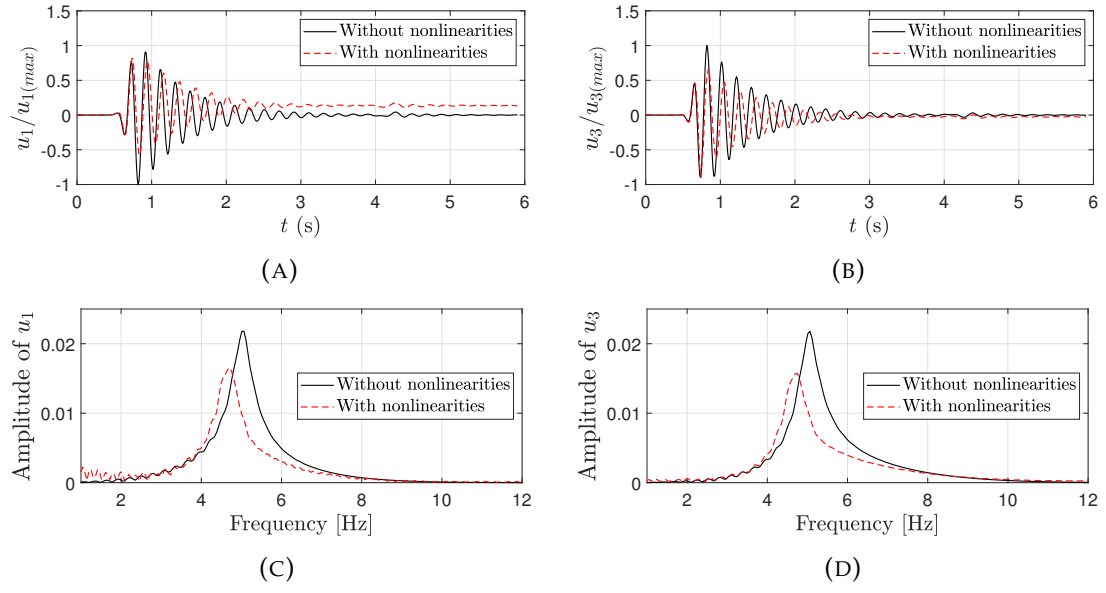

FIGURE 5.12: Comparisons of displacement components u_j of an observation point on the roof relative to its base between the results for the model without and with the nonlinearities. Material properties of *case 1* and the geometry of type 2 are considered. (**A**) Normalized displacement u_1, (**B**) normalized Fourier amplitude of u_1, (**C**) normalized displacement u_3, and (**D**) normalized Fourier amplitude of u_3.

TABLE 5.8: Elapsed computation time for the hybrid model of *case 1* using the sequential analysis when the nonlinearities are included. All units are in minutes.

Geometry	BEM computation	Substructure generation	Global SSD solution	TD solution
Type 1	3	8	28	44.2
Type 2	5	21	32	46.4
Type 3	25	90	58	56.2

source of nonlinearities and the BE-FE interface. The drawback of this approach is that it is not applicable to cases with widespread nonlinearities, such as liquefaction cases. Since a frequency domain computation needs to be finished before the time domain one, it also tends to be more expensive for problems with a short duration of excitation, e.g., explosion analysis. However, it is advantageous for problems with mild or medium nonlinearities and long excitation duration. It is also shown that the state of the soil and the structural members can be represented realistically since geostatic and static loading steps can be inserted seamlessly. Other advantages are that there is no additional iteration required, and it can be applied directly to existing commercial FEM software without creating an additional controller.

5.5 Chapter summary

In this chapter, the idea of using sequential computations to solve SSI problems with nonlinearities and its modification to overcome numerical differentiability problems are detailed. Numerical experiments of a simple structure considering soft and hard soils show that the method has advantages and limitations.

This chapter is followed by four chapters describing different practical application examples. Applications of the sequential frequency-time domain procedure for 2D and 3D dynamic SSI problems are presented in Chapter 9.

Chapter 6

Application I: Dynamic behaviour of typical integral bridges

6.1 Chapter overview

This chapter discusses the application of the hybrid BEM-FEM for a case study of the dynamic behavior of typical integral bridges. This chapter demonstrates the versatility of the hybrid method, including the numerical enhancements described in Chapter 3, particularly when the dynamic load is applied from within the FE region, see equation (3.20). Integral bridge concept is of great interest due to its intensive soil-structure interaction. The problem is described through general and mathematical perspectives in Section 6.2, followed by a discussion of the modeling approach in 6.3 and the results in Section 6.4. The content of this chapter is published in H.D.B. Aji, M. Basnet, F. Wuttke (2020). "A numerical study on the influences of underlying soil and backfill characteristics on the dynamic behaviour of typical integral bridges". In: *Bauingenieur* 95.11, pp. 2-11. DOI:10.37544/0005-6650-2020-11-35.

6.2 Introduction and problem description

The integral bridge concept was developed to overcome the maintenance and performance problems caused by the degradation or failure of movable joints and bearings. Despite its role in eliminating or reducing the stresses due to lateral movement and forces, joints and bearings are commonly not durable, less redundant, and expensive to maintain. Their non-performance can lead to collateral damages (Moehle and Eberhard, 2003; Waldin, Jennings, and Routledge, 2012). The integral concept is realized by building the superstructure monolithically with its supporting substructure, i.e., abutments or piers, thus, eliminating

the need for joints or bearings. Although studies showed that the application of integral bridge concept can have advantages, such as economically better in the initial and long-term phases, better performance during earthquake, simpler construction and better vehicular experience (Arsoy, Barker, and Duncan, 1999; Aji, 2014), its behaviour is not fully understood and agreed by members of scientific community, engineers as well as regulators.

One of the distinct points of the behaviour of integral bridges is the **strong soil-structure interaction**, which occurs due to the bridge's structural members' continuity and contact with the adjacent backfill and underlying soil. This is particularly more significant in the case of short-span or high-stiffness superstructure. From the standpoint of dynamic-resistant design, the integral bridge dynamic characteristic, quantified through the system's natural frequencies and damping ratio, cannot be assessed in the same manner as non-integral ones.

Studies regarding the influence of soil-structure interaction on the dynamic response of bridges can be found in Werner, Beck, and Levine, 1987; Werner, Beck, and Nisar, 1990; Wilson and Tan, 1990, among others. In Goel, 1997 and Goel and Chopra, 1997, studies regarding the influence of abutments and soil nonlinearities can be found. A study by Martinez, Mateo, and Alarcon, 1996, using 3D BEM in the frequency domain, investigated the stiffness of vertical walls of abutment and wingwalls, in contact with embankment, without the contribution of the vertical resistance from the soil under the foundation of the abutment. A simplified method of abutment stiffness is sometimes preferred to reduce the computational burden, such as in Karantzikis and Spyrakos, 2000. Results of the numerical-analytical approach where the soil reactions are represented by a combination of translational and rotational springs can be found in Spyrakos and Loannidis, 2003, while a 3D time history FEM of a semi-integral bridge can be found in Barbosa and Silva, 2007. The sensitivity of the bridge's seismic response with respect to different bridge modeling approaches was studied by using FEM and nonlinear springs in Aviram, Mackie, and Stojadinovic, 2008. Later, more complex models were compared to simpler ones in Erhan and Dicleli, 2014 where, besides nonlinear hysteretic springs, dashpots and soil columns were used to model radiation damping and free-field motion of nearby soil, respectively. These studies showed that mode shapes, natural frequencies, ultimate base shear strength, and peak displacement were altered by the models. A study by Zangeneh Kamali, 2018, which combines field measurement as well as FEM and FEM-BEM results on short-span railway integral bridge, found that the effect of

surrounding soil on the response depends on the ratio between the flexural stiffness of the bridge and the dynamic stiffness of the foundation-soil system and to the ratio between the resonant frequency of the soil layer and the fundamental frequency of the bridge. The study also showed the modeling limitation currently experienced by the existing available numerical procedure, which may affect the accuracy of the computation.

In this study, the developed 3D hybrid BEM-FEM approach is taken to assess **the influence of the underlying soil and backfill material properties to the dynamic behaviour of typical integral bridges**, expressed by the resonance frequencies of the coupled system, and comparison to the results obtained via the conventional method, where a combination of encastré grounding and frequency-independent springs is used, are presented. Four typical single-span integral abutment bridges are analysed in a steady-state dynamic manner for this study. In addition, the effects of deck length and curved alignment are also explored. The current study is focused on the identification of dynamic characteristics of the bridge-soil system, which is active during the daily operation of the bridge rather than the ultimate capacity. Thus, material and geometric nonlinearities are not considered.

The bridge superstructure, abutments, and the backfill behind the abutments are modeled by using the finite element method, which is chosen due to its modeling accessibility, extensive element library as well as its efficiency in modeling complex structural systems in the finite domain. On the other hand, the underlying soil is computed using the BEM, which can account for the dynamic problem of the unbounded domain and satisfy Sommerfeld's radiation condition in the far-field zone.

The decomposition of the problem domain is as follows. Let us consider a coupled system in Figure 6.1. An elastic isotropic semi-infinite geological region is denoted as Ω_0 with boundary of $\Gamma_{\Omega_0} = \Gamma_B \cup \Gamma_{int}$ and material properties of C_{P_0} & C_{SV_0}, which are the longitudinal and shear wave velocities. The boundary Γ_B is the free-surface of Ω_0 whilst the Γ_{int} is the contact interface between Ω_0 and Ω_1. The Ω_1 is the finite continuum with surface Γ_S and material properties C_{P_1} & C_{SV_1}. Thus, Ω_0 represents the surrounding media up to the far-field region while Ω_1 represents the structure and can include a near-field object such as, in this case study, soil backfilling. The computation of the integral bridge models using hybrid BEM-FEM follows the procedures described in Section 2.6, see Figure 2.9.

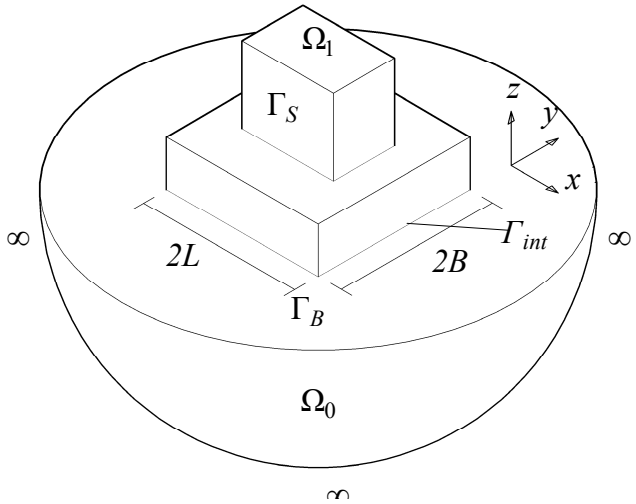

FIGURE 6.1: Illustration of a soil-structure interaction problem using 3D hybrid BEM-FEM.

6.3 Simulation and parametric analysis

To evaluate the influence of deck length and curved alignment, **4 typical integral bridges** are modeled. These are typical overhead crossing, single-span concrete integral bridges with monolithic superstructure-abutment joints resting on a half-space shown in Figure 6.2. The deck lengths are chosen as 35 m & 45 m, which are then cross-combined with alignment sets of straight and curved, the latter with a radius of 400 m, see Table 6.1. Other geometrical dimensions are kept constant: the width of the bridge is 12 m; the abutment height and thickness are 7.6 m and 0.5 m, respectively, with wingwalls extending to 1 : 1 slope; the superstructure consists of a 30 cm thick deck, and 5 T-girders distanced at 2.5 m with 1.6 m height and 1.0 m high diaphragm.

TABLE 6.1: The bridge models.

No.	Span length (m)	radius of curvature (m)
1	35	∞
2	35	400
3	45	∞
4	45	400

Two numerical approaches are utilized to illustrate the effect of modeling on dynamic identification: (1) **a hybrid BEM-FEM approach** and (2) **a conventional approach** where encastré groundings, i.e., fixed restraints, are applied along the bottom center-line of the abutment, i.e., perpendicular to the traffic direction, and frequency-independent springs are applied to the walls of the abutment and

TABLE 6.2: The material properties of the soil considered in the simulation.

No.	C_{SV} (m/s)	ρ (kg/m^3)	μ (MPa)
1	100	1650	16.50
2	250	1800	112.50
3	375	1840	258.75
4	500	1890	472.50

wingwalls to represent the passive soil resistance, see Figure 6.2b. In the hybrid numerical approach, the backfills are modeled as a continuum and included in the FE subdomain, while it is left out of the numerical model in the conventional one. In both approaches, the deck-diaphragm-girder system of the superstructure is meshed using integrated beam and shell elements. The abutments and the wingwalls are discretized using continuum elements. As a result of the far-field computation, the BEM substructure is directly attached to the continuous surface formed behind the wingwalls and backfills and under the spread footings. In Figure 6.2c, the BE subdomain prior to condensation is the green-colored surfaces.

The concrete properties of the bridge are as follows: Young's modulus of 300 GPa, Poisson's ratio of 0.2, and density of 2400 kg/m^3. The underlying soil and backfill materials considered for the parametric analysis are laid out in Table 6.2, where μ is the shear modulus. Poisson's ratio of 1/3 is assigned for all soil materials. The interface between the structure and backfill is frictional, with a friction angle of 20°. The interface between the FEM and BE subdomains is of tied constraint. For the study of the influence of the underlying soil, the properties no. 2 of Table 6.2 are assigned to the backfill, while the properties of the underlying soil are varied. For the study of the backfill's influence, the properties no. 2 are assigned to the underlying soil, and the properties of the backfill are varied.

In the conventional model, **the spring values** are computed following the lateral passive earth pressure according to *Eurocode 7* 2004 using the following assumptions: (1) the density of the soil is 18 kN/m^3; (2) the mode of wall movement is rotational one (type "a" of Table C.2 in *Eurocode 7* 2004); (3) the calculation is based on the 1.1% wall rotation to generate half mobilised passive resistance ($0.5\sigma_P$) of dense soil (Table C.2 of *Eurocode 7* 2004); (4) the passive earth pressure coefficient is calculated based on Figure C.2.1 of *Eurocode 7* 2004 with soil internal friction angle taken as 30° and the soil-wall friction angle taken as 20°.

For the conventional approach, the system identification is performed using

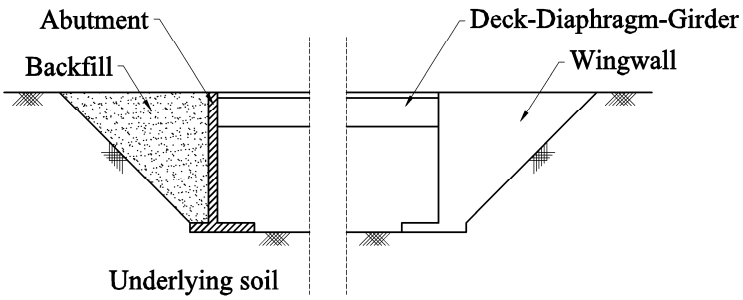

(A)

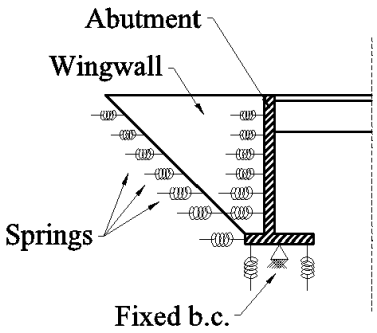

(B)

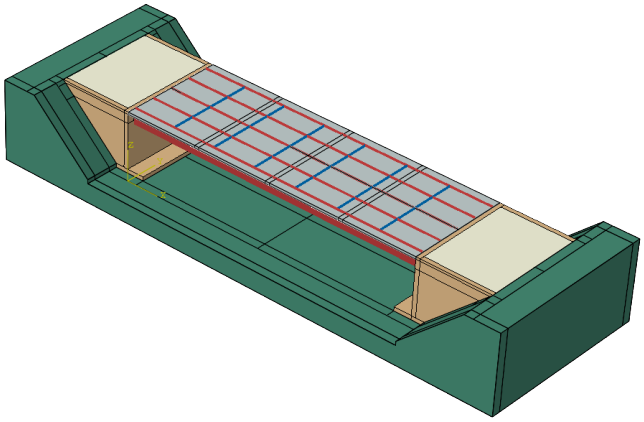

(C)

FIGURE 6.2: The integral bridge under consideration: (**A**) an illustrative cross section of the hybrid BEM-FEM approach, (**B**) an illustrative cross section of the conventional approach, and (**C**) an isometric view of bridge model 1 using BEM-FEM, where the BEM region is green-colored.

eigenfrequency extraction while in the hybrid simulations, the resonant frequencies of the coupled system are generated by applying **one- or multi-directional distributed load** located at the deck. Six mode shapes that are considered in this study are shown in Figure 6.3 for bridge model 4. For example, mode shape one

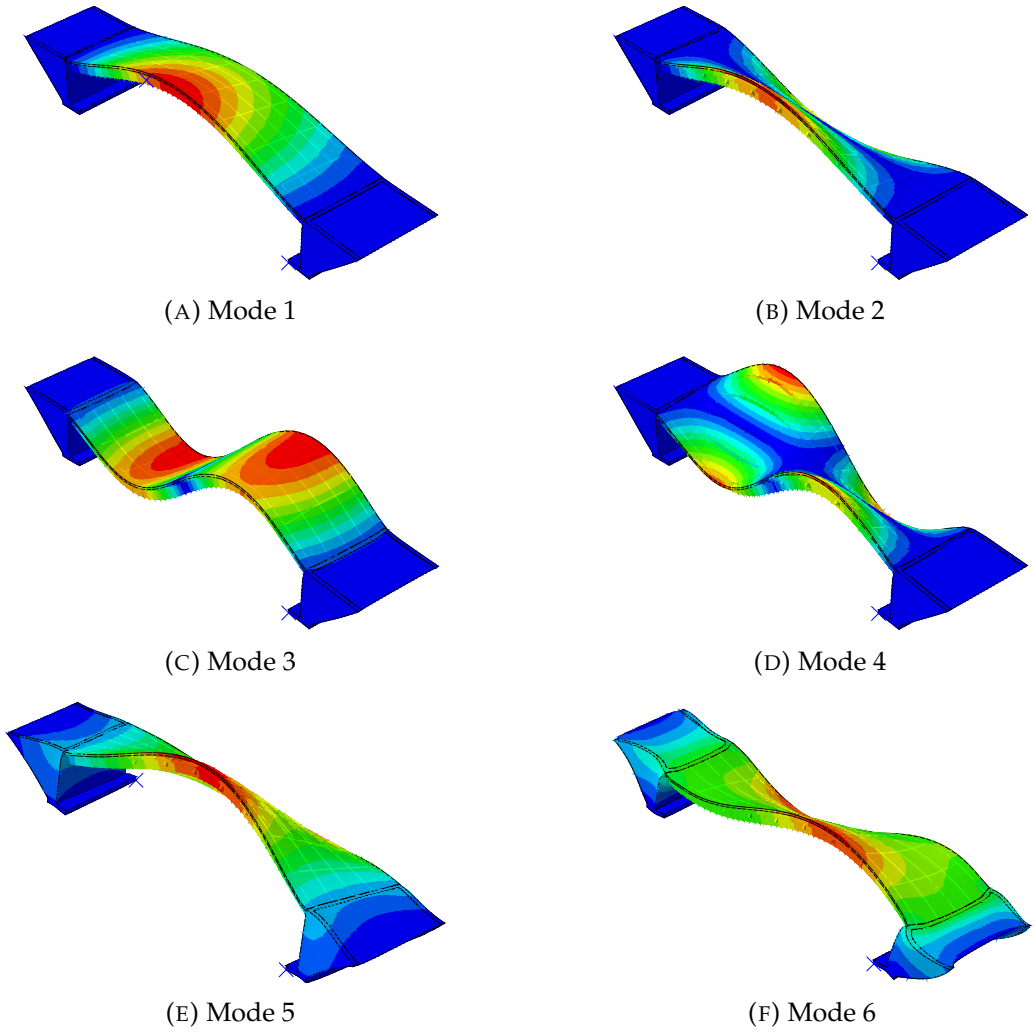

(A) Mode 1 (B) Mode 2

(C) Mode 3 (D) Mode 4

(E) Mode 5 (F) Mode 6

FIGURE 6.3: Six mode shapes of the integral bridge considered in this study, shown for bridge model 4.

is generated by uniform vertical distributed load while mode shape two is generated by the coupled left-right vertical distributed load. Load patterns 5 and 6 are horizontal uniform distributed loads in the transversal and longitudinal direction, respectively. The magnitude of the distributed load is 1 Pascal. In each activated mode shape, the displacement is measured at the degree of freedom and the point at the deck, which represents the maximum response consistently.

6.4 Results and discussion

The results for the simulations with varying underlying soil for each bridge model are presented in Figures 6.4, 6.5, 6.6, and 6.7. The results for simulations with varying backfill are shown in Figures 6.8, 6.9, 6.10, and 6.11. In these figures, the

natural frequencies for the corresponding mode shapes obtained from the conventional approach are presented as discrete plots and scaled for visibility. Load pattern five consistently generates two mode shapes: (1) rotational-dominant mode shape, found in the mode shape generated by load pattern 2 (Figure 6.3b), and (2) translational-dominant mode shape. No longitudinal translational mode shape was obtained from the conventional approach due to the fixed restraints used in the model.

For the bridge model with curved alignment, load pattern 1 generates two mode shapes with closely spaced resonant frequencies. These mode shapes are the 1^{st} and 2^{nd} mode shapes in Figures 6.3a and 6.3b, respectively. Comparing Figures 6.4 and 6.6, it can be seen that **the range of alteration of the resonant frequencies is lower on long-span bridge**. For load patterns 1, 2, and 5, where the same movement mode is shared between both abutments, softer underlying soil provides less restraining effect. Thus, lower resonant frequency and higher damping are observed. These restraining effect patterns are less clear in a shorter bridge for load patterns 3 and 4, where each abutment experiences different movement modes. However, the pattern of the damping alteration is still evident. An exception is found on the longitudinal mode shape generated by load pattern six, where the higher horizontal restrain from stiffer soil yields higher damping and frequency. The coupled system's responses due to the load patterns 1 to 4 are dominated by **the stiffness of the superstructure**. In contrast, the responses due to load patterns 5 and 6 are controlled by **the soil-structure interaction**, and thus, higher resonant frequencies alteration is observed from these load patterns.

In Figures 6.8 and 6.10, the damping effect coming from softer backfill is clear in load patterns 1, 2, and 4; the opposite effect is found in load patterns 5 and 6; and no significant effect found from the response to load pattern 3. In all considered mode shapes, the alteration of the resonant frequencies due to the backfill is less pronounced than the observed effect from the underlying soil. This is due to the role of the wingwalls, which stiffness is much higher than the considered backfill. Thus, **they dominate the force transfer from the superstructure to the underlying soil**. In the mode shapes 5 and 6, where higher soil-structure interaction is incorporated, the stiffer backfill provides higher damping.

These results highlight that the dynamic behaviour of a soil-structure system with strong SSI, such as those in integral bridges (or integral abutment bridges), is

highly dependent on the underlying soil properties and the structure's configuration itself. As shown in the figures, the numerical prediction of this dynamic behaviour depends on the type of method and model used to represent the problem. A relatively simple model with encastré grounding and frequency-independent springs can provide a rough estimation of the dynamic behaviour. The identified natural frequencies from such an approach can be taken with some safety margin. However, this approach is insufficient when a more accurate estimation of the system's natural frequencies and damping values is inquired, especially for those with strong SSI. In practice, the identification of the dynamic characteristic can significantly influence the design of the structure as well as the type of vehicles serviced by the structure.

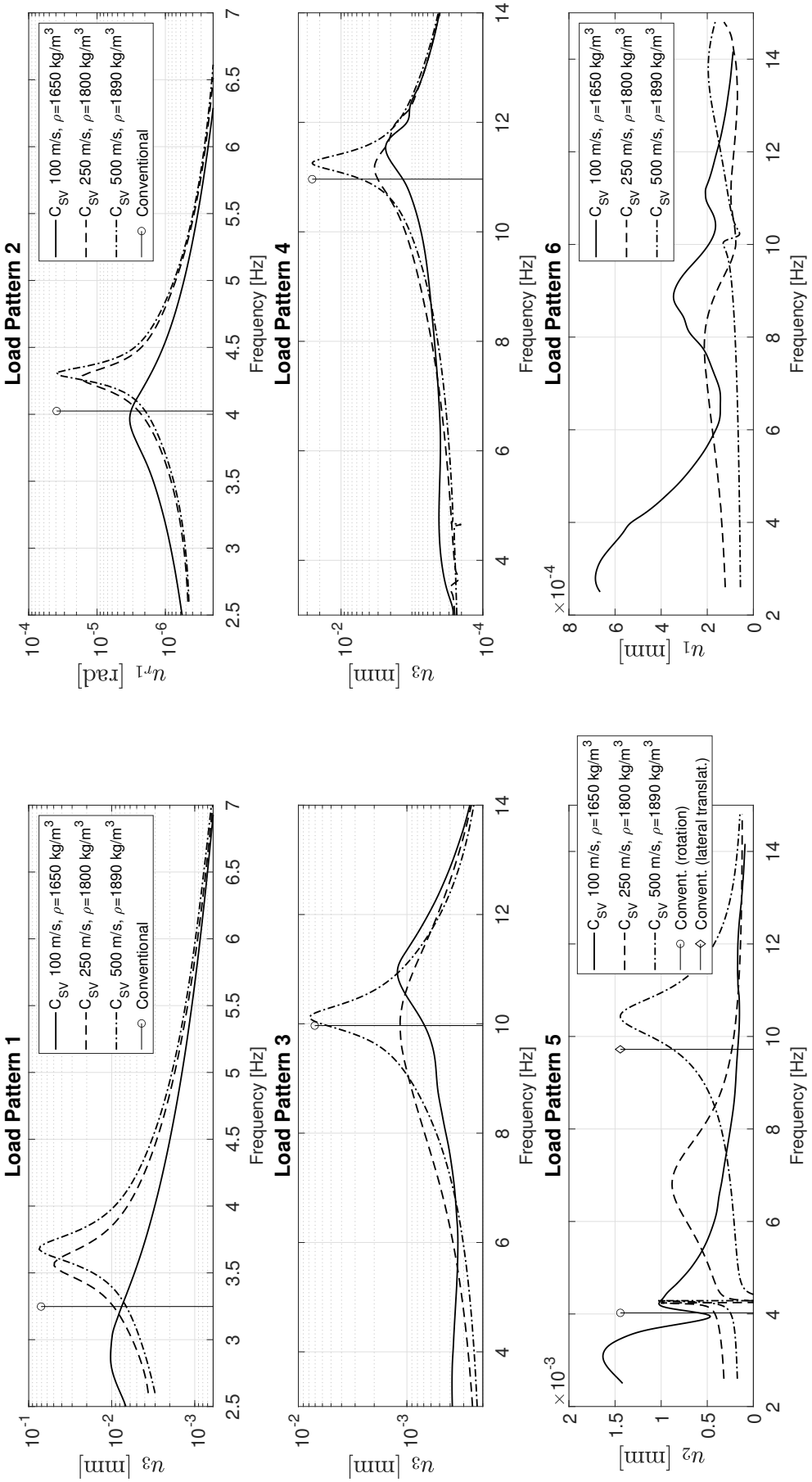

FIGURE 6.4: Comparisons of displacement response magnitudes for six load patterns for bridge model 1 (L=35 m, straight) with different underlying soil properties.

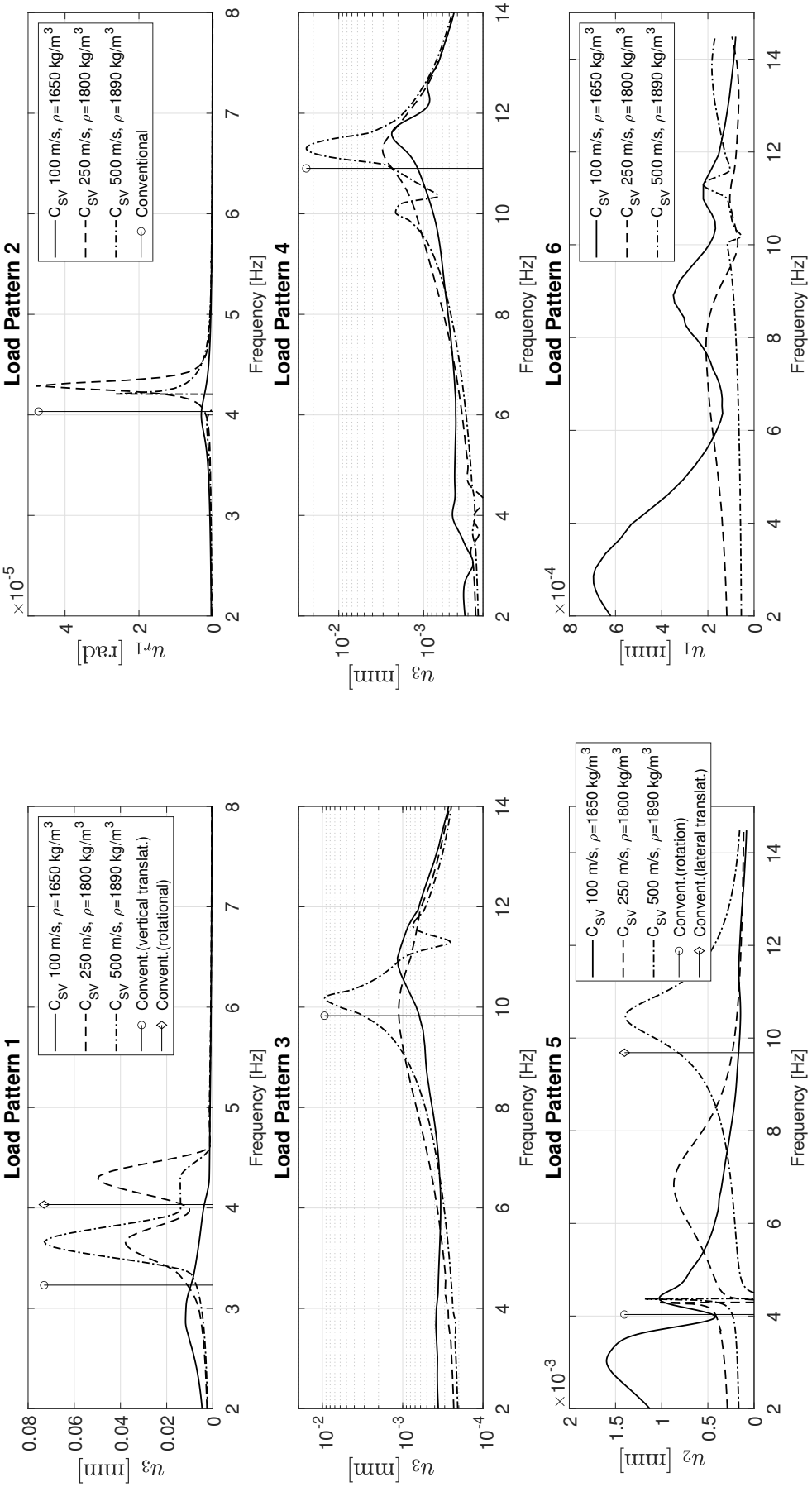

FIGURE 6.5: Comparisons of displacement response magnitudes for six load patterns for bridge model 2 (L=35 m, R=400 m) with different underlying soil properties.

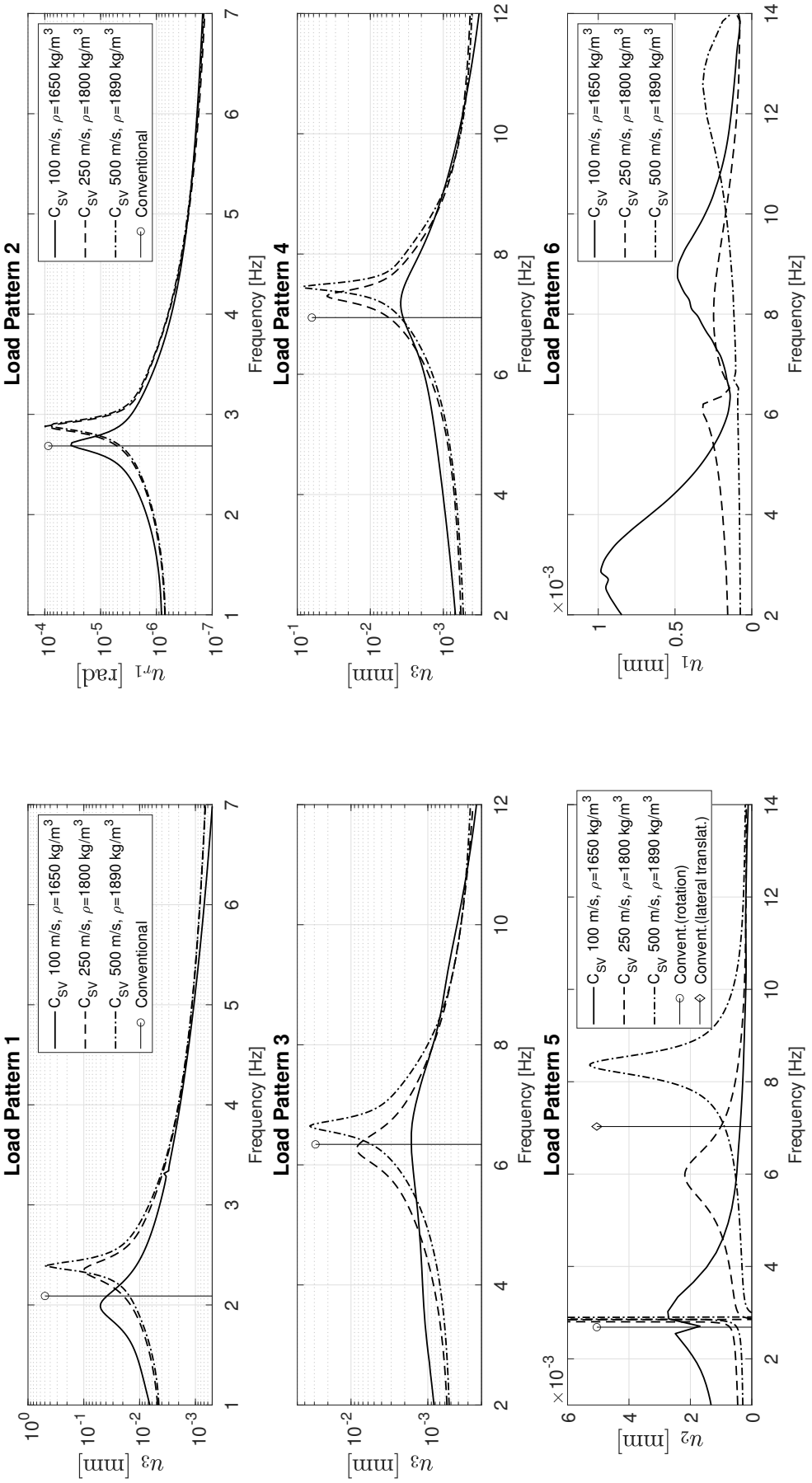

FIGURE 6.6: Comparisons of displacement response magnitudes for six load patterns for bridge model 3 (L=45 m, straight) with different underlying soil properties.

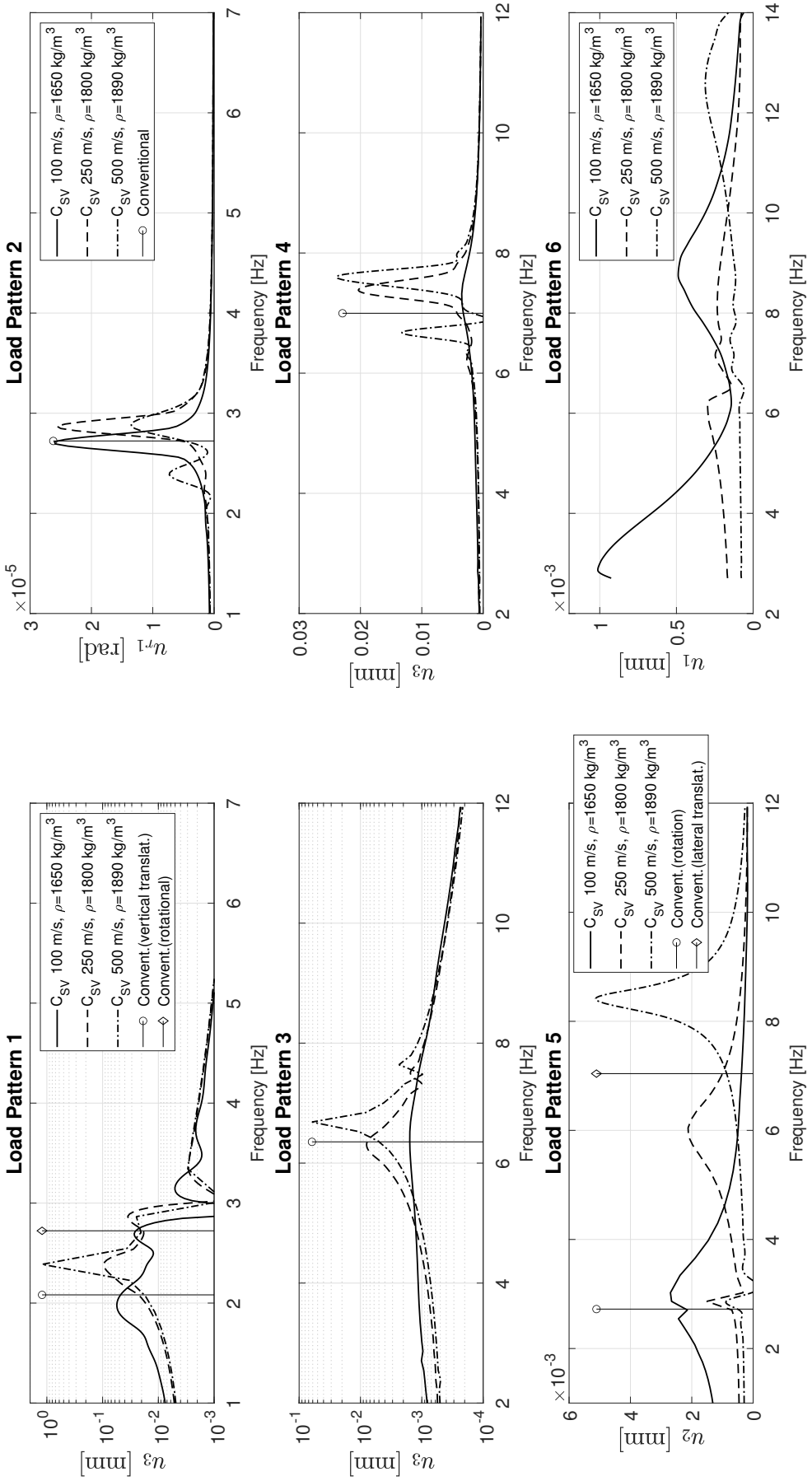

FIGURE 6.7: Comparisons of displacement response magnitudes for six load patterns for bridge model 4 (L=45 m, R=400 m) with different underlying soil properties.

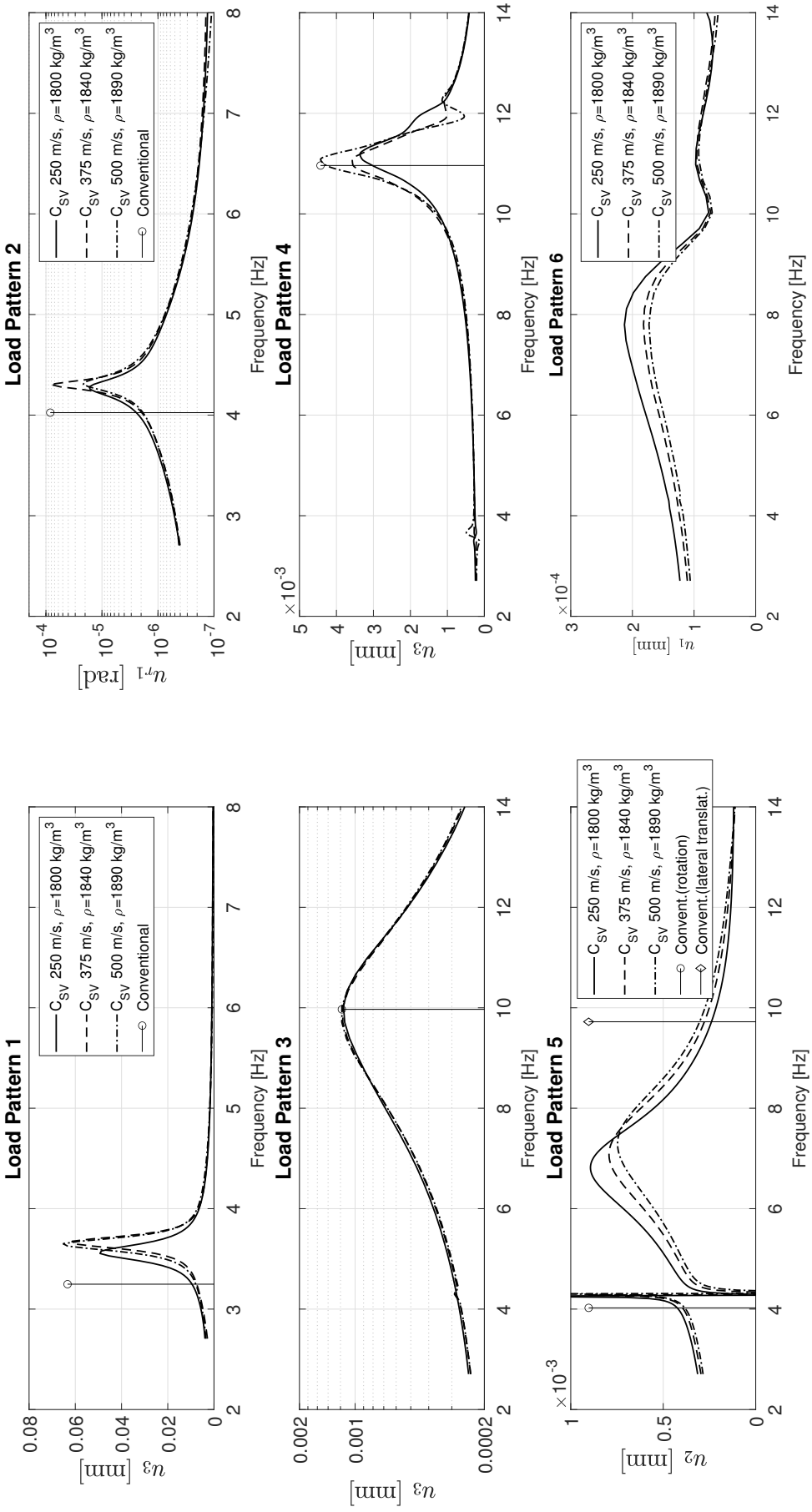

FIGURE 6.8: Comparisons of displacement response magnitudes for six load patterns for bridge model 1 (L=35 m, straight) with different backfill properties.

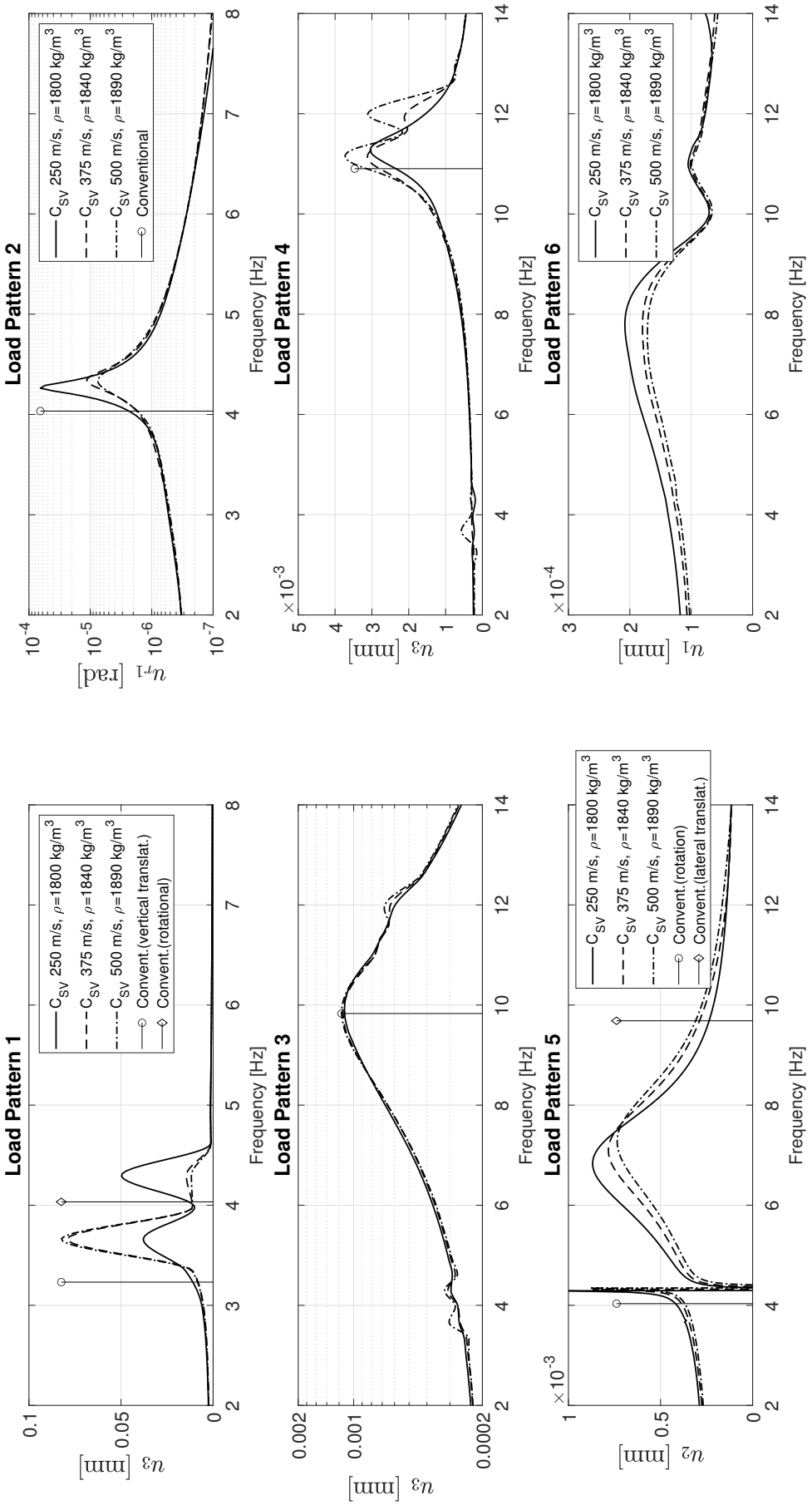

FIGURE 6.9: Comparisons of displacement response magnitudes for six load patterns for bridge model 2 (L=35 m, R=400 m) with different backfill properties.

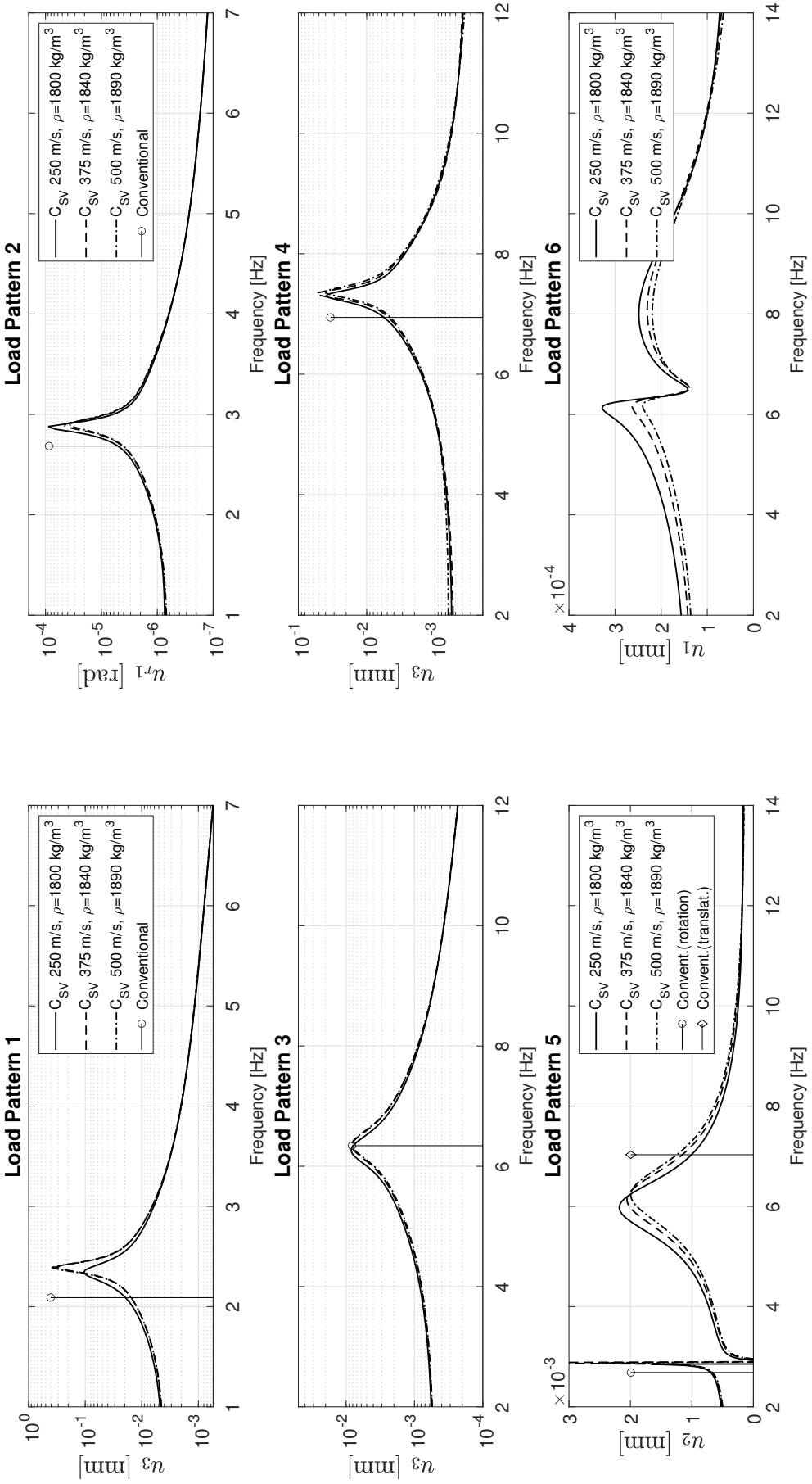

FIGURE 6.10: Comparisons of displacement response magnitudes for six load patterns for bridge model 3 (L=45 m, straight) with different backfill properties.

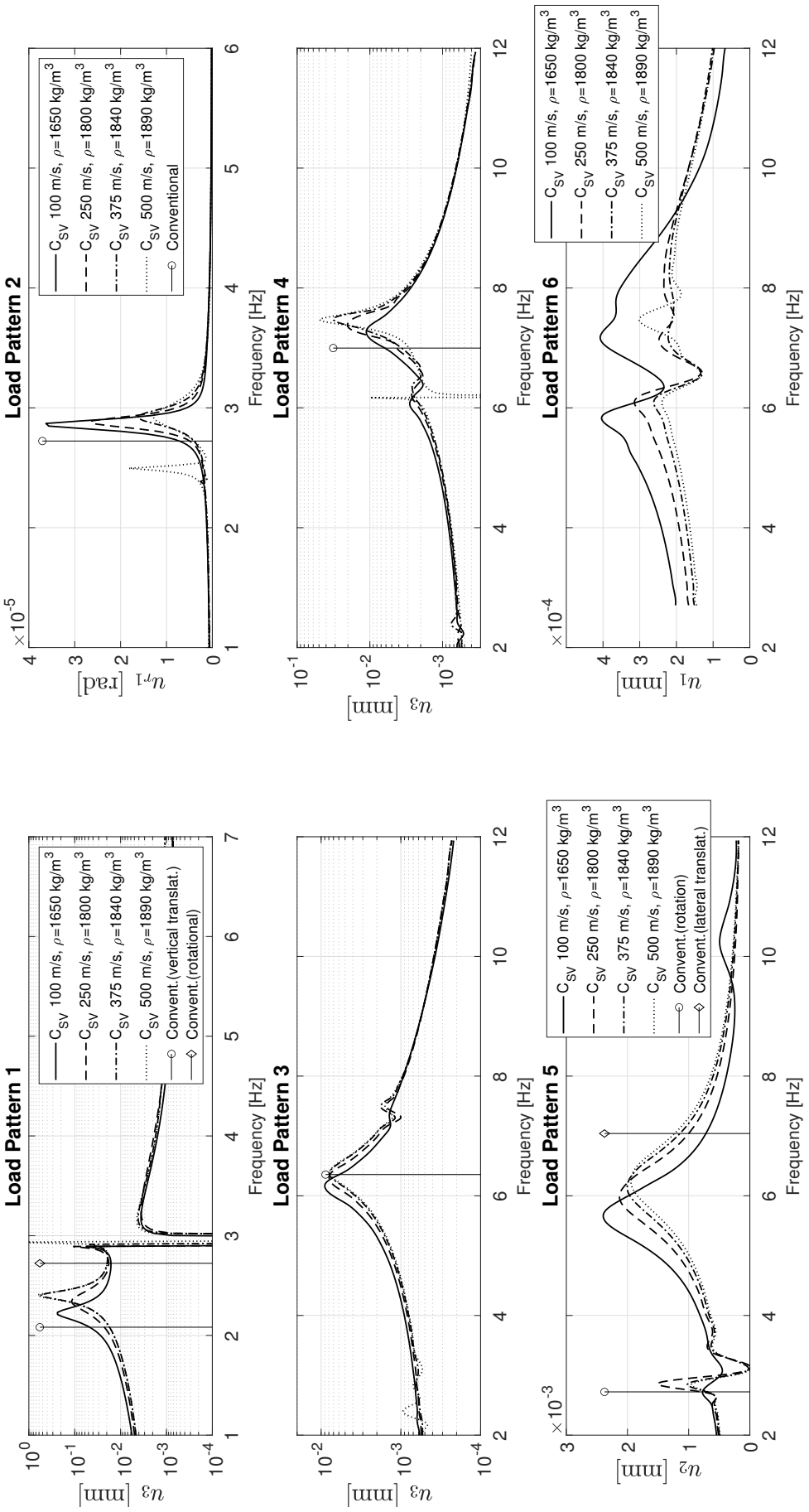

FIGURE 6.11: Comparisons of displacement response magnitudes for six load patterns for bridge model 4 (L=45 m, R=400 m) with different backfill properties.

Chapter 7

Application II: Simulations of foundation-soil-foundation dynamic interaction including damaged state of geological material

7.1 Chapter overview

In this chapter, the developed hybrid BEM-FEM is applied to case studies of foundation-soil-foundation interaction. In addition, the damaged state of the geological material is taken into consideration. The problem statement is given in Section 7.2 followed by the description of the damage model in Section 7.3. The details regarding the parametric study and discussion of the results are presented in Section 7.4. The content of this chapter is published in H.D.B. Aji, F. Wuttke, P. Dineva (2021). "3D hybrid model of foundation-soil-foundation dynamic interaction". In: *Z. für Angew. Math. Mech.* (*ZAMM*) 101, e202000351. DOI: 10.1002/zamm.202000351.

7.2 Problem statement

In coordinate system $Ox_1x_2x_3$, consider 3D finite geological region Ω_1 which is embedded in a semi-infinite elastic isotropic media Ω_0 with transient dynamic load generated by an embedded source at point $\mathbf{X}_0(X_{01}, X_{02}, X_{03})$, see Figure 3.1. The description of both domains, Ω_0 and Ω_1, is the same as in Section 3.2 following Figure 3.1.

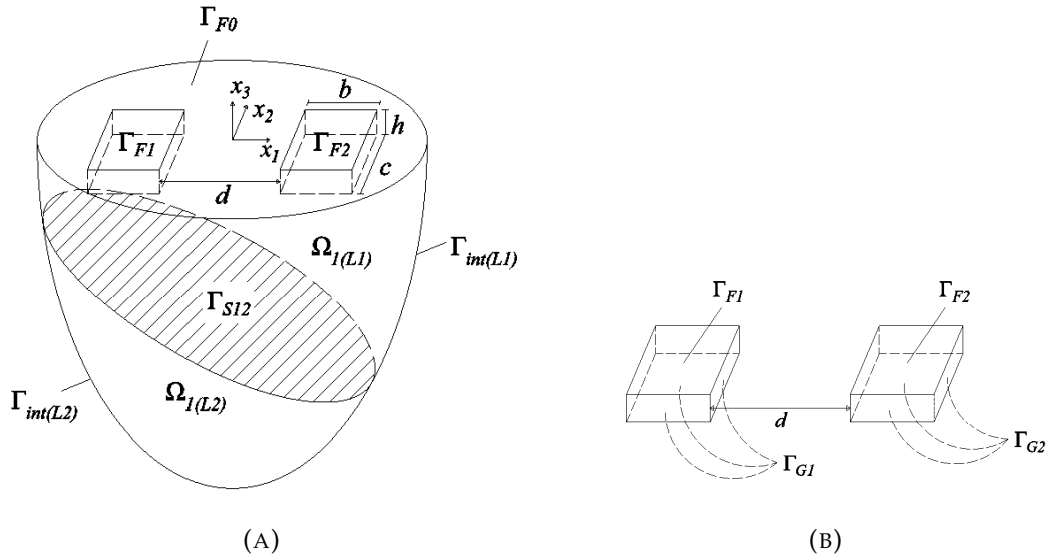

(A) (B)

FIGURE 7.1: The problem geometry: (**A**) the geometry of the finite region Ω_1; and (**B**) two rectangular foundations embedded in the top layer of Ω_1.

The concrete geometry of the finite region Ω_1 is given in Figure 7.1a. The finite region Ω_1 consists of two layers: (a) layer 1 in the domain $\Omega_{1(L1)}$ with boundaries of Γ_F, $\Gamma_{int(L1)}$, Γ_{S12}; (b) and layer 2 in the domain $\Omega_{1(L2)}$ with boundaries of $\Gamma_{int(L2)}$, Γ_{S12}. Note that the normal vectors to the interface boundary between both layers Γ_{S12} are equal in magnitude but *opposite* in sign. There are two identical rectangular foundations in the first layer with length b, width c and height h. The distance between both foundations is d. The top sides of the left and right foundation are free surfaces and are denoted as Γ_{F1} and Γ_{F2}, while the embedded surfaces are collected in Γ_{G1} and Γ_{G2}, see Figure 7.1b. Material properties of the geological semi-infinite zone Ω_0 are density ρ_0; Lamé moduli λ_0, μ_0; and wave velocities C_{P_0} and C_{S_0}, while the material properties of both layers in the finite range Ω_1 are as follows: λ_1, μ_1, C_{P_1}, C_{S_1} for the layer one and λ_2, μ_2, C_{P_2}, C_{S_2} for the layer two. The material properties of the foundations are denoted by λ_f, μ_f, C_{P_f}, and C_{S_f}.

Comparing Figures 3.1, 7.1a and 7.1b, it can be seen that the free-surface of the finite region Ω_1 denoted by Γ_F in Figure 3.1 corresponds to $\Gamma_F = \Gamma_{F0} \cup \Gamma_{F1} \cup \Gamma_{F2}$ in Figure 7.1a, whereas Γ_{F0} is the free-surface outside the top sides of both foundations. The interface contact boundary Γ_{int} between the finite zone Ω_1 and semi-infinite one Ω_0 shown in Figure 3.1 is the surface $\Gamma_{int(L1)} \cup \Gamma_{int(L2)}$, see Figure 7.1a.

In resume **the boundaries of both zones** are as follows:

- In the finite near-field geological zone Ω_1:
  - The external boundary is $\Gamma_{\Omega_1} = \Gamma_{int} \cup \Gamma_F = \Gamma_{int} \cup \Gamma_{F0} \cup \Gamma_{F1} \cup \Gamma_{F2}$, where $\Gamma_{int} = \Gamma_{int(L1)} \cup \Gamma_{int(L2)}$.
  - The internal boundary is $\Gamma_{S12} \cup \Gamma_{G1} \cup \Gamma_{G2}$.
- In the semi-infinite far-field geological zone Ω_0, the boundary is $\Gamma_{\Omega_0} = \Gamma_B \cup \Gamma_{int}$.

The current work aims to solve the 3D elastodynamic problem for the above-described geometry and to evaluate the wave field in the finite layered zone Ω_1 with two elastic foundations taking into account the influence of the wave field in the dynamically loaded semi-infinite region, type and characteristics of the dynamic source, layering effect in the finite zone, foundation-soil-foundation interaction effect, and soil damaged state.

The equations of motion for Ω_1 and Ω_0 are given in equations (2.73) and (3.1), respectively. **Point source approximation** such as in (3.1) is a simple, convenient model to simulate weak seismic events, such as aftershocks or faults with negligible size, compared to the dimension of the seismic zone, see Nakano, 1923; Poursartip, Fathi, and Tassoulas, 2020. Other approaches for including **the seismic loads in the computational model** are the following: (i) simulating the seismic source as a double-couple, see Stein and Wysession, 1991; (ii) simulating the fault rupture as a double-couple sequence (dynamic rupture model), see Galvez et al., 2014; Aki and Richards, 1980; (iii) introducing the effects of the seismic source to the model indirectly, i.e., this is the case of incident wave loaded the boundary of the object under consideration, see Manolis et al., 2017.

The computation of the hybrid BEM-FEM model considering an embedded transient dynamic source follows those described in Section 3.2 and Section 2.6 using tied contact pair detailed in Section 3.5, see Figure 3.2.

7.3 Damage model description

The damaged state of the geological material is described by the damage model proposed in Chuhan and Gross, 1998, where the dispersion phenomenon of elastic waves in a solid permeated by a random distribution of micro-cracks is considered. The material characteristics of solids can be significantly affected by micro-cracks which give rise to stiffness degradation of the solid compared to its originally uncracked state. A radical difference between wave fields in cracked and

uncracked media is presented by two phenomena referred to as wave dispersion and wave attenuation. In materials with dispersed micro-cracks, the solid is seen by the incident wave as an attenuated and dispersive continuum, even though the cracked solid is still perfectly elastic, see Chuhan and Gross, 1998. The essence of the damage model proposed in Chuhan and Gross, 1998, and its advisability for solving the above-defined foundation-soil-foundation interaction problem will be briefly discussed here.

There are the following **basic assumptions**: (a) the solid is homogeneous, isotropic, and linear elastic with distributed slit micro-cracks; (b) the location and orientation of micro-cracks is random; (c) the dilute approximation is adopted, i.e., geometrical and dynamical interactions amongst individual cracks are neglected; (d) the crack-faces are not in touch, and the traction-free boundary condition is satisfied; and (e) all slit micro-cracks are identical with the same half-length a^*. This approximation has the consequence that the analysis is only appropriate for small crack densities, denoted by n_{cr}, and less favourable for an intermediate and dense concentration of micro-cracks. However, as noted in Chuhan and Gross, 1998, the dilute approach in most current problems known in material science should be entirely adequate. From a practical point of view, the significance of the dilute approximation is that one can use explicit formulas for computing the attenuation coefficient and the effective wave velocity rather than resort to other cumbersome models.

The effective medium approach is applied based on homogenization by using a representative volume element (RVE), large enough compared to the dimensions of the micro-cracks and small enough compared to the solid dimensions. The RVE should be able to show the microscopic details and represent the cracked solid's overall average behavior. A statistically homogeneous elastic solid presents the original heterogeneous cracked solid with macroscopic isotropy, with the same overall average response as the original one. The effective medium of the cracked solid remains linear, causal (overall average response of the effective medium can be influenced only by past events), and passive (no energy can be created within the effective solid) as in its originally uncracked state. As in the case of visco-elastic wave propagation in a homogeneous material, the overall average dynamic response can be described by a complex and frequency-dependent wave number $k(\omega)$, defined by $k^{eff}(\omega) = \omega / C^{eff}(\omega) + i\alpha^{eff}(\omega)$. Once the complex wave number $k^{eff}(\omega)$ of the effective medium has been obtained, the effective wave phase velocity $C^{eff}(\omega) = \omega / \Re[k^{eff}(\omega)]$ and the attenuation coefficient $\alpha^{eff}(\omega) = \Im[k^{eff}(\omega)]$ can be defined by taking the real and imaginary part of

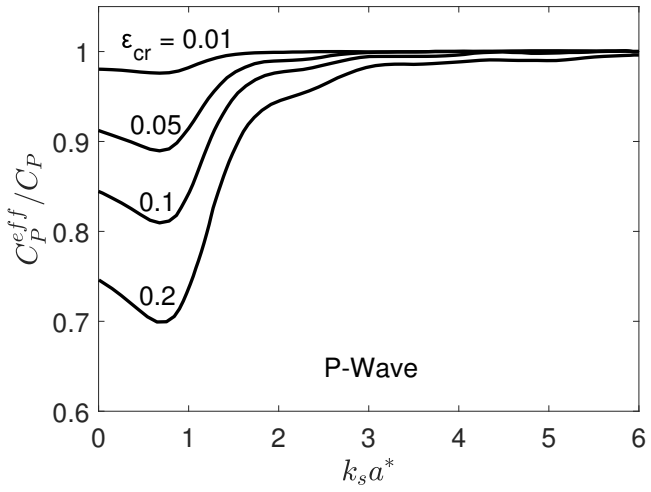

(A)

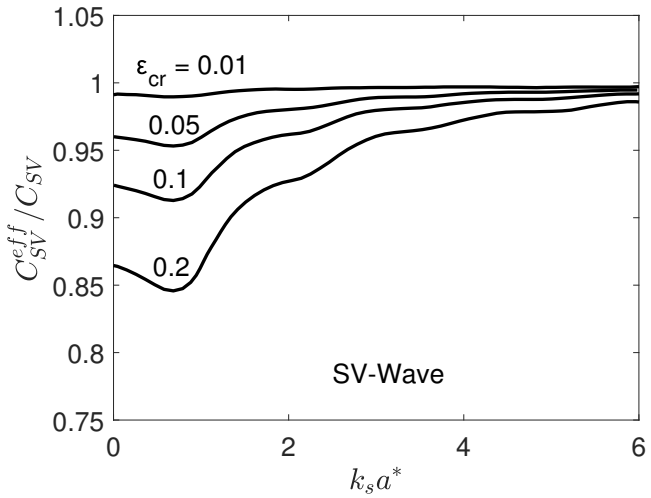

(B)

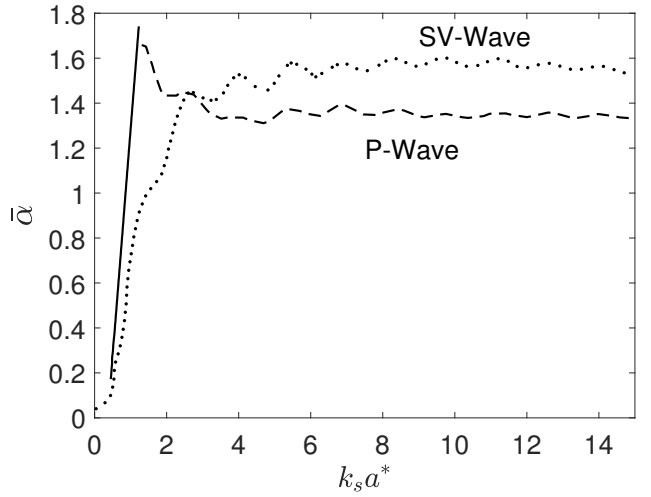

(C)

FIGURE 7.2: Normalized effective wave phase velocities versus $k_s a^*$ in (**A**) and (**B**); and normalized attenuation coefficient $\bar{\alpha}$ versus $k_s a^*$ in (**C**), after Chuhan and Gross, 1998.

$k^{eff}(\omega)$. In Chuhan and Gross, 1998, both the theory of Foldy Foldy, 1945 and the causal approach based on Kramers, 1927; Kronig, 1926, relations are applied to define the complex effective wave characteristics $k^{eff}(\omega), C^{eff}(\omega)$ and $\alpha^{eff}(\omega)$, respectively. These effective complex characteristics are obtained in Chuhan and Gross, 1998, via the help of the BEM numerical procedure for the calculation of scattering cross-section of a single micro-crack denoted by γ_{sc}. The coefficient γ_{sc} describes the amount of energy lost by an incident wave due to its scattering by the micro-crack. For the aim of the present work, the authors used the results in Chuhan and Gross, 1998, for the case of randomly oriented slit cracks but under the assumption of a small attenuation coefficient. Figures 7.2a, 7.2b and 7.2c show the normalized effective wave phase velocities C_P^{eff}/C_P, C_S^{eff}/C_S and normalized attenuation coefficient $\bar{\alpha} = 4\alpha^{eff}a^*/\pi\varepsilon_{cr}$ versus $k_s a^*$, where $k_s = \omega/C_S$; C_P and C_S are the longitudinal and shear wave velocities of the uncracked solid; and $\varepsilon_{cr} = (4n/\pi)(a^*)^2$ is the crack-density parameter introduced in Budiansky and O'connell, 1976.

It can be seen from Figures 7.2a to 7.2c that when the dimensionless wave number $k_s a^*$ belongs to the interval (0.0, 0.5], then the normalized attenuation coefficient $\bar{\alpha}$ belongs to the interval (0.0, 0.05], the normalized effective wave velocity C_P^{eff}/C_P belongs to the interval [0.745, 0.69] at $\varepsilon_{cr} = 0.2$, and the normalized effective wave velocity C_S^{eff}/C_S belongs to the interval [0.865, 0.845] at $\varepsilon_{cr} = 0.2$. Thus, at the mentioned frequency interval (0.0, 0.5], the imaginary part $\alpha^{eff}(\omega)$ of the complex wave number $K^{eff}(\omega)$ is negligibly small compared with its real part $\omega/C^{eff}(\omega)$. The numerical results concerning the damaged geological material are obtained in such a frequency interval providing a negligible small attenuation coefficient. The effective material characteristics (elastic moduli and density for damaged material case) are calculated for a fixed crack-density parameter ε_{cr} following results in Figure 7.2.

7.4 Parametric study and discussion of the results

The aim of this section is to reveal the complex character of the 3D wave field that develops in a finite layered soil region containing two elastic foundations and rests in a homogeneous elastic isotropic half-space with an embedded source of dynamic transient excitation. The parametric study consists of two parts. The first part considers a short-range dynamic excitation of a small layered finite region with two embedded foundations (case study 1). It is followed by the second

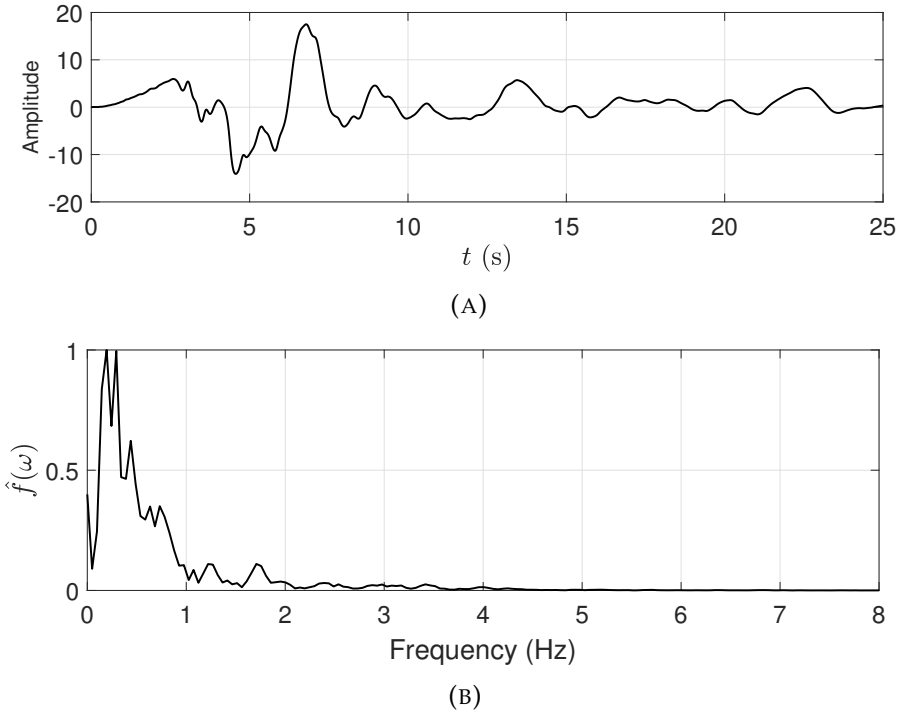

FIGURE 7.3: The time history (**A**) and amplitude spectrum, normalized to the maximum absolute value, (**B**) of the transient excitation.

part, a study regarding a long-range dynamic excitation case of two foundations embedded in a multi-layered sedimentary basin (case study 2).

It is assumed that **the time history function** of the dynamic force input at the embedded source follows the 90-degree component of the displacement time history recorded by Newhall station during the Northridge earthquake on 17 January 1994. The record has a peak displacement of 17.595 cm and is available at www.strongmotioncenter.org. To reduce the computational cost, the time history is trimmed to include only the record in the time range $t = [1,\ 26]$ s. It is subsequently filtered using a band-pass of 0.1-25 Hz and then detrended. After that, it is transformed into the Fourier domain and normalized by the amplitude spectrum's maximum absolute value. The frequency range considered for the analysis is [0, 8] Hz with a resolution of 0.0488 Hz. The time history function's time step and the subsequent inverse-FFT results are 0.02 s. The treated time history and the normalized absolute amplitude spectrum are shown in Figure 7.3. Note that the time-function of the seismic record is used formally as a time-function of the transient dynamic excitation concentrated in a defined below point $\mathbf{X}_0$.

TABLE 7.1: The material properties considered for the parametric study of case 1.

Region	λ (MN/m^2)	μ (MN/m^2)	ν	ρ (kg/m^3)
Ω_0	1 050.00	525.00	1/3	2 100
Ω_0^*	392.82	392.82	0.25	2 100
$\Omega_{1(L1)}$	65.63	43.75	0.30	1 575
$\Omega_{1(L2)}$	105.00	105.00	0.25	1 680
Foundations	6 666.67	10 000.00	0.20	2 500
Foundations*	388.89	583.33	0.20	2 500
Foundations**	95.83	143.75	0.20	2 500

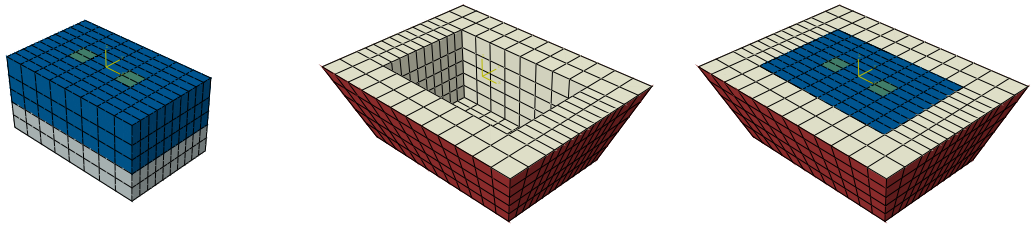

(A) (B) (C)

FIGURE 7.4: The model geometry for the parametric study of case 1: (**A**) the FEM region, (**B**) the BEM region, and (**C**) the whole BEM-FEM model.

7.4.1 Case study 1

The geometry of the model of the first case study is shown in Figure 7.4. The finite soil region Ω_1 (Figure 7.4a) is a cuboid with widths of 8 m and 5 m in x_1 and x_2 directions, respectively. It consists of two layers namely $\Omega_{1(L1)}$ at the top and $\Omega_{1(L2)}$ at the bottom. The thicknesses of $\Omega_{1(L1)}$ and $\Omega_{1(L2)}$ layers are 2.5 m and 1.5 m, respectively. Two identical elastic foundations with dimensions of 1.0 m x 1.0 m x 1.0 m are embedded in $\Omega_{1(L1)}$ with distance d between them. The free surface of the half-space discretized in the BEM model is 2 m at the shortest, which corresponds to a ratio β_S of 31.25.

The material properties considered for the parametric study are laid out in Table 7.1 where the Lamé moduli, Poisson's ratios, and the densities are given. Two states of geological material in the semi-infinite region Ω_0 are compared: undamaged and damaged. The latter is marked Ω_0^* in Table 7.1 and the effective phase velocities ratios C_P^{eff}/C_P and C_S^{eff}/C_S are 0.749 and 0.865, respectively, see Figure 7.2, at the crack-density parameter $\varepsilon_{cr} = 0.2$ and at $k_s a^*$ close to zero.

The numerical model is **discretized** using 400 quadratic hexahedral finite elements, 348 active quadratic quadrilateral boundary elements, and 104 dummy

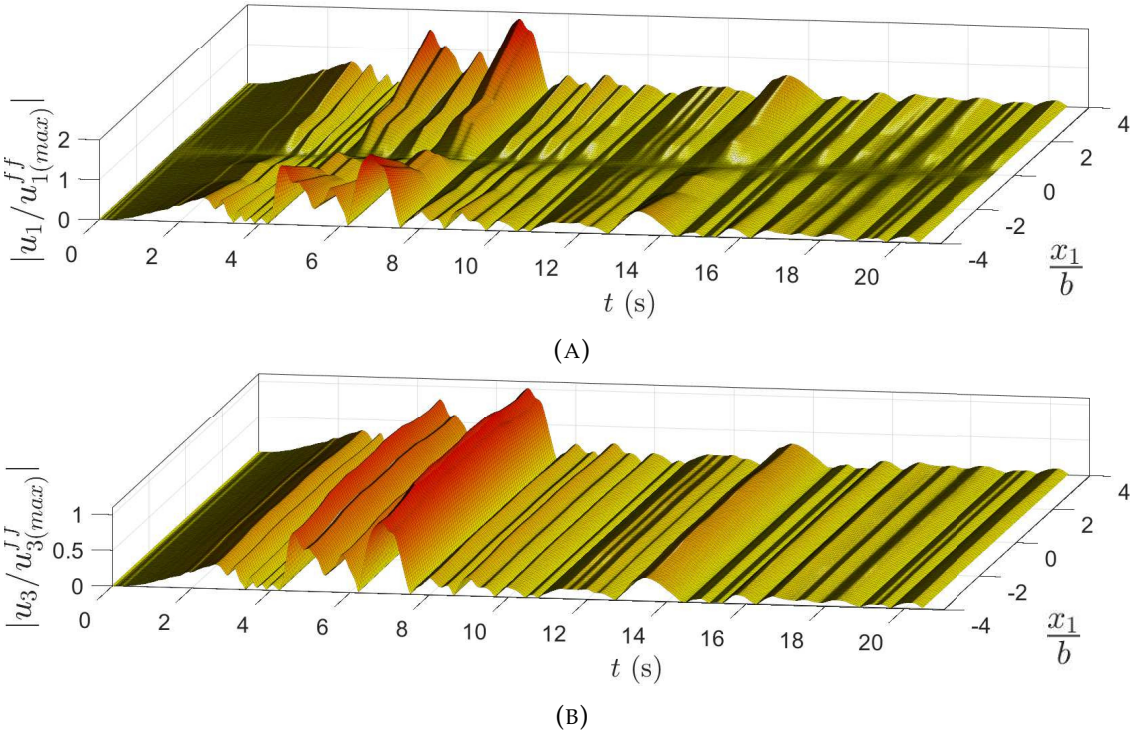

FIGURE 7.5: Normalized amplitudes of displacement components in case study 1 along the line $x_2 = 0$, $x_3 = 0$ versus $\frac{x_1}{b}$ and versus time t (s) in the case of undamaged soil in the semi-infinite region Ω_0 with embedded dynamic source 1 and a separation distance between foundations $d = 2$ m: (**A**) $|u_1|$ and (**B**) $|u_3|$.

boundary elements. The maximum element size is 1 m which is approximately 1/20 of the shortest shear wavelength λ_S of the materials in Table 7.1 when considering the frequency of 8 Hz as the highest input component.

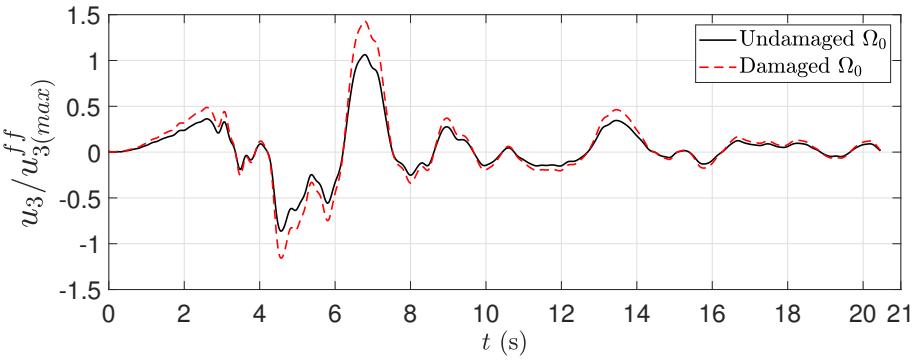

FIGURE 7.6: Comparison of normalized displacement component u_3 in case study 1 versus time t (s) between results for undamaged and damaged soil in the semi-infinite region Ω_0 with embedded dynamic source 1 and a separation distance between foundations $d = 2$ m at observer point **x**(0, 0, 0).

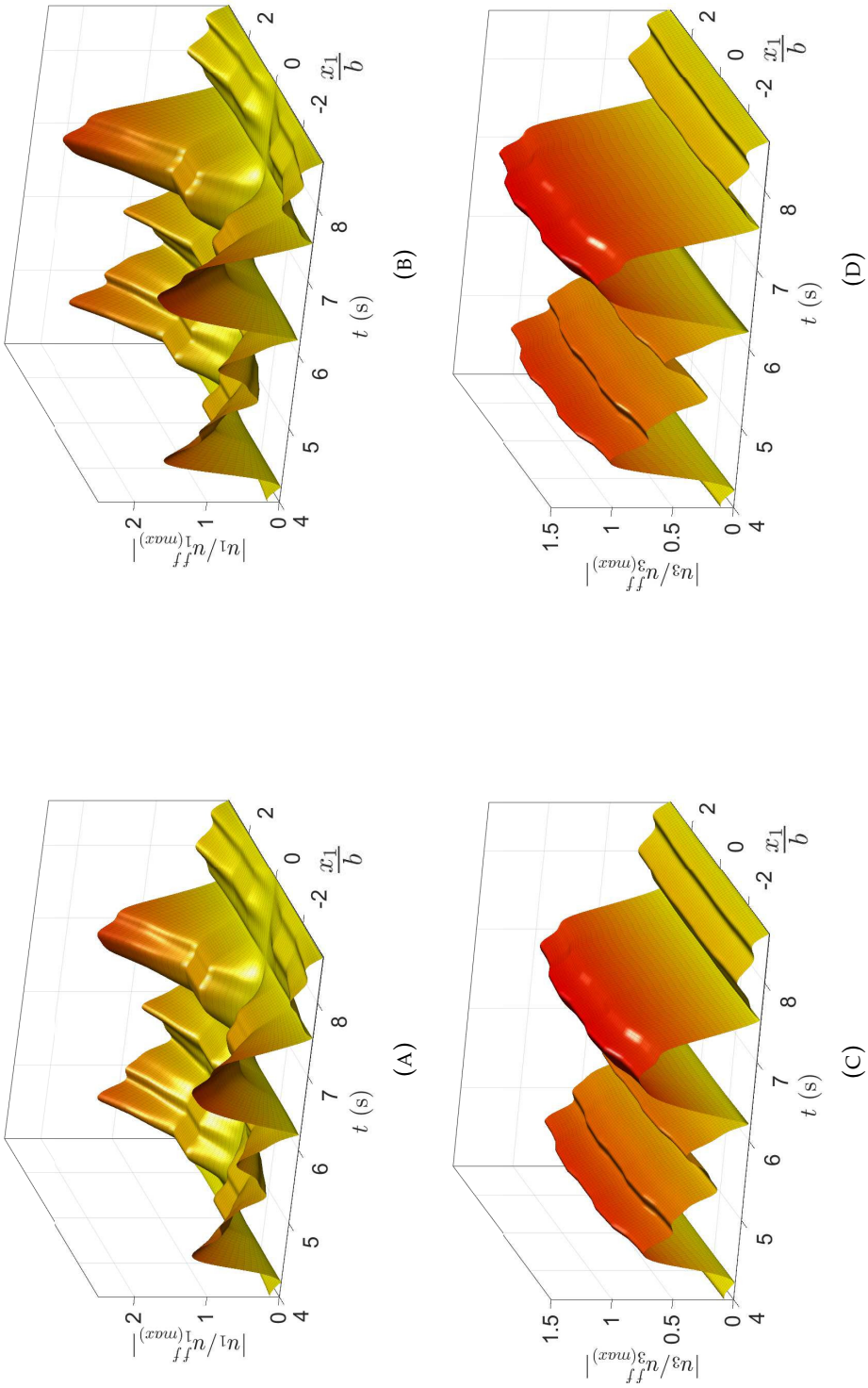

FIGURE 7.7: Normalized displacement amplitudes in case study 1 along the line $x_2 = 0$, $x_3 = 0$ versus $\frac{x_1}{b}$ in the time interval [4.0, 8.62] s in the cases of undamaged (**A, C**) and damaged (**B, D**) soil in the semi-infinite region Ω_0 with the embedded dynamic source 1 and a distance between foundations $d = 2$ m: (**A**), (**B**) $|u_1|$; (**C**), (**D**) $|u_3|$.

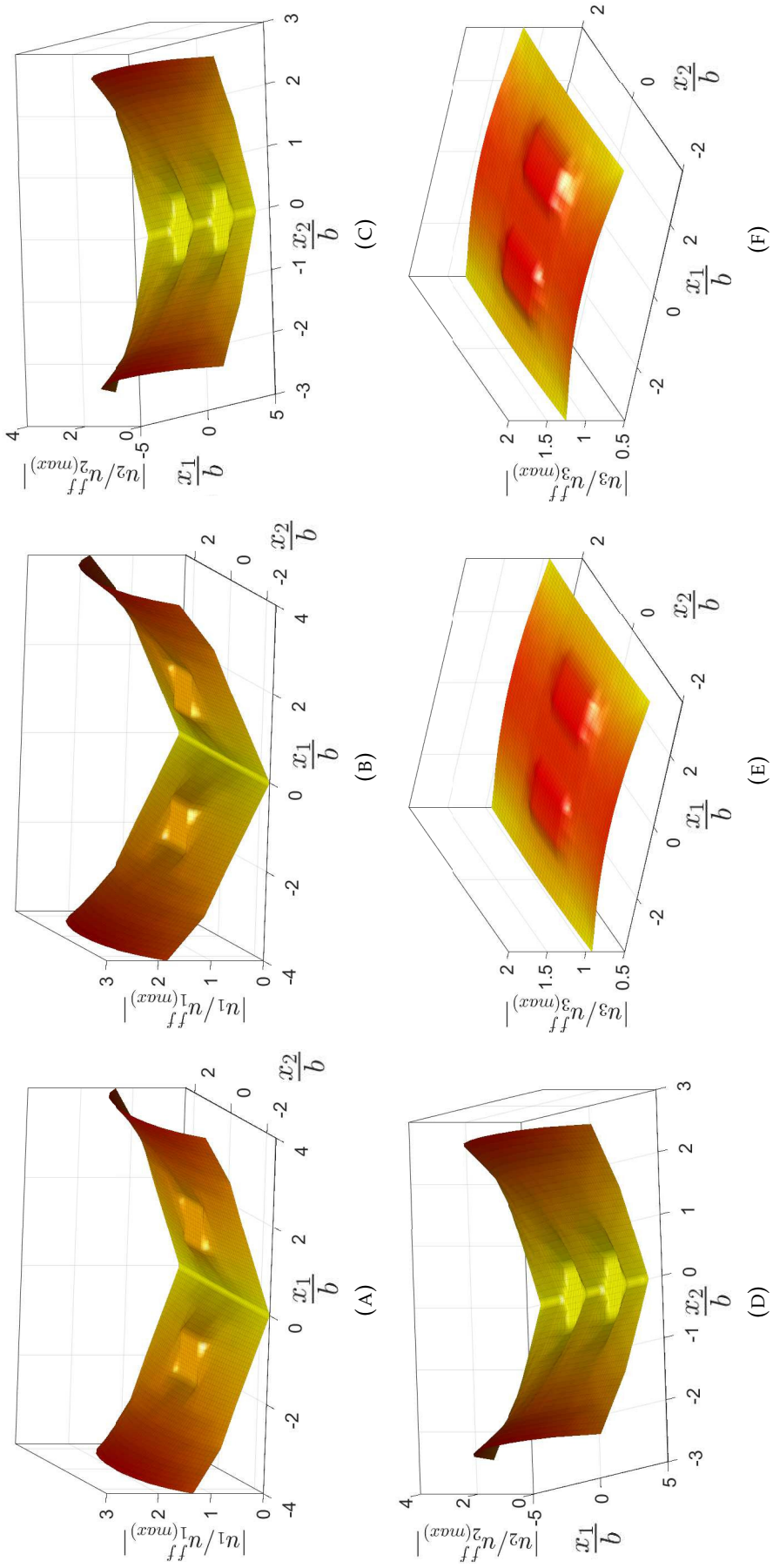

FIGURE 7.8: Normalized displacement amplitudes $|u_i|$ in case study 1 along the plane $x_3 = 0$ in the cases of undamaged (**A, C, E**) and damaged (**B, D, F**) soil in semi-infinite region Ω_0 with embedded dynamic source 1 and distance between foundations $d = 2$ m at a fixed time $t = t^*$, where t^* is the time of the displacement peak: (**A**), (**B**) $|u_1|$; (**C**), (**D**) $|u_2|$; (**E**), (**F**) $|u_3|$.

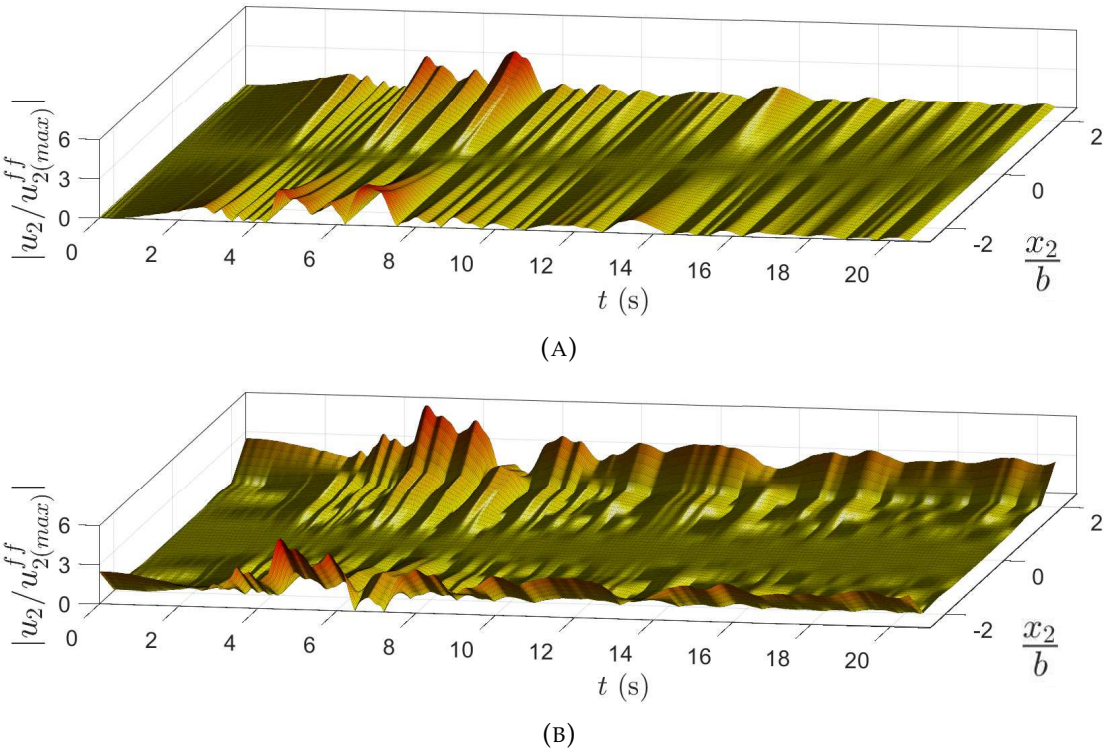

FIGURE 7.9: Normalized amplitudes of displacement component $|u_2|$ in case study 1 along the line $x_1 = 0$, $x_3 = 0$ versus $\frac{x_2}{b}$ and versus time t (s) in the case of undamaged soil in the semi-infinite region Ω_0 with embedded dynamic source 1 and foundations arrangement as follows: (**A**) arrangement 1 with d = 1 m and (**B**) arrangement 1 with d = 0.25 m.

Two different locations of the embedded dynamic source with amplitude $f_i^{(\Omega_0)}$(0, 0, 10^{10} N) are used in the simulations denoted as dynamic source 1 with location $\mathbf{X}_0$(0, 0, -10 m) and dynamic source 2 with location $\mathbf{X}_0$(1 m, -0.5 m, -8 m). The following arrangements of both foundations are considered: (a) arrangement 1, where the line connecting the centers of the surface walls of both foundations is parallel to the axis Ox_1 and the distance between them is d = 2 m, 1 m, 0.5 m and 0.25 m; (b) arrangement 2, where the line connecting the centers of the surface walls of both foundations is parallel to the diagonal of the free-surface of the finite region Ω_1 and d = 1 m.

Figures 7.5-7.8 compare the results for **undamaged and damaged geological material** in the semi-infinite region Ω_0, at arrangement 1 of the foundations with d = 2 m and in the case of dynamic source 1. Synthetic seismograms at observer points along the line $x_2 = 0$, $x_3 = 0$ are shown in Figure 7.5. Note that the normalized amplitudes of displacement component u_2 are zero along the lines x_1. This figure shows the absolute displacement component normalized by the

maximum value of the free-field displacement from the same dynamic source one and measured at **x**(4 m, 0, 0), **x**(0, 2.5 m, 0) and **x**(0, 0, 0) for u_1, u_2 and u_3, respectively. The seismograms in the case of the damaged state follow a similar form to that of the undamaged case but with around 30% increase in amplitudes as shown by the plot of the normalized displacement component u_3 versus time at observer point **x**(1.5 m, 0, 0), see Figure 7.6. Normalized displacement amplitudes along the line $x_2 = 0$, $x_3 = 0$ are shown in Figure 7.7 where the results are focused around the displacement peak in the time interval $t = [4.0,\ 8.62]$ s.

Figure 7.8 illustrates the effect of the damaged state of the semi-infinite geological region Ω_0 on the normalized displacement amplitudes $|u_i|$ along the free-surface plane $x_3 = 0$ of the finite region Ω_1 at a fixed time moment $t = t^*$, where t^* is the fixed time moment when the response displacement component u_3 has its peak.

Figure 7.9 presents **the arrangement effect** at different separation distances between foundations on the second displacement component $|u_2|$ along the line $x_1 = 0,\ x_3 = 0$. The results show that when the foundations are at a distance of 0.25 m from each other, significant change in the displacement wave field is visible. Figure 7.10 illustrates the differences in the displacement component u_2 along the plane $x_3 = 0$ in the finite region Ω_1 at a fixed time t^* between the results of arrangement 1, $d = 1$ m; arrangement 2, $d = 1$ m; arrangement 1, $d = 0.5$ m; and arrangement 1, $d = 0.25$ m. Both Figures 7.9-7.10 are obtained for the undamaged state of Ω_0 and show that the types of foundation arrangement and distance between them are responsible factors for the dynamic response.

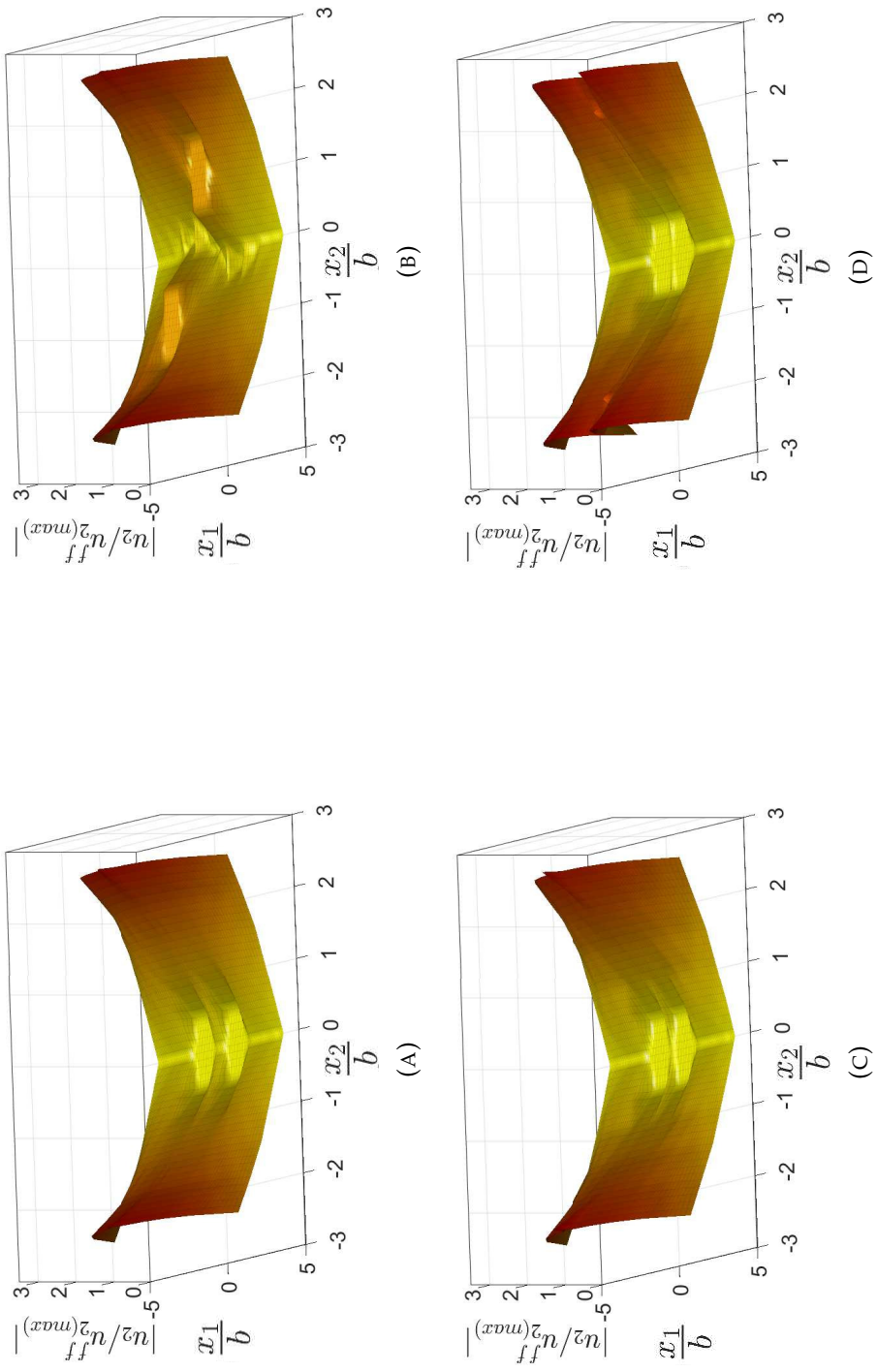

FIGURE 7.10: Normalized amplitude of displacement component $|u_2|$ in case study 1 along plane $x_3 = 0$ at a fixed time $t = t^*$, where t^* is the time of displacement peak, in the case of undamaged soil in the semi-infinite region Ω_0 with dynamic source 1. The foundations arrangements are as follows: (**A**) arrangement 1 with $d = 1$ m, (**B**) arrangement 2 with $d = 1$ m, (**C**) arrangement 1 with $d = 0.5$ m and (**D**) arrangement 1 with $d = 0.25$ m.

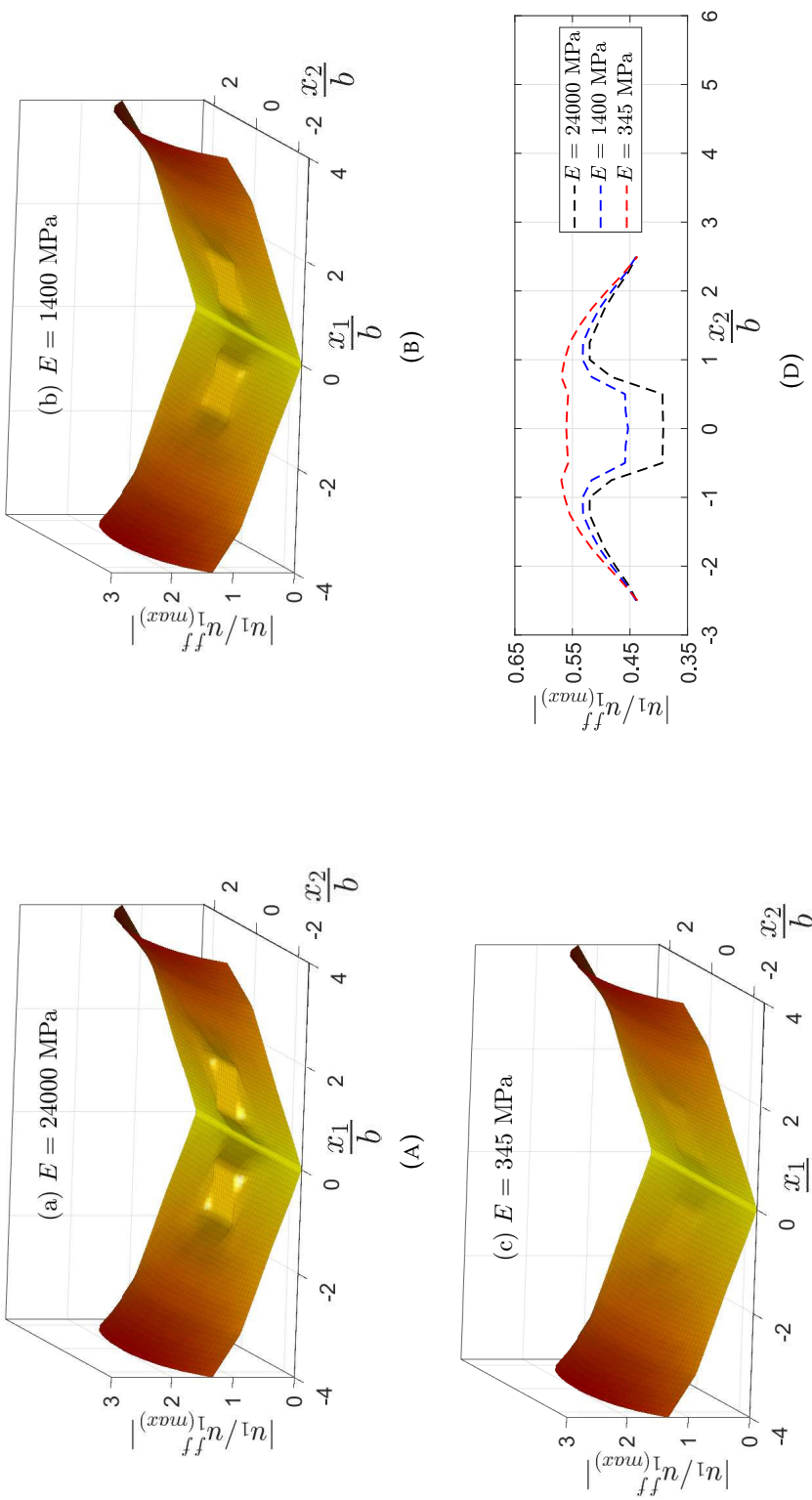

FIGURE 7.11: Normalized amplitudes of displacement component u_1 in case study 1 at a fixed time of displacement peak $t = t^*$ in the case of elastic foundations arrangement 1, a separation distance between foundations $d = 1$ m, and their elastic properties are different. Observer points are along the plane $x_3 = 0$ in (**A**), (**B**), (**C**) and along the line $x_1 = 1.5$ m, $x_3 = 0$ versus $\frac{x_2}{b}$ in (**D**).

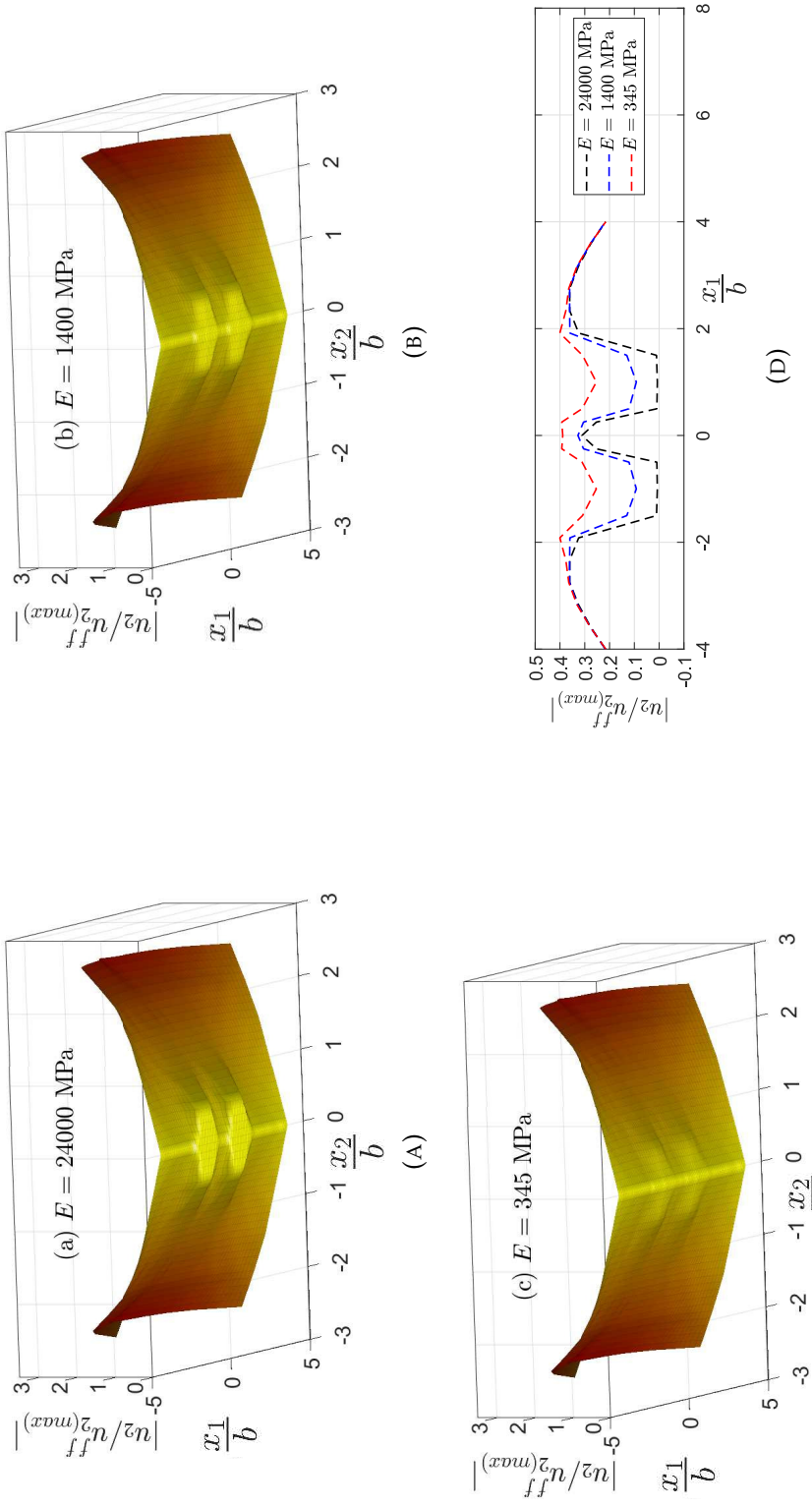

FIGURE 7.12: Normalized amplitudes of displacement component u_2 in case study 1 at a fixed time of displacement peak $t = t^*$ in the case of elastic foundations arrangement 1, a separation distance between foundations $d = 1$ m, and their elastic properties are different. Observer points are along the plane $x_3 = 0$ in (**A**), (**B**), (**C**) and along the line $x_2 = 0.5$ m, $x_3 = 0$ versus $\frac{x_1}{b}$ in (**D**).

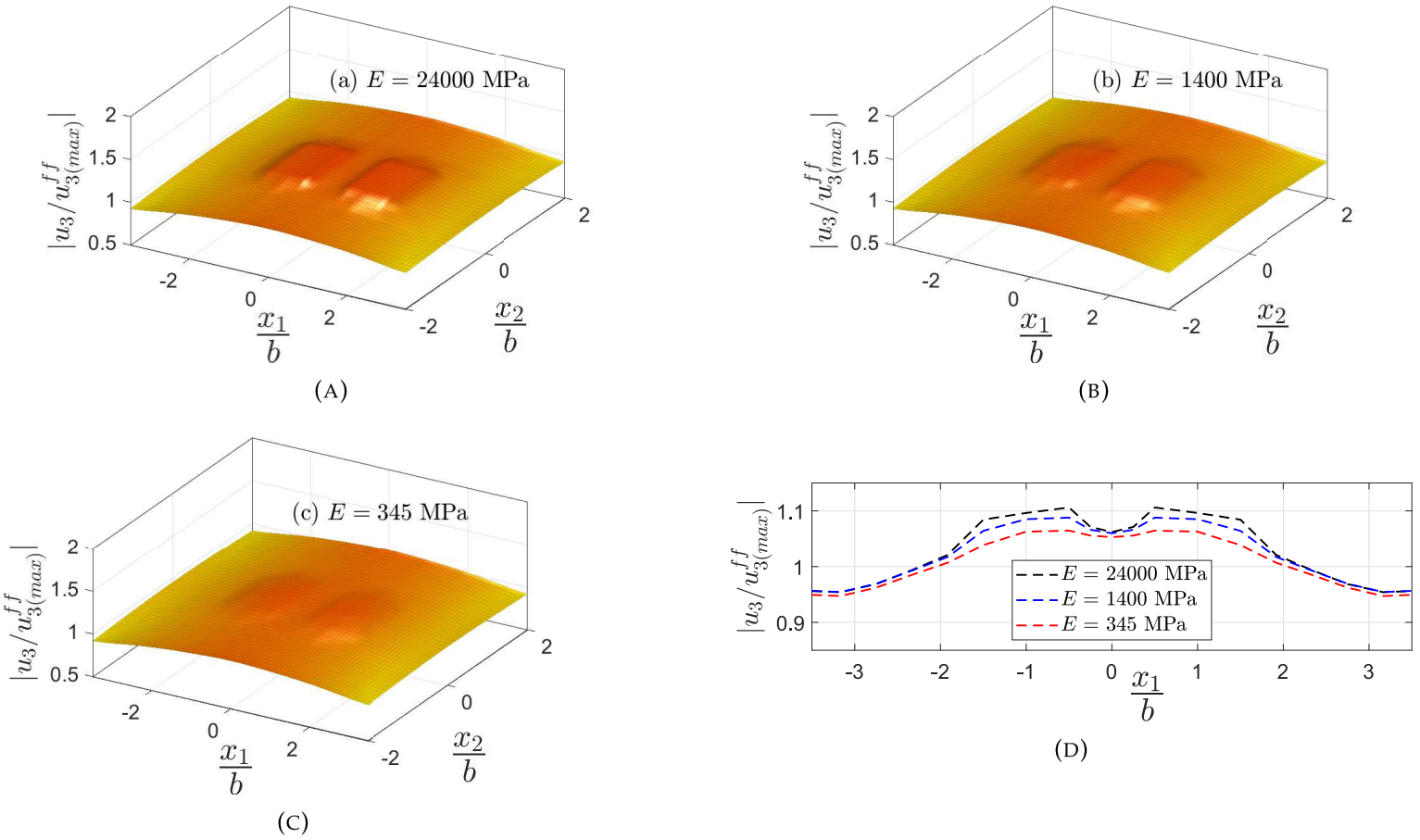

FIGURE 7.13: Normalized amplitudes of displacement component u_3 in case study 1 at a fixed time of displacement peak $t = t^*$ in the case of elastic foundations arrangement 1, a separation distance between foundations $d = 1$ m, and their elastic properties are different. Observer points are along the plane $x_3 = 0$ in (**A**), (**B**), (**C**) and along the line $x_2 = 0.5$ m, $x_3 = 0$ versus $\frac{x_2}{b}$ in (**D**).

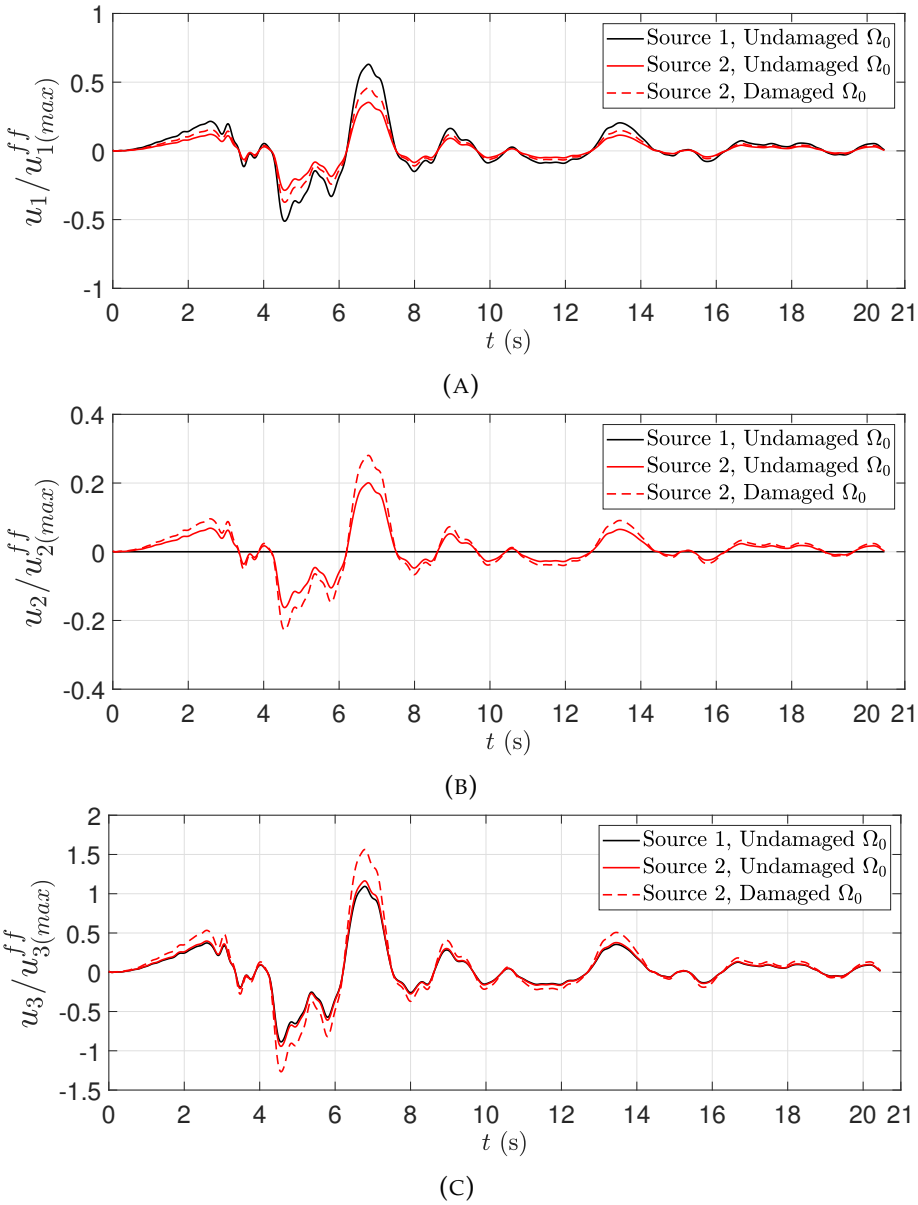

FIGURE 7.14: Normalized displacement components u_i in case study 1 at observer point **x**(1 m, 0, 0) versus time t (s) in the cases of undamaged and damaged soil in the semi-infinite region Ω_0 with dynamic source 1 and source 2 and a separation distance between foundations $d = 2$ m: (**A**) u_1, (**B**) u_2 and (**C**) u_3.

Further, we consider **elastic foundations with strongly reduced stiffness properties** due to aging, weathering, cracking, damage or other deteriorating effects, see Pitilakis and Karatzetzou, 2014. The following reduced elastic properties for masonry foundation are given: Poisson's ratio 0.2 and Young's modulus $E = 1400$ MPa (Foundations* in Table 7.1) and 345 MPa (Foundations** in Table 7.1). These foundation characteristics are used in Figures 7.11-7.13. These figures depict normalized amplitudes of displacement components $|u_1|$ (Fig. 7.11), $|u_2|$ (Fig. 7.12) and $|u_3|$ (Fig. 7.13) along the free-surface of the finite region Ω_1 at a

fixed time moment of the peak of the displacement component u_3 in the cases of the foundations' arrangement 1, fixed separation distance $d = 1$ m and the following elastic properties of both foundations: (a) $E = 24000$ MPa, (b) $E = 1400$ MPa and (c) $E = 345$ MPa. Note that for the other considered cases presented in Figures 7.5-7.10 and Figure 7.14, the elastic property of the foundations is $E = 24000$ MPa (Foundations in Table 7.1).

Normalized displacement components u_i at observer point $x(1, 0, 0)$ for the model with foundations arrangement one and $d = 2$ m due to the dynamic signal coming from the dynamic source one and source two are compared in Figure 7.14.

7.4.2 Case study 2

The geometry of the model of the second parametric case study is shown in Figure 7.15 where a sedimentary basin with a half-sphere geometry with a diameter of 40 m is considered. The basement rock of the basin is represented as a semi-infinite region Ω_0, and the finite region Ω_1 consists of 4 layers of elastic isotropic sediment. Two identical elastic foundations with a size of 6 m $\times$ 6 m and thickness of 1 m are embedded in the top layer with a separation distance of 2 m. Cut views of the model in the ABAQUS pre-processor are presented in Figure 7.16. The largest element size in the BEM and FEM models is 1.5 m, corresponding to 1/13 of the shortest shear wavelength. The length of the discretized free surface is 6 m which leads to β_S of 416. Other than consideration regarding the ratio β_S,

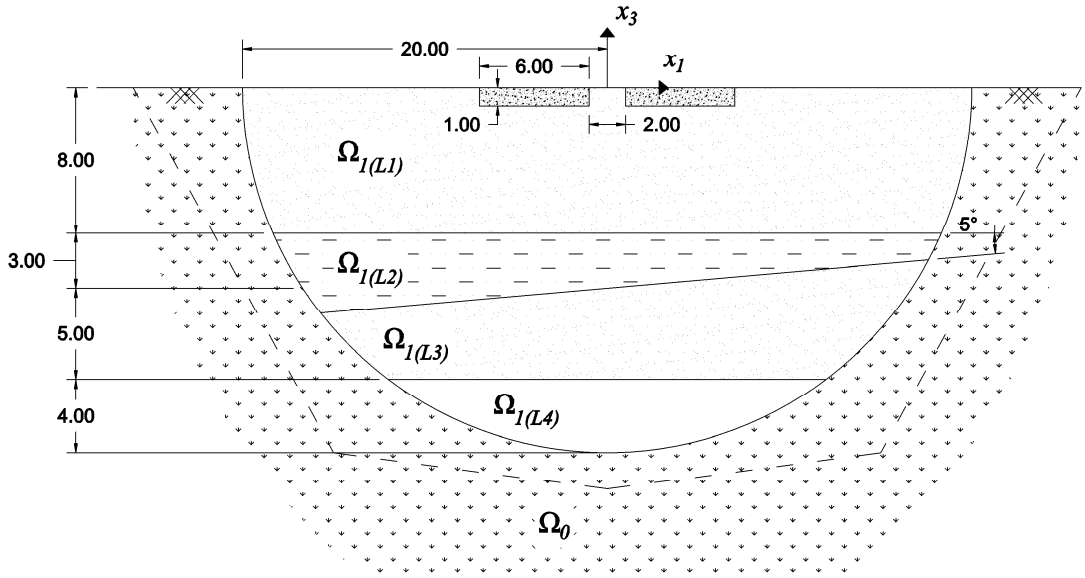

FIGURE 7.15: The model geometry for parametric case study 2.

TABLE 7.2: The material properties considered for the parametric study of case 2.

Region	λ (MN/m^2)	μ (MN/m^2)	ν	ρ (kg/m^3)
Ω_0	1 050.00	525.00	1/3	2 100
Ω_0^*	392.82	392.82	0.25	2 100
$\Omega_{1(L1)}$	62.63	43.75	0.30	1 575
$\Omega_{1(L2)}$	392.82	392.82	0.25	2 100
$\Omega_{1(L3)}$	62.63	43.75	0.30	1 575
$\Omega_{1(L4)}$	105.00	105.00	0.25	1 680
Foundations	6 666.67	10 000.00	0.20	2 500

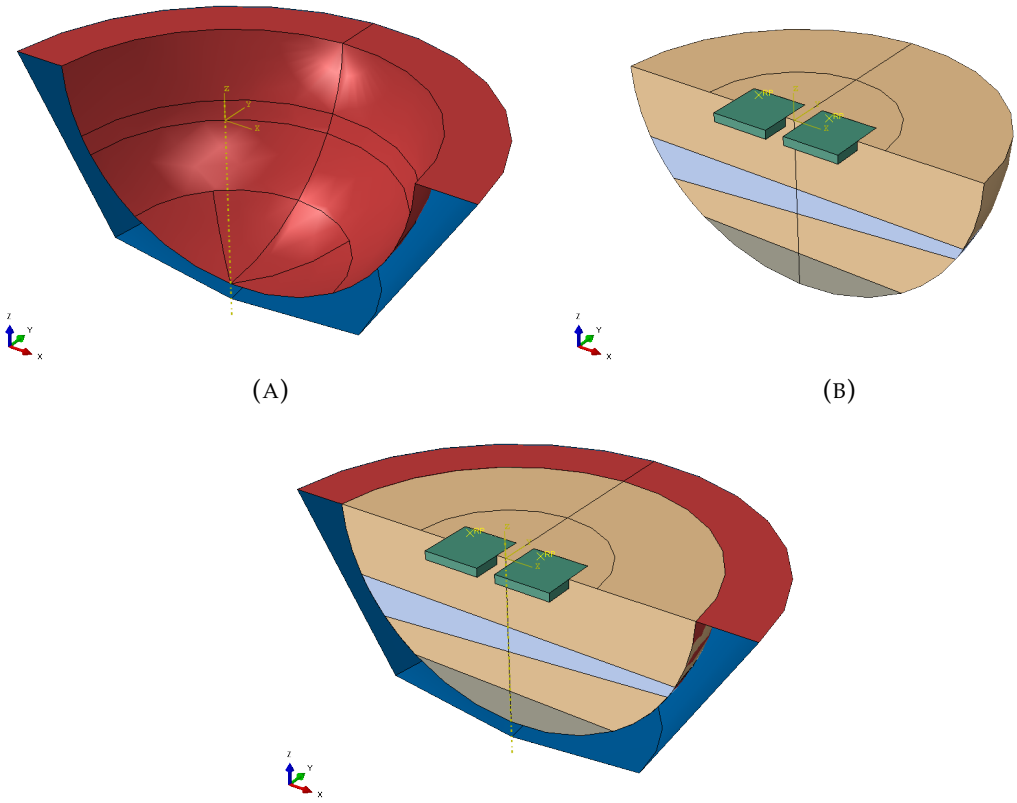

(A) (B)

(C)

FIGURE 7.16: Cut views of the model of case study 2 in ABAQUS/CAE: (**A**) the BE model, (**B**) the FE model, and (**C**) the complete model.

this length is taken to avoid creating a thin beam polygon which leads to numerical inaccuracy, either in the static or dynamic case. The material properties for each layer in the finite region Ω_1, the foundations, the semi-infinite region Ω_0 and its damaged state Ω_0^* are given in Table 7.2. The same assumption is taken for the damaged state of the basement rock as the one for case study 1 at fixed crack-density parameter $\varepsilon_{cr} = 0.2$.

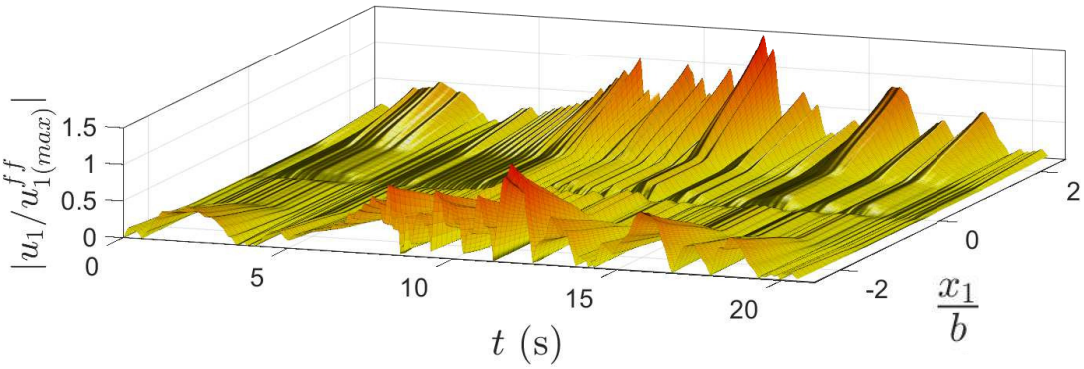

(A)

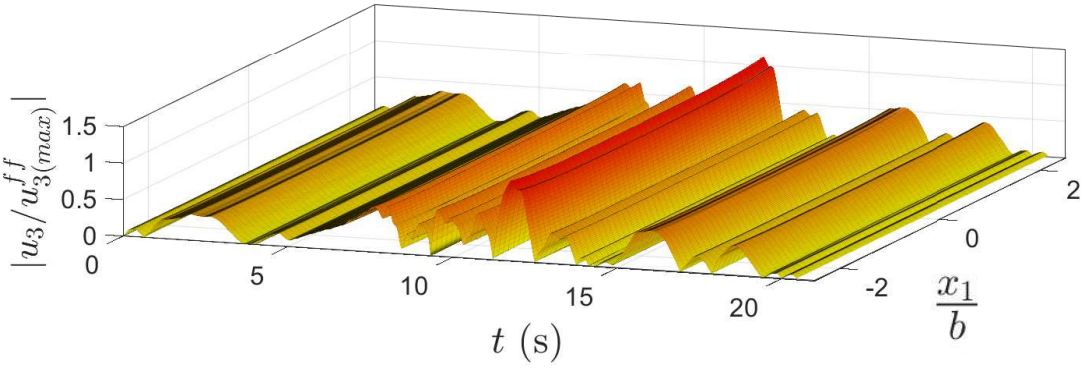

(B)

FIGURE 7.17: Normalized amplitudes of displacement $|u_i|$ in case study 2 along the line $x_2 = 0$, $x_3 = 0$ versus $\frac{x_1}{b}$ and versus time t (s) in the case of undamaged basement rock in the semi-infinite region Ω_0 with embedded dynamic source 3: (**A**) $|u_1|$ and (**B**) $|u_3|$.

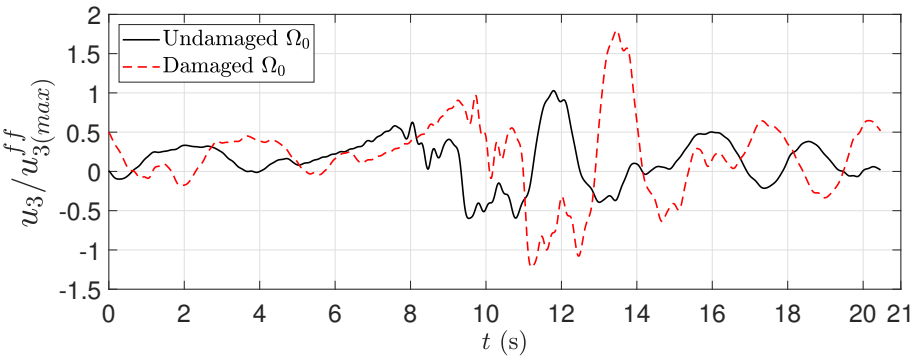

FIGURE 7.18: Comparison of the normalized displacement component u_3 at observer point **x**(4 m, 0, 0) in case study 2 versus time t (s) between results for undamaged and damaged basement rock in the semi-infinite region Ω_0 considering the embedded dynamic source 3.

The dynamic source, designated as dynamic source 3, is set at location $\mathbf{X}_0$(0, 0, -5000 m) with amplitude of $f_i^{(\Omega_0)}$(0, 0, 10^{12} N) and using the same time function shown in Figure 7.3. The normalized amplitudes of displacement along the line

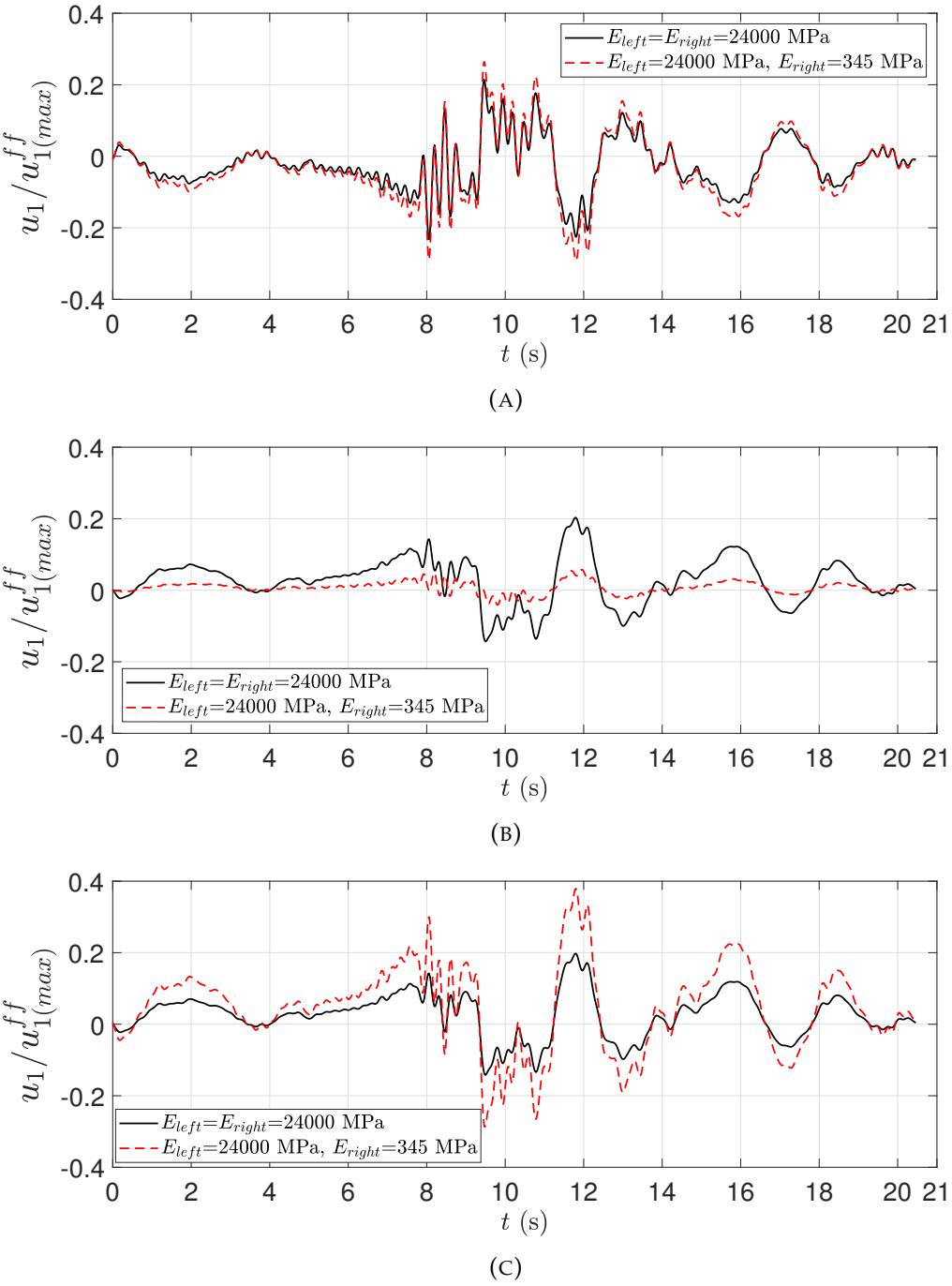

FIGURE 7.19: Comparisons of the normalized displacements u_1 in case study 2 versus time t (s) between results for the cases where both foundations have the same elastic properties (E = 24000 MPa) and different elastic properties (E_{left} = 24000 MPa, E_{right} = 345 MPa). Embedded dynamic source 3 is considered. The displacements are measured at the following observer points: (**A**) **x**(-4 m, 0, 0); (**B**) **x**(1 m, 0, 0); **c**) **x**(7 m, 0, 0).

$x_2 = 0$, $x_3 = 0$ versus time t (s) are shown in Figure 7.17 while comparison between the results for undamaged and damaged states of the basement rock

at observer point **x**(4 m, 0, 0) is presented in Figure 7.18. The latter figure also shows the propagating wave's arrival time delay in the damaged state due to its lower wave velocity. Figure 7.19 draws normalized amplitudes of displacement u_1 at observer points **x**(-4 m, 0, 0), **x**(1 m, 0, 0) and **x**(7 m, 0, 0) in the case both foundations have different elastic properties, i.e., $E_{left} = 24000$ MPa for the left-side foundation and $E_{right} = 345$ MPa for the right foundation. The reference values used for normalization are taken from the displacement result of the free-field model at points **x**(20 m, 0, 0) and **x**(0, 0, 0) for u_1 and u_3, respectively.

7.5 Chapter summary

This chapter presents case studies involving foundation-soil-soundation interaction and dilute approximation of damaged geological media and foundation. All results of the parametric study plotted in Figures 7.5-7.19 reveal **some trends** which can be summarized below.

(a) Obviously, the phenomenon of *dynamic site effects* can be seen in most of the figures presented in this section, see Figures 7.5-7.11, 7.17-7.19. This is due to the well-known fact that the wave field that develops at the free-surface results from a complex interplay of geometric and material factors. Most figures show a great difference between the displacement wave zones near and far away from the foundations. More specifically, earthquakes and other dynamic events are triggered by source characteristics that release energy in the form of waves. These waves filter through geological media on their way to the free surface. They are greatly affected by the material properties and structure of the soil layers with embedded engineering structures and the semi-infinite region under them, including local topography. As a result, dynamic signals' spatial and temporal variation differs considerably for nearby stations in the same locality and even for the same dynamic event. To date, it has been proven difficult to incorporate site effects in the engineering design of underground structures because of the sheer complexity of the problem. This partially reflects in the relative paucity of numerical models capable of handling irregular site geometry, multiple soil deposits, and the availability of underground engineering facilities.

(b) The local geological soil conditions (layering or soil damage) change the characteristics of the surface dynamic response. The damaged state of the soil material provokes two base phenomena, wave attenuation and dispersion, accompanied by decreasing soil stiffness. The effect of the damaged

state of the soil is visible in almost all of Figures 7.5-7.8, 7.14 and 7.18. All numerical results reveal the influence of the soil micro-structure state change on the seismic wave picture. The maximal percentage differences observed between displacements obtained for undamaged and damaged soils in Figure 7.7 are 30.67% and 34.18% for u_1 and u_3, respectively, while the differences between the displacements in Figure 7.14 are 30.18%, 39.88% and 34.31% for u_1, u_2 and u_3, respectively. The maximum difference observed in Figure 7.18 is 74.80%.

(c) The sensitivity of the dynamic response to the *dynamic source location* can be seen in the obtained results in Figure 7.14 for the observer point $x(1,0,0)$ in the cases of two different dynamic source locations when all the rest model parameters are fixed. The source location strongly changes the 3D dynamic response in the same observer point, especially when it combines with the damaged state of the soil.

(d) In the whole system, *elastic properties of both foundations* also plays an important role. This is illustrated in Figures 7.11-7.13. The wave pictures for all three displacement components along the free surface of the finite local geological region reveal a strong sensitivity to the foundation stiffness reduction. There exist observer points for which the foundation stiffness reduction leads to 50% increase in the seismic response. Figure 7.19 also illustrates that the difference in elastic properties of both foundations plays an important role in the dynamic response of the region under consideration.

(e) The effect of the *foundation-soil-foundation dynamic interaction* is illustrated in Figures 7.9-7.10, where it is visible that different geometrical arrangements of both foundations have a significant impact on the wave field along the free-surface. The results obtained in the cases of foundations arrangement 1 with separation distances between foundations of 1 m, 0.5 m, and 0.25 m clearly illustrate the influence of foundation-soil-foundation interaction on the dynamic response in Figures 7.10a, 7.10c and 7.10d. The geometry of the foundations' diagonal disposition at a fixed distance of 1 m is projected in the wave picture shown in Figure 7.10b. The wave zone near the foundations accurately and visibly reflects the geometry of their mutual location in all Figures 7.10a, 7.10b, 7.10c, and 7.10d.

Chapter 8

Application III: Structure-soil-structure interaction in an arbitrary layered half-space

8.1 Chapter overview

This chapter discusses the application of the developed hybrid BEM-FEM, combined with the layer-wise condensation method, to case studies of structure-soil-structure interaction, taking into account the influence of arbitrary layered half-space. The introduction and problem statement are given in Section 8.2. The numerical simulations and discussion of the results are presented in Section 8.3. The content of this chapter is published in H.D.B. Aji, F. Wuttke, P. Dineva (2022). "3D structure-soil-structure interaction in an arbitrary layered half-space". In: *Soil Dynamics and Earthquake Engineering* 159, 107352. DOI: 10.1016/j.soildyn.2022.107352.

8.2 Introduction and problem statement

In most SSI studies, only the coupling between the structure and the neighbouring soil is considered, and dynamic interaction with other structures/foundations is often ignored. The problem of the interaction of adjacent structures through the underlying and surrounding soil, referred to as **Structure-Soil-Structure Interaction** (**SSSI**), has received less attention. The pioneering works in this field are the papers by Wong and Trifunac, 1975; Triantafyllidis and Prange, 1987; and BEM models in Qian and Beskos, 1995; Qian and Beskos, 1996; Karabalis and Mohammadi, 1998. The hybrid FEM-BEM models of SSSI are developed in Wang and Schmid, 1992; Qian, Tham, and Cheung, 1996; Padrón, Aznárez, and Maeso, 2009;

Álamo et al., 2015. Interesting results for the aseismic design of structures are presented in Knappett, Madden, and Caucis, 2015, and Aldaikh et al., 2016, where physical modeling of the SSSI problem is used as a research tool and reveals its effect on the dynamics of adjacent structures. Discrete (reduced-order) models have been effectively applied in evaluating the SSSI effects on the dynamic response of buildings, see Mulliken and Karabalis, 1998; Alexander, Ibraim, and Aldaikh, 2012; Vicencio and Alexander, 2018a; Vicencio and Alexander, 2018b; Vicencio and Alexander, 2019; Vicencio and Alexander, 2021. In Vicencio and Alexander, 2021, a group of buildings or a city block under seismic excitation in 3D is considered. The authors propose a new methodology based solely on defining auto-rotational and inter-rotational spring coefficients for the elastic half-space. The only input informations required are the soil class, the height, footprint dimensions, and the planar coordinates of the buildings. The response of idealized building clusters during earthquakes, their effects on the ground motion, and how individual buildings interact with the soil and each other is addressed in Isbiliroglu, Taborda, and Bielak, 2015. Numerical results show that the SSSI effects vary with the number and dynamic properties of the buildings, their separation, and their impedance with respect to the soil.

The problem statement is as follows. In a coordinate system $Ox_1x_2x_3$, consider a finite geological region Ω_1 which is located in the first layer of a semi-infinite elastic isotropic layered media Ω_0 with an embedded transient dynamic source at point $\mathbf{X}_0(X_{01}, X_{02}, X_{03})$, see Figure 4.1.

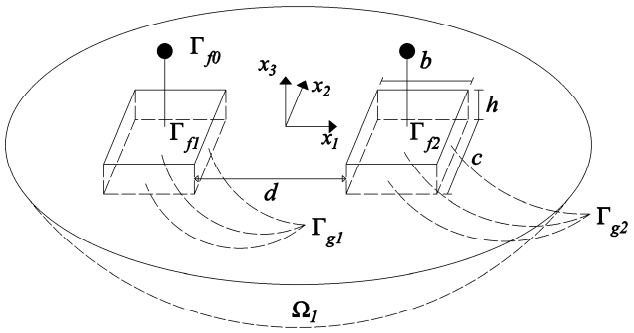

FIGURE 8.1: The finite region Ω_1 with two structures and embedded foundations.

The interface boundary between both regions Ω_1 and Ω_0 is with notation Γ_{int}. Note that Γ_{int} for each region has the opposite normal vector. The finite region Ω_1 contains two structures with embedded identical rectangular rigid/flexible

foundations with length b, width c and height h. The distance between both foundations is d, see Figure 8.1. The top sides of the left and right foundations are free surfaces and are denoted as Γ_{f1} and Γ_{f2}, while the embedded surfaces are collected in notations Γ_{g1} and Γ_{g2}. The external boundary of the finite region Ω_1 is $\Gamma_{\Omega_1} = \Gamma_{int} \cup \Gamma_F$, where $\Gamma_F = \Gamma_{f0} \cup \Gamma_{f1} \cup \Gamma_{f2}$. Here, Γ_{f0} is the free-surface in Ω_1 outside the top sides of both foundations. The internal boundaries inside zone Ω_1 are the boundaries $\Gamma_{g1} \cup \Gamma_{g2}$. Although the rectangular foundation shape is defined, an arbitrary geometry of the foundation could be considered as well. The foundations support two structures tied to the foundation's surface along their contact edge or surface. For simplicity, the structures are presented as a single-degree-of-freedom column model in Figure 8.1. However, a multi-degree-of-freedom system with any type of stress/displacement elements available in ABAQUS or combination of those elements can be considered.

Two foundations' conditions are considered: **rigid and flexible**. In the rigid case, all the degrees of freedom of the foundations' solid elements are tied to a single reference node. For the structures, only the flexible state is considered.

The external semi-infinite zone Ω_0 is layered with $N+1$ homogeneous elastic isotropic layers Ω_{0k}, $k = 1, 2, ..., N+1$, with infinitely extended boundaries. These layers are with arbitrary geometry of their boundaries Γ_i, $i = 1, 2, ..., N+1$, where the boundary Γ_{N+1} is the boundary between the N^{th} layer and the semi-infinite in depth $(N+1)^{th}$ layer containing the dynamic source $\mathbf{X}_0$. The free-surface boundary Γ_1 is the top boundary of the first layer where the finite region Ω_1 is located. Note that notation Γ_1 is the free surface of the first layer but outside the surface Γ_F, which is the free surface of the region Ω_1. The boundary of the semi-infinite region Ω_0 is defined as the boundary of all $N+1$ layers, i.e., $\Gamma_{\Omega_0} = \Sigma_{k=1}^{N+1} \Gamma_{\Omega_{0k}}$. The boundary of the first Ω_{01} layer is denoted as $\Gamma_{\Omega_{01}} = \Gamma_1 \cup \Gamma_{int} \cup \Gamma_2$, the boundary of the N^{th} layer is $\Gamma_{\Omega_{0N}} = \Gamma_N \cup \Gamma_{N+1}$ and the boundary of the $N+1$ layer $\Gamma_{\Omega_{0N+1}} = \Gamma_{N+1}$. Note that the layers $[1, N]$ are infinite along Ox_1 and Ox_2 axes and are finite only in Ox_3 direction.

The material properties of the geological semi-infinite zone Ω_0 are density ρ_{0k}, Lamé constants λ_{0k}, μ_{0k}, longitudinal wave velocity $C_{P_{0k}}$ and shear wave velocity $C_{S_{0k}}$, where $k = 1, 2, ..., N+1$. The material properties of the finite range Ω_1 are λ_1, μ_1, C_{P_1}, and C_{S_1}, while the material properties of the foundations and the structures are denoted by λ_f, μ_f, C_{P_f}, and C_{S_f}.

The initial boundary-value problem for wave propagation in the geological region under consideration consists of the governing equation in 3D elastodynamics, initial conditions, and boundary conditions as discussed in Section 4.

The computation of the layered half-space, the assembly of the BEM and FEM matrices and vectors, and the computation of the hybrid BEM-FEM model follow the procedures described in the same section.

8.3 Numerical simulations

Two case studies are presented. The 1st case study considers a wave propagation problem through a layered half-space with irregular interfaces extending to infinity, in which a finite region Ω_1 is located, see Figure 8.3. Two containment structures with embedded foundations are located in the finite zone, see Figure 8.4. The ground and the structures are exposed to low-frequency vibrations emitted by a close dynamic source. In the 2nd case study, the same structures located in a finite region are considered. This finite zone rests on a layered media in which curved boundaries reach the free surface. A long-distance dynamic source radiating transient waves is located in the seismic bed, see Figure 8.11.

Two types of time function $f(t)$ are considered. The 1st one (*type A*) is a Ricker wavelet which has frequency range of [0, 5] Hz, a dominant frequency of 2 Hz, and a time-delay of 1 s. After the application of FFT, the amplitude spectrum is normalized to the maximum absolute value (Figures 8.2a, 8.2b). The 2nd time function (*type B*) is based on the 90-degree component of the displacement time history recorded during the Northridge earthquake 1994 by Newhall station, which is available at `http://www.strongmotioncenter.org`. The time history has a time interval of 0.02 s, and it is trimmed to only include the record in the time range $t = [1, 26]$ s to reduce computation time (Figures 8.2c, 8.2d). A transfer function is applied to adjust the ground motion record to the depth of the point source $\mathbf{x}_0$.

8.3.1 Case study 1

The geological profile of the supporting soil is given in Figure 8.3 where four layers are presented. The finite region containing both structures is in the top surface layer. Each of the interfaces between the layers is curved about a line parallel to x_2 axis with different radii and extends to infinity. The finite region Ω_1 is a cuboid with a width of 400 m and a depth of 25 m. The BEM region's free surface is 1 km $\times$ 1 km. A cut view of the model in ABAQUS/CAE is given in Figure 8.5. Two foundations are embedded in the top layer. The foundations are 60 m $\times$ 60 m wide and 3.5 m thick. The separation distance between the foundations d is 40 m. Foundations of this size can be applied to tanks, cooling towers, large

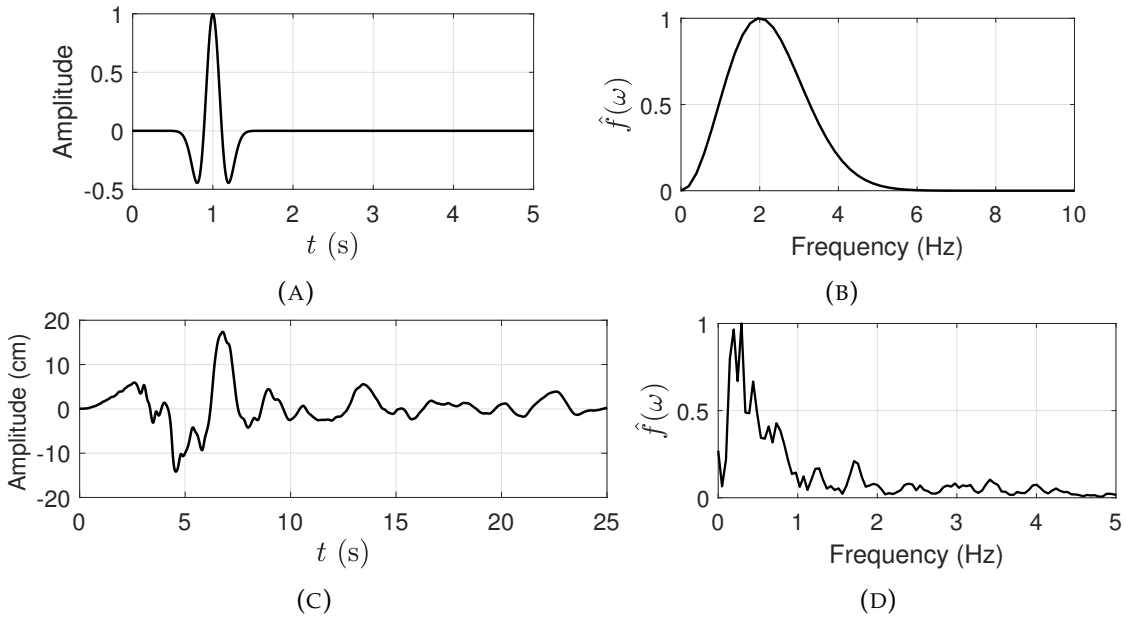

FIGURE 8.2: The time functions considered for the case studies: (**A**) the time history and (**B**) amplitude spectrum, normalized to the maximum absolute value, of the Ricker wavelet; (**C**) the trimmed time history of Northridge earthquake 1994 (90-degree displacement component); and (**D**) its amplitude spectrum, after application of a transfer function and normalization to the maximum absolute value.

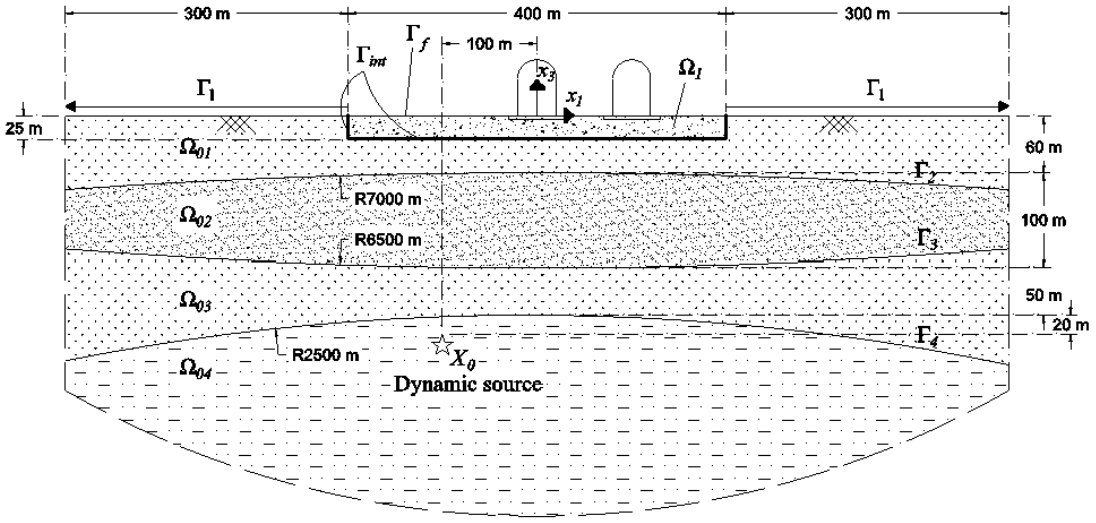

FIGURE 8.3: The model geometry of case study 1

industrial chimneys, water towers, nuclear reactors, etc. The foundations under consideration support structures common for nuclear containment purposes. The geometry of the structures is 55 m high, a combination of a cylinder and a dome. The cylinder has a radius of 20 m and a height of 35 m, while the dome has the same radius and height of 20 m. The wall of the structures is 1.6 m thick, see

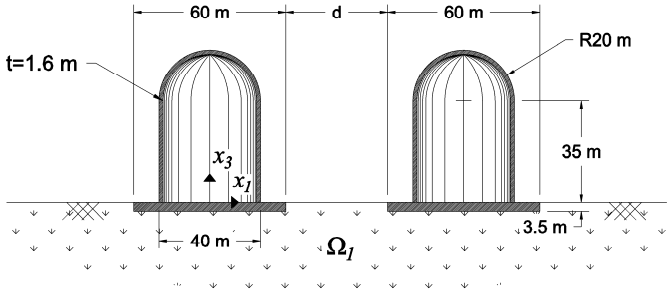

FIGURE 8.4: The geometry of two containment structures with embedded spread foundations in the finite region Ω_1 in case studies 1 and 2.

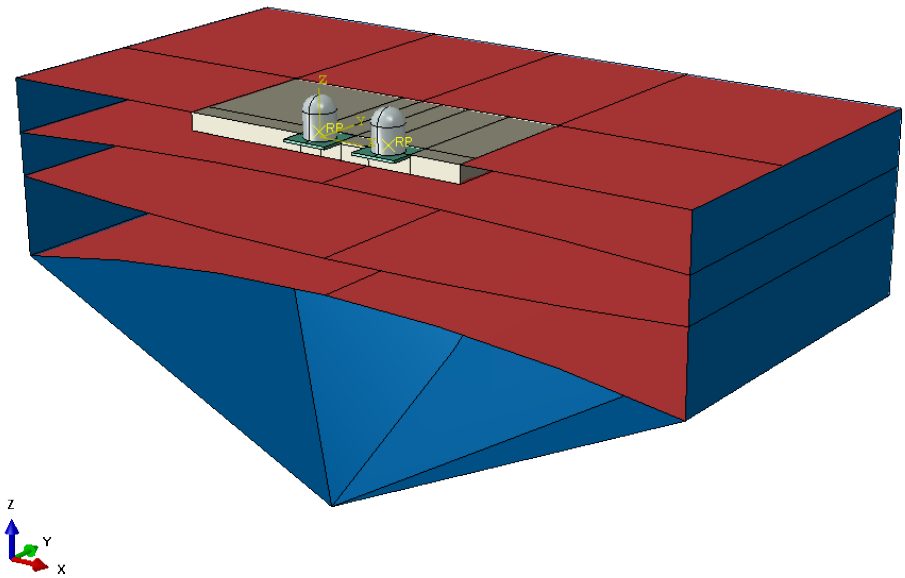

FIGURE 8.5: A cut view of the model of case study 1 in ABAQUS/CAE.

Figure 8.4. The two structures will be referred to as the west and east structures by taking the x_2 direction as the north.

The material properties of the soil layers, foundations, and structures are laid out in Table 8.1. Two cases of material properties are considered: (**A**) *Case 1a*, when the material properties of the finite region Ω_1 are the same as the properties of the layer Ω_{01} and this describes the SSI of both structures resting on the layered half-space; (**B**) *Case 1b*, when the material properties of the layers Ω_{01} and Ω_{03} are different from those of the finite region Ω_1. This presents the case of SSI of both structures located in the finite geological region, which rests on a layered half-space. No structural damping is considered for this case study, although there is no limitation.

TABLE 8.1: The material properties considered for the parametric study of case 1.

Region	λ (MN/m^2)	μ (MN/m^2)	ν	ρ (kg/m^3)
$\Omega_{01} = \Omega_{03}$ (*case 1a*)	825.00	412.50	1/3	1 650
$\Omega_{01} = \Omega_{03}$ (*case 1b*)	1 072.50	536.50	1/3	2 145
Ω_{02}	1 600.00	1 600.00	0.25	2 500
Ω_{04}	2 760.00	4 140.00	0.20	2 875
Ω_1	825.00	412.50	1/3	1 650
Structures and foundations	9 722.22	14 583.33	0.20	2 500

The whole domain under consideration is exposed to a dynamic excitation emitting from a point source at $\mathbf{X}_0$(-100 m, 0, -230 m). The time function is a Ricker wavelet (*type A*, Figures 8.2a & 8.2b) with a frequency range of [0, 5] Hz, duration of 10 s, and time resolution of 0.01 s. In the Fourier domain, the amplitude vector is $f_i^{(\Omega_0)}$(10^8 N, 0, 0) and the frequency resolution is 0.1953 Hz. The mesh element sizes of the BEM region and the soil part of the FEM region are 1/5 and 1/10, respectively, of the shortest wavelength, while the mesh element size of the structures is 1/40 of the shortest wavelength. The foundations are meshed using 702 hexahedral solid elements, and the containment structures are meshed by 1161 quadrilateral shell elements.

Figure 8.6 shows **synthetic seismograms** of the horizontal displacement u_1 at observer points along the lines $x_2 = x_3 = 0$ and $x_1 = x_3 = 0$ obtained for *case 1a* and *case 1b* of material properties. The models for flexible foundations without and with structures are considered. Both models give different wave pictures, and the seismic response's dependence on the surrounding soils' material properties is visible. Figure 8.7 shows the synthetic seismograms of the displacement component u_3 for *case 1a* of material properties. A free-field homogeneous half-space model with material properties of the lowest layer Ω_{04} is considered a reference model. The maximal displacements obtained at point $\mathbf{x}$(0, 0, 0) for the case of the reference model are used for normalization in these figures. Thus, Figures 8.6-8.7 illustrate the wave amplification in the geological region due to the arbitrary layering in the far-field zone and due to the effect of the inertial soil-structure interaction by comparing the results for flexible foundations without and with structures. The strong influence of the surrounding soil on the structure-soil-structure interaction phenomenon is clearly shown.

Figures 8.8-8.10 illustrate the **time-dependent displacement components** u_1

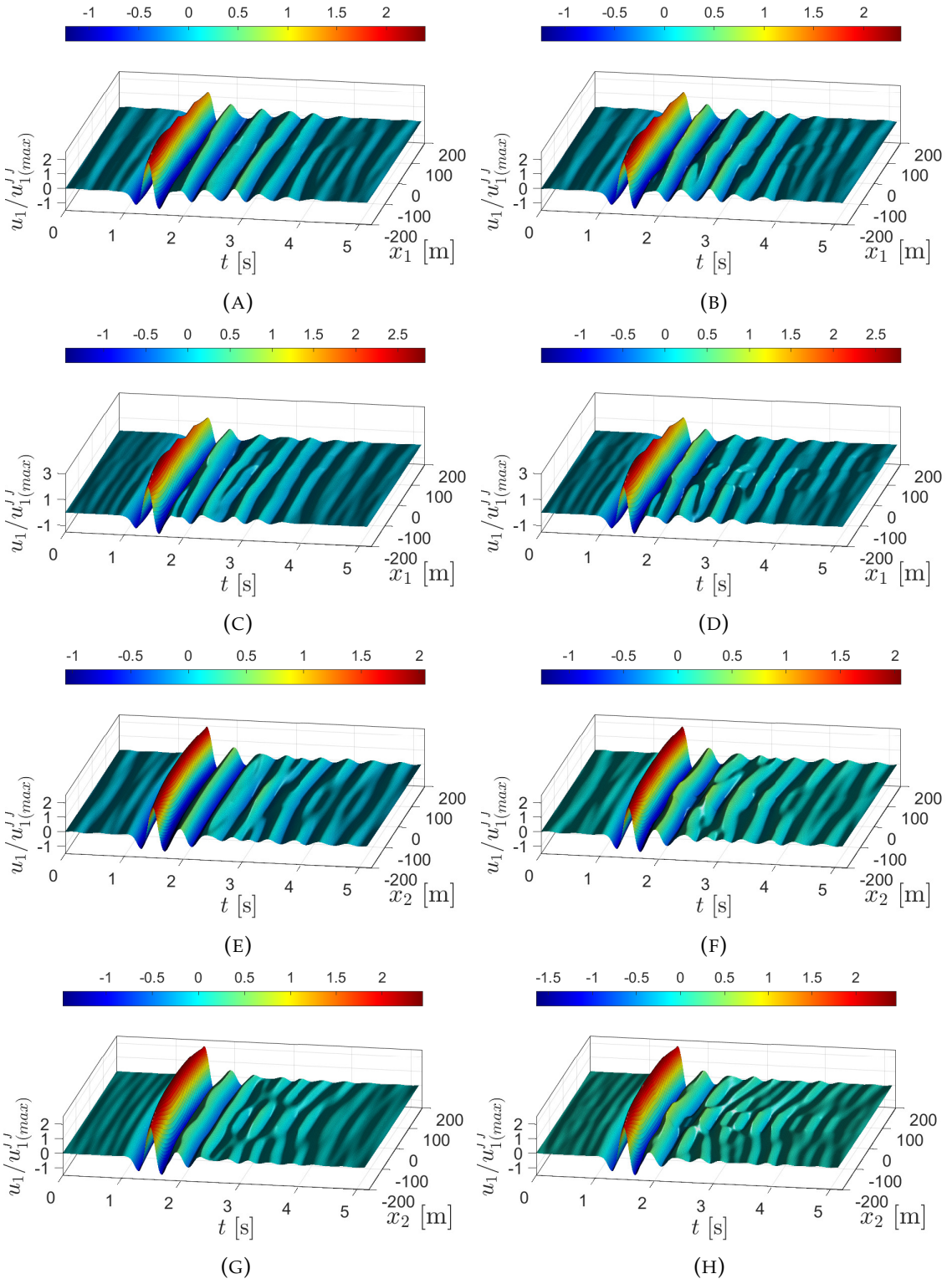

FIGURE 8.6: Normalized displacement component u_1 along the lines $x_2 = x_3 = 0$ (Figs. **A, B, C,** and **D**) and $x_1 = x_3 = 0$ (Figs.**E, F, G,** and **H**) for case study 1 with the material properties of *case 1a* (Figs. **A, B, E,** and **F**) and *case 1b* (Figs. **C, D, G,** and **H**) under the following conditions: (Figs. **A, C, E,** and **G**) flexible foundations without structures and (Figs. **B, D, F, and H**) flexible foundations with structures.

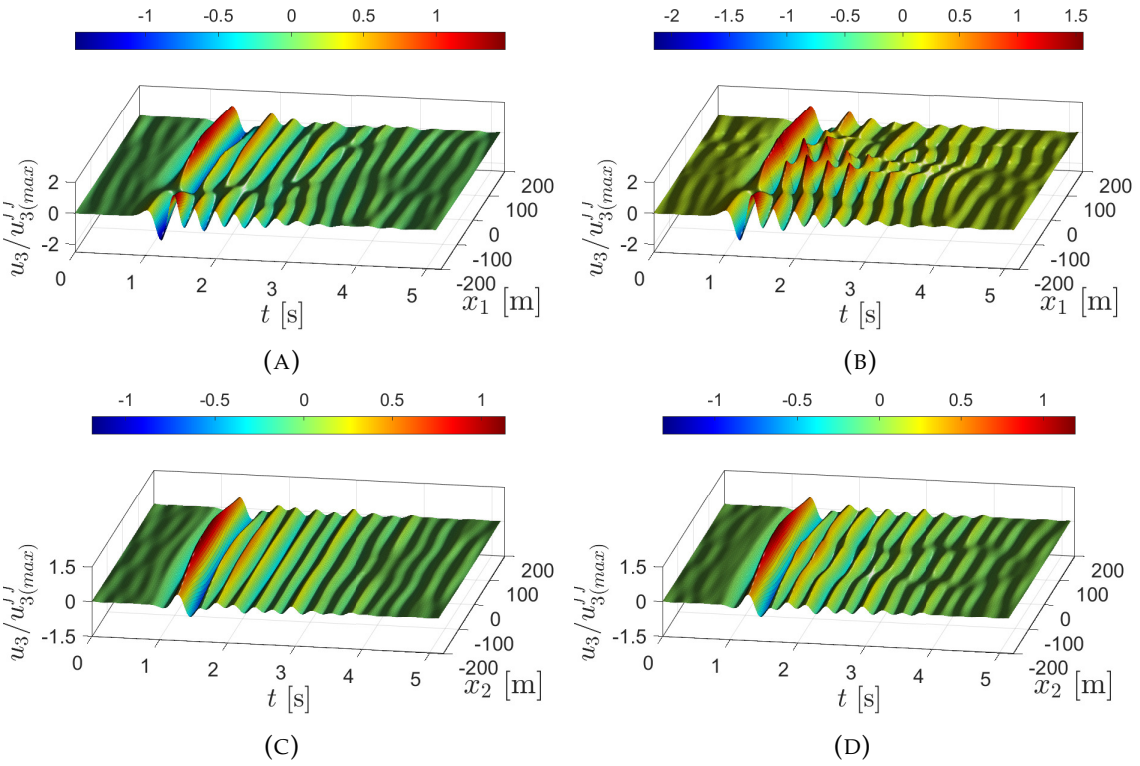

FIGURE 8.7: Normalized displacement component u_3 along the lines $x_2 = x_3 = 0$ (Figs. **A, B**) and $x_1 = x_3 = 0$ (Figs. **C, D**) for *case 1a* under the following conditions: (Figs. **A, C**) flexible foundations without structures and (Figs. **B, D**) flexible foundations with structures.

and u_3 of the west structure's tip relative to its center-base point and the corresponding frequency dependent amplitudes for different heights of the west structure. Structures heights of 55 m (Figure 8.8), 32 m (Figure 8.9), and 87 m (Figure 8.10) are considered, which correspond to pseudo-natural frequencies f_{west} of 5.59 Hz, 10.71 Hz, and 2.85 Hz, respectively. The material properties are as in the *case 1a*. These pseudo-natural frequencies are obtained by conventional frequency extraction analysis of the model containing the foundation and the structure sans the soil and by applying fixed displacement boundary conditions on the foundation.

The results obtained by the model with only the west structure are compared to those obtained by the models with the following types of the east structure: (1) the east structure has an equal natural frequency to the west structure, $f_{east} = f_{west}$; (2) the east structure has a natural frequency approximately twice that of the west one, $f_{east} \approx 2.0 f_{west}$; and (3) the east structure has a natural frequency close to half of that of the west one, $f_{east} \approx 0.5 f_{west}$. The results are normalized to the maximal absolute displacement response of the west structure for the case

without the east one.

Figures 8.8 show that an adjacent construct with equal natural frequency can induce strong resonance in both horizontal and vertical directions. The same effect but a weaker grade is observed for the horizontal displacements obtained for a relatively more rigid structure, see Figure 8.9. This is because the frequency content of the excitation is well below the structure's natural frequency. A more substantial influence of the east structure with $f_{east} = 0.52 f_{west}$ was found in the vertical response. This is likeky caused by the east structure's rocking response, which is in the low-frequency regime similar to the west structure's response. Combination of the low-frequency rocking response with the larger mass of the taller structure then lead to a stronger resonance. The same effect was not found in Figure 8.8 because the taller structure responses mainly in bending. A mild influence of the east structure was found in the softer structure (87 m) because it dissipates the incoming energy through bending, see Figure 8.10.

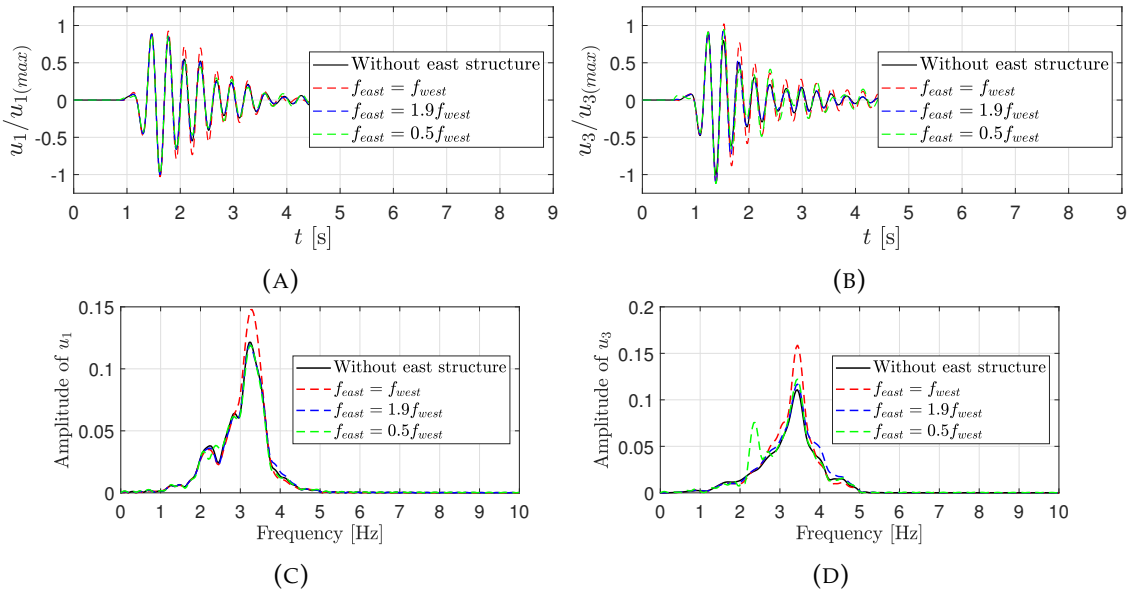

FIGURE 8.8: Normalized displacement components u_1 and u_3 of the west structure tip relative to its center-base point. *Case 1a* considering the west structure with 55 m height (Figure 8.4) and varying types of east structure: (**A**) u_1 versus time, (**B**) u_3 versus time, (**C**) Fourier amplitude of u_1, and (**D**) Fourier amplitude of u_3.

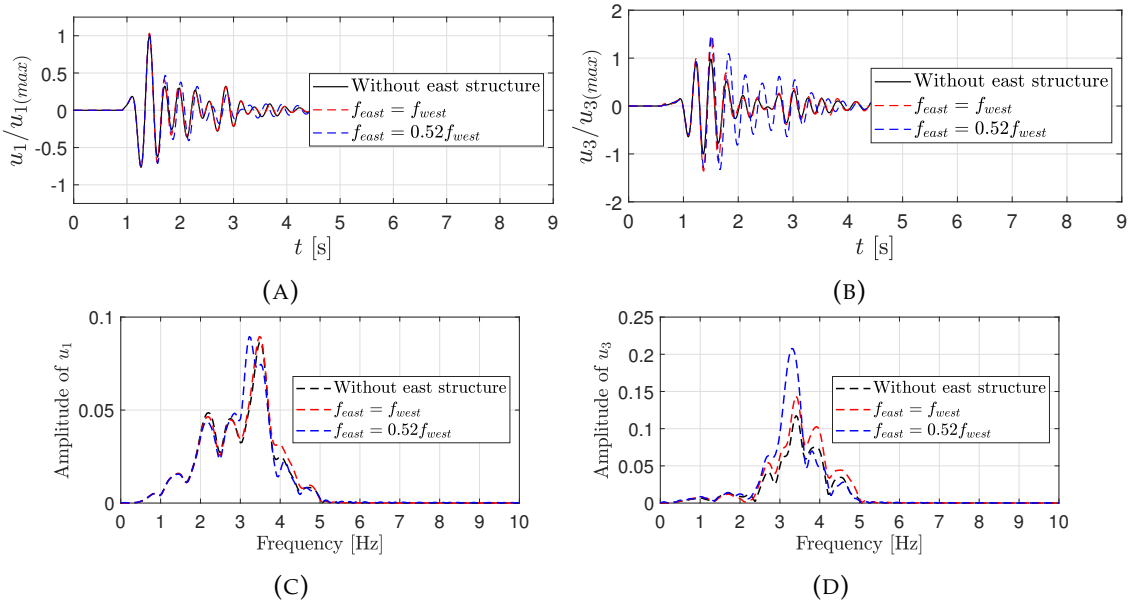

FIGURE 8.9: Normalized displacement components u_1 and u_3 of the west structure tip relative to its center-base point. *Case 1a* considering the west structure with 32 m height and varying types of east structure: (**A**) u_1 versus time, (**B**) u_3 versus time, (**C**) Fourier amplitude of u_1, and (**D**) Fourier amplitude of u_3.

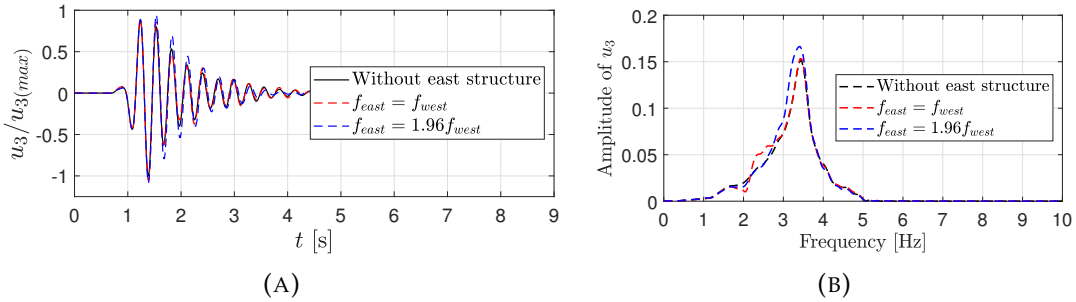

FIGURE 8.10: Normalized displacement component u_3 of the west structure tip relative to its center-base point. *Case 1a* considering the west structure with 87 m height and varying types of east structure: (**A**) u_3 versus time and (**B**) Fourier amplitude of u_3.

8.3.2 Case study 2

In the 2nd case study, the influence of a long-distance ground-borne vibration propagating to a finite sedimentary basin with two adjacent structures located in a layered half-space is examined. The problem is illustrated in Figure 8.11 where the semi-infinite half-space is comprised of three layers, and the finite region contains two containment structures identical to those in case study 1. The containment structures are referred to as the west and east structures analogously to those in case study 1. Each of the inter-layer boundaries reaches the free-surface $x_3 = 0$. The material properties are given in Table 8.2, where *cases 2a* and *2b* have a sense analogous to those in the *cases 1a* and *1b*.

Both of the **time functions** $f(t)$ described above are considered. The time function of *type A* is a Ricker wavelet with a frequency range of [0, 5] Hz, duration of 8 s, and time resolution of 0.0156 s. In the frequency domain, the resolution is 0.1252 Hz, and the amplitude vector is $f_i^{(\Omega_0)}(10^9$ N, 0, 0), see Figures 8.2a, 8.2b. The 2nd time function is the Northridge earthquake 1994 ground motion record (*type B*, see Figures 8.2c, 8.2d), where the amplitude vector in the frequency domain is $f_i^{(\Omega_0)}(10^9$ N, 0, 0) and the frequency resolution is 0.0244 Hz.

The point source is located at $\mathbf{X}_0$(-1 km, 0, -1 km), $\mathbf{X}_0$(-632.45 m, 0, -1264.9 m), or at $\mathbf{X}_0$(0, 0, -1414.2 km). For the time function of *type B*, a transfer function is applied to adjust the ground motion record to a depth of 1264.9 m. The normalization of the results is performed with respect to the maximal displacement at point $\mathbf{x}(0, 0, 0)$ obtained for the homogeneous half-space model with the material properties of the layer Ω_{03}. No structural damping is considered in the simulations for the time function of *type A*, while a 10% structural damping is used in the simulations using the time function of *type B*.

Since each layer has a boundary or boundaries reaching the free surface

TABLE 8.2: The material properties considered for the parametric study of case 2.

Region	λ (MN/m^2)	μ (MN/m^2)	ν	ρ (kg/m^3)
Ω_{01} (*case 2a*)	900.00	450.00	1/3	1 800
Ω_{01} (*case 2b*)	1 470.00	980.00	0.30	2 000
Ω_{02}	1 368.00	684.00	1/3	1 900
Ω_{03}	1 470.00	980.00	0.30	2 000
Ω_1	900.00	450.00	1/3	1 800
Structures and foundations	9 722.22	14 583.33	0.20	2 500
Structures and foundations*	972.22	1 458.33	0.20	2 500

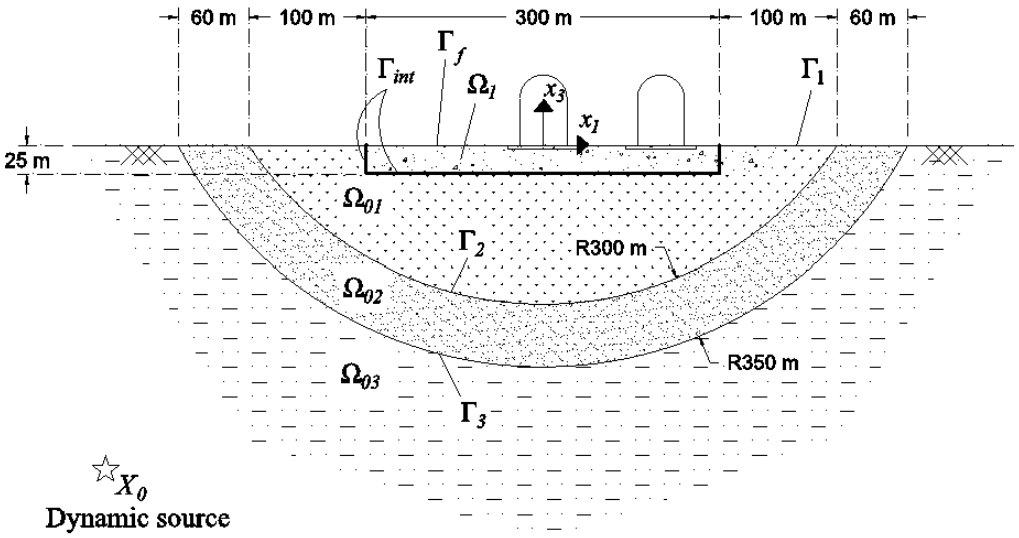

FIGURE 8.11: The model geometry of case study 2

$x_3 = 0$, the solution's accuracy is independent of the ratio of r_{BX_0}. Thus, the dynamic source can be placed anywhere within the bottom layer. Additionally, a supplementary condensation algorithm is required prior to step 2.a of the procedure described in Section 4.5. In this additional step, the matrices and vector components belonging to the free surface of the previous layer are condensed into the components belonging to the layering interface. The procedure is identical to the one described in section 4.6.

Figures 8.12-8.13 compare the results for the cases of foundations **without and with structures** and material properties of *case 2a* and *2b* where the time function is the Ricker wavelet. These figures clearly illustrate how the soil layering and the SSI strongly influence the wave field along the surface. Note that when the structures are excluded, the kinematic interaction between the foundations has an insignificant effect on the wave field because the wavelength is relatively longer than the foundations.

Further, we consider structures with **the following foundations' types**: rigid, flexible, flexible with low stiffness (Structures and foundations* in Table 8.2), and flexible with only one structure on the west present. The influence of the inertial interaction in combination with the rigidity of the foundations is clearly illustrated in Figure 8.14 showing the displacement components u_1 and u_3 along the line $x_2 = x_3 = 0$.

Figure 8.15 shows the relative displacement of the west structure's tip with respect to its center-base point for the models of foundations with structures under varying separation distance d. Material properties of *case 2b* are considered.

The seismic sources are located at points $\mathbf{X}_0$(-632.45 m, 0, -1264.9 m) and $\mathbf{X}_0$(0, 0, -1414.2 m) in Figure 8.15, which result in wave propagation angles of 63.43° or 90°, respectively, to the center-top of the west foundation. Normalization of the results is to the maximal absolute displacement responses of the single west structure when the east structure does not exist. In the former figure, a mild influence of the east structure on the west one's displacement responses u_1 and u_3 can be observed. The latter figure shows that a strong influence of the east structure on the vertical response u_3 of the west structure occurs in the cases of separation distance d of 20 m and 40 m. However, this was not observable for the horizontal response u_1. This is caused by the relative position of the point source at $\mathbf{X}_0$(0, 0, -1414.2 m) to the structures and the applied amplitude vector $f_i^{(\Omega_0)}$(10^9 N, 0, 0) which result in surface waves dominating the ground motion at the position of the structures. The displacement responses of the west structure without the east structure obtained for point sources located at $\mathbf{X}_0$(-632.45 m, 0, -1264.9 m) and $\mathbf{X}_0$(0, 0, -1414.2 m) show that at the frequency of 3.9 Hz, which is one of the dominant frequencies of the responses, the foundation under west structure is rotated by 2.64E-4° and 3.25E-3°, respectively, about x_2-axis. The higher rocking movement leads to a stronger interaction between the vertical responses of the structures.

Figures 8.16 and 8.17 show the simulation results for dynamic point source of *type B*, located at point $\mathbf{X}_0$(-632.45 m, 0, -1264.9 m). It is assumed that the material properties are the same as those of the *case 2a*, and it is accounted for 10% structural damping. The wave fields along the line $x_2 = x_3 = 0$ are presented in Figure 8.16 for cases with two containment structures at a fixed separation distance of 40 m. The west structure's height is 55 m, while the east structure has the following properties: ***(A)*** pseudo-natural frequency equal to that of the west structure, i.e., $f_{east} = f_{west}$, and ***(B)*** pseudo-natural frequency of approximately half of those of the west structure, i.e., $f_{east} \approx 0.5 f_{west}$. Figure 8.17 compare the displacement components u_1 and u_3 of the west structure's tip relative to its center-base point for the above ***(A)*** and ***(B)*** cases. The solutions are normalized analogously, such as those in Figures 8.8–8.10. Figure 8.17 reveals that the maximal horizontal and vertical displacement responses of the west structure are increased by 0.77% and by 1.83%, respectively, in the case ***(A)***. In the case ***(B)***, the horizontal and vertical responses of the west structure are increased by 7.17% and 6.41%, respectively. The influence of the lower frequency character of the east structure's behaviour on the response of the adjacent building is clearly illustrated in Figures 8.16 and 8.17.

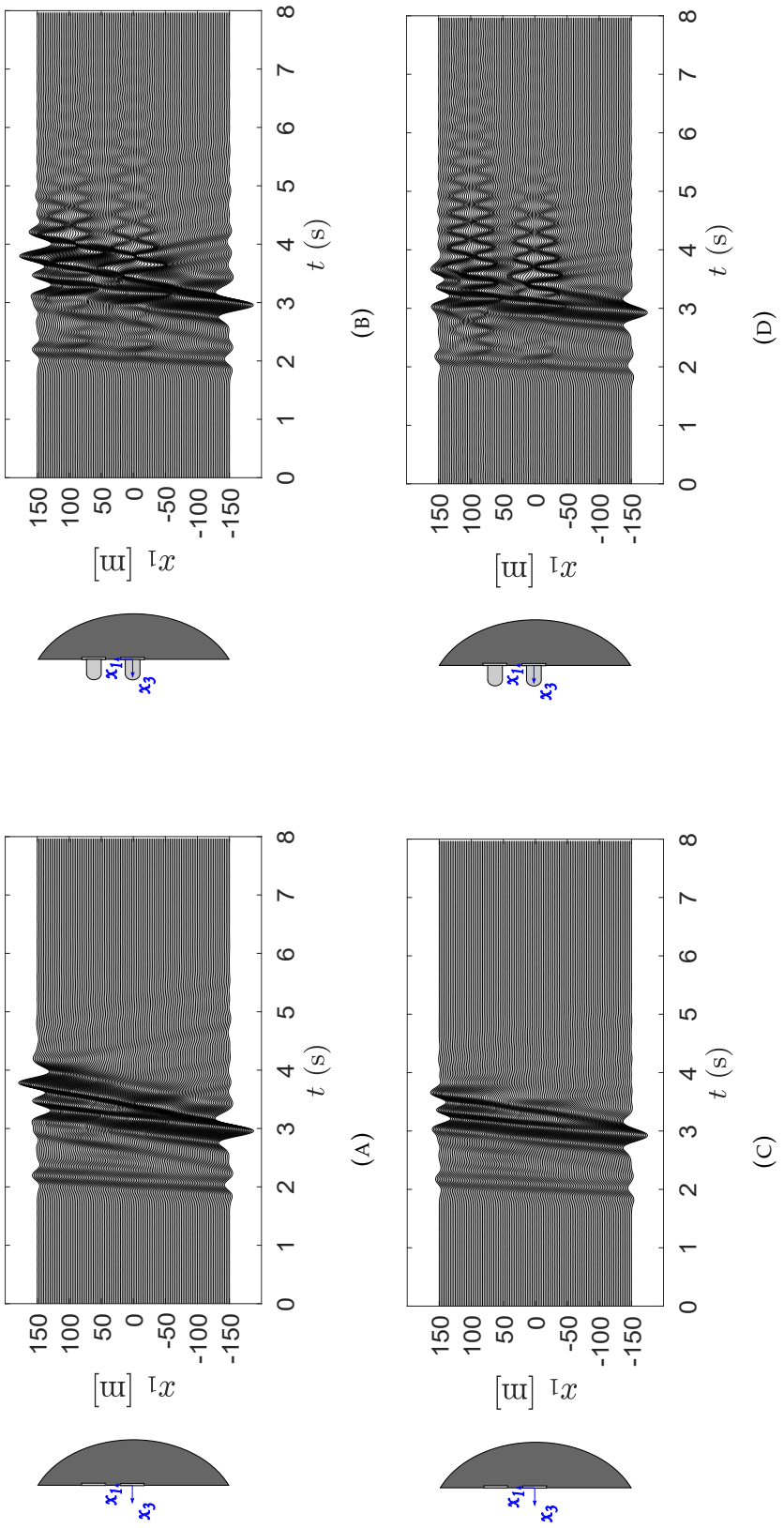

FIGURE 8.12: Comparisons of normalized displacement component u_3 along the line $x_2 = x_3 = 0$ for *case 2a* (Figs. **A, B**) and *case 2b* (Figs. **C, D**) under the following conditions: (Figs. **A, C**) foundations without structures and (Figs. **B, D**) foundations with structures. The seismic source of *type A* is embedded at $\mathbf{X}_0$(-1 km, 0, -1 km).

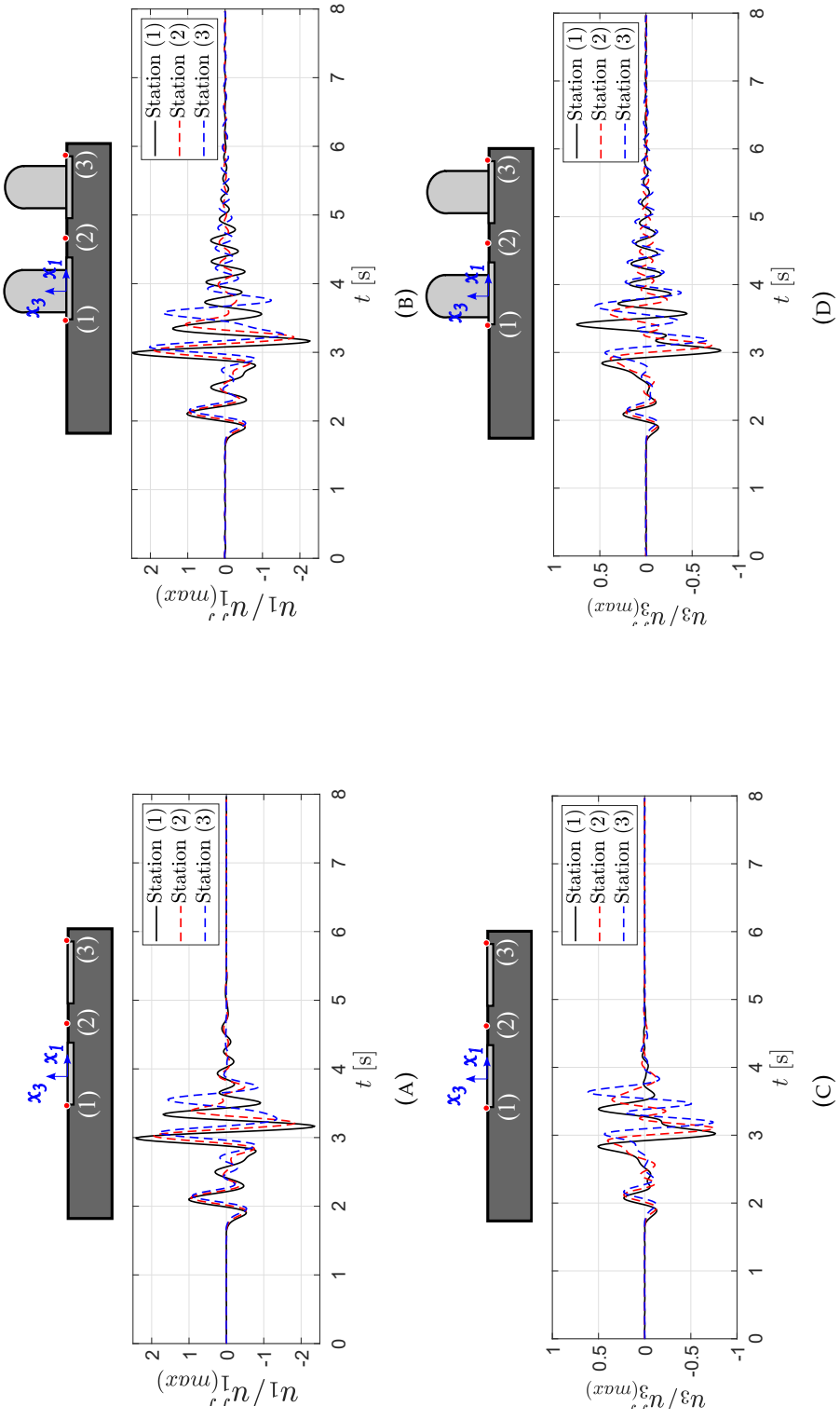

FIGURE 8.13: Comparisons of normalized displacement components u_1 (Figs. **A, B**) and u_3 (Figs. **C, D**) at observer points 1, 2, and 3 along the line $x_2 = x_3 = 0$ versus time for *case 2b* under the following conditions: foundations without structures in Figs. **A, C** and foundations with structures in Figs. **B, D**. The seismic source of *type A* is embedded at $\mathbf{X}_0$(-1 km, 0, -1 km).

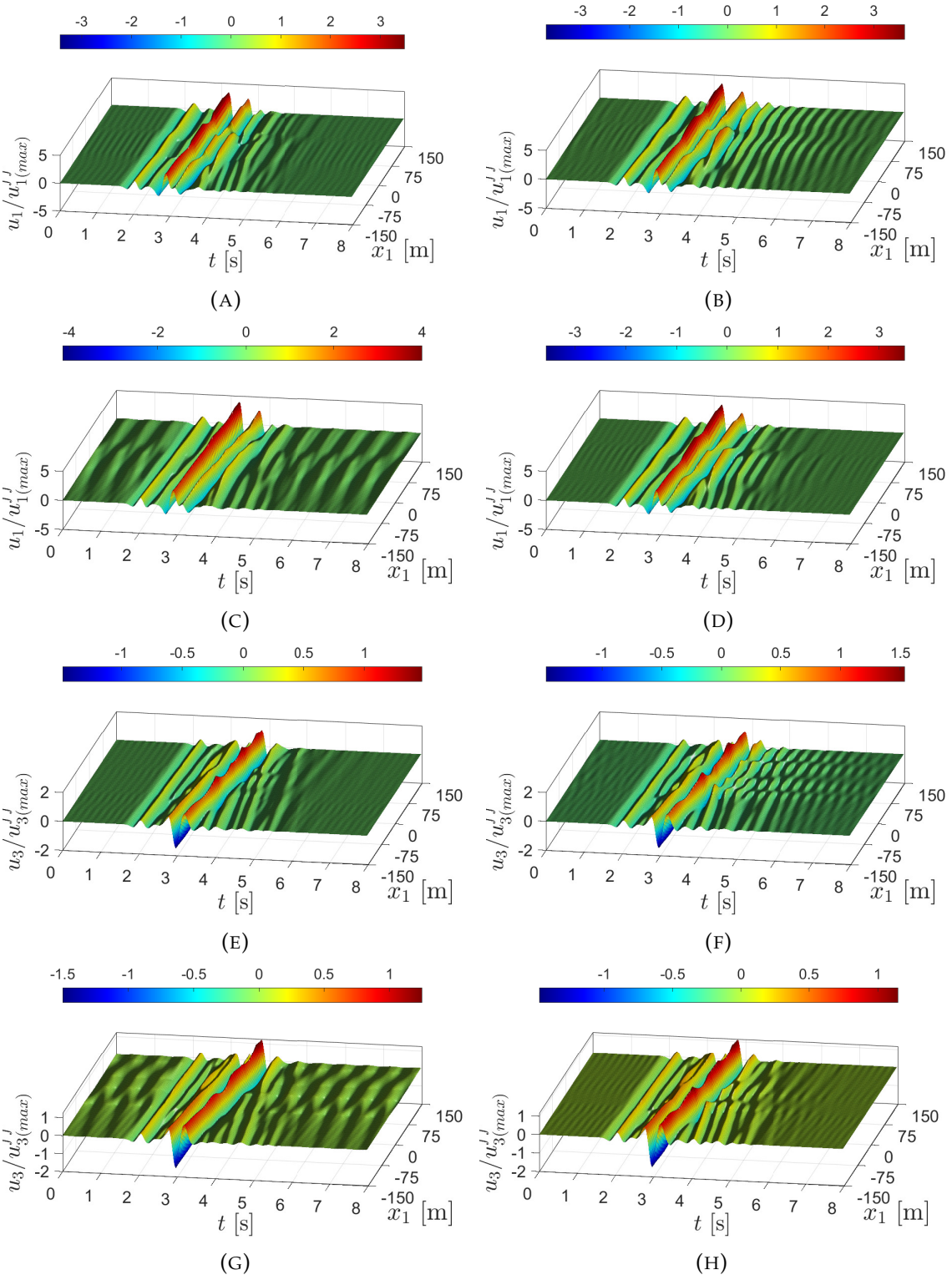

FIGURE 8.14: Normalized displacement components u_1 (Figs. **A, B, C,** and **D**) and u_3 (Figs.**E, F, G,** and **H**) along the line $x_2 = x_3 = 0$ for foundations with structures under the following conditions: (Figs. **A, E**) rigid foundations, (Figs. **B, F**) flexible foundations, (Figs. **C, G**) flexible foundations with low stiffness, and (Figs. **D, H**) single flexible foundation with structure. The seismic source of *type A* is embedded at $\mathbf{X}_0$(-1 km, 0, -1 km), and *case 2a* is under consideration.

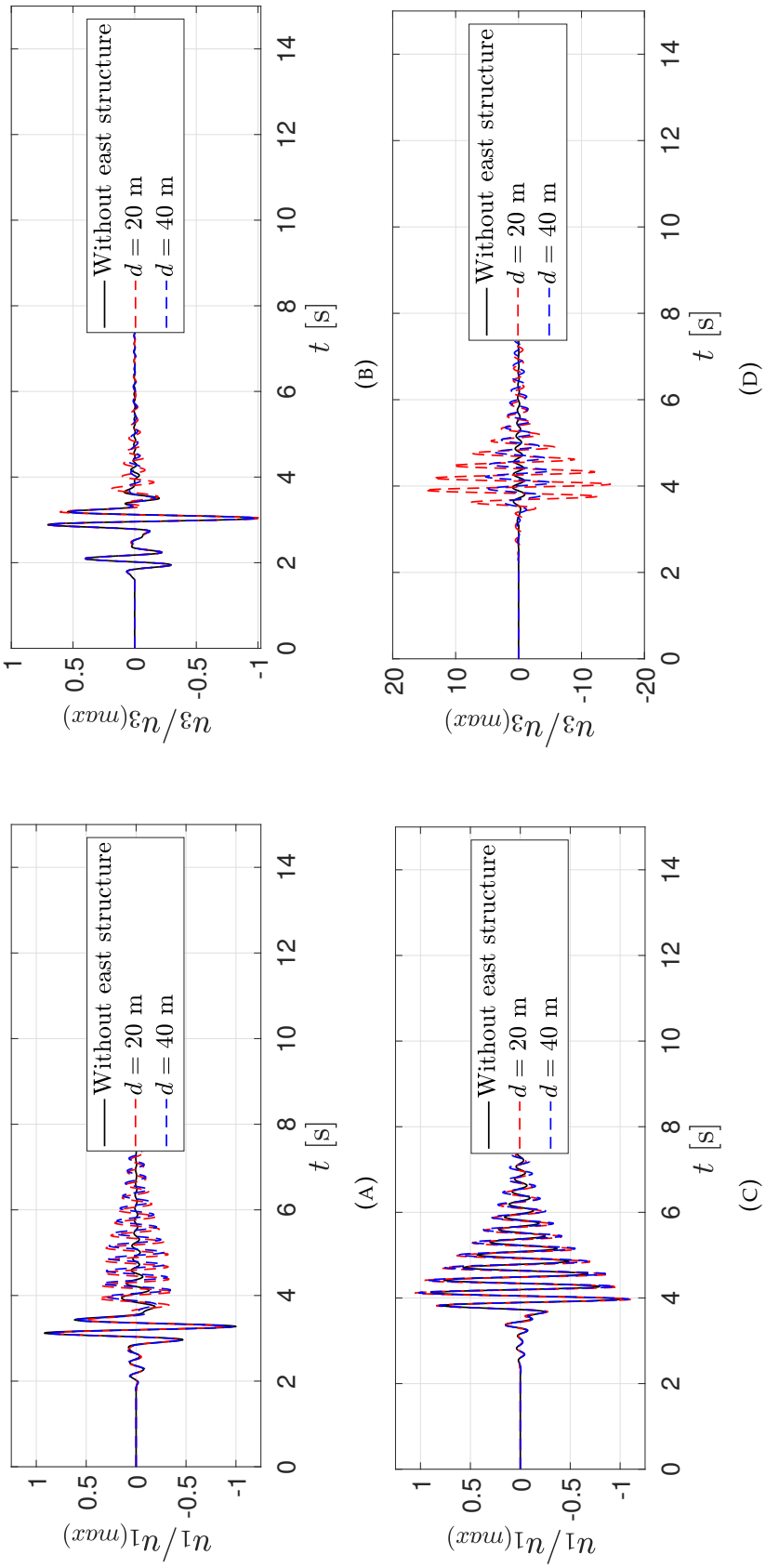

FIGURE 8.15: Normalized displacement components u_1 and u_3 of the west structure's tip relative to its center-base point for study *case* 2*b* and arrangement of foundations with structures at varying separation distance d: (**A, C**) u_1 versus time and (**B, D**) u_3 versus time. The seismic source of *type A* is embedded at $\mathbf{X}_0$(-632.45 m, 0, -1264.9 m) in Figs. (**A, B**) and at $\mathbf{X}_0$(0, 0, -1414.2 m) in Figs. (**C, D**).

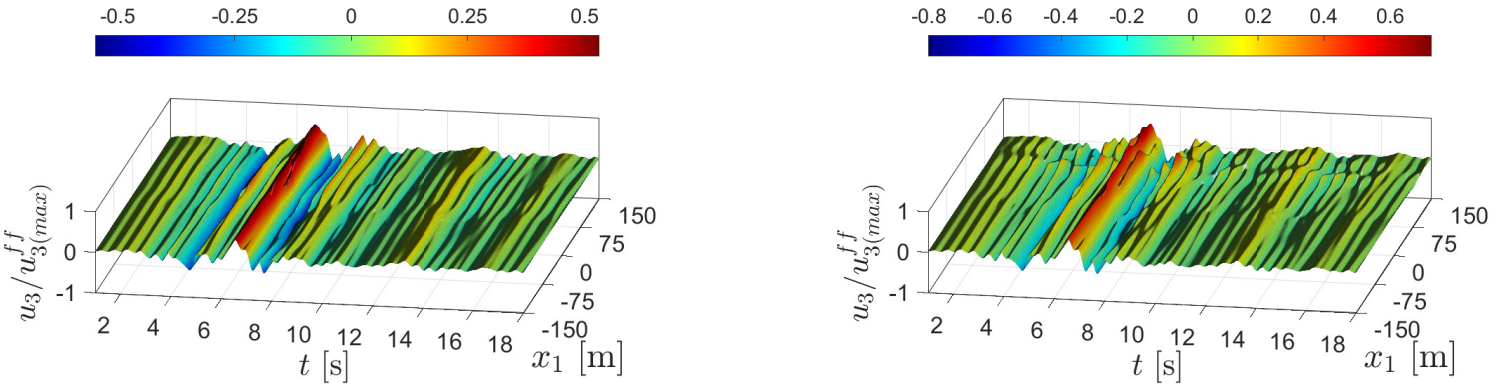

(A) (B)

FIGURE 8.16: Normalized displacement component u_3 along the line $x_2 = x_3 = 0$ for *case 2a* considering the west structure with 55 m height and the following types of east structure: (**A**) $f_{east} = f_{west}$ (**B**) $f_{east} = 0.5 f_{west}$. The seismic source of *type B* is embedded at $\mathbf{X}_0$(-632.45 m, 0, -1264.9 m).

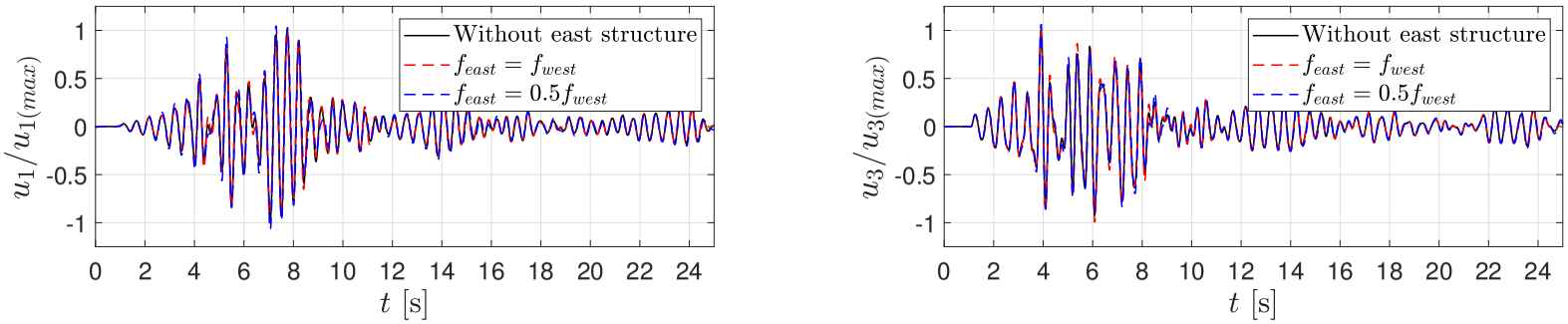

(A) (B)

FIGURE 8.17: Normalized displacement components u_1 (**A**) and u_3 (**B**), versus time, of the west structure's tip relative to its center-base point for *case 2a* considering the west structure with 55 m height and varying types of east structure. The seismic source of *type B* is embedded at $\mathbf{X}_0$(-632.45 m, 0, -1264.9 m).

8.4 Chapter summary

The two case studies of soil-structure systems on arbitrary layered half-space and the detailed geometric and parametric considerations described above illustrate a complex wave picture. The soil layering, mechanical characteristics of the far-field zone, the three-dimensional character of the dynamic wave propagation, the type and location of the dynamic source, the type and dynamic behaviour of the structures, and the structure-soil-structure interaction phenomenon strongly influence the seismic response.

Chapter 9

Application IV: Nonlinear dynamic SSI of an arch bridge and a multi-storey building.

9.1 Chapter overview

In this chapter, the application of the hybrid numerical method, in combination with the layer-wise condensation method and the sequential analysis, for case studies involving nonlinear dynamic soil-structure interaction is presented. The general description of the problem is given in Section 9.2. Case study 1 is presented in Section 9.3 followed by case study 2 in Section 9.4. The former discusses the simulation of the nonlinear dynamic response of an arch bridge in 2D plane strain in response to a short-distance ground excitation, while the latter considers a multi-storey building subjected to medium-distance ground vibrations. Case study 3 in Section 9.5 focuses on the application of the hybrid method involving a large-scale actual geometry. The industrial application of the double-couple source formulation in 2D and 3D is presented here.

9.2 General description

Three numerical case studies are presented to demonstrate the applicability of the hybrid BEM-FEM in combination with the LWC and SFTD approaches in solving complex dynamic SSI problems. The first case study considers a concrete arch bridge spanning approximately 200 m over two regions with distinct soil properties. The structure is located in a layered geological profile, and the whole domain is subjected to a short-distance dynamic transient excitation originated from a source at $\mathbf{X}_0$. The dynamic source is computed either as a point source or a

double-couple source. The problem is analysed in 2D. The influences of arbitrary layering and nonlinearities on the bridge's dynamic responses are studied.

In the second case study, a multi-storey building subjected to a ground-borne vibration, which originated from a distance point source, is simulated. The building's irregular plan results in a twisting mode shape that necessitates a 3D approach. The third case study deals with a 3D large-scale geological model obtained from a database that is processed for a seismic computation.

Two types of time function $f(t)$ based on the 90-degree component of the displacement time history recorded during the Northridge earthquake 1994 by Newhall station are considered, see Section 8.3. In the 1st time function (*type A*), only the displacement record in the time range $t = [1, 14.7]$ s is used. The time function is then extended with zeroth entries until $t = 41$ s (Figures 9.1a, 9.1b). This is chosen so that the simulation time window is sufficient for the damping effect. The 2nd time function (*type B*) is using the displacement record in the time range $t = [1, 26]$ s, see Figures 9.1c, 9.1d. No transfer function is applied to the ground motion record. A bandpass filter of $[0.05, 25]$ Hz is applied to both time functions. Smoothings are also applied to the vicinity of the trimming points to avoid artificial high-frequency contents.

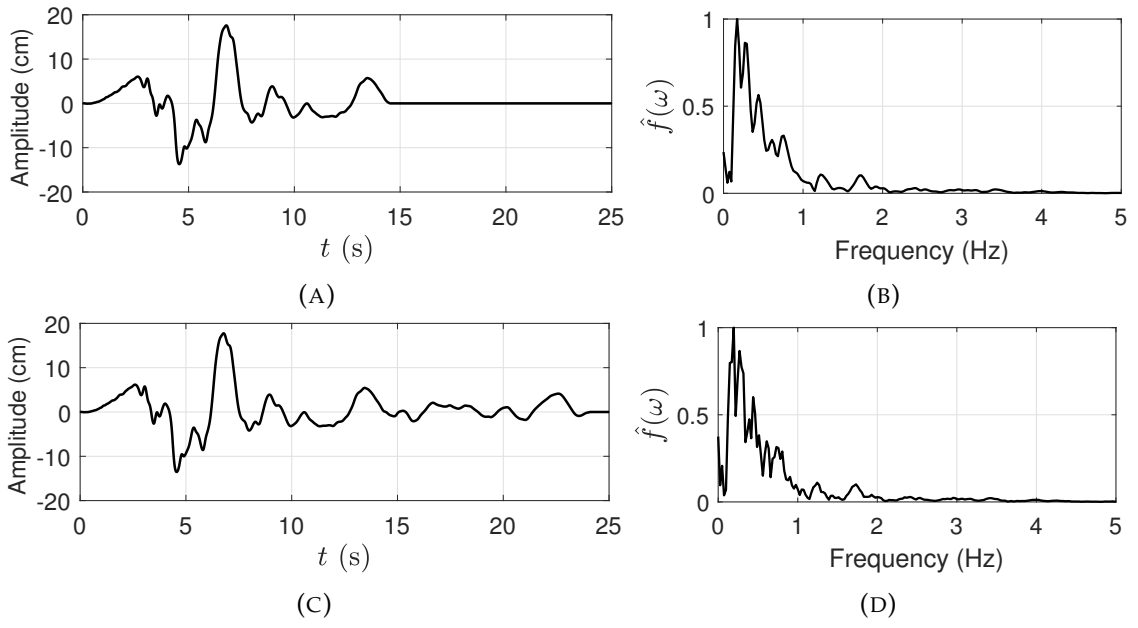

FIGURE 9.1: The time functions considered for the case studies: (**A**) the time history of *type A* and (**B**) its normalized amplitude spectrum; and (**C**) the time history *type B* and (**D**) its normalized amplitude spectrum.

The problem statement follows those described in Section 7.2 for a single-layered BEM model and Section 8.2 for a multi-layered one. One exception is that

only a single structure is considered in each case study.

As before, the BEM and FEM regions are denoted as Ω_0 and Ω_1. The interface boundary between both regions is with notation Γ_{int}. Note that Γ_{int} for each region has the opposite normal vector. The finite region Ω_1 contains a structure and can contain LN number of near-field soil regions, $\Omega_{1(j)}, j = L1, L2, ..., LN$. In case study 1, where a 2D plane strain problem is simulated, the coordinate system is Ox_1x_2 instead of $Ox_1x_2x_3$.

The external semi-infinite zone Ω_0 is layered with $N+1$ homogeneous elastic isotropic layers Ω_{0k}, $k = 1, 2, ..., N+1$, with infinitely extended boundaries. These layers are with arbitrary geometry of their boundaries Γ_i, $i = 1, 2, ..., N+1$, where the boundary Γ_{N+1} is the boundary between the N^{th} layer and the semi-infinite in depth $(N+1)^{th}$ layer containing the dynamic source $\mathbf{X}_0$.

The material properties of the geological semi-infinite zone Ω_0 are density ρ_{0k}; Lamé moduli λ_{0k}, μ_{0k}; wave velocities $C_{P_{0k}}$, $C_{S_{0k}}$; where $k = 1, 2, ..., N+1$. The material properties of the finite range Ω_1 are $\lambda_{1(j)}$, $\mu_{1(j)}$, $C_{P_{1(j)}}$, and $C_{S_{1(j)}}$, where $j = L1, L2, ..., LN$, and the material properties of the foundations and the structures are denoted by λ_f, μ_f, C_{P_f}, and C_{S_f}. Material nonlinearity is considered in the soil and the structural members. The Mohr-Coulomb model and Drucker-Prager (cap) plasticity model are two constitutive models for the soil. The two constitutive models are chosen to simplify the computation since the focus is on the application of the method. Note that constitutive models which simulate early nonlinear behaviour in soil, e.g., hypoplastic model (Herle and Gudehus, 1999), may not be suitable in this application since it introduces widespread nonlinearity on the soil region. In addition to the material nonlinearity, frictional and separable contact between the soil and foundation is also taken into account.

The initial boundary-value problem for wave propagation in the geological region under consideration consists of governing equations in 3D elastodynamics, initial conditions, and boundary conditions, as discussed in Section 4. Initial conditions of stresses are applied to the soil region to establish geostatic stress prior to the implicit dynamic computation. The computation of the layered half-space, the assembly of the BEM and FEM matrices and vectors, and the computation of the hybrid BEM-FEM model follow the procedures described in the same section.

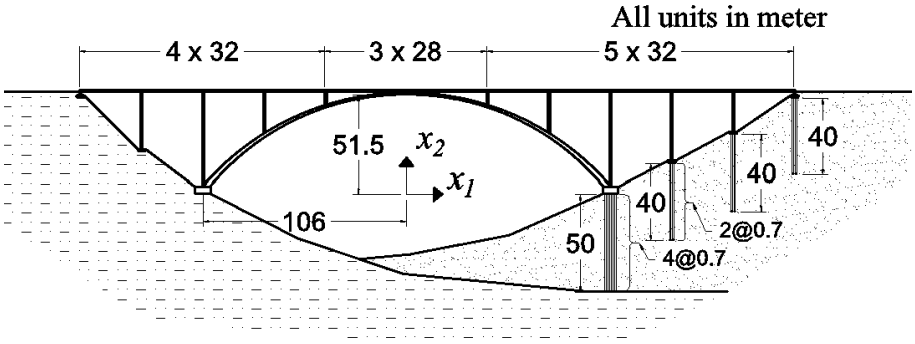

FIGURE 9.2: The bridge geometry of case study 1.

TABLE 9.1: The material properties considered for case study 1.

Region	λ (MN/m^2)	μ (MN/m^2)	ν	ρ (kg/m^3)
$\Omega_{1(L1)}$	441.00	220.50	1/3	1 800
$\Omega_{1(L2)}$	1 620.00	1 620.00	0.25	2 000
Ω_{01}	1 620.00	1 620.00	0.25	2 000
Ω_{02}	3 024.00	3 024.00	0.25	2 100
Ω^*_{02}	147.00	220.50	0.25	1 800
Ω_{03}	3 450.00	5 175.00	0.20	2 300
Structure and foundations	8 333.35	12 500.00	0.20	2 500

9.3 Case study 1

The 1st case study considers the dynamic response of a concrete arch bridge subjected to a short-distance transient excitation from a line source at $\mathbf{X}_0$, see Figure 9.2. The bridge is built over a valley with **different material properties in each bank**. The west bank, assuming the positive x_1-direction as the east, is composed of stiff material while the east bank is a sediment basin composed of a softer one, see Figure 9.3. Due to this, **pile foundations** are used to support the east part of the bridge. The four piles of the east foundation of the arch structure reach the stiff soil layer at a depth of 50 m, while the rests rely on frictional resistance, i.e., floating piles. The arch bridge has a c.t.c. distance of 212 m, and its crown is 51.5 m high from the foundation level. The bridge is analysed in 2D plane strain. The arch structure is 2.75 m thick at the base and 1 m thick at the crown. The piers are 1 m thick, and the piles are 0.7 m thick. A continuous connection is assumed between the piers and the slab. The bridge and the sedimentary basin are located on top of a geological profile that consists of three layers, as shown in Figure 9.3. The arch bridge, the sedimentary basin, and a portion of the stiff soil layer are modeled in the FE subdomain, while the rest of the geological profile is modeled in the BE subdomain.

The material properties considered for this case study are laid out in Table

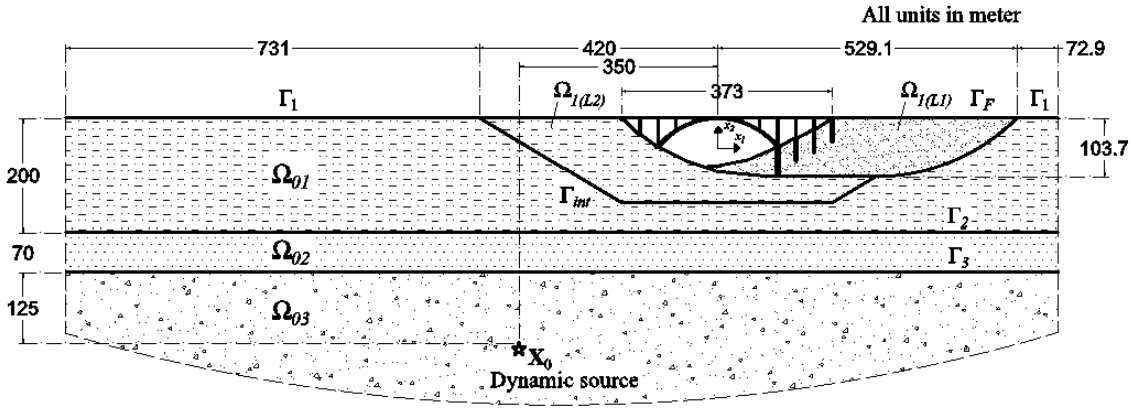

(A)

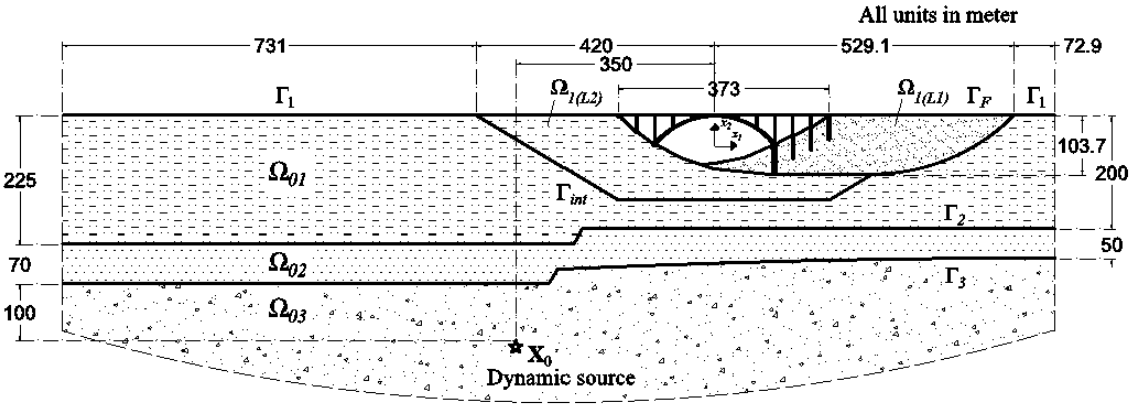

(B)

FIGURE 9.3: The model geometries of case study 1: (**A**) the geometry of *type 1* and (**B**) the geometry of *type 2*.

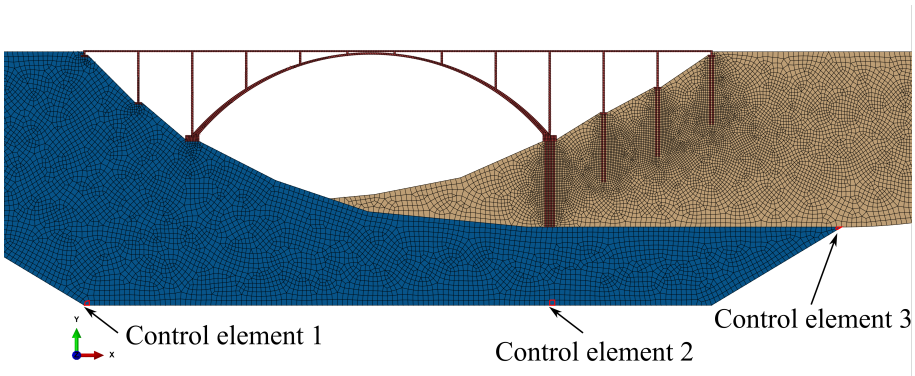

FIGURE 9.4: Three control elements of case study 1.

9.1. A 10% structural damping is applied to all materials in the frequency domain phase. The damping definition is replaced with the Rayleigh coefficient of $\alpha_R = 2.356$ and $\beta_R = 0.00079577$ in the time domain phase. Nonlinear material

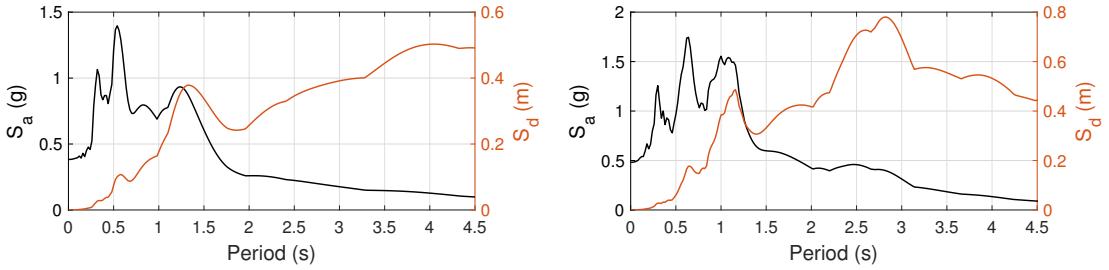

FIGURE 9.5: The spectral acceleration and displacement of the ground motion (horizontal component) measured at the east arch's base due to (**A**) a point source and (**B**) a double-couple source.

behaviour is defined for the soft soil region $\Omega_{1(L1)}$ using Mohr-Coulomb elasto-plastic criterion: friction angle of 25°, dilation angle of 5°, and cohesion of 5 kPa. **Frictional and separable contact definitions** are used for the soil-foundation and soil-pile interfaces located on the bridge's east side. The frictional coefficient is defined as 0.8. Tied contact is used for the soil-foundation interfaces located on the west side. In addition, the Mohr-Coulomb definition is also used for the concrete material: friction angle of 42°, dilation angle of 0°, and cohesion of 15 MPa. No tension cut-off or crack definition is used for this case study. The material properties of Ω^*_{02} are only used in the study of the influence of irregular geometry. They are not considered in the study of the influence of nonlinearities.

Two types of geometry of the semi-infinite domain are modeled to study **the influence of arbitrary layering** on the dynamic response of the bridge. In the geometry of *type 1*, the layering interfaces of the semi-infinite region Γ_1 and Γ_2 are horizontal lines, see Figure 9.3a. In the 2nd type of geometry, an irregularities along the interface is included, see Figure 9.3b. These irregularities can be present due to a minor fault or other historical geological events. In both types of geometry, a ratio of $r_{B\mathbf{X}_0} \geq 1.7$ is maintained, see Section 4.7.

Time function *type A* is applied to a line source located at $\mathbf{X}_0$(-350 m, -395 m). For **the point-source case**, the amplitude vector in the frequency domain is $f_i^{(\Omega_{03})}$(5.0E11 N, 0, 0). The time function has a time interval of 0.02 s and a frequency resolution of 0.024406 Hz. In the case of a **double-couple source**, the fault geometry is described as $\{\phi_{DC} = 90°, \delta_{DC} = 45°$, and $\gamma_{DC} = 90°\}$, while the seismic moment is M_0 = 1.0E8 Nm. The point-source formulation is used for the study of the influence of nonlinearities, while the double-couple one is used for the study of the influence of arbitrary layering.

In order to accurately simulate the nonlinear soil strength and the loading

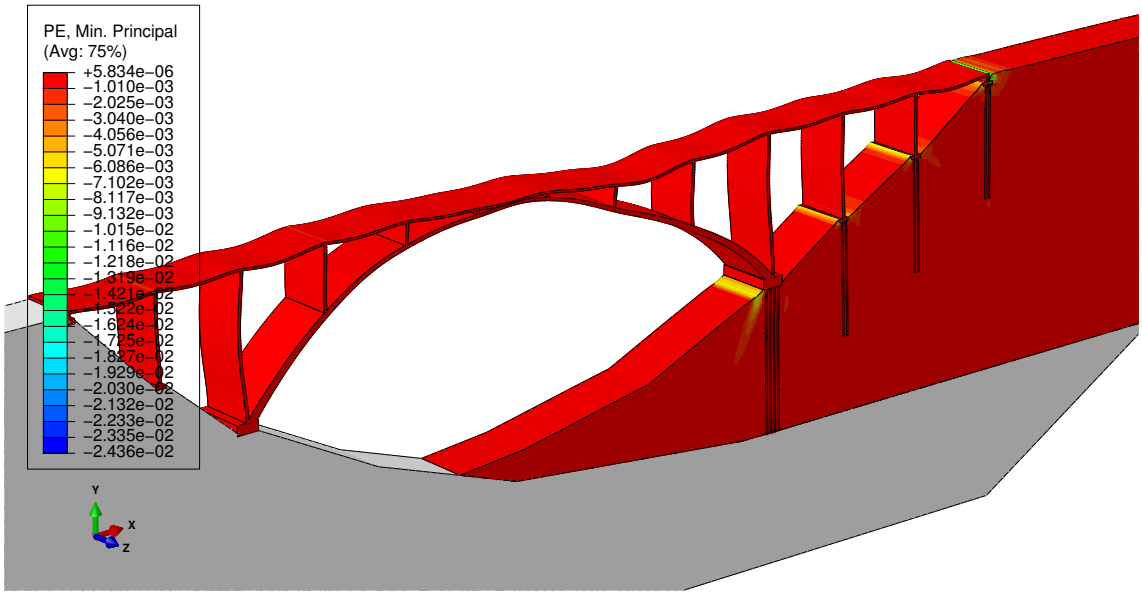

FIGURE 9.6: A minimum principal plastic strain plot of the geometry of *type 1*'s result (view with extrusion and a deformation scale of 25).

condition of the system, **a geostatic and a static loading step** are inserted before the implicit dynamic analysis step. Due to the irregular contour of the valley, the geostatic step is performed by first running **a dummy geostatic step**, i.e., without any other static or dynamic step. In this dummy step, the initial geostatic stress, the gravity load, and overburden loadings are applied to the model as a normal geostatic step. In addition, encastré boundary conditions are applied to all soil regions, and the reaction forces of all of the fixed nodes are recorded using the command "*Node print, nset=*node_set_name*" followed by "RF" in the next line. The recorded reaction forces are then used as nodal forces in the actual geostatic step. Using this approach, the initial geostatic stress can be established in an irregular and layered soil model with a highly satisfactory result.

In the geostatic step, **overburden surface loads** equivalent to 1 m high material are applied to the west and east banks. In the static loading step, the gravity load is applied to the bridge structure with an additional 200 kg/m load applied on its top surface. No traffic load is assumed.

For this case study, CPE4 and CPE3 (plane strain) elements of ABAQUS are used for the finite region, while B21 (beam) elements of ABAQUS are used for the BEs. In this implementation of using the beam element as a BE, the material is placed on the left-hand side of the element's direction. The finite and boundary element sizes are $\lambda_S/20$ of the shortest wavelength.

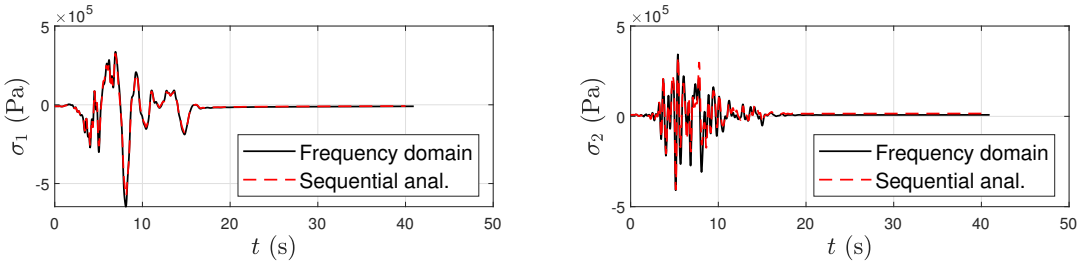

(A) Control element 2

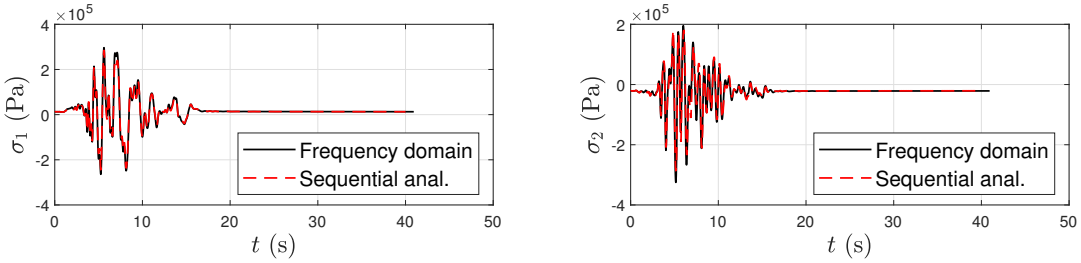

(B) Control element 3

FIGURE 9.7: Comparisons of stress components σ_j at integration points in the control elements between the results for the hybrid model in the frequency domain and for the sequential analysis with the nonlinearities. The geometry of *type 2* is considered.

The control elements that are chosen to check the compliance of the compatibility and equilibrium condition of stress are shown in Figure 9.4. The comparison of the stress components σ_1 and σ_2 between the frequency domain and the sequential analysis results are presented in Figure 9.7. The *MSE*s σ_1 and σ_2 for the time range of $t = [0.4, 25]$ s are 0.526% and 0.68%, respectively, while the *MAE*s are 3.81% and 3.86%, respectively. In Section 5.4, it is shown that these values are sufficient to obtain a consistent result.

The dynamic transient point-source excitation results in a strong ground motion, which spectral acceleration and displacement for the horizontal component are shown in Figure 9.5. Figure 9.6 shows the east bank's minimum **principal plastic strain** plot. The highest plastic strains are found in the slope area near the arch's east foundation, the slope near the east-most foundation, and the backfill behind this foundation. Further details also reveal that the piles under the east foundation of the arch experience plastic strain. This is due to the nature of an arch structure, which transfers the vertical loads it carries into horizontal loads in the foundation, in combination with the high horizontal shaking of the applied ground motion.

Figure 9.8 shows the comparison of displacement components $u_j, j = 1, 2$, measured at the bridge's crown for the sequential analysis results between the cases without and with the nonlinearities. In Figure 9.9, the same comparison

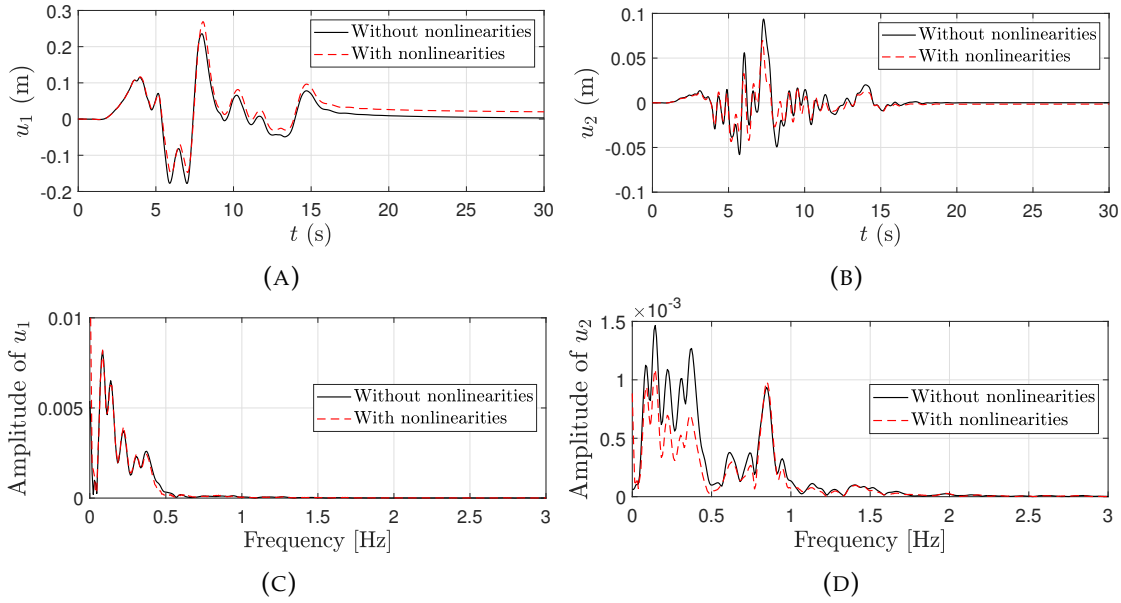

FIGURE 9.8: Comparisons of displacement components u_j measured at the bridge's crown for the results of the sequential analysis between without and with the nonlinearities. The geometry of *type 2* is considered. (**A**) u_1 versus time and (**B**) its Fourier amplitude, (**C**) u_2 versus time and (**D**) its Fourier amplitude.

is given for the displacement measured at the crown relative to the east foundation. These figures show that the nonlinearities of the surrounding soil and the slippage and detachment of the foundation and the pile can significantly affect the structure's response. Although Figure 9.8 shows reduced absolute displacements, Figure 9.9 reveals 34.39% increases in the maximum relative horizontal displacement. In contrast, the relative vertical response is increased in the lower frequency range. This implies that the structural members experience higher internal forces due to the nonlinearities. Principal stresses measured at the base of the east-arch show that an increase of 66.81% in the tension stress and a decrease of 13.21% in the compression stress are observed when the nonlinearities are considered, see Figure 9.10.

Comparisons between the results of the analyses using **two types of geometry** are given in Figure 9.11. In this figure, a double-couple type dynamic excitation is considered, and the material properties of Ω_{02}^{*} are used instead of Ω_{02}. The displacements are normalized to the maximum displacement of the result for geometry *type 1*. It can be observed that the change in the layering's interface affects the structure's displacement. Compared to the results obtained for the geometry of *type 1*, the horizontal and vertical normalized displacements of the results for the geometry of *type 2* are 18.57% and 22.89% higher. When the material properties of Ω_{02} are considered, the relative differences are below 3%. These results

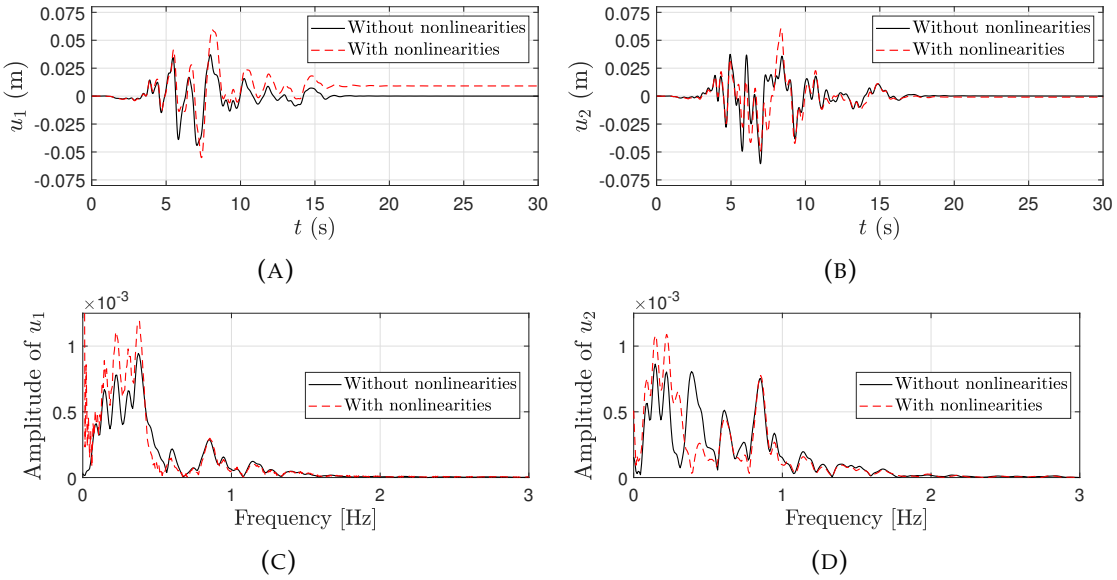

FIGURE 9.9: Comparisons of displacement components u_j measured at the bridge's crown relative to the east foundation's base for the results of the sequential analysis between without and with the nonlinearities. The geometry of *type 2* is considered. (**A**) u_1 versus time and (**B**) its Fourier amplitude, (**C**) u_2 versus time and (**D**) its Fourier amplitude.

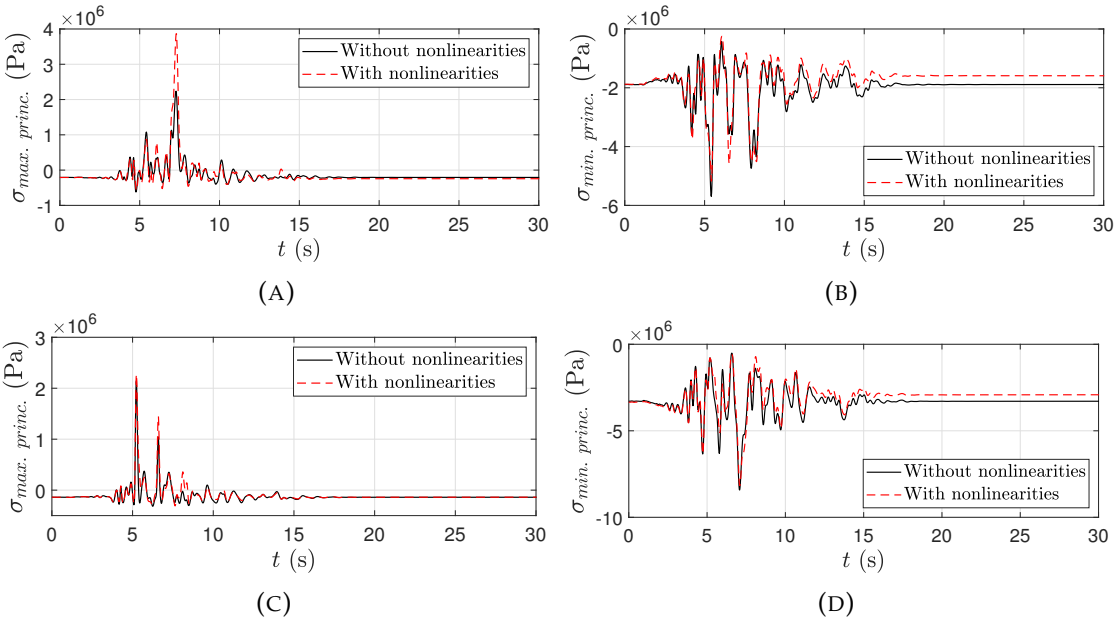

FIGURE 9.10: Comparisons of maximum and minimum principal stresses measured at elements at the east arch's base (**A** and **B**) and west arch's base (**C** and **D**) for the results of the sequential analysis between without and with the nonlinearities. The geometry of *type 1* is considered. $\sigma_{max.princ.}$ versus time in (**A** and **C**) and $\sigma_{min.princ.}$ versus time in (**B** and **D**).

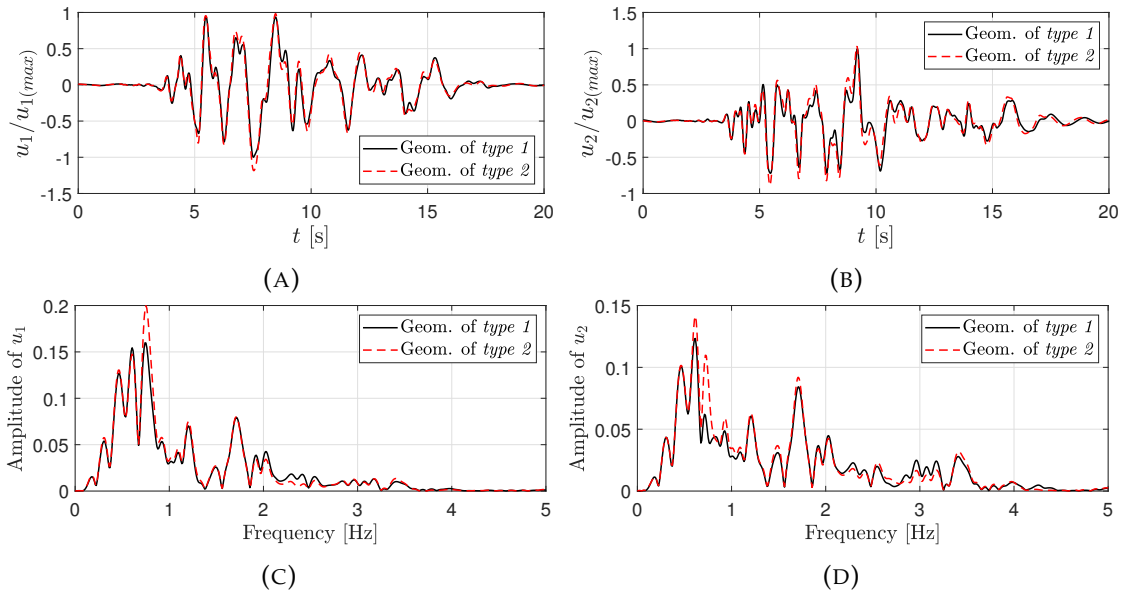

FIGURE 9.11: Comparisons of normalized displacement components u_j measured at the bridge's east foundation base for the results between geometries of *type 1* and *type 2*. A double-couple source type is considered. (**A**) u_1 versus time and (**B**) u_2 versus time, (**C**) Fourier amplitude of u_1, and (**D**) Fourier amplitude of u_2.

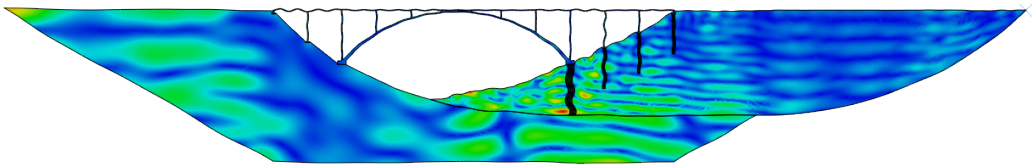

FIGURE 9.12: The wave field in the finite region for the simulation with the geometry of *type 2* and a double-couple source. The frequency is 18.51 Hz

show that the effect of geometrical irregularities/discontinuities depends on the propagating waves' length. One can also see the differences between the wave field produced by a single-point source and a double-couple one by comparing Figures 9.9 and 9.11 or the spectral responses in Figure 9.5. The double-couple solution results in a wave field with more potent high-frequency contents. Figure 9.12 depicts the wave field in the finite region at a frequency of 18.51 Hz due to a double-couple source.

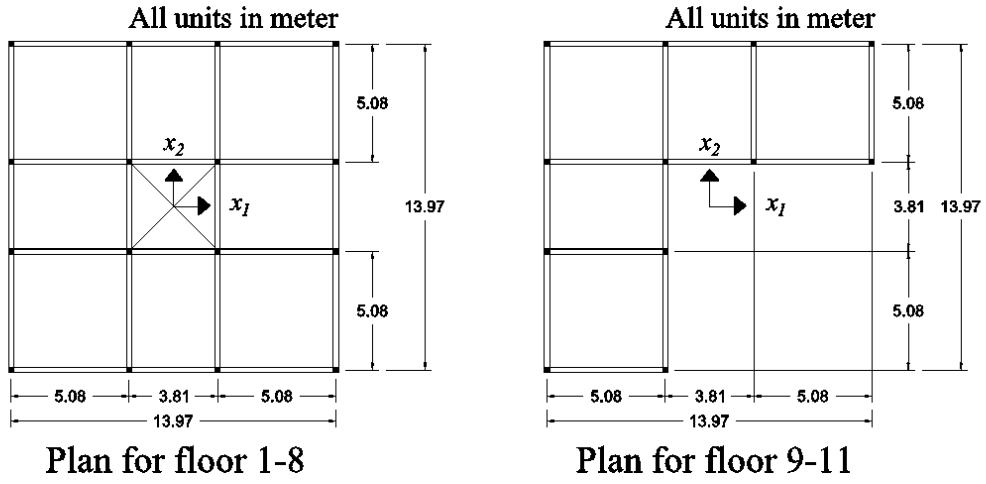

FIGURE 9.13: The floor plan of the multi-storey building for case study 2.

9.4 Case study 2

The model geometry for the second case study is presented in Figures 9.13, 9.14, and 9.15. A multi-storey building with one basement and 11 floors is considered. The floor plan is partially reduced from floor 9 to floor 11, which results in a setback in the southeast side (positive x_2 direction as the north). 1.4 m square footings support the structure in 4 corners and 2 m square footings in other areas. A floating monopile supports each footing with an embedded length of 8 m and a diameter of 0.7 m. The footings are fully embedded into the soil (Figure 9.14). The finite zone contains the structure, the foundations, and the surrounding soil, while the semi-infinite region is modeled using BEM.

The columns and beams are steel, while the slabs, footings, and piles are concrete. The soil properties are assumed to be homogeneous for the semi-infinite region Ω_0 and the near-field region Ω_1. It is assumed that the soil is preconsolidated or preloaded before construction. **The material properties** are given in Table 9.2. The section profiles of the column and the beams are of the box shape, and the dimensions are laid out in Table 9.3. The slabs have a thickness of 20 cm, and reinforcement bars are installed in two directions. The inclusion of the damping definition and its values are the same as in case study 1, i.e., a structural damping of 10% and its equivalent Rayleigh coefficients.

A transient dynamic excitation in the type of **a point source** with the time function of *type B* is considered for this case study (Figure 9.1). The time interval

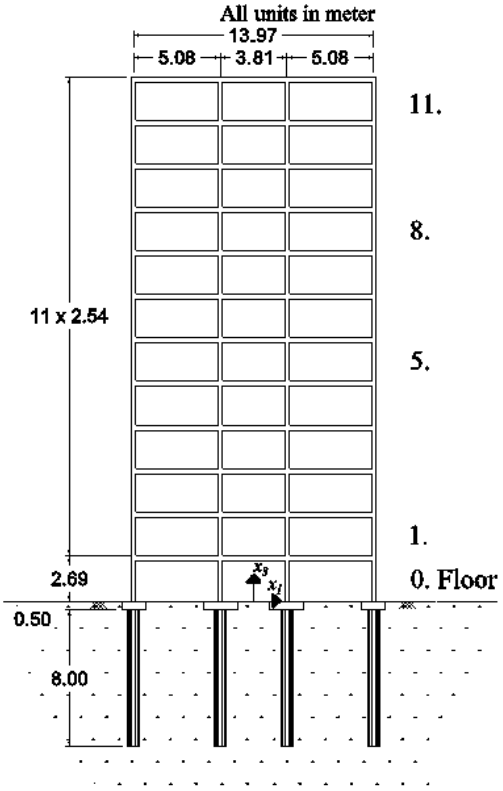

FIGURE 9.14: The cross section of the multi-storey building.

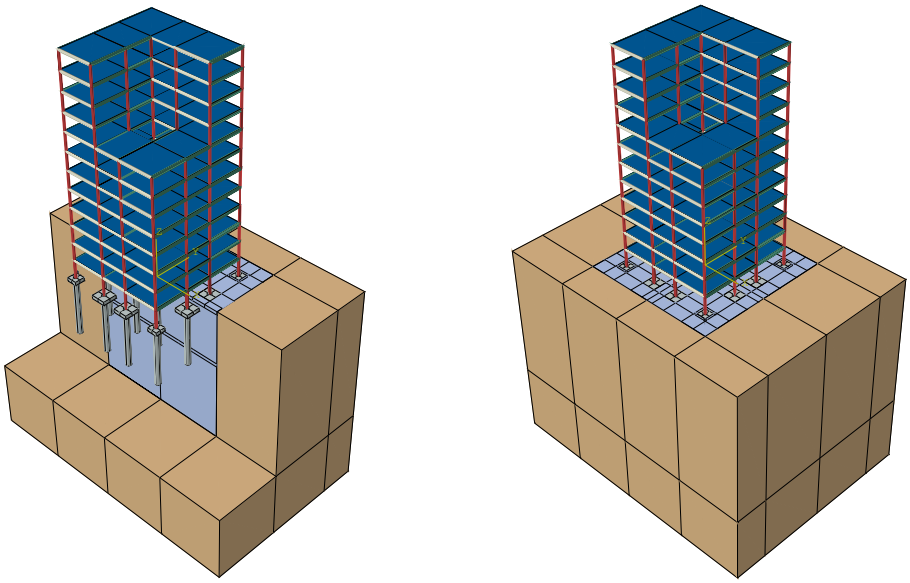

(A) (B)

FIGURE 9.15: The CAD model for case study 2 in ABAQUS/CAE. (A) An isometric view with parts partially hidden to expose the pile foundations, and (B) a view of the model sans the BEM region.

is 0.078 s, and the frequency resolution is 0.02504 Hz. The amplitude vector in

TABLE 9.2: The material properties for case study 2 with a point source dynamic excitation.

Region	λ (MN/m^2)	μ (MN/m^2)	ν	ρ (kg/m^3)
Slabs, footings, and piles	8 333.35	12 500.00	0.20	2 500
Columns and beams	80 000.00	80 000.00	0.25	7 800
Ω_0 & Ω_1	441.00	220.50	1/3	1 800

TABLE 9.3: The section profiles for beams and columns (box shape).

Member	width (mm)	height (mm)	thickness (mm)
Column	220	220	22
Beam in x_1-dir.	200	250	20
Beam in x_2-dir.	200	300	20

the frequency domain is $f_i^{\Omega_0}$(1.25E13 N, 0, 0). The dynamic point source is located at $\mathbf{X}_0$(-1 km, 0, -1 km). For the frequency domain computation, 256 discrete frequencies are computed.

The elements used for the model are as follows. S4 shell elements of ABAQUS are used for the BEs with a size of $\lambda_S/8.5$ of the shortest wavelength. The finite region comprises line, shell, and solid elements for the beams/columns, slabs, and footings/piles/soil, respectively. The line and shell elements' size is $\lambda_S/34$ while the largest size of the solid finite elements is $\lambda_S/17$.

The material nonlinearities are applied to the soil in the vicinity of the footings as well as to the piles and the steel members. Two types of nonlinear material behaviour are used for the soil. The first type is the Mohr-Coulomb criterion with the following values: friction angle of 35°, dilation angle of 0°, and cohesion of 250 kPa. The second type is the modified Drucker-Prager (cap) plasticity. Section 23.3 of ABAQUS manual (Smith, 2014) details the implementation of the constitutive models. By matching the Drucker-Prager yield surface to the Mohr-Coulomb parameters defined before, the following parameters are obtained: friction angle of 54.81° and cohesion of 960.49 kPa. Those values describe the yield surface in the mean stress versus the deviatoric stress plane. Other than that, a cap eccentricity parameter of 0.1 and a flow stress ratio of 0.778 are used. The former value is chosen so that the cap surface does not lay in the negative (tensile) stress area. The plastic flow is defined using the cap hardening definition and a base mean stress of 180 kPa (Figure 9.16). The material behaviour of the steel is defined as bilinear material with a yield stress of 150 MPa. A frictional and separable contact definition is used for the soil-footing and soil-pile interfaces with a frictional coefficient of 0.5.

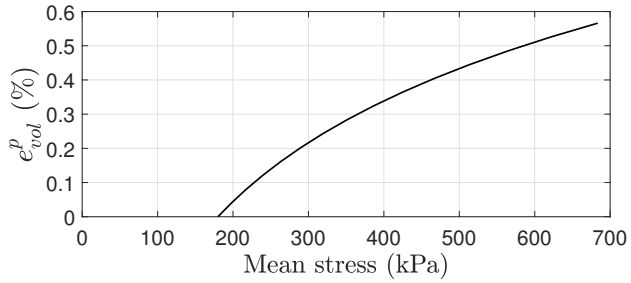

FIGURE 9.16: The cap hardening definition used for the Drucker-Prager (cap plasticity) material model in case study 2. ε^p_{vol} is the volumetric plastic strain.

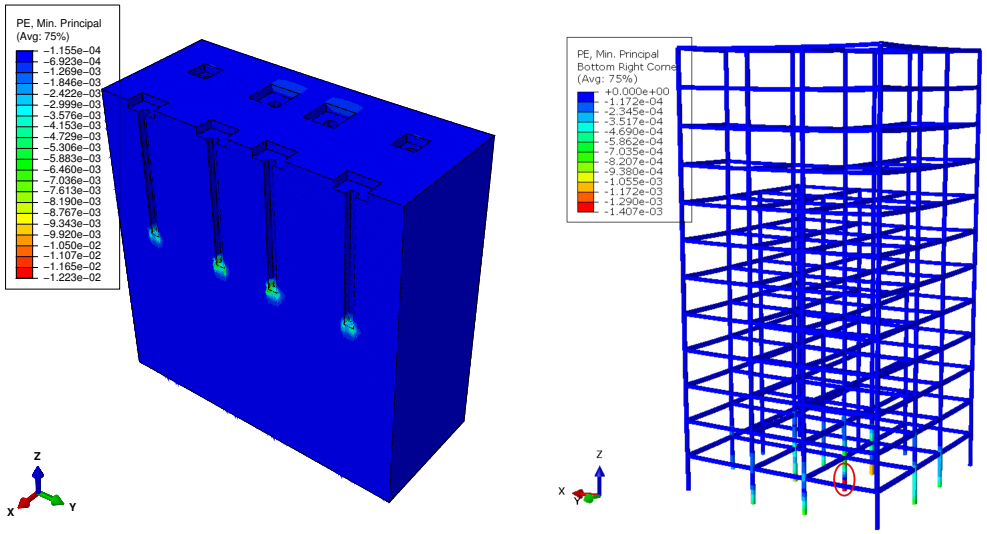

(A) (B)

FIGURE 9.17: Minimum principal plastic strain plots: (**A**) soil region near the foundations (modified Drucker-Prager model) and (**B**) the structural members.

The dummy geostatic step establishes the initial **geostatic stress** in the model. In addition to the geostatic stress due to the gravity, an overburden pressure of 180 kPa is applied on the ground's top surface to represent the preconsolidation. Afterward, **a static loading step** is performed where gravity is applied to the structure and foundation. Distributed loads of 500 kg/m^2 are applied to all slabs to represent additional dead and live loads.

An eigenfrequency extraction analysis is performed by applying fixed boundary conditions on the side and bottom surfaces of the finite soil region. It reveals that the structure is dominated by twisting mode shapes due to its configuration. **The fundamental frequency** is 0.662 Hz, followed by ten other natural frequencies below 5 Hz.

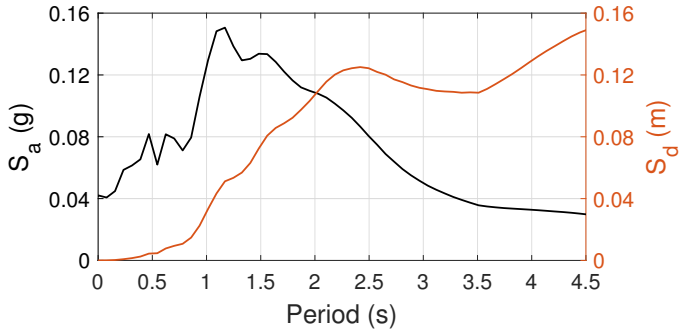

FIGURE 9.18: The spectral acceleration and displacement of the ground motion (horizontal component) measured at a column's base due to the point-source excitation.

The resulting ground motion measured at the base of one of the columns is presented as **spectral acceleration and displacement** in Figure 9.18. The stresses measured at **control elements** for the sequential analysis result show that the *MSE*s are below 0.6% and the *MAE*s are below 1.5% in comparison to the frequency domain analysis result, meaning that a consistent result is likely reached.

The minimum principal plastic strain plots for the soil region surrounding the pile foundations and for the structural members are presented in Figure 9.17. It shows the material nonlinearities using the modified Drucker-Prager model that occur in the soil surrounding the base of the piles. It also shows the plastic joints forming in the columns' base. The columns under the reduced floor plan remain elastic throughout the simulation. A comparison of the minimum principal stresses measured at two integration points of the cross-section on one of the column's bases between without and with the nonlinearities is shown in Figure 9.19. It shows that the maximum compressive stress is capped at the yield stress of 150 MPa when the nonlinearities are activated. The element's location is marked by the red ellipse in Figure 9.17b.

Figure 9.20 compares the displacement components u_j measured at a point in the roof for the sequential analyses results between without and with the nonlinearities being included, while Figure 9.21 compares the relative displacements of the same point with respect to its base. The cap plasticity model is used for the results in both figures. The figures show that, in this case, the nonlinearities have a relatively minor effect on the building's response. The maximum horizontal displacements for the result with the Mohr-Coulomb model and the cap plasticity model are 5.56% and 10.23% lower, respectively, than the one without the nonlinearities. At the same time, the building's natural frequencies are practically unchanged. The relative vertical displacement plot shows that minor permanent

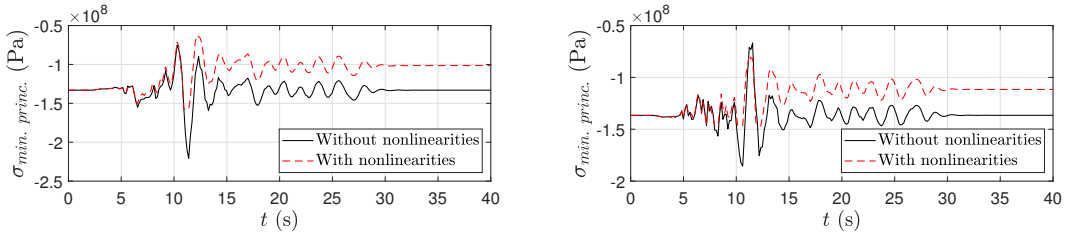

(A) (B)

FIGURE 9.19: Minimum principal stress plots measured at two integration points of an element in a column's base.

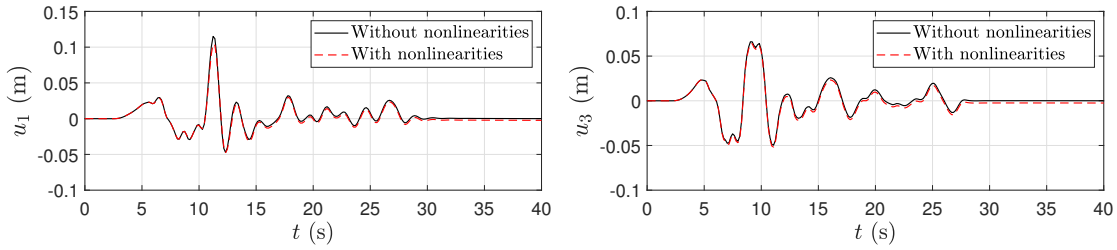

(A) (B)

FIGURE 9.20: Comparison of displacement components u_j measured at a point on the building's roof for the results of the sequential analysis between without and with the nonlinearities. The cap plasticity model is used. (**A**) u_1 versus time and (**B**) u_3 versus time.

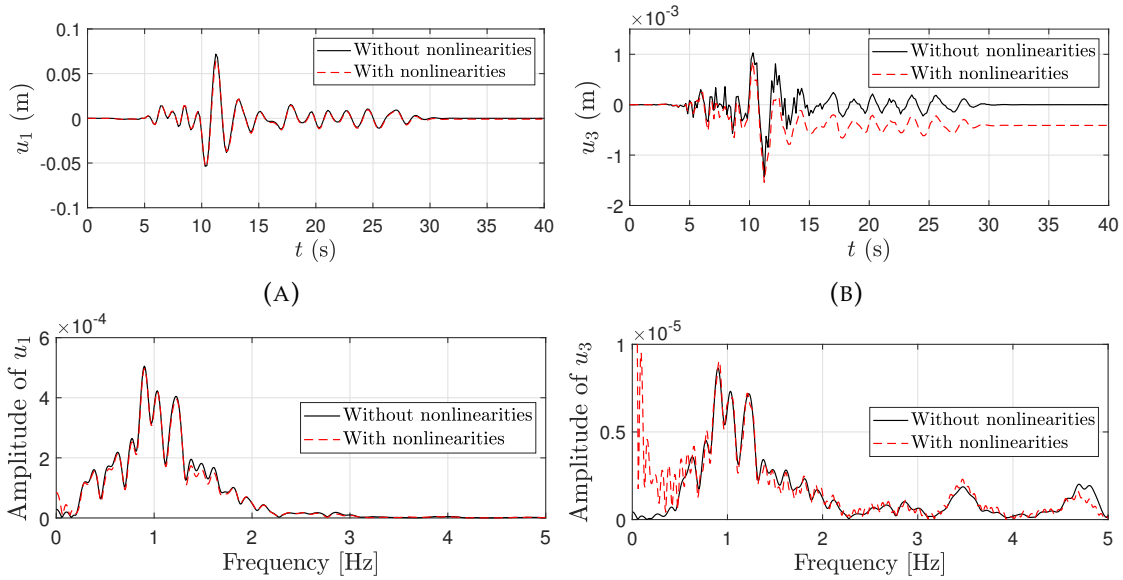

(A) (B)

(C) (D)

FIGURE 9.21: Comparison of displacement components u_j at a point on the building's roof relative to its base for the results of the sequential analysis between without and with the nonlinearities. The cap plasticity model is used. (**A**) u_1 versus time, (**B**) u_3 versus time, (**C**) Fourier amplitude of u_1, and (D) Fourier amplitude of u_3.

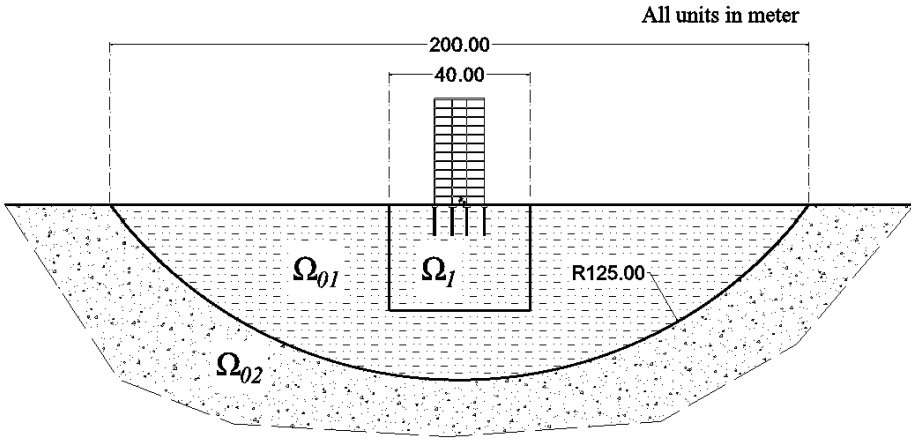

FIGURE 9.22: The cross section of case study 2 considering double-couple sources.

TABLE 9.4: The material properties for case study 2 with double-couple sources.

Region	λ (MN/m^2)	μ (MN/m^2)	ν	ρ (kg/m^3)
Ω_0 & Ω_{01}	441.00	220.50	1/3	1 800
Ω_{02}	1 620.00	1 620.0	0.25	2 000

displacements have taken place.

The minor effect on the nonlinearities can be attributed to the relatively weak ground motion and the building's configuration, which can redistribute the load from the yielding members to the columns on the setback area as they remain in a linear elastic state. The vertical load increases the stress experienced by the structural members but also prevents sliding on the soil-foundation interface. The embeddment effect from the piles also adds to this effect.

The simulation is extended to a transient dynamic excitation problem caused by **double-couple sources**. In this case, the same time function (*type B*) is chosen. It is then normalized to its maximum absolute value in the time domain and multiplied with a seismic moment M_0 of 2.5E15 Nm to create the rupture's time history. The seismic moment is equivalent to an earthquake with a moment magnitude 4.2 M_W (Hanks and Kanamori, 1979). The fault geometry is as follows: $\{\phi_{DC} = 270°, \delta_{DC} = 0°$, and $\gamma_{DC} = 90°\}$. The fault's plane is 400 m $\times$ 400 m with a center located at $\mathbf{X}_0$(-4 km, 0, -4 km). Twenty-five double-couple sources (N_{DC}), in a grid of 100 m, are used to model the rupture's plane. The event is initiated at the fault's center and propagates with the speed of $0.95 \times C_S$ along the fault's plane (Beresnev and Atkinson, 1997). The energy of the rupture is distributed equally to the sources.

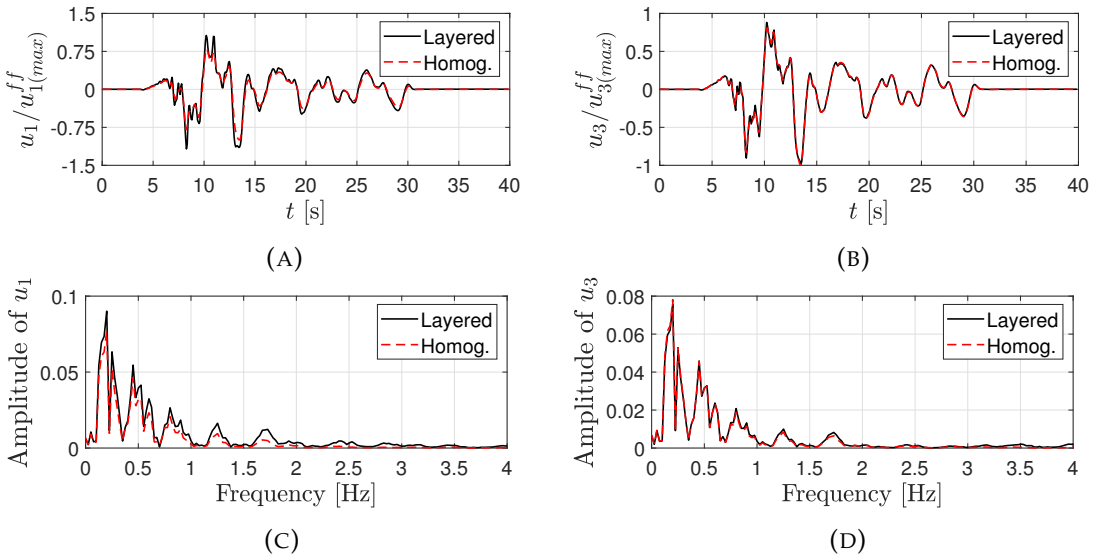

FIGURE 9.23: Displacement components u_j measured at a column's base with a distance of 5661.8 m from the dynamic source. The numerical results are normalized and compared to the analytical result for a homogeneous half-space: (**A**) u_1, (**B**) u_3, (**C**) amplitude of u_1, and (**D**) amplitude of u_3.

The geological profile is modified to simulate **a site amplification** in a layered media. The structure is founded on a sedimentary basin with a horizontal diameter of 200 m and a depth of 50 m; see Figure 9.22. The layers outside the finite region are modeled using BEM and referred to as Ω_{01} and Ω_{02}. The material properties of the soil regions are laid out in Table 9.4, while the properties of the structure and foundations remain the same.

Comparisons of displacement components u_j between the numerical results measured at a column's base and the analytical solution for a half-space in Figure 9.23 show that the horizontal displacement is amplified by 17.63%. At the same time, the vertical one is insignificantly influenced. This can be attributed to the bedrock's high phase velocities, which lead to long wavelengths. For example, the shear wavelength at a frequency of 6 Hz is 150 m, which is longer than the basin's depth. The SSI effect also does not significantly influence the recorded displacement due to the stark foundations' embeddment effect and the relatively stiff supporting soil.

The spectral displacement and acceleration measured at the column's base is shown in Figure 9.24. Horizontal displacements measured at the roof relative to its base show a peak of around 0.05 m, which confirms that a period lengthening does not take place. The ground motion's high-frequency content also results in the structure's higher mode response as shown in Figure 9.25.

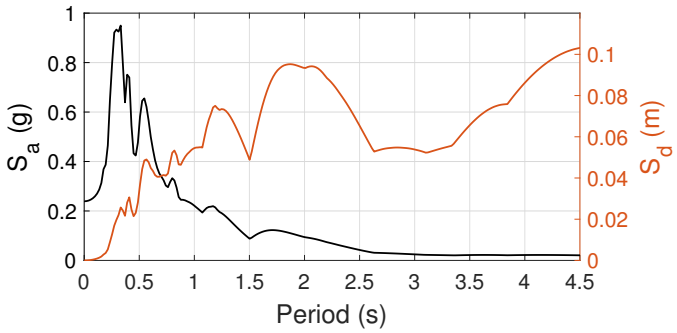

FIGURE 9.24: The spectral acceleration and displacement of the ground motion (horizontal component) measured at a column's base due to double-couple dynamic sources.

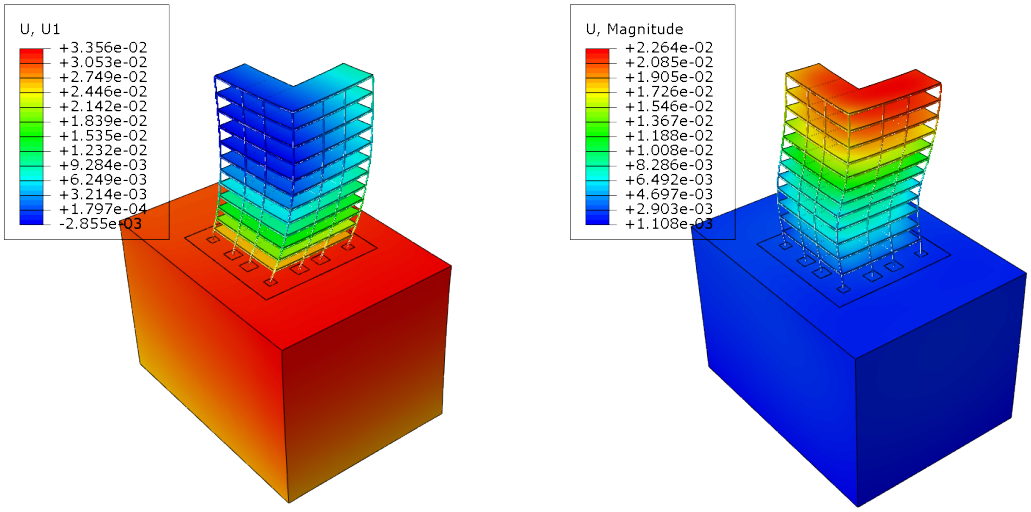

(A) (B)

FIGURE 9.25: The structure's deformation (scaled) due to double-couple sources showing the rotational and higher mode responses at the time (**A**) $t = 10.32$ s and (**B**) $t = 7.60$ s.

9.5 Case study 3

The third case study aims to demonstrate the application of the enhanced hybrid method in dealing with a real arbitrary geological geometry obtained from the field. In this case, the **3D model of the German North Sea** is taken as an example. The geometry can be obtained as an ASCII file (.ts*) from gst.bgr.de or www.gpdn.de. The 3D horizon model considered for this study covers an area of 6 km $\times$ 6 km with the center located at the global coordinate of **x**(355.90 km, 6021.98 km). The model is **scaled down by a factor of two** to reduce computational load. In this case study, the arbitrary complex geological profile is computed using BEM, while the finite zone contains a near-field soil region and a multi-storey structure. The BE model is within the horizontal coordinates of $\mathbf{x}_1[0,$

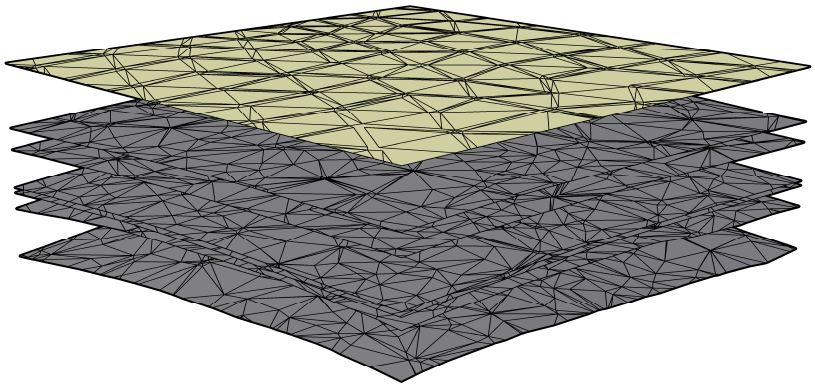

FIGURE 9.26: The horizon model of case study 3 in AutoCAD.

TABLE 9.5: The material properties considered for case study 3.

Region	λ (MN/m^2)	μ (MN/m^2)	ν	ρ (kg/m^3)
Ω_1 & Ω_{01}	1 651.54	2 477.31	0.20	1 990
Ω_{02}	2 129.02	3 193.52	0.20	2 000
Ω_{03}	2 592.36	3 888.55	0.20	2 000
Ω_{04}	2 597.91	3 896.87	0.20	2 100
Ω_{05}	1 695.33	2 543.00	0.20	2 100
Ω_{06}	5 077.03	7 615.54	0.20	2 200
Ω_{07}	7 086.48	10 629.72	0.20	2 200

3000 m] and $\mathbf{x}_2$[0, -3000 m]. The finite region is a cuboid with a horizontal length of 400 m and a depth of 99.154 m, and it is located within the coordinates $\mathbf{x}_1$[2300, 2700 m] and $\mathbf{x}_2$[-1300 m, -1700 m]. The ground's surface is at $x_3 = 0$.

The model geometry is in the form of horizon data, describing each geological layer's surface. To process the data, the polygons in the ASCII files are converted into a set of polyline commands for AutoCAD using MATLAB. The model geometry is then generated using AutoCAD's script function. The CAD model is shown in Figure 9.26.

Afterward, vertical faces and a bottom face are added to ensure the geometry constitutes a closed polygon, i.e., the additional faces will act as dummy elements. Interfaces with the finite region in the topmost layer are generated. The surfaces are then combined into a single surface entity and exported as an ACIS (.sat*) file, which is compatible to be imported in ABAQUS. The imported horizon model in ABAQUS is shown in Figure 9.27. Each layer interface is facing outward of its lower layer. This means that the elements' node sequences are reversed for the upper layers' computations. The FE model is presented in Figure 9.28.

The time function considered here is a Ricker wavelet (see Figure 8.2), with a primary frequency of 1 Hz, a time interval of 0.018773 s, a duration of 15 s, and a delay of 1.5 s. Transient dynamic excitation in the form of a double-couple source is simulated. **The seismic moment** M_0 is 3.0E13 Nm, which is equivalent to a moment magnitude M_W of 2.95. This scale of seismicity can be induced by energy exploration or carbon sequestration. The fault geometry is $\{\phi_{DC} = 30°, \delta_{DC} = 65°$, and $\gamma_{DC} = 40°\}$. The source is located at $\mathbf{X}_0$(1500 m, -1500 m, -1103 m).

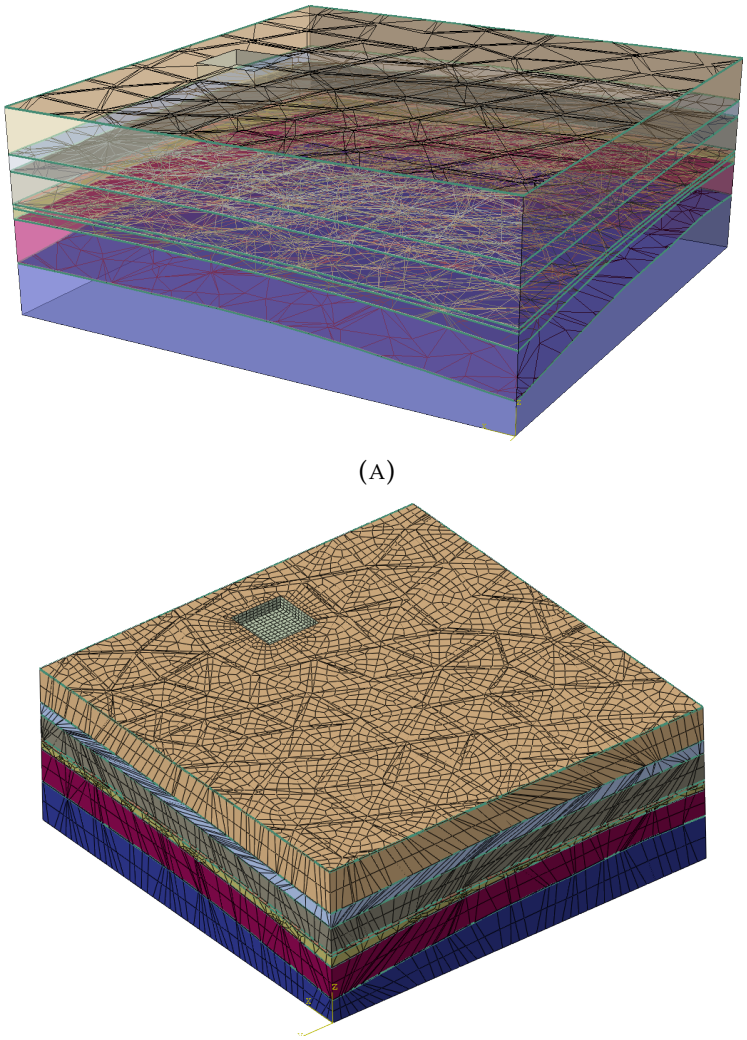

(A)

(B)

FIGURE 9.27: The horizon model of case study 3 in ABAQUS: (**A**) a translucent isometric view and (**B**) the mesh of the BE model.

The material properties for the geological layers are detailed in Table 9.5, which are derived following the wave velocities proposed by Jaritz et al., 1991. The material properties for the foundation and structure are the same as in Table 9.2.

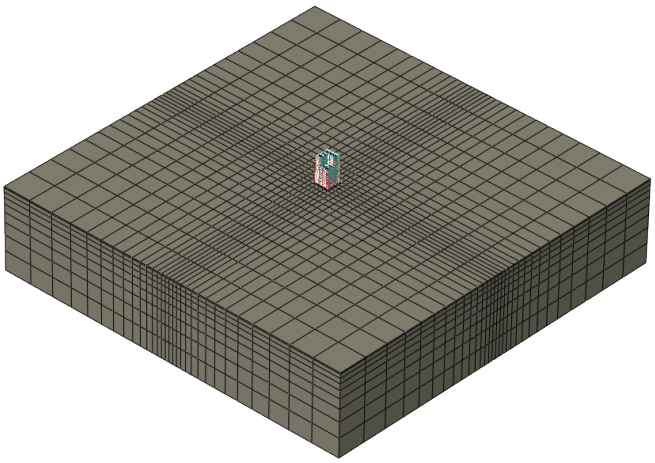

FIGURE 9.28: The FE model of case study 3 in ABAQUS.

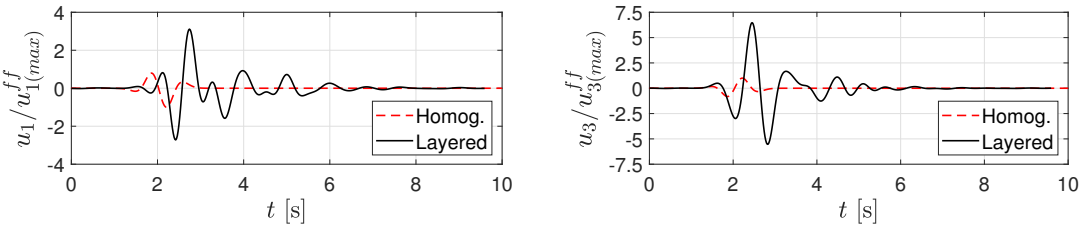

(A) (B)

FIGURE 9.29: Displacement components u_j measured at a point on the finite region's surface with a distance of **r**(1000 m, 0, 1103 m) from the dynamic source. The numerical results are normalized and compared to the analytical result for a homogeneous half-space: (**A**) u_1 and (**B**) u_3.

The main challenges in working with horizon data are the presence of (1) elements with null area and (2) rifts along the surface. The former is caused by surface polygons whose two of their nodes share the exact coordinates. The latter is due to how faults and surface discontinuities are drawn in a horizon model. Additional algorithms are written to identify and rectify these problems. The former is solved by identifying elements with null Jacobian, while the latter is rectified by identifying elements whose adjacent elements are less than their number of sides. For example, a triangular element must have three adjacent elements that share two nodes. After the elements are identified, the nodes along the rift are collected, and additional polygons (elements) are created to close the rift.

Figure 9.29 compares the displacement components u_j measured at **x**(2500 m, -1500 m, 0), i.e., at the center-top of the finite region, with the analytical solution for a homogeneous half-space (equation 3.72). These plots depict the amplification and wave scattering due to the geological layering. The induced wave field

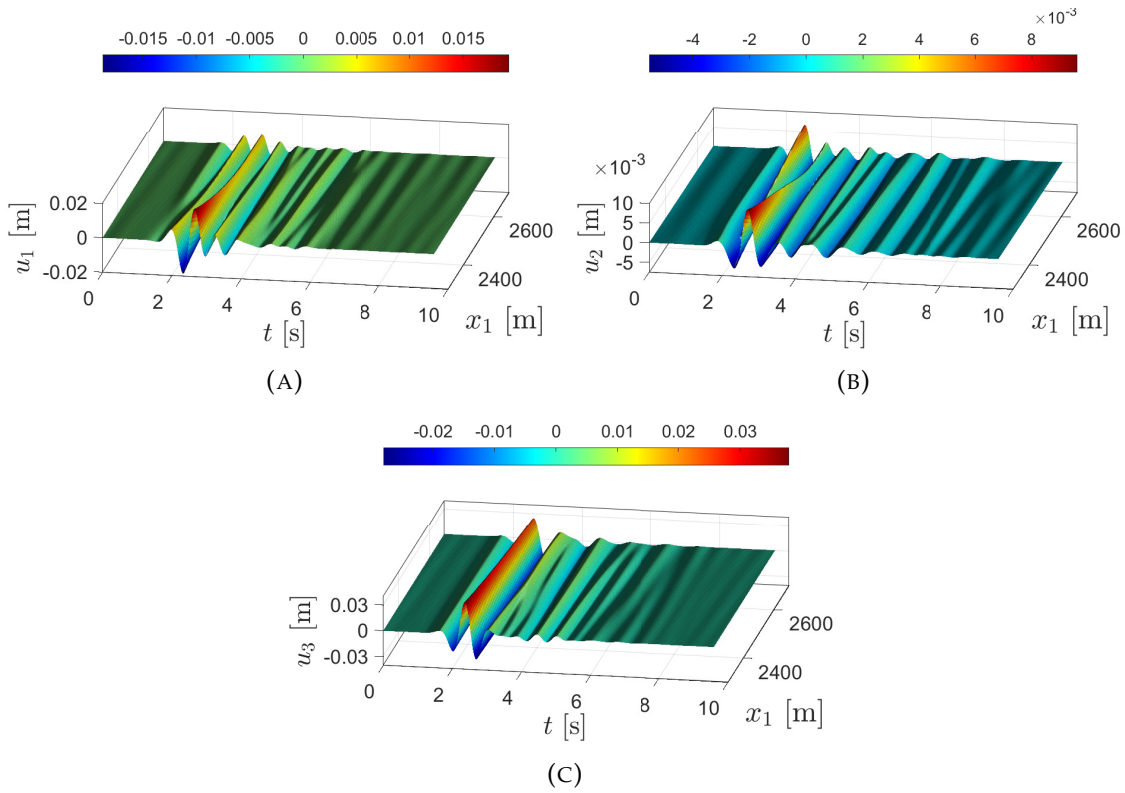

FIGURE 9.30: Displacement components u_j measured along the line $x_2 = -1500$ m, $x_3 = 0$ versus time t. (**A**) u_1, (**B**) u_2, and (**C**) u_3.

along the line $x_2 = -1500$ m, $x_3 = 0$, i.e., in line with the propagating wave's direction, is shown in Figure 9.30. The presence of a structure does not affect the wave field due to the high stiffness of the surface layer. This figure also shows displacements in the x_2-direction that is otherwise zero in the case of a homogeneous media because the relative distance between the source and measured line in this direction is zero. The layering causes these effect.

9.6 Chapter summary

The three case studies presented here clearly demonstrate the effectiveness and versatility of the hybrid BEM-FEM in combination with the LWC method and the sequential analysis to solve nonlinear dynamic SSI problems. The importance of the consideration for nonlinear material and contact behaviour is illustrated. A soil-structure system's response and the section forces can be significantly underestimated, and thus, it can result in an inadequate or inefficient dynamic design. The hybrid numerical tool combined with the sequential analysis is clearly at a disadvantage when dealing with widespread or severe nonlinearity cases. However, it also brings clear advantages in its ability to model realistic responses

considering material and contact nonlinearities and stress-dependent material behaviour. It is also advantageous regarding computational cost since the time domain BEM and nested iterations are avoided. For case study 1, 400 discrete frequencies are computed. The computation time for the frequency domain phase is 149 minutes, while the time domain phase is 78 minutes when considering the nonlinearities. The computation time for case study 2, where 256 frequencies are computed, is 277 minutes and 235 minutes for the frequency and time domains, respectively. The elapsed time for case study 3 is around 2900 minutes due to the high number of involved elements and nodes. The advantage of the LWC method is apparent in this particular case since the necessary random-access memory and storage can be limited to the requirement of each layer.

Chapter 10

Conclusions and outlook

10.1 Conclusions

The consideration of soil-structure interaction and its effect is essential in the determination of the dynamic-resistant design. This is true not only in the context of earthquake-resistant design but also for low-level vibrations engineering. However, the practical application of dynamic soil-structure interaction analysis/design tools for practicing engineers still needs to be improved. This dissertation is an endeavour addressed to this. A numerical tool based on the hybrid BEM-FEM is successfully implemented using ABAQUS commercial software and in-house MATLAB® code. To improve its efficiency, accuracy, and applicability, several basic procedures are incorporated, namely the handling of different types of dynamic sources, handling of arbitrary non-smooth nodes using dummy BEs, symmetry-algorithm to reduce BEM computation load, and handling of non-conforming BE-FE interface. Verification studies conducted for compliance functions of a rigid foundation and incident wave problems show excellent agreements with existing reference and analytical solutions, respectively.

In approaching realistic SSI problems, it is crucial to consider that the underlying soil is commonly multi-layered with arbitrary interface geometry. Furthermore, its material properties can vary over the depth without following a particular pattern. The layer-wise condensation is developed to address this. It is based on the formulation of multi-domain BEM and the condensation procedure. The derivation of the method and its scheme for numerical implementation is presented. The method is proven to significantly reduce the computational memory requirement for the computation of arbitrary layered half-space. The results of the verification study for compliance functions of a rigid massless foundation and wave propagation problems show that the method can accurately compute the wave field due to arbitrary layering.

Another challenge addressed here is the consideration of secondary nonlinearities, i.e., the material, geometrical, and contact nonlinearities. In this regard, the sequential frequency-time domain procedure is developed and implemented. The relatively simple approach makes it possible to include nonlinearities in hybrid BEM-FEM simulations while avoiding the use of the time domain BEM and without requiring additional iterations. Verification studies shows that the procedure can result in a consistent output, and error measurement is established.

Four application chapters of dynamic SSI problems are presented, ranging from 2D plane strain to 3D problems. The 1st application concerns with revealing the role of the underlying soil and backfill material properties on the dynamic behaviour of typical integral bridges. The outcomes show that the underlying soil has a strong influence on the resonant frequencies as well as the damping of the system, especially on shorter bridges. The range of frequency alteration is found to be significantly higher in mode shapes that incorporate more soil-structure interaction, i.e., mode shapes with longitudinal or transversal motions, compared to mode shapes dominated by the flexural stiffness of the bridge. It is also revealed that the consideration of the wingwalls in the model, an aspect that is often missing in the 2D approach, influences the results as the wingwalls act as the dominating links between the bridge and the soil. Because of this, the backfill, which fills the space between the wingwalls and the supporting soil, has a relatively minor influence on the bridge's dynamic behaviour.

The next application presents case studies of foundation-soil-foundation interaction subjected to ground-borne vibrations. The damaged state of the geological media is considered by using dilute approximation. To study the influence of arbitratry layering, two case studies are presented in the third application chapter, where two containment structures subjected to short- and medium-range transient excitations are examined. These case studies are aimed to investigate the following key factors: (1) the dynamic site effect due to impedance contrast of soil layers, (2) lateral inhomogeneity effect, (3) influence of the dynamic source properties, (4) existence of damage process in soils, (5) conversion of body waves into surface waves, and (6) foundation-soil-foundation or structure-soil-structure dynamic interaction. The results show that the complex wave field on the surface and the structure's response are highly influenced by these key factors and their interactions.

The fourth application chapter presents two case studies of dynamic SSI considering the secondary nonlinearities: an arch bridge analysed in 2D plane strain

and a 3D multi-storey building. The results show that the maximum relative displacement and the section's internal forces can be underestimated when material and contact nonlinearities are neglected. It is also shown that an exemplary building configuration can minimize the impact of a system's nonlinear behavior. A third case study highlights the applicability of the enhanced method to deal with complex arbitrary geometry from actual data. The challenges and workflow to process the data are detailed.

These outcomes highlight the importance of the consideration SSI effect, including the influence of the arbitrary layering of the geological profile and the secondary nonlinearities, in the dynamic analyses of soil-structure systems. The various case studies presented in this dissertation mark the ability of this hybrid BEM-FEM implementation to model realistic cases.

10.2 Outlook

Potential future works for this study are as follows:

- Extension of the hybrid BEM-FEM incorporating the fast-multipole BEM is necessary to enhance the computation speed.
- Further extension is also required to improve the hybrid BEM-FEM formulation to consider poroelastic material behaviour in the semi-infinite region.
- To increase the modeling flexibility, further improvement to handle non-conforming interface between BE subdomains is necessary.
- A comparative study of the dynamic behaviour of integral bridges based on field experiments is necessary to validate and calibrate the simulation result.
- Further study can also investigate the influence of other structural and geological aspects on the dynamic behaviour of integral bridges, i.e., the influence of flexural stiffness, abutment thickness, skew alignment, arbitrary soil layering, etc.
- Further works and deeper analyses in regard to structure-soil-structure interaction or soil-multi-structure interaction are possible. Within this scope, improvement for handling large domains is necessary, which would make it possible to consider 3D site-city interaction.
- The hybrid numerical tool can be further developed into an application, e.g., a MATLAB® Toolbox, that can be released for the general public.

List of Publications

The following articles contain the main part of this work.

- **H.D.B. Aji**, M. Basnet, F. Wuttke (2020). "A numerical study on the influences of underlying soil and backfill characteristics on the dynamic behaviour of typical integral bridges". In: *Bauingenieur* 95.11, pp. 2-11. DOI: 10.37544/0005-6650-2020-11-35.

  Author's contributions: conceptualization, methodology, software, validation, formal analysis, writing—original draft, writing—editing, visualization.

- **H.D.B. Aji**, F. Wuttke, P. Dineva (2021). "3D hybrid model of foundation-soil-foundation dynamic interaction". In: *Z. für Angew. Math. Mech.* (*ZAMM*) 101, e202000351. DOI: 10.1002/zamm.202000351.

  Author's contributions: conceptualization, methodology, software, validation, formal analysis, writing—original draft, writing—editing, visualization.

- **H.D.B. Aji**, F. Wuttke, P. Dineva (2022). "3D structure-soil-structure interaction in an arbitrary layered half-space". In: *Soil Dynamics and Earthquake Engineering* 159, 107352. DOI: 10.1016/j.soildyn.2022.107352.

  Author's contributions: conceptualization, methodology, software, validation, formal analysis, writing—original draft, writing—editing, visualization.

Other relevant publications:

- M.B. Basnet, **H.D.B. Aji**, F. Wuttke, P. Dineva (2017). "Impedance function for a soil-tunnel system in poroelastic geomaterial by hybrid BEM-FEM simulations". 15. D-A-CH-Tagung 2017 Erdbebeningennieurwesen und Baudynamik, Weimar, Germany.

- M.B. Basnet, **H.D.B. Aji**, F. Wuttke, P.S. Dineva (2018). "Impedance functions of rigid foundation on inhomogeneous elastic and poroelastic media using hybrid BEM-FEM approach", 6. VDI-Fachtagung, Baudynamik 2018, Würzburg, Germany.
- **H.D.B. Aji**, M.B. Basnet, F. Wuttke (2019). "Hybrid BEM-FEM assessment on the dynamic behaviour of integral bridge" , 7th ECCOMAS Thematic Conference on Computational Methods in Structural Dynamics and Earthquake Engineering, COMPDYN 2019, Creta, Greece.
- T. Heiland, A. Stark, **H.D.B. Aji**, F. Wuttke (2022). "Einfluss der Boden-Bauwerk-Interaktion auf die dynamische Characteristik von eisenbahnrahmenbrücken". VDI Baudynamik 2379, Würzburg.
- T. Heiland, **H.D.B. Aji**, F. Wuttke, L. Stempniewski, A. Stark (2023). "Influence of soil-structure interaction on the dynamic characteristics of railroad frame bridges". In: *Soil Dynamics and Earthquake Engineering* 167, 107800. DOI: 10.1016/j.soildyn.2023.107800.

Bibliography

Abate, G. et al. (2010). "Numerical modeling of a shaking table test for soil-foundation-superstructure interaction by means of a soil constitutive model implemented in a FEM code". In: *Geotechnical and Geological Engineering* 28, pp. 37–59.

Achenbach, J. D. (1975). *Wave Propagation in Elastic Solids*. Ed. by J. D. Achenbach. North-Holland Series in Applied Mathematics and Mechanics. Amsterdam: Elsevier, pp. 202–261. DOI: https://doi.org/10.1016/B978-0-7204-0325-1.50011-4.

Aji, H. D. B. (2014). "Numerical study of cyclic thermo-mechanical ratcheting effects on backfill of integral bridges". MA thesis. Bauhaus-Universität Weimar.

Aki, K. and P. G. Richards (1980). *Quantitative Seismology*. University Science Book, California. ISBN: 978-1-891389-63-4.

Aldaikh, Hesham et al. (Oct. 2016). "Shake table testing of the dynamic interaction between two and three adjacent buildings (SSSI)". In: *Soil Dynamics and Earthquake Engineering* 89, 219–232. DOI: 10.1016/j.soildyn.2016.08.012.

Alexander, N., E. Ibraim, and H. Aldaikh (Jan. 2012). "A simple discrete model for interaction of adjacent buildings during earthquakes". In: *Computers & Structures* 124. DOI: 10.1016/j.compstruc.2012.11.012.

Antes, H. and O. Von Estorff (1989). "Dynamic response analysis of rigid foundations and of Elastic Structures by Boundary Element Procedures". In: *Soil Dynamics and Earthquake Engineering* 8, pp. 68–74.

Archer, J. S. (1965). "Consistent matrix formulations for structural analysis using finite-element techniques." In: *AIAA Journal* 3.10, pp. 1910–1918. DOI: 10.2514/3.3279.

Arsoy, S., R. M. Barker, and J. M. Duncan (1999). *The behavior of integral abutment bridges*. Tech. rep. FHWA/VTRC 00-CR3. Virginia Transportation Research Council. URL: https://rosap.ntl.bts.gov/view/dot/19507.

ATC-3 (1978). *Tentative provisions for the development of seismic regulations of buildings: a coooperative effort with the design profession, building code interests, and the research community*. Washington, D.C.: National Bureau of Standards.

Aviram, A., K. Mackie, and B. Stojadinovic (Dec. 2008). "Effect of Abutment Modeling on the Seismic Response of Bridge Structures," Earthquake Engineering

and Engineering Vibration, 7(4): 395-402". In: *Earthquake Engineering and Engineering Vibration* 7, pp. 395–402. DOI: 10.1007/s11803-008-1008-3.

Baffet, Daniel et al. (2012). "Long-time stable high-order absorbing boundary conditions for elastodynamics". In: *Computer Methods in Applied Mechanics and Engineering* 241-244, pp. 20–37. ISSN: 0045-7825. DOI: https://doi.org/10.1016/j.cma.2012.05.007.

Banerjee, P. and Roy Butterfield (Sept. 1975). "Boundary Element Methods in Geomechanics". In.

Barbosa, A. and M. Silva (Nov. 2007). "Bridge abutment interaction under seismic loading". In.

Bard, P.-Y. et al. (2006). "Site-City Interaction". In: *Assessing and Managing Earthquake Risk*. Springer Netherlands.

Bathe, K.-J. (1996). *Finite Element Procedures*. Prentice-Hall, New Jersey. ISBN: 0-13-301458-4.

Beer, G., I. Smith, and C. Duenser (2008). *The Boundary Element Method with Programming, for Engineers and Scientists*. SpringerWienNewYork. ISBN: 978-3-211-71574-1.

Beresnev, Igor A. and Gail M. Atkinson (1997). "Modeling finite-fault radiation from the ω_n spectrum". In: *Bulletin of the Seismological Society of America* 87.1, pp. 67–84. URL: https://doi.org/10.1785/BSSA0870010067.

Bielak, Jacobo (1978). "Dynamic response of non-linear building-foundation systems". In: *Earthquake Engineering & Structural Dynamics* 6.1, pp. 17–30. DOI: https://doi.org/10.1002/eqe.4290060104.

Bode, Ch., R. Hirschauer, and S. Savidis (2002). "Soil-structure interaction in the time-domain using Half-space Green's functions". In: *Soils Dynamics and Earthquake Engineering* 22, pp. 283–295.

Bolisetti, Chandrakanth, Andrew S. Whittaker, and Justin L. Coleman (2018). "Linear and nonlinear soil-structure interaction analysis of buildings and safety-related nuclear structures". In: *Soil Dynamics and Earthquake Engineering* 107, pp. 218–233. ISSN: 0267-7261. DOI: https://doi.org/10.1016/j.soildyn.2018.01.026.

Boumaiza, D. and B. Aour (Aug. 2014). "On the efficiency of the iterative coupling FEM–BEM for solving the elasto-plastic problems". In: *Engineering Structures* 72, 12–25. DOI: 10.1016/j.engstruct.2014.03.036.

Bransch, Martin (2010). "Elasto-plastic analysis with a coupled FEM/SBFEM approach". PhD thesis. Technical University Carolo-Wilhelmina of Braunschweig.

Brebbia, C. A. (1978). *The Boundary Element Method for Engineers*. Pentech Press, London.

Brebbia, C. A. and P. Georgiou (1979). "Combination of boundary and finite elements in elastostatics". In: *Appl. Math. Model* 3, pp. 212–220.

Budiansky, Bernard and Richard J. O'connell (1976). "Elastic moduli of a cracked solid". In: *International Journal of Solids and Structures* 12.2, pp. 81–97. ISSN: 0020-7683. DOI: https://doi.org/10.1016/0020-7683(76)90044-5.

Bycroft, G. N. (1956). "Forced vibrations of a rigid circular plate on a semi-infinite elastic space and on an elastic stratum". In: *Philos. Trans. Royal Soc. London Ser. A, Math. Phys. Sci.* 248, pp. 327–368.

Cao, Z. et al. (Mar. 2021). "Decarbonizing concrete: deep decarbonization pathways for the cement and concrete cycle in the United States, India, and China". In.

CEN (2004). *EN 1998-5: Eurocode 8: Design of structures for earthquake resistance – Part 5: Foundations, retaining structures and geotechnical aspects*. Brussels.

Chaillat, Stéphanie, Marc Bonnet, and Jean-François Semblat (2009). "A new fast multi-domain BEM to model seismic wave propagation and amplification in 3D geological structures". In: *Geophysical Journal International* 177, pp. 509–531. DOI: 10.1111/j.1365-246X.2008.04041.x. URL: https://hal.archives-ouvertes.fr/hal-00338211.

Chopra, A. K. (1995). *Dynamics of structures: theory and applications to earthquake engineering*. Prentice-Hall.

Chuhan, Z., S. Chongmin, and O. A. Pekau (1991). "Infinite boundary elements for dynamic problems of 3-D half space". In: *International Journal for Numerical Methods in Engineering* 31.3, pp. 447–462. DOI: https://doi.org/10.1002/nme.1620310304.

Chuhan, Z. and D. Gross (1998). *On Wave Propagation in Elastic Solids with Cracks*. Southampton: Computational Mechanics Publication.

Chuhan, Z. and J. P. Wolf (1998). *Dynamic Soil–Structure Interaction*. Elsevier Science. ISBN: 9780080530581.

Coleman, Justin L., Chandrakanth Bolisetti, and Andrew S. Whittaker (2016). "Time-domain soil-structure interaction analysis of nuclear facilities". In: *Nuclear Engineering and Design* 298, pp. 264–270. ISSN: 0029-5493. DOI: https://doi.org/10.1016/j.nucengdes.2015.08.015.

Courant, R. (1943). "Variational methods for the solution of problems of equilibrium and vibrations". In: *Bulletin of the American Mathematical Society* 49.1, pp. 1–23. DOI: bams/1183504922.

Cruse, T. A. (1969). "Numerical solutions in three dimensional elastostatics". In: *International Journal of Solids and Structures* 5.12, pp. 1259–1274. ISSN: 0020-7683. DOI: https://doi.org/10.1016/0020-7683(69)90071-7.

Cruse, T. A. (1973). "Application of the boundary-integral equation method to three dimensional stress analysis". In: *Computers & Structures* 3.3, pp. 509–527. ISSN: 0045-7949. DOI: https://doi.org/10.1016/0045-7949(73)90094-1.

Dassault Systèmes Simulia Corp (2014). *ABAQUS Theory Manual, Version 6.14*. English. Dassault Systèmes Simulia Corp. United States: Dassault Systèmes Simulia Corp.

Dineva, P. et al. (2014). "Seismic soil-tunnels interaction via BEM part I. Mechanical model". In: *J. of Theoretical and Appl. Mech.* 44.3, pp. 31–48.

Dominguez, J. (1993). *Boundary Elements in Dynamics*. Computational Engineering. Computational Mechanics Publications. ISBN: 9781853122583.

Elleithy, W. (2008). "Analysis of problems in elasto-plasticity via an adaptive FEM–BEM coupling method". In: *Computer Methods in Applied Mechanics and Engineering* 197.45, pp. 3687–3701. ISSN: 0045-7825. DOI: https://doi.org/10.1016/j.cma.2008.02.018.

Elleithy, W. and R. Grzhibovskis (2009). "An adaptive domain decomposition coupled finite element–boundary element method for solving problems in elasto-plasticity". In: *International Journal for Numerical Methods in Engineering* 79.8, pp. 1019–1040. DOI: https://doi.org/10.1002/nme.2608.

Elleithy, W. M., H. J. Al-Gahtani, and M. El-Gebeily (2001). "Iterative coupling of BE and FE methods in elastostatics". In: *Engineering Analysis with Boundary Elements* 25.8, pp. 685–695. ISSN: 0955-7997. DOI: https://doi.org/10.1016/S0955-7997(01)00054-6.

Elleithy, Wael M., Masataka Tanaka, and Artur Guzik (2004). "Interface relaxation FEM–BEM coupling method for elasto-plastic analysis". In: *Engineering Analysis with Boundary Elements* 28.7, pp. 849–857. ISSN: 0955-7997. DOI: https://doi.org/10.1016/j.enganabound.2003.12.002.

Erbaş, Barış et al. (Sept. 2018). "Approximate analysis of surface wave-structure interaction". In: *Journal of Mechanics of Materials and Structures* 13, pp. 297–309. DOI: 10.2140/jomms.2018.13.297.

Erbaş, Bariş et al. (2017). "The near-resonant regimes of a moving load in a three-dimensional problem for a coated elastic half-space". In: *Mathematics and Mechanics of Solids* 22.1, pp. 89–100. DOI: 10.1177/1081286514555451.

Erhan, S. and M. Dicleli (Nov. 2014). "Effect of dynamic soil–bridge interaction modeling assumptions on the calculated seismic response of integral bridges". In: *Soil Dynamics and Earthquake Engineering* 66, 42–55. DOI: 10.1016/j.soildyn.2014.06.033.

Eurocode 7 (2004). Eurocode 7: Geotechnical design – Part 1: General rules. Europoean Comitte for Standardization (CEN).

FEMA (Dec. 2020). *FEMA P-2091: A Practical Guide to Soil-Structure Interaction*. Washington, D.C.: Federal Emergency Management Agency.

Feng, Y. T. and D. R. J. Owen (1996). "Iterative solution of coupled FE/BE discretizations for plate-foundation interaction problems". In: *International Journal for Numerical Methods in Engineering* 39.11, pp. 1889–1901. DOI: https://doi.org/10.1002/(SICI)1097-0207(19960615)39:11<1889::AID-NME934>3.0.CO;2-Z.

Ferreira, A. J. M. and N. Fantuzzi (2009). *MATLAB Codes for Finite Element Analysis*. Springer, Berlin. ISBN: 978-3030479510.

Ferro, Alex Nieto (2013). "Nonlinear dynamic soil-structure interaction in earthquake engineering". PhD thesis. École Centrale Paris.

Fish, J. and T. Belytschko (2007). *A First Course in Finite Elements*. John Wiley & Sons Ltd., England. ISBN: 978-0-470-03580-1.

Foldy, L. (1945). "Multiple scattering theory of waves". In: *Phys. Rev.* 67, pp. 107–119.

Fontara, Ioanna-Kleoniki (2015). "Simulation of seismic wave fields in inhomogeneous half-plane by non-conventional BEM". PhD thesis. Lehrstuhl Geomechanik und Geotechnik, CAU Kiel.

Fontara, Ioanna-Kleoniki et al. (2018). "Finite element implementation of efficient absorbing layers for time harmonic elastodynamics of unbounded domains". In: *Soil Dynamics and Earthquake Engineering* 114, pp. 625–638. ISSN: 0267-7261. DOI: https://doi.org/10.1016/j.soildyn.2018.06.026.

François, S. (May 2008). "Nonlinear modelling of the response of structures due to ground vibrations". PhD thesis. K. U. Leuven.

François, S., P. Coulier, and G. Degrande (2015). "Finite element–boundary element coupling algorithms for transient elastodynamics". In: *Engineering Analysis with Boundary Elements* 55, pp. 104–121.

Freisinger, J., M. Hackenberg, and G. Müller (2020). "A coupled Integral Transform Method - Finite Element Method approach to model the Soil Structure Interaction of finite (3D) and length invariant (2.5D) systems". In: *Journal of Sound and Vibration* 482, p. 115443. ISSN: 0022-460X. DOI: https://doi.org/10.1016/j.jsv.2020.115443.

Gajan, Sivapalan et al. (Feb. 2010). "Application and validation of practical tools for nonlinear soil-foundation interaction analysis". In: *Earthquake Spectra* 26. DOI: 10.1193/1.3263242.

Gallagher, R. H., J. Padlog, and P. P. Bijlaard (1962). "Stress analysis of heated complex shapes". In: *ARS Journal* 32.5, pp. 700–707. DOI: 10.2514/8.6128.

Galvez, P. et al. (May 2014). "Dynamic earthquake rupture modelled with an unstructured 3-D spectral element method applied to the 2011 M9 Tohoku earthquake". In: *Geophysical Journal International* 198, pp. 1222–1240. DOI: 10.1093/gji/ggu203.

Galvín, P. and A. Romero (2014a). "A 3D time domain numerical model based on half-space Green's function for soil–structure interaction analysis". In: *Computational Mechanics* 53, pp. 1073–1085. DOI: https://doi.org/10.1007/s00466-013-0949-1.

– (2014b). "A MATLAB toolbox for soil–structure interaction analysis with finite and boundary elements". In: *Soil Dynamics and Earthquake Engineering* 57, pp. 10–14. DOI: https://doi.org/10.1016/j.soildyn.2013.10.009.

Ganguly, S., J. B. Layton, and C. Balakrishna (2000). "Symmetric coupling of multizone curved Galerkin boundary elements with finite elements in elasticity". In: *International Journal for Numerical Methods in Engineering* 48.5, pp. 633–654. DOI: https://doi.org/10.1002/(SICI)1097-0207(20000620)48:5<633::AID-NME874>3.0.CO;2-K.

Gazetas, G. (1991). "Formulas and charts for impedances of surface and embedded foundations". In: *Journal of Geotechnical Engineering* 117.9, pp. 1363–1381. DOI: 10.1061/(ASCE)0733-9410(1991)117:9(1363).

Gazetas, G. and Marios Apostolou (Mar. 2004). "Nonlinear Soil-Structure Interaction: Foundation Uplifting and Soil Yielding". In: *Third UJNR Workshop on Soil-Structure Interaction*. Menlo Park, California, USA.

Goel, R. K. (1997). "Earthquake characteristics of bridges with integral abutments". In: *Journal of Structural Engineering* 123.11, pp. 1435–1443. DOI: 10.1061/(ASCE)0733-9445(1997)123:11(1435).

Goel, Rakesh K. and Anil K. Chopra (1997). "Evaluation of bridge abutment capacity and stiffness during earthquakes". In: *Earthquake Spectra* 13.1, pp. 1–23. DOI: 10.1193/1.1585929.

Greengard, L. and V. Rokhlin (1987). "A fast algorithm for particle simulations". In: *Journal of Computational Physics* 73.2, pp. 325–348. ISSN: 0021-9991. DOI: https://doi.org/10.1016/0021-9991(87)90140-9.

Greengard, L. F. (1987). "The Rapid Evaluation of Potential Fields in Particle Systems". PhD thesis. USA.

Hackenberg, M. (2016). *A Coupled Integral Transform Method - Finite Element Method Approach to Model the Soil-Structure-Interaction*. Schriftenreihe des Lehrstuhls für Baumechanik. Shaker Verlag. ISBN: 9783844049718. URL: https://books.google.de/books?id=9WReAQAACAAJ.

Halabian, Amir M. and M. Hesham El Naggar (2002). "Effect of non-linear soil–structure interaction on seismic response of tall slender structures". In: *Soil Dynamics and Earthquake Engineering* 22.8, pp. 639–658. ISSN: 0267-7261. DOI: https://doi.org/10.1016/S0267-7261(02)00061-1.

Hanks, T. C. and H. Kanamori (May 1979). "A moment magnitude scale". In: *J. Geophys. Res.* 84.B5, pp. 2348–50. DOI: 10.1029/JB084iB05p02348.

Harden, Chad et al. (Aug. 2005). *Numerical modeling of the nonlinear cyclic response of shallow foundations*. Research rep. 2005/04. PEER 2005/04. Berkeley: Pacific Earthquake Engineering Research Center.

Herle, Ivo and Gerd Gudehus (Sept. 1999). "Determination of parameters of a hypoplastic constitutive model from properties of grain assemblies". In: *Mechanics of Cohesive-Frictional Materials* 4, pp. 461 –486. DOI: 10.1002/(SICI)1099-1484(199909)4:5<461::AID-CFM71>3.0.CO;2-P.

Hilber, Hans M., Thomas J. R. Hughes, and Robert L. Taylor (1977). "Improved numerical dissipation for time integration algorithms in structural dynamics". In: *Earthquake Engineering & Structural Dynamics* 5.3, pp. 283–292. DOI: https://doi.org/10.1002/eqe.4290050306.

Hrennikoff, A. (Mar. 1941). "Solution of Problems of Elasticity by the Framework Method". In: *Journal of Applied Mechanics* 8.4, A169–A175. ISSN: 0021-8936. DOI: 10.1115/1.4009129.

Isbiliroglu, Yigit, Ricardo Taborda, and Jacobo Bielak (Feb. 2015). "Coupled soil-structure interaction effects of building clusters during earthquakes". In: *Earthquake Spectra* 31, p. 141208072728004. DOI: 10.1193/102412EQS315M.

Itasca Consulting Group, Inc. (Jan. 2022). *FLAC3D 7.0 Documentation, Dynamic Modelling Considerations*. Accessed 7 February 2022. URL: http://docs.itascacg.com/flac3d700/flac3d/docproject/source/options/dynamic/considerations/considerations.html.

Jaritz, W. et al. (1991). "Regionale Analyse der seismischen Geschwindigkeiten in Nordwestdeutschland". In: *Geopyshik* 45, pp. 23–57.

Kaplunov, J., D. Prikazchikov, and L. Sultanova (May 2018). "Justification and refinement of Winkler–Fuss hypothesis". In: *Zeitschrift für angewandte Mathematik und Physik* 69. DOI: 10.1007/s00033-018-0974-1.

Kaplunov, Julius and D. A. Prikazchikov (2013). "Explicit Models for Surface, Interfacial and Edge Waves". In: *Dynamic Localization Phenomena in Elasticity, Acoustics and Electromagnetism*. Ed. by Richard V. Craster and Julius Kaplunov. Vienna: Springer Vienna, pp. 73–114. ISBN: 978-3-7091-1619-7. DOI: 10.1007/978-3-7091-1619-7_3.

Kaplunov, Julius and Danila A. Prikazchikov (2017). "Chapter One - Asymptotic Theory for Rayleigh and Rayleigh-Type Waves". In: ed. by Stéphane P.A. Bordas and Daniel S. Balint. Vol. 50. Advances in Applied Mechanics. Elsevier, pp. 1–106. DOI: https://doi.org/10.1016/bs.aams.2017.01.001.

Karabalis, D. L. and D. E. Beskos (1984). "Dynamic response of 3-D rigid surface foundations by time domain boundary element method". In: *Earth. Engnq. Struct. Dyn.* 12, pp. 73–93.

Karabalis, Dimitris L. and Mohsen Mohammadi (1998). "3-D dynamic foundation-soil-foundation interaction on layered soil". In: *Soil Dynamics and Earthquake Engineering* 17.3, pp. 139–152. ISSN: 0267-7261. DOI: https://doi.org/10.1016/S0267-7261(97)00047-X.

Karantzikis, Michael and Constantine Spyrakos (Jan. 2000). "Seismic analysis of bridges including soil–abutment interaction". In.

Kausel, Eduardo (1994). "Thin-layer method: Formulation in the time domain". In: *International Journal for Numerical Methods in Engineering* 37.6, pp. 927–941. DOI: https://doi.org/10.1002/nme.1620370604.

– (2010). "Early history of soil–structure interaction". In: *Soil Dynamics and Earthquake Engineering* 30.9. Special Issue in honour of Prof. Anestis Veletsos, pp. 822–832. ISSN: 0267-7261. DOI: https://doi.org/10.1016/j.soildyn.2009.11.001.

Kawamoto, J. D. (1983). "Solution of nonlinear dynamic structural systems by a hybrid frequency-time domain approach". PhD thesis. Dept. of Civil Engineering, Massachusetts Institute of Technology.

Knappett, J. A., P. Madden, and K. Caucis (2015). "Seismic structure–soil–structure interaction between pairs of adjacent building structures". In: *Géotechnique* 65.5, pp. 429–441. DOI: 10.1680/geot.SIP.14.P.059.

Kramer, S. L. (1996). *Geotechnical Earthquake Engineering*. Prentice-Hall international series in civil engineering and engineering mechanics. Prentice Hall. ISBN: 9788131707180. URL: https://books.google.de/books?id=ws5HtVum3g8C.

Kramers, H. A. (1927). "La diffusion de la limiere par les atomes". In: *Estratto diagli Atti del Congresso Internazionale de Fisica Coma* 2, pp. 545–557.

Kronig, R. L. (1926). "On the theory of dispersion of X-rays". In: *J. Opt. Soc. Am.* 12, pp. 547–557.

Lamb, H. (1904). "On the propagation of tremors over the surface of an elastic solid". In: *Philosophical Transactions of the Royal Society of London* Series A, pp. 1–42.

Álamo, Guillermo et al. (Nov. 2015). "Structure-soil-structure interaction effects on the dynamic response of piled structures under obliquely incident seismic

shear waves". In: *Soil Dynamics and Earthquake Engineering* 78, pp. 142–153. DOI: 10.1016/j.soildyn.2015.07.013.

Liao, H. J. et al. (June 2007). "Analysis of Soil-Structure Interaction with Finite Element Method". In: *Engineering Plasticity and Its Applications*. Vol. 340. Key Engineering Materials. Trans Tech Publications Ltd, pp. 1279–1284. DOI: 10.4028/www.scientific.net/KEM.340-341.1279.

Lin, Chia-Ching et al. (1996). "An iterative finite element-boundary element algorithm". In: *Computers & Structures* 59.5, pp. 899–909. ISSN: 0045-7949. DOI: https://doi.org/10.1016/0045-7949(95)00285-5.

Liu, Yijun (2009). *Fast Multipole Boundary Element Method, Theory and Applications in Engineering*. Cambridge University Press. ISBN: 978-1-107-65566-9.

Logan, D., ed. (2007). *A First Course in the Finite Element Method*. ISBN: 0-534-55298-6.

Lysmer, J. and R. L. Kuhlemeyer (1969). "Finite-Dynamic Model for Infinite Media". In: *Journal of Engineering Mechanics Division* 95, pp. 859–878.

Manolis, G. D. and G. D. Beskos (1988). *Boundary Element Methods In Elastodynamics*. London: Allen and Unwin.

Manolis, G. D. et al. (2017). *Seismic Wave Propagation in Non-Homogeneous Elastic Media by Boundary Elements*. Springer International Publishing. DOI: 10.1007/978-3-319-45206-7_1.

Mantic, V. (1993). "A new formula for the C-matrix in the Somigliana identity". In: *Journal of Elasticity* 33.3, pp. 191–201. DOI: 10.1007/BF00043247.

Martinez, A., J. Mateo, and E. Alarcon (1996). "Dynamic soil-structure interaction in bridge abutments". In: *Advances in Boundary Element Methods*, pp. 135–143.

McHenry, D. (1943). "A lattice analogy for the solution of stress problems". In: *Journal of the Institution of Civil Engineers* 21.2, pp. 59–82. DOI: 10.1680/ijoti.1943.13967.

Mckenna, Frank (Sept. 2011). "OpenSees: A framework for earthquake engineering simulation". In: *Computing in Science & Engineering* 13, pp. 58 –66. DOI: 10.1109/MCSE.2011.66.

Melosh, R. J. (1961). "A stiffness matrix for the analysis of thin plates in bending". In: *Journal of the Aerospace Sciences* 28.1, pp. 34–42. DOI: 10.2514/8.8850.

– (1963). "Structural analysis of solids". In: *Journal of the Structural Division* 89, pp. 205–248.

Moehle, J. P. and M. O. Eberhard (2003). "Bridge Engineering Handbook". In: CRC Press. Chap. Earthquake damage to bridges.

Mossessian, T. K. and M. Dravinski (1990). "Amplification of elastic waves by a three dimensional valley. Part 1: steady state response". In: *Earth. Eng. Struc. Dyn.* 19, pp. 667–680.

Mulliken, Jeffrey S. and Dimitris L. Karabalis (1998). "Discrete model for dynamic through-the-soil coupling of 3-D foundations and structures". In: *Earthquake Engineering & Structural Dynamics* 27.7, pp. 687–710. DOI: https://doi.org/10.1002/(SICI)1096-9845(199807)27:7<687::AID-EQE752>3.0.CO;2-O.

Mylonakis, G. and G. Gazetas (2000). "Seismic soil-structure interaction: Beneficial or detrimental?" In: *Journal of Earthquake Engineering* 4.3, pp. 277–301. DOI: 10.1080/13632460009350372.

Mylonakis, George et al. (2006). "The role of soil in the collapse of 18 piers of Hanshin Expressway in the Kobe earthquake". In: *Earthquake Engineering & Structural Dynamics* 35.5, pp. 547–575. DOI: https://doi.org/10.1002/eqe.543.

Nakano, H. (1923). "Notes on the nature of the forces which gives rise to the earthquake motions". In: *Seismological Bull. Cent. Metrological Obs. Jpn.* 1.1, pp. 90–120.

NEHRP (1997). *Recommended provisions for seismic regulations for new buildings and other structures*. Vol. Part 1 and 2. Washington, D.C.: Building Seismic Safety Council.

Obrembski, Christophe, Didier Clouteau, and Nicolas Greffet (May 2005). "Algorithme "temps-fréquence" pour ladynamique non linéaire en interaction sol-structure". In: *7e colloque national en calcul des structures*. hal-01813063.

Padrón, L.A., J.J. Aznárez, and O. Maeso (2009). "Dynamic structure–soil–structure interaction between nearby piled buildings under seismic excitation by BEM–FEM model". In: *Soil Dynamics and Earthquake Engineering* 29.6, pp. 1084–1096. ISSN: 0267-7261. DOI: https://doi.org/10.1016/j.soildyn.2009.01.001. URL: https://www.sciencedirect.com/science/article/pii/S0267726109000025.

Panagiotopulos, C. G. and G. D. Manolis (2011). "Stability issues in 3D BEM formulations for transient elastodynamics". In: *Transactions on Modelling and Simulation* 52. DOI: 10.2495/BE110131.

Pitilakis, D. et al. (Apr. 2006). "Soil-structure interaction: Linear, equivalent linear and nonlinear approximation for the soil behavior modeling; a comparative study". In: *100th Anniversary Earthquake Conference*. San Francisco, CA.

Pitilakis, Dimitris and Anna Karatzetzou (Apr. 2014). "Dynamic stiffness of monumental flexible masonry foundations". In: *Bulletin of Earthquake Engineering* 13. DOI: 10.1007/s10518-014-9611-3.

Poursartip, Babak, Arash Fathi, and John L. Tassoulas (2020). "Large-scale simulation of seismic wave motion: A review". In: *Soil Dynamics and Earthquake*

Engineering 129, p. 105909. ISSN: 0267-7261. DOI: https://doi.org/10.1016/j.soildyn.2019.105909.

Qian, J. and D. E. Beskos (1995). "Dynamic interaction between 3-D rigid surface foundations and comparison with the ATC-3 provisions". In: *Earthquake Engineering & Structural Dynamics* 24.3, pp. 419–437. DOI: https://doi.org/10.1002/eqe.4290240309. eprint: https://onlinelibrary.wiley.com/doi/pdf/10.1002/eqe.4290240309.

– (1996). "Harmonic wave response of two 3-D rigid surface foundations". In: *Soil Dynamics and Earthquake Engineering* 15.2, pp. 95–110. ISSN: 0267-7261. DOI: https://doi.org/10.1016/0267-7261(95)00026-7. URL: https://www.sciencedirect.com/science/article/pii/0267726195000267.

Qian, J., L. G. Tham, and Y. K. Cheung (1996). "Dynamic cross-interaction between flexible surface footings by combined BEM and FEM". In: *Earthquake Engineering and Structural Dynamics* 25.5, pp. 509–526. URL: https://eurekamag.com/research/018/777/018777572.php.

Reissner, E. (1936). "Stationare axialsymmetrische durch eine schuttelnde masse erregte schwingungen eines homogenen elastischen halbraumes". In: *Ingenieur-Archiv* 7 (6), 381–396.

Resendiz, D. and J. M. Roesset (1987). "Soil-structure interaction in Mexico City during 1985 earthquake". In: *The Mexico Earthquakes of 1985*. Ed. by M. A. Cassaro and E. M. Romero, pp. 193–203.

Richart, F. E., R. D. Woods, and J. R. Hall (1970). *Vibrations of Soils and Foundations*. Prentice-Hall, New Jersey.

Rizos, D. C. and Z. Wang (2002). "Coupled BEM–FEM solutions for direct time domain soil–structure interaction analysis". In: *Engineering Analysis with Boundary Elements* 26.10, pp. 877–888. ISSN: 0955-7997. DOI: https://doi.org/10.1016/S0955-7997(02)00057-7. URL: https://www.sciencedirect.com/science/article/pii/S0955799702000577.

Rizzo, F. J. (1967). "An integral equation approach to boundary value problems of classical elastistatic". In: *Quarterly of Applied Mathematics* 25.1, pp. 83–95. (Visited on 04/10/2022).

Rizzo, F. J. and D. J. Shippy (1968). "A formulation and solution procedure for the general non-homogeneous elastic inclusion problem". In: *International Journal of Solids and Structures* 4.12, pp. 1161–1179. ISSN: 0020-7683. DOI: https://doi.org/10.1016/0020-7683(68)90003-6.

Rokhlin, V. (1985). "Rapid solution of integral equations of classical potential theory". In: *Journal of Computational Physics* 60.2, pp. 187–207. ISSN: 0021-9991. DOI: https://doi.org/10.1016/0021-9991(85)90002-6.

Schanz, M. and H. Antes (1997a). "A new visco- and elastodynamic time domain Boundary Element formulation". In: *Computational Mechanics* 20, pp. 452–459. DOI: https://doi.org/10.1007/s004660050265.

– (1997b). "Application of 'Operational Quadrature Methods' in time domain boundary element methods". In: *Meccanica* 32, pp. 179–186. DOI: https://doi.org/10.1023/A:1004258205435.

Schauer, M. and G. R. Rodriguez (2019). "A coupled FEM-SBFEM approach for soil-structure-interaction analysis using non-matching meshes at the near-field far-field interface". In: *Soil Dynamics and Earthquake Engineering* 121, pp. 466–479. ISSN: 0267-7261. DOI: https://doi.org/10.1016/j.soildyn.2019.01.033.

Smith, Michael (2014). *ABAQUS/Standard User's Manual, Version 6.14*. English. United States: Dassault Systèmes Simulia Corp.

Soares, D. (Oct. 2008). "An optimised FEM-BEM time-domain iterative coupling algorithm for dynamic analyses". In: *Comput. Struct.* 86.19–20, 1839–1844. ISSN: 0045-7949. DOI: 10.1016/j.compstruc.2008.04.001.

Soares, D. and L. Godinho (2015). "Inelastic 2D analysis by adaptive iterative BEM–FEM coupling procedures". In: *Computers & Structures* 156, pp. 134–148. ISSN: 0045-7949. DOI: https://doi.org/10.1016/j.compstruc.2015.05.007.

Soares, D., W. J. Mansur, and O. Von Estorff (2007). "An efficient time-domain FEM/BEM coupling approach based on FEM implicit Green's functions and truncation of BEM time convolution process". In: *Computer Methods in Applied Mechanics and Engineering* 196.9, pp. 1816–1826. ISSN: 0045-7825. DOI: https://doi.org/10.1016/j.cma.2006.10.001.

Soares Jr, D., O. von Estorff, and W. J. Mansur (June 2004). "Iterative coupling of BEM and FEM for nonlinear dynamic analyses". In: *Computational Mechanics* 34, pp. 67–73. DOI: 10.1007/s00466-004-0554-4.

Spyrakos, C. and G. Loannidis (2003). "Seismic behavior of a post-tensioned integral bridge including soil–structure interaction (SSI)". In: *Soil Dynamics and Earthquake Engineering* 23.1, pp. 53–63. ISSN: 0267-7261. DOI: https://doi.org/10.1016/S0267-7261(02)00150-1.

Spyrakos, C. C. and D. E. Beskos (1986). "Dynamic response of flexible strip-foundations by boundary and finite elements". In: *Soil Dynamics and Earthquake Engineering* 5.2, pp. 84–96. ISSN: 0267-7261. DOI: https://doi.org/10.1016/0267-7261(86)90002-3.

Stein, S. and M. Wysession (1991). *An Introduction to Seismology, Earthquakes, and Earth Structure*. Wiley-Blackwell. ISBN: 978-0-865-42078-6. DOI: 10.1063/1.1629009.

Sung, T. Y. (1953). "Vibrations in semi-infinite solids due to periodic surface loadings". In: *Symp. on Dyn. Test. of Soils ASTM-STP* 56, pp. 35–64.

Tamhidi, Aidin and Mohammad Ali Ghannad (2020). "The Effect of Soil Modeling on the Nonlinear Response of SDOF Structures". In: *Structures Congress 2020*, pp. 432–448. DOI: 10.1061/9780784482896.040.

Triantafyllidis, Th. and B. Prange (1987). "Dynamic subsoil-coupling between rigid rectangular foundations". In: *Soil Dynamics and Earthquake Engineering* 6.3, pp. 164–179. ISSN: 0267-7261. DOI: https://doi.org/10.1016/0267-7261(87)90013-3. URL: https://www.sciencedirect.com/science/article/pii/0267726187900133.

Turner, M. J. et al. (1956). "Stiffness and Deflection Analysis of Complex Structures". In: *Journal of the Aeronautical Sciences* 23.9, pp. 805–823. DOI: 10.2514/8.3664.

U.S.G.S. (June 2012). *Magnitude 9.1 - Off the West Coast of Northern Sumatra*. Accessed 28 March 2022. U.S. Department of the Interior. URL: https://web.archive.org/web/20120817004055/http://earthquake.usgs.gov/earthquakes/eqinthenews/2004/us2004slav/#summary.

Vasilev, G. et al. (2015). "Soil-structure interaction using BEM–FEM coupling through ANSYS software package". In: *Soil Dynamics and Earthquake Engineering* 70, pp. 104 –117. DOI: https://doi.org/10.1016/j.soildyn.2014.12.007.

Vicencio, Felipe and Nicholas Alexander (May 2018a). "Dynamic interaction between adjacent buildings through nonlinear soil during earthquakes". In: *Soil Dynamics and Earthquake Engineering* 108, p. 130 141. DOI: 10.1016/j.soildyn.2017.11.031.

– (Nov. 2018b). "Higher mode seismic structure-soil-structure interaction between adjacent building during earthquakes". In: *Engineering Structures* 174, pp. 322–337. DOI: 10.1016/j.engstruct.2018.07.049.

Vicencio, Felipe and Nicholas A. Alexander (2019). "Dynamic Structure-Soil-Structure Interaction in unsymmetrical plan buildings due to seismic excitation". In: *Soil Dynamics and Earthquake Engineering* 127, p. 105817. ISSN: 0267-7261. DOI: https://doi.org/10.1016/j.soildyn.2019.105817.

– (2021). "Method to evaluate the dynamic structure-soil-structure interaction of 3-D buildings arrangement due to seismic excitation". In: *Soil Dynamics and Earthquake Engineering* 141, p. 106494. ISSN: 0267-7261. DOI: https://doi.org/10.1016/j.soildyn.2020.106494.

von Estorff, O. and M. Firuziaan (2000). "Coupled BEM/FEM approach for nonlinear soil/structure interaction". In: *Engineering Analysis with Boundary Elements* 24.10, pp. 715–725. ISSN: 0955-7997. DOI: https://doi.org/10.1016/S0955-7997(00)00054-0.

von Estorff, O. and C. Hagen (Aug. 2005). "Iterative coupling of FEM and BEM in 3D transient elastodynamics". In: *Engineering Analysis with Boundary Elements* 29, pp. 775–787. DOI: 10.1016/j.enganabound.2005.04.004.

Vucetic, Mladen (1994). "Cyclic Threshold Shear Strains in Soils". In: *Journal of Geotechnical Engineering* 120.12, pp. 2208–2228. DOI: 10.1061/(ASCE)0733-9410(1994)120:12(2208).

Waldin, J., J. Jennings, and P. Routledge (2012). "Critically damaged bridges & concepts for earthquake recovery". In.

Wang, S. and G. Schmid (1992). "Dynamic structure-soil-structure interaction by FEM and BEM". In: *Computational Mechanics* 9.3, pp. 347–357. ISSN: 1432-0924. DOI: https://doi.org/10.1007/BF00370014.

Wearing, J. L., M. A. Sheikh, and M. C. Burstow (1991). "A Combined Finite Element Boundary Element Approach for Elasto-Plastic Analysis". In: *Boundary Integral Methods*. Ed. by Luigi Morino and Renzo Piva. Berlin, Heidelberg: Springer Berlin Heidelberg, pp. 500–509. ISBN: 978-3-642-85463-7.

Werner, S. D., J. L. Beck, and M. B. Levine (1987). "Seismic refraction evaluation of Meloland road overpass using the 1979 Imperial Valley earthquake records". In: *Earthquake Eng. and Structural Dynamics* 15, pp. 249–274.

Werner, S. D., J. L. Beck, and A. Nisar (1990). "Dynamic tests and seismic excitation of a bridge structure". In: *The 4th U.S. Natl. Conference on Earthquake Engineering*. Vol. 1, pp. 1037–1046.

Wilson, J. C. and B. S. Tan (1990). "Bridge abutments: Assessing their influence on earthquake response of meloland road overpass". In: *Journal of Engineering Mechanics*, pp. 1838–56. DOI: 10.1061/(ASCE)0733-9399(1990)116:8(1838).

Wilson, R. B. and T. A. Cruse (1978). "Efficient implementation of anisotropic three dimensional boundary-integral equation stress analysis". In: *International Journal for Numerical Methods in Engineering* 12.9, pp. 1383–1397. DOI: https://doi.org/10.1002/nme.1620120907.

Winkler, E. (1867). *Die Lehre von der Elasticitaet und Festigkeit*. Prag, Dominicus.

Wolf, J. P. (1985). *Dynamic Soil-Structure Interaction*. Prentice-Hall international series in civil engineering and engineering mechanics. Prentice Hall. ISBN: 013221565901.

Wong, H. L. and M. D. Trifunac (Dec. 1975). "Two-dimensional, antiplane, building-soil-building interaction for two or more buildings and for incident planet SH

waves". In: *Bulletin of the Seismological Society of America* 65.6, pp. 1863–1885. ISSN: 0037-1106. DOI: 10.1785/BSSA0650061863.

Yashinsky, Mark (1998). *The Loma Prieta, California Earthquake of October 17, 1989: Performance of the Built Environment-Highway Systems*. Tech. rep. 1552-B. U.S. Geological Survey.

Yön, Burak, Erkut Sayın, and Onur Onat (2017). "Earthquakes and Structural Damages". In: *Earthquakes*. Ed. by Taher Zouaghi. Rijeka: IntechOpen. Chap. 13. DOI: 10.5772/65425.

Z. Jahromi, Hamid, Bassam Izzuddin, and Lidija Zdravkovic (Mar. 2008). "Partitioned analysis of nonlinear soil-structure interaction using iterative coupling". In: *Interaction and multiscale mechanics* 1. DOI: 10.12989/imm.2008.1.1.033.

Zangeneh Kamali, A. (2018). *Dynamic Soil-Structure Interaction Analysis of Railway Bridges : Numerical and Experimental Results*. QC 20180315.

Zienkiewicz, O. C., D. W. Kelly, and P. Bettess (1977). "The coupling of the finite element method and boundary solution procedures". In: *International Journal for Numerical Methods in Engineering* 11.2, pp. 355–375. DOI: https://doi.org/10.1002/nme.1620110210.

Experiences and studies have shown that soil-structure interaction (SSI) effect has a vital role in the dynamic behaviour of a soil-structure system. Despite this, analyses involving dynamic SSI are still challenging for practicing engineers due to their complexity and accessibility. In this thesis, the hybrid BEM-FEM implementation is aimed at practicality by combining commercial software and an in-house code. The pre-processing task can be performed under one graphical environment, and it is enhanced with the capability to compute different types of dynamic sources and other improvements to increase its eff ciency, accuracy, and modeling f exibility.

Further, the underlying soil is commonly a layered prof le with arbitrary geometries. Most existing solutions solve the problem through simplif cation of the geometry and pattern. One of the main contributions in this thesis is the development of layer-wise condensation method to solve these cases using hybrid BEM-FEM. The method signif cantly reduces the computational memory requirement. Another challenge in the dynamic SSI addressed in this work is the consideration of secondary nonlinearities. Existing solutions using the time domain BEM and iterative hybrid method are computationally costly, and implementation of such a hybrid method on commercial software is tedious. The solution to address this case using a sequential frequency-time domain procedure is presented. The relatively simple approach makes it possible to consider the nonlinearities in the simulation without using the time domain BEM and without requiring additional iterations.

Case studies demonstrating the application of the enhanced hybrid method are presented including cases of 2D and 3D bridges, containment structures, and a 3D multi-storey structure under point source and double-couple source excitations. These case studies illustrate the role of following critical factors in SSI problems: (1) the dynamic site effect due to impedance contrast of soil layers, (2) lateral inhomogeneity effect, (3) inf uence of the dynamic source properties, (4) conversion of body waves into surface waves, (5) soil-foundation or soil-structure dynamic interaction, and (6) inf uence of secondary nonlinearities.

ISSN: 2365-7162